The NIST CENTER for NEUTRON RESEARCH

2010
Accomplishments and Opportunities

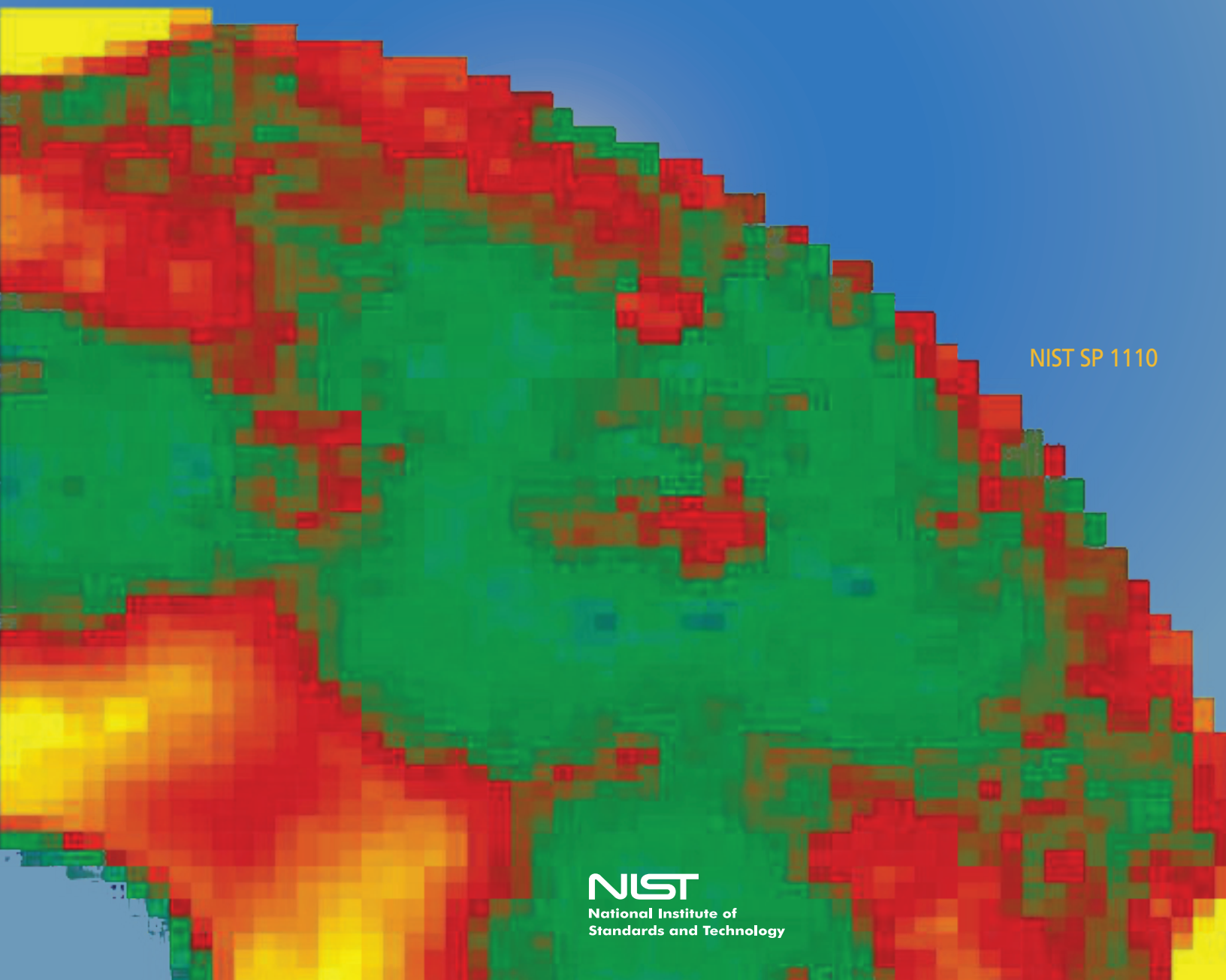

NIST SP 1110

NIST
National Institute of
Standards and Technology

This page intentionally blank.

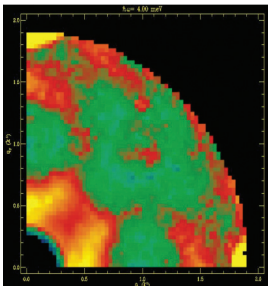

ON THE COVER

Neutron intensity in a constant energy cut in the *x,y* plane at 4 meV for *Q* values ranging from 0 $Å^{-1}$ to 2 $Å^{-1}$ displaying phonons and magnetic excitations in a compound of $FeTe_{0.7}Se_{0.3}$ at 30 K. Investigations in this class of materials are focused on the subtle interplay between superconductivity and magnetism. Data, courtesy of NCNR's Songxue Chi, are from the MACS instrument…20 g of aligned sample, 2 hour scan.

2010 NIST Center for Neutron Research

Accomplishments and Opportunities

NIST Special Publication 1110

Robert M. Dimeo, Director

Ronald L. Cappelletti, Editor

December 2010

National Institute of Standards and Technology
Patrick Gallagher, Director

U.S. Department of Commerce
Gary Locke, Secretary

DISCLAIMER

Certain commercial entities, equipment, or materials may be identified in this document in order to describe an experimental procedure or concept adequately. Such identification is not intended to imply recommendation or endorsement by the National Institute of Standards and Technology, nor is it intended to imply that the entities, materials, or equipment are necessarily the best available for the purpose.

National Institute of Standards and Technology
Special Publication 1110

Natl. Inst. Stand. Technol. Spec. Publ. 1110, 88 pages
(December 2010)

CODEN: NSPUE2

U.S. GOVERNMENT PRINTING OFFICE-WASHINGTON: 2010

For sale by the Superintendent of Documents,
U.S. Government Printing Office

Internet: bookstore.gpo.gov Phone: 1.866.512.1800
Fax: 202.512.2104 Mail Stop: SSOP, Washington, DC 20402-0001

Table of Contents

iv FOREWORD

1 THE NIST CENTER FOR NEUTRON RESEARCH

2 NIST CENTER FOR NEUTRON RESEARCH INSTRUMENTS

4 NCNR IMAGES 2010

HIGHLIGHTS

CONDENSED MATTER

6 Core-shell magnetic morphology of magnetite nanoparticles

8 Electric field control of magnetization in multiferroic $HoMnO_3$: the importance of magnetic domains

10 Frustrated magnetism and superconductivity in $Fe_{1+y}Se_{0.4}Te_{0.6}$

12 Lattice distortion and magnetic quantum phase transition in $CeFeAs_{1-x}P_xO$

14 Tuning the magnetic and structural properties of $Fe_{1+x}Te$

BIOLOGY

16 Neutron reflectometry study of the conformation of HIV Nef bound to lipid membranes

18 How does the stiffness of lipid vesicles change as they interact with pore-forming peptides?

20 Bilayer membrane dynamics in NSAID-phospholipid adducts

ENGINEERING

22 A method for the measurement of retained austenite content in steels

24 Probing artificial muscles with neutrons

CHEMICAL PHYSICS

26 'Molecular headphones', SANS and MD modeling of protein denaturing

28 Coordinatively-unsaturated metal-organic frameworks for hydrogen storage

30 Graphite oxide framework (GOF) materials for hydrogen storage

32 New insight into the crystal structure of highly piezoelectric PZT: a single crystal diffraction study

34 Multiple filling of voids improves thermoelectric efficiency of skutterudites

SOFT MATTER

36 Observation of thickness fluctuations in surfactant membranes

38 Neutron transmission measurements of concentration profiles in non-homogeneous shear flows

40 Mechanism of molecular exchange in copolymer dispersions

42 How does ionic liquid distribute between microphase-separated domains of a block copolymer?

NEUTRON PHYSICS

44 Decoherence-free neutron interferometry

ADVANCES IN MEASUREMENT

46 Software for biological soft condensed matter science

47 Following lithium through battery components and functioning prototypes

48 Peering inside: imaging an object's interior while clarifying its elemental makeup

49 Time-resolved SANS with sub-millisecond resolution (t-SANS)

50 Elemental analysis of a single-wall carbon nanotube candidate reference material

51 NEUTRON SOURCE OPERATIONS

52 EXPANSION INITIATIVE

55 FACILITY DEVELOPMENT

58 SERVING THE SCIENCE AND TECHNOLOGY COMMUNITY

60 THE CENTER FOR HIGH RESOLUTION NEUTRON SCATTERING (CHRNS)

63 AWARDS 2010

65 PUBLICATIONS

80 INSTRUMENTS AND CONTACTS

CONTACTS (inside back cover)

Foreword

I am pleased to present to you this year's annual report for the NIST Center for Neutron Research, containing a sample of the NCNR's recent accomplishments and opportunities in 2010. At this time last year, construction work for the NCNR Expansion Project was underway for the expanded guide hall and technical support building (TSB). A lot can happen in a year! The civil construction is complete and staff have moved into the TSB, now known as the "K-wing" of building 235. The guide hall extension, which will house both relocated and new cold neutron instruments, was empty when we took ownership of it in August, but now contains equipment for the Expansion including guide casings, shielding, and instrument components. And much more equipment is on its way.

Change was not only evident with the inauguration of the two new buildings but also in staffing. After six years of service to NCNR and NIST, Wade Richards, Chief of Reactor Operations and Engineering, retired. Wade led the Reactor Operations group through a period of significant change and growth, culminating with the successful relicensing in 2009. This was an outstanding apex to a noteworthy career. In order to carry on the tradition of excellence in reactor operations, Sean O'Kelly, who joined the NCNR in 2009, was appointed Chief of Reactor Operations and Engineering. Sean brings with him not only extensive technical knowledge but also significant experience managing a reactor facility.

It was yet another great year for facility operations thanks to our dedicated staff. The reactor operated at full power (20 MW) for 267 days, marking this year as one of the highest in source and instrument availability. Numerous developments contributed to a successful year. In this report you will read about technical developments such as our growing ^{3}He neutron spin filter program which is providing entirely new measurement capabilities for our users. This technology is fast becoming a standard capability for neutron beam experiments as is evident in the rapidly growing number of experiments and published results. The quality of science done with NCNR facilities continues to be excellent and is reflected in resulting high impact publications. Innovations and developments permitting users to more easily perform the best measurements can be attributed to many factors but the most important one is clearly our highly talented and dedicated staff.

The upcoming year will be one of very intense activity. In order to carry out the reactor reliability enhancements that are part of the Expansion Project and the American Recovery and Reinvestment Act, the reactor will be shut down for 11 months starting in April 2011. During this time we will also undertake numerous instrumentation and beam delivery projects that will set the stage for the next phase of facility development at the NCNR. We have been carefully planning the sequence of activities for some time to ensure that a new and improved facility is available to the scientific community on schedule.

As ever, the reason for the NCNR is the excellent science that comes from the many researchers who use our facility. I continue to enjoy walking through the facility and talking with our users about their latest exciting experiments. You will find specific research highlights in the pages that follow. I hope that you enjoy reading them as much as I have.

The NIST Center for Neutron Research

Neutrons provide a uniquely effective probe of the structure and dynamics of materials ranging from water moving in waste-storage glasses to magnetic domains in memory storage materials. The properties of neutrons (outlined below) can be exploited using a variety of measurement techniques to provide information not otherwise available. The positions of atomic nuclei in crystals, especially of those of light atoms, can be determined precisely. Atomic motion can be directly measured and monitored as a function of temperature or pressure. Neutrons are especially sensitive to hydrogen, so that hydrogen motion can be followed in H-storage materials and water flow in fuel cells can be imaged. Residual stresses such as those deep within oil pipelines or in highway trusses can be mapped. Neutron-based measurements contribute to a broad spectrum of activities including in engineering, materials development, polymer dynamics, chemical technology, medicine, and physics.

The NCNR's neutron source provides the intense, conditioned beams of neutrons required for these types of measurements. In addition to the thermal neutron beams from the heavy water or graphite moderators, the NCNR has a large area liquid hydrogen moderator, or cold source, that provides long wavelength guided neutron beams for the major cold neutron facility in the U.S.

There are currently 29 experiment stations: four provide high neutron flux positions for irradiation, and 25 are beam facilities most of which are used for neutron scattering research. The subsequent pages provide a schematic description of our instruments. More complete descriptions can be found at www.ncnr.nist.gov/instruments/. Construction of a second guide hall is now complete (see pp. 52-54) and five new instruments are under development.

Present guide hall and instruments.

The Center supports important NIST measurement needs, but is also operated as a major national user facility with merit-based access made available to the entire U.S. technological community. Each year, more than 2000 research participants from government, industry, and academia from all areas of the country use the facility. Beam time for research to be published in the open literature is without cost to the user, but full operating costs are recovered for proprietary research. Access is gained mainly through a web-based, peer-reviewed proposal system with user time allotted by a beamtime allocation committee twice a year. For details see www.ncnr.nist.gov/beamtime.html. The National Science Foundation and NIST co-fund the Center for High Resolution Neutron Scattering (CHRNS) that operates six of the world's most advanced instruments (see pp. 60-62). Time on CHRNS instruments is made available through the proposal system. Some access to beam time for collaborative measurements with the NIST science staff can also be arranged on other instruments.

Why Neutrons?

Neutrons reveal properties not readily probed by photons or electrons. They are electrically neutral and therefore easily penetrate ordinary matter. They behave like microscopic magnets, propagate as waves, can set particles into motion losing or gaining energy and momentum in the process, and they can be absorbed with subsequent emission of radiation to uniquely fingerprint chemical elements.

WAVELENGTHS – in practice range from ≈ 0.01 nm (thermal) to ≈ 1.5 nm (cold) (1 nm = 10 Å), allowing the formation of observable interference patterns when scattered from structures as small as atoms to as large as biological cells.

ENERGIES – of millielectronvolts, the same magnitude as atomic motions. Exchanges of energy as small as nanoelectronvolts and as large as tenths of electronvolts can be detected between samples and neutrons, allowing motions in folding proteins, melting glasses and diffusing hydrogen to be measured.

SELECTIVITY – in scattering power varies from nucleus to nucleus somewhat randomly. Specific isotopes can stand out from other isotopes of the same kind of atom. Specific light atoms, difficult to observe with x-rays, are revealed by neutrons. Hydrogen, especially, can be distinguished from chemically equivalent deuterium, allowing a variety of powerful contrast techniques.

MAGNETISM – makes the neutron sensitive to the magnetic moments of both nuclei and electrons, allowing the structure and behavior of ordinary and exotic magnetic materials to be detailed precisely.

NEUTRALITY – of the uncharged neutrons allows them to penetrate deeply without destroying samples, passing through walls that condition a sample's environment, permitting measurements under extreme conditions of temperature and pressure.

CAPTURE – characteristic radiation emanating from specific nuclei capturing incident neutrons can be used to identify and quantify minute amounts of elements in samples as diverse as ancient pottery shards and lake water pollutants.

NIST Center for Neutron Research Instruments

[1] BT-5 Perfect Crystal Ultra-Small Angle Neutron Scattering (USANS) Diffractometer for microstructure up to 10^4 nm, part of CHRNS.

[2] BT-4 Filter Analyzer Neutron Spectrometer with cooled Be/Graphite filter analyzer for chemical spectroscopy.

[3] BT-2 Neutron Imaging Facility for imaging hydrogenous matter in large components such as water in fuel cells and lubricants in engines, in partnership with General Motors.

[4] BT-1 Powder Diffractometer with 32 detectors; incident wavelengths of 0.208 nm, 0.154 nm, and 0.159 nm, with highest resolution of $\delta d/d \cong 8 \times 10.^{-4}$

[5] BT-9 Thermal Triple Axis Spectrometer for measurements of excitations and structure in condensed matter.

[6] BT-8 Residual Stress Diffractometer optimized for depth profiling of residual stresses in large components.

[7] VT-5 Thermal Neutron Capture Prompt Gamma-ray Activation Analysis Instrument with a neutron fluence rate of 3×10^8 cm $^{-2}$ s^{-1} used for quantitative elemental analysis of bulk materials. Generally used for the analysis of highly hydrogenous materials (≅1 % H) such as foods, oils, and biological materials.

[8] BT-7 Thermal Triple Axis Spectrometer with large double focusing monochromator, and interchangeable analyzer/detectors systems.

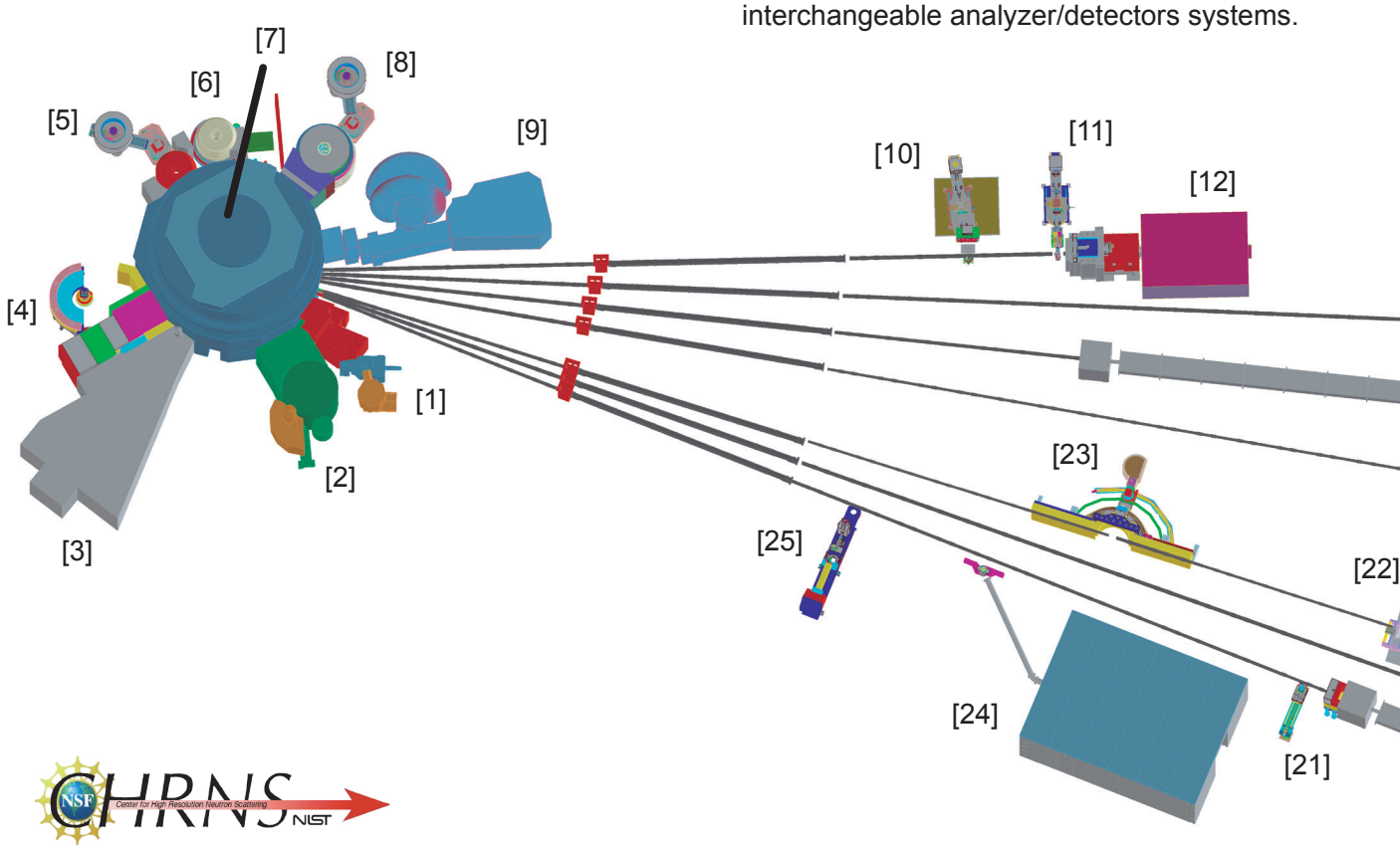

CHRNS
Center for High Resolution Neutron Scattering
NSF
NIST

The Center for High Resolution Neutron Scattering (CHRNS) is a partnership between NIST and the National Science Foundation that develops and operates neutron scattering instrumentation for use by the scientific community. The following instruments are part of the Center: 1 (USANS), 9 (MACS), 13 (HFBS), 14 (NG-3 SANS), 15 (DCS), 22 (NSE), and 23 (SPINS).

[9] NG-0 MACS cold neutron triple axis crystal spectrometer (being commissioned) with double focusing monochromator and multiple crystal analyzer/detectors that can be flexibly configured for several energies simultaneously or for high throughput at one energy, part of CHRNS.

[10] NG-1 Advanced Neutron Diffractometer / Reflectometer (AND/R) a vertical sample reflectometer with polarization analysis and off-specular reflection capabilities for measuring reflectivities down to 10^{-8}.

[11] NG-1 Vertical Sample Reflectometer instrument with polarization analysis capability for measuring reflectivities down to 10^{-8} to determine subsurface structure.

[12] NG-1 Cold Neutron Depth Profiling instrument for quantitative profiling of subsurface impurities.

[13] NG-2 Backscattering Spectrometer (HFBS) high intensity inelastic scattering instrument with energy resolution < 1 μeV, for studies of motion in molecular and biological systems, part of CHRNS.

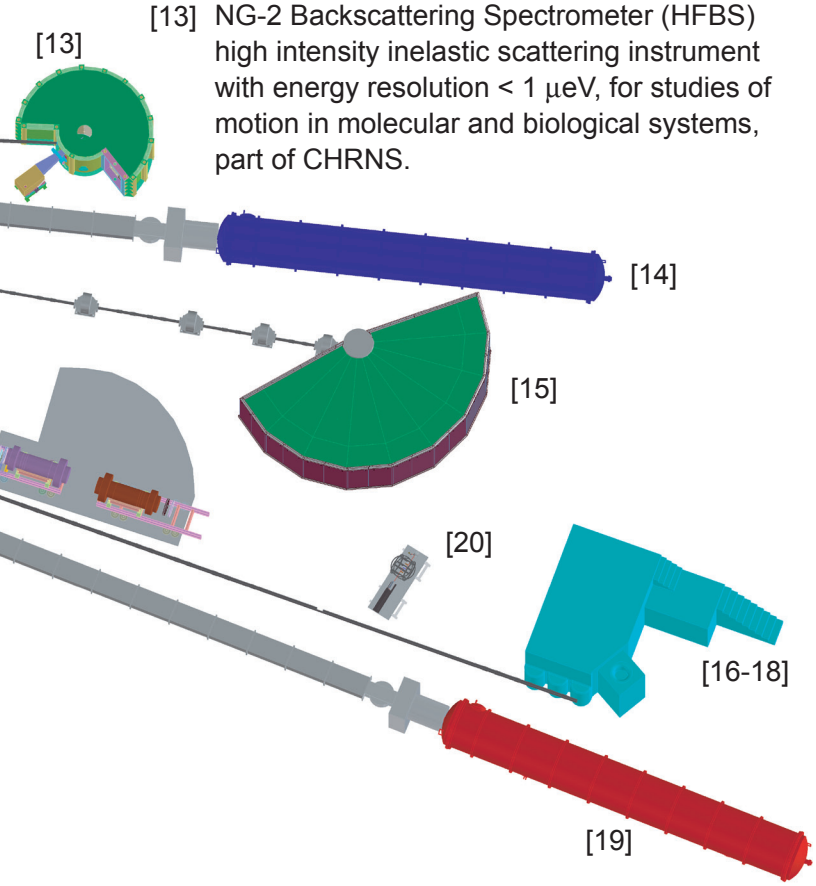

[14] NG-3 30 m SANS for microstructure measurements, part of CHRNS.

[15] NG-4 Disk Chopper Time-of-Flight Spectrometer for studies of diffusive motions and low energy dynamics of materials. Wavelengths from ≅ 0.18 nm to 2.0 nm give corresponding energy resolutions from ≅ 2 meV to < 10 μeV, part of CHRNS.

[16-18] NG-6 Neutron Physics Station offering three cold neutron beams having wavelengths of 0.5 nm, 0.9 nm, and “white” that are available for fundamental neutron physics experiments.

[19] NG-7 30 m SANS for microstructure measurements, in partnership with NIST, and ExxonMobil.

[20] NG-6 Neutron Physics Test Bed for developing measurement techniques and detectors.

[21] NG-7 Prompt Gamma Activation Analysis, cold neutron fluxes allow detection limit for H of 1 μg to 10 μg, depending on the matrix. Focused beams are available for profiling.

[22] NG-5 Neutron Spin-Echo Spectrometer (NSE) for measuring dynamics from 100 ns to 10 ps, in partnership with ExxonMobil, part of CHRNS.

[23] NG-5 Spin-Polarized Triple Axis Spectrometer (SPINS) using cold neutrons with position sensitive detector capability for high-resolution studies, part of CHRNS.

[24] NG-7 Neutron Interferometry and Optics Station with perfect crystal silicon interferometer. A vibration isolation system provides exceptional phase stability and fringe visibility.

[25] NG-7 Horizontal Sample Reflectometer allows reflectivity measurements of free surfaces, liquid/vapor interfaces, as well as polymer coatings.

NCNR Images 2010

NCNR's Juscelino Leão and middle school teacher Lauren Rogers look for crystals emerging from solution.

Wow! NCNR Summer School students encounter great data!

Alex Ye, SHIP student, developed a crystal orientation program with NCNR's William Ratcliff.

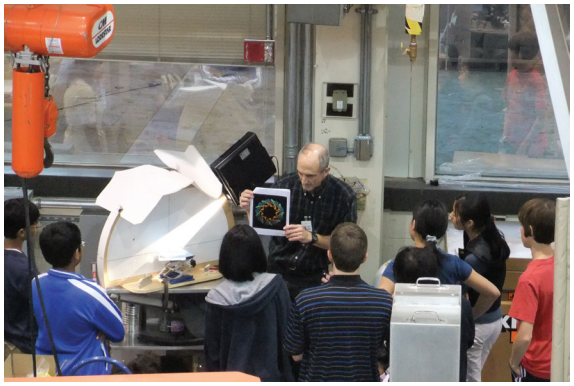

Chuck Majkrzak demonstrates diffraction and shows an image of a wreath-like macromolecule.

Cabot Corp's Jennifer Gough-Belleau prepares samples for a SANS/USANS measurement.

NCNR's Antonio Faraone lends a NSE hand to ORNL's Gerot Rothner and Dave Wesolowski.

Four generations of Reactor Operations Chiefs: Sean O'Kelly (present), Wade Richards, Sy Weiss and Tawfik Raby (original).

Don't try this at home, Dr. Lynn warns. You have to be a professional to shatter rose petals with liquid nitrogen. Safety glasses, everyone?

Springtime at the NCNR

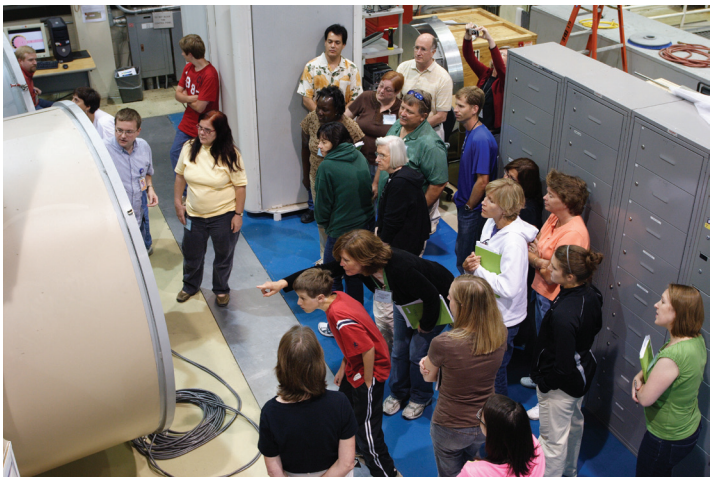

Really! There was a neutron there just 15 minutes ago! But young scientist Nathan Wade remains skeptical.

Notre Dame's Morton Eskildsen applies SANS to reveal the metastable vortex phases in MgB_2.

Does water move in waste-storage glass? Ask PNNL's Kyle Alvine.

NCNR, including expansion buildings, as seen from the air, Sept. 18, 2010.

NIST PECASE awardees Craig Brown (NCNR) and Dean De Longchamp (Polymers) flank Presidential Science Advisor, Jon Holdren.

Core-shell magnetic morphology of magnetite nanoparticles

K.L. Krycka[1], R.A. Booth[2], C.R. Hogg[2], Y. Ijiri[3], J.A. Borchers[1], W.C. Chen[1,4], S.M.Watson[1], M. Laver[5], T.R. Gentile[1], L.R. Dedon[3], S. Harris[3], J.J. Rhyne[6], and S. A. Majetich[2]

Magnetic nanoparticles hold great promise for applications as diverse as hyperthermic treatment of cancer (requiring a high degree of co-operative magnetic interaction) to compact data storage (where individual bits must act independently). However, this long-range, collective magnetic behavior is affected not only by the concentration and distance between particles, but also by their internal magnetic structure or morphology. Little is known about this internal magnetic response to magnetic stimuli, especially of those embedded deep within a nanoparticle assembly, since conventional probes either measure only the total net magnetic moment or are surface limited. In this article we highlight a novel application of small-angle neutron scattering (SANS) with polarization analysis to measure the 3D magnetic morphology for a collection of nanoparticles [1]. Applied to 9 nm magnetite nanoparticles [2] closely packed together into face-centered cubic (FCC) crystal lattice, this technique revealed an unexpected magnetic core-shell morphology under conditions for which all the magnetic moments nominally appear to be aligned or "saturated" using convention probes.

Magnetite (Fe_3O_4) was long ago discovered as lodestone used for making compasses and has a magnetic moment about one-fifth that of iron. It is biocompatible and resistant to oxidation, making it an ideal candidate for biomedical applications. Recent developments allow chemists to tailor the size of the spherical nanoparticles they produce with high precision so each one looks nearly identical (less than 10 % full width half maximum in diameter variation) and to array them into highly ordered nanoparticle crystals. Intriguingly, the smaller the nanoparticles become, the less magnetic moment they contain per mass in comparison with magnetite in macroscopic form. This has widely been attributed to surface disordering, but direct proof has remained elusive.

SANS is ideal probe of nanoscale magnetism because it is highly penetrating (not surface limited) and it scatters from both nuclear and magnetic structures with sub-nanometer resolution. Neutrons have a spin which can be made to align parallel (+) or anti-parallel (–) to a particular direction with application of a small guide field and appropriate optics. By analyzing the spin of the neutrons after they have scattered from the sample of interest, that is whether they remain in the same orientation (denoted ++ and – –) or if they flip 180° (+ – and – +), we have developed an analytical approach that uniquely separates the nuclear scattering (N^2) from the magnetic moments aligned with the neutron polarization axis ($M^2_{||}$) and those perpendicular to it ($M^2_{\perp}$) [1].

The scattering patterns of Fig. 1 were taken in a nominally saturating field of 1.2 T at 200 K, cold by human standards, but well above the blocking temperature at which the magnetic moments would be expected to be "frozen" into place. Moving away from the beam stop (seen as a central hole) the size of the features measured decrease as $Q = 2\pi/\text{distance}$. In non spin-flip scattering a structural ring at 0.080 $Å^{-1}$ originates from the (111) reflection of the face-centered cubic arrangement of the nanoparticles. Scattering from magnetic moments aligned along the applied field direction (horizontal) either add to or subtract from this ring (– – and ++, respectively) along the vertical direction (Fig. 1a and 1c). Conversely, spin-flip scattering

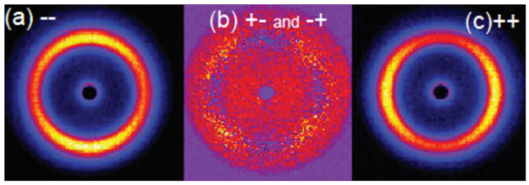

FIGURE 1: Two-dimensional SANS images (shown here at 1.2 T, 200 K) taken at NCNR beam line NG3. Non spin-flip data (a and c) are dominated by a nuclear Bragg peak at 0.080 $Å^{-1}$, while spin-flip (b) is entirely magnetic.

[1]NIST Center for Neutron Research, National Institute of Standards and Technology, Gaithersburg, MD 20899
[2]Carnegie Mellon University, Pittsburgh, PA
[3]Oberlin College, Oberlin, OH 44074
[4]University of Maryland, College Park, MD 20742
[5]Paul Scherrer Institute, Villigen, Switzerland
[6]Los Alamos National Laboratory, Los Alamos, NM 87545

is entirely magnetic (steering wheel pattern of Fig. 1b). $M^2\perp$ can be observed along the horizontal and vertical directions, while at 45°, 135°, 225°, and 315° from the horizontal, the spin-flip scattering is dominated by $M^2_{||}$. To further analyze each component we process sector cuts of +/− 10 degrees along each of the axes discussed to produce Fig. 2. Notice how much stronger the nuclear peak is than the magnetic peak – this is why polarization analysis is key.

To model our data we have to take into account both the shape of the nanoparticles (form factor) and they way in which they pack together (structure factor). The models used to fit the data are shown as solid lines in Fig. 2. N^2 is modeled by spheres 9 nm in diameter, while $M^2_{||}$ is modeled by a 7 nm diameter sphere of moments pointing along the applied field direction. In both of these cases the nanoparticles exhibit the long-range packing from being assembled into FCC crystallites. $M^2\perp$, however, is modeled by a 1 nm thick shell of magnetic spins pointed perpendicular to the applied field. These $M^2\perp$ shells additionally form clusters, or domains, of ≈ 10 nanoparticles that select a common perpendicular orientation. Together, this model (Fig. 3) fully explains where the missing moments go and rules out surface disordering [1].

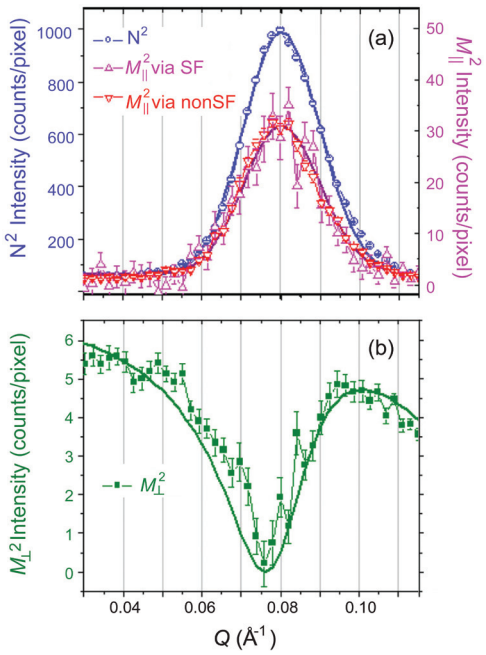

FIGURE 2: Data are scaled so that the N^2 Bragg peak height is 1000. (a) Note the intensity difference between N^2 (left axis) and $M^2_{||}$ (right axis) peaks at 0.08 Å^{-1}. (b) Note the $M^2\perp$ dip at 0.075 Å^{-1}, a value that constrains the shell thickness.

Furthermore, we have found that it is possible to modify the thickness of this magnetic shell canted perpendicular to the applied field using temperature and field. Holding the field at 1.2 T, the shell was found to be 1.5 nm thick

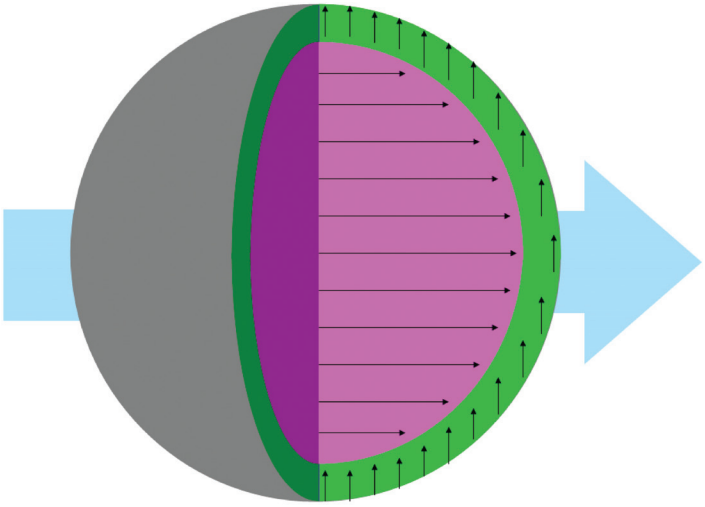

FIGURE 3: The data in Fig. 2a and 2b are fit (solid lines) by a model shown here schematically. It consists of a 7 nm diameter core that magnetically follows the applied field (blue arrow) and a 1 nm thick shell that is canted perpendicular to it.

between 300 K and 320 K; at 160 K to 200 K it was 1.0 nm thick, and at 10 K the signature of a shell was not observed. At 300 K in remanence (only a 0.005 T polarization guide) the nanoparticles feel no intra-particle magnetic interactions nor experience the effects of applied field. Neither ordered nor disordered shells are observed. Thus, the magnetic shells observed under high field conditions are magnetically induced rather than structural in origin. We speculate that this unexpected magnetic core-shell phenomenon results from the combination of surface anisotropy [3] (*i.e.*, the tendency for spins at a surface to point away from the interior) and the presence of closely-packed nearest neighbor nanoparticles that forces these outward-pointing surface spins to collectively order.

In conclusion, polarization analyzed SANS revealed that the missing magnetism from closely-packed magnetite nanoparticles subjected to a high magnetic field environment reappears as ordered, magnetic shells canted perpendicular to the applied field. The shells exhibit a collective behavior over ≈ 10 nanoparticles, and their thickness varies with temperature. This discovery is particularly exciting because it suggests a possible new mechanism by which to tailor magnetic interparticle "cross-talk" without necessarily altering nanoparticle packing.

References

[1] K.L. Krycka et al., Phys. Rev. Lett. **104**, 207203 (2010).
[2] S. Sun et al., J. Am. Chem. Soc. **126**, 273 (2004).
[3] L. Berger et al., Phys. Rev. B **77**, 104431 (2008).

Electric field control of magnetization in multiferroic $HoMnO_3$: the importance of magnetic domains

B. G. Ueland[1], J. W. Lynn[1], M. Laver[1,2], Y. J. Choi[3], S.-W. Cheong[3]

Multiferroics are materials with coexisting types of ferroic order (*e.g.*, ferroelectricity (FE), magnetic order, or ferroelasticity.) Multiferroics that possess coupling between FE and magnetic order are very rare but are of particular interest both from a scientific viewpoint and for applications because they offer the possibility of electrically manipulating their magnetization or magnetically manipulating their electric polarization. $HoMnO_3$ is such a multiferroic, with a FE transition of 850 K, antiferromagnetic (AFM) order of the Mn^{3+} at $T_N = 72$ K, and two Mn spin reorientation transitions at $T_{SR} = 40$ K and $T_{Ho} \approx 5$ K. Anomalies in the dielectric susceptibility at these various magnetic transitions indicate that coupling exists between the FE and AFM order [1,2,3], with the most striking result coming from optical experiments that claim bulk ferromagnetic order is induced and reversibly altered through application of an electric field [2].

Surprisingly however, recent x-ray and neutron scattering experiments have found no evidence for any electric field induced ferromagnetism [4,5]. Dielectric function studies have shown the importance of coupling between AFM and FE domain walls in this and similar materials [3], and it is possible for a net magnetization to arise from uncompensated spins within AFM domain walls, which may explain the previously observed electric field induced magnetization. To shed light on this problem, we have performed small angle neutron scattering (SANS) experiments while applying electric fields to search for any net magnetization occurring within AFM domain walls. We indeed find magnetic scattering in this large length scale regime that is electric-field sensitive, providing a possible explanation for the previously observed electric field induced magnetization [6].

Fig. 1a shows the temperature dependence of the total counts on the SANS 2-D detector normalized to the incident flux. The counts increase with decreasing temperature, level off between 40 K ≤ T ≤ 150 K, and then increase more quickly below T_{SR}, indicating that additional SANS occurs below T_{SR}. After subtracting

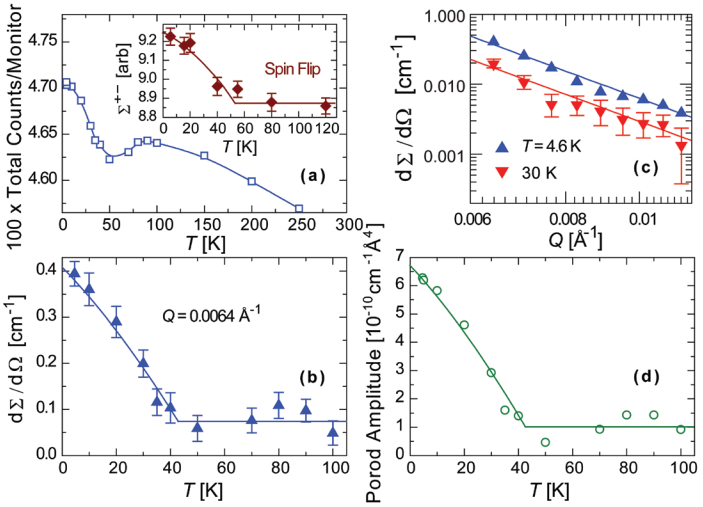

FIGURE 1: (a) Temperature dependence of the normalized total counts. The inset shows the spin flip scattering cross section determined from the sum of the radially averaged polarized SANS data. (b) Temperature dependence of the average scattering cross section for $\boldsymbol{Q} = 0.0064$ Å^{-1}. (c) Semilog plot of the average scattering cross section at two temperatures. The lines are fits to the Porod law which has a ~ $\boldsymbol{Q}^{-4}$ dependence. (d) The Porod amplitude versus temperature as determined from the fits shown in (c). Lines are guides to the eye unless otherwise noted.

$T = 150$ K data to eliminate contributions from structural scattering and then averaging over the 2D SANS data we obtain the average scattering cross section, $[d\Sigma/d\Omega](|\boldsymbol{Q}|)$ (not shown). At each temperature, the average cross section decreases with increasing $|\boldsymbol{Q}|$, and is larger at lower temperatures, for low $|\boldsymbol{Q}|$. To illustrate this point, we plot $[d\Sigma/d\Omega](|\boldsymbol{Q}|=0.0064$ Å$^{-1})$ as a function of temperature and see in Fig. 1b that it increases with decreasing temperature upon cooling below T_{SR}, indicating that the similar rise in Fig. 1a may possess a component coming from magnetic scattering.

Fig. 1c shows that the average scattering cross section follows a power law for at least $|\boldsymbol{Q}| < 0.012$ Å^{-1} and fits to the data for each temperature yield the expected slope of −4 for the Porod law. Hence, this scattering results from structures much larger than $d = 2\pi / |\boldsymbol{Q}| \approx 100$ Å, and the Porod amplitude versus temperature (Fig. 1d) is similar to data in Fig. 1a and 1b, being constant at high temperatures but abruptly increasing with decreasing temperature below T_{SR}. Polarized SANS measurements of the spin flip cross section, Σ^{+-} (inset to Fig. 1a) show a rise in Σ^{+-}

[1]NIST Center for Neutron Research, National Institute of Standards and Technology, Gaithersburg, Maryland 20899
[2]University of Maryland, College Park, Maryland 20742
[3]Rutgers University, Piscataway, New Jersey 08854

below T_{SR}, similar to the rises observed in Fig. 1a, b, and d, demonstrating that the abrupt increase in the scattering intensity below T_{SR} indeed has a magnetic component. These data allow us to associate the observed increase in the Porod scattering below T_{SR} (Fig. 1d) with a net magnetization developing within AFM domain walls.

To illustrate the experiment's sensitivity to magnetic domains and domain walls, Fig. 2a shows the change in the SANS intensity I with increasing *magnetic* field, $\mu_0 H$, at various temperatures. We see that the initial slope of $I(\mu_0 H)$ increases as the temperature decreases, as is typical for field-induced scattering in magnetic systems, and that I saturates above $\mu_0 H \approx 4$ T at $T = 4$ K, similar to a canonical magnetization versus field curve. The Porod amplitude as a function of $\mu_0 H$ (Fig. 2b) increases with increasing field for $\mu_0 H > 1$ T until 4 T, similar to Fig. 2a. Since applying a magnetic field will first reorient the spins within magnetic domains and then change the size/number of domains, we associate these data with field induced changes to the magnetic domain structure.

To determine the effect of an *electric* field on the scattering, Fig. 2c shows the temperature dependence of the total normalized 2-D detector counts while applying $E = 25$ kV/cm, after either field cooling or zero-field cooling. In the field cooled data, the counts increase with increasing temperature until $T \approx T_{SR}$, while for the zero-field cooled data they decrease. Above T_{SR} subsequent changes in the total counts with increasing temperature are qualitatively similar to E = 0 data. The difference between the field cooled and zero-field cooled data for $T < T_{SR}$ indicates that the electric field induces a different macroscopic ground state, and that the induced ground state depends on the cooling protocol. The temperature dependence of field cooled polarized SANS data is shown in Fig 2d, indicating that the electric field affects the magnetic scattering in the same temperature range as in Fig. 2c.

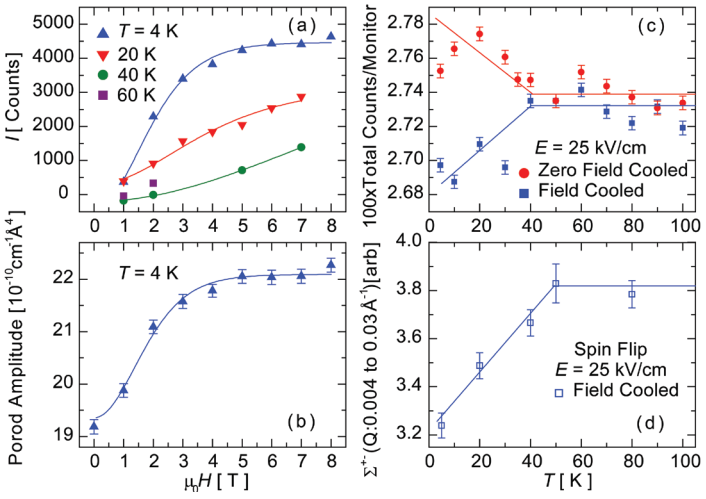

FIGURE 2: (a) Change in SANS intensity with an applied magnetic field at various temperatures. Data are shown after subtracting the zero-field data at each temperature. (b) The Porod amplitude versus magnetic field at T = 4 K. (c) Normalized total SANS intensity versus temperature for warming with E = 25 kV/cm applied, after either field cooling (squares) or zero-field cooling (circles). (d) Field cooled spin flip scattering cross section versus temperature for warming with E = 25 kV/cm. Lines are guides to the eye.

In the absence of a magnetic field, an ideal antiferromagnetic possesses no net magnetization. However, in $HoMnO_3$ we have shown that the increase in low Q scattering with decreasing temperature below $T_{SR} = 40$ K comes from magnetic structures (Fig. 1a inset) and that this magnetic scattering is affected by an electric field (Fig. 2c and d). Using our interpretation of the data in Fig. 2a and 2b, we postulate that the increase in magnetic scattering at low temperature for $E = 0$ and $\mu_0 H = 0$ in Fig. 1 is due to the development of a net magnetization within AFM domain walls. Thus, the increase in the Porod amplitude with decreasing temperature in Fig. 1d is due to either an increase in the contrast or in the number of AFM domain walls.

While AFM domains generally are not energetically favorable, effects such as lattice strain, defects, grain boundaries, or in particular FE domains can cause their formation and lower the free energy. Furthermore, AFM domain walls can possess a net uncompensated magnetization, since they have lower symmetry than the bulk material. Indeed, AFM domain walls have been observed in multiferroics [3], and pinning between FE and AFM domains in both $YMnO_3$ and $HoMnO_3$ has been observed [7]. Since applying a strong enough electric field will alter the FE domains, we explain the change in the magnetic SANS intensity upon application of an electric field in terms of pinned FE and AFM domain walls. Thus, when an electric field is applied, the change to the FE domains adjusts the AFM domains pinned to them, causing a change in the magnetization stemming from the AFM domain walls. Hence, our data indicate that the previously observed electric-field-induced magnetization may originate from uncompensated spins in AFM domain walls, rather than conventional long range magnetic order. Nevertheless, the coupling of the electric field to magnetic domain walls could prove useful in device applications.

References

[1] O. P. Vajk, M. Kenzelmann, J. W. Lynn, S. B. Kim, and S-W. Cheong , Phys. Rev. Lett. **94**, 087601 (2005).

[2] Th. Lottermoser, T. Lonkai, U. Amann, D. Hohlwein, J. Ihringer, and M. Fiebig, Nature **430**, 541 (2004).

[3] B. Lorenz, A. P. Litvinchuk, M. M. Gospodinov, and C. W. Chu, Phys. Rev. Lett. **92**, 087204 (2004).

[4] S. Nandi, A. Kreyssig, L. Tan, J. W. Kim, J. Q. Yan, J. C. Lang, D. Haskel, R. J. McQueeney, and A. I. Goldman, Phys. Rev. Lett. **100**, 217201 (2008).

[5] O. P. Vaijk and J. W. Lynn, private communication.

[6] B. G. Ueland, J. W. Lynn, M. Laver, Y. J. Choi, and S.-W. Cheong Phys. Rev. Lett. **104**, 147204 (2010).

[7] M. Fiebig, Th. Lottermoser, D. Fröhlich, A. V. Goltsev, and R. V. Pisarev, Nature **419**, 818 (2002).

Frustrated magnetism and superconductivity in $Fe_{1+y}Se_{0.4}Te_{0.6}$

V. Thampy[1], J. A. Rodriguez[2,3], Y. M. Qiu[2,3], W. Bao[4], T.J. Liu[5], J. Hu[5], B. Qian[5], D. Fobes[5], Z.Q. Mao[5], and C. Broholm[1,2]

A wide range of metallic magnets develop superconductivity when magnetism is suppressed by pressure or chemical substitution. The discovery of iron superconductors offers new insight to this phenomenon and has reignited the search for higher temperature superconductors. In this quest, the new MACS spectrometer at NIST [1] has turned out to be an exciting new tool.

Containing only square lattice iron layers, $Fe_{1+y}Se$ is arguably the simplest member of the new family. The exact role of chalcogen stoichiometry remains unclear, but a lattice distortion and modulated magnetism is found in $Fe_{1+y}Se_{1-x}Te_x$ for x=0, and following a mixed regime for $0.1 < x < 0.3$, bulk superconductivity occurs for $x > 0.3$ [2]. Figure 1 shows momentum space maps of low energy magnetic neutron scattering in the normal (top) and superconducting (middle) state of $Fe_{1+y}Se_{0.4}Te_{0.6}$. While itinerant magnets such as chromium have sharp peaks from Fermi surface nesting, the red and yellow regions of intense scattering at 1 meV in Fig. 1a show that spin fluctuations in $FeSe_{0.4}Te_{0.6}$ cover a large fraction of the Brillouin zone. Such fluctuations indicate magnetic ambivalence as in frustrated magnets with a macroscopic ensemble of near degenerate states. At higher energies (6 meV, Fig. 1b) a doubly peaked maximum close to (0.5,0.5,0) indicates incommensurate correlations from Fermi surface nesting or competing exchange interactions.

The connection to superconductivity is apparent from the suppression of low energy fluctuations in the superconducting state (see Fig. 1c and 1e). Magnetic neutron scattering satisfies a sum-rule which ensures the total cross section remains unchanged as spectral weight is redistributed in Q-ω space. Our experiments show different destinations for normal state scattering as superconductivity develops.

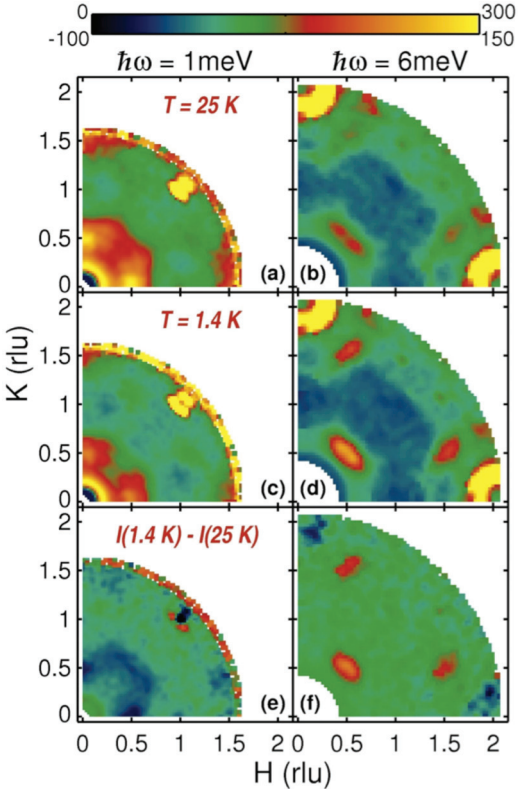

FIGURE 1: Images of inelastic neutron scattering at 1 meV (left column) and 6 meV (right column) in the normal state (T = 25 K) and in the superconducting state (T = 1.4 K) of $Fe_{1+y}Se_{0.4}Te_{0.6}$. The bottom two frames (e-f) show the difference between superconducting and normal state data. The color bar indicates counts per minute. Temperature insensitive features result from Bragg feedthrough and/or phonons.

Figure 1f shows enhancement of magnetic scattering at $\hbar\omega$ = 6 meV for elliptical regions associated with Q = (0.5,0.5,0) nesting of electron and hole pockets of the Fermi surface. A staple of magnetic superconductors, the corresponding spectroscopic resonance in $Fe_{1+y}Se_{0.4}Te_{0.6}$ is evidence the (s+−) superconducting gap function has opposite signs on the nesting electron and hole Fermi surfaces [3].

The comprehensive mapping capabilities of MACS also reveal elastic magnetic scattering close to Q = (0.5,0,0) at low temperatures. The unusually broad peaks there indicate that interstitial sites might be seeding magnetic oscillations of the $Fe_{1+y}Te$ variety [4], which link up at low temperatures to form a spin glass. While the (1/2,0,0) point corresponds to socalled double stripes where third nearest neighbor antiferromagnetic interactions are satisfied, the (1/2,1/2,0) point corresponds to satisfied

[1]Johns Hopkins University, Baltimore, MD 21218, USA
[2]NIST Center for Neutron Research, National Institute of Standards and Technology, Gaithersburg, MD 20899
[3]University of Maryland, College Park, MD 20740
[4]Renmin University of China, Beijing 100872, China
[5]Tulane University, New Orleans, Louisiana 70118

second nearest neighbor interactions. In both cases near neighbor correlations are mixed; both ferro *and* antiferromagnetic. The variety of magnetic correlations indicates a strongly fluctuating spin system, which lacks a leading magnetic instability; a desirable situation evidently, for superconductivity.

Figure 2 distinguishes and details the temperature dependence of distinct parts of low energy magnetism in $Fe_{1+y}Se_{0.4}Te_{0.6}$. While the suppression of inelastic scattering near Q = (0.5,0.5,0) occurs with a characteristic temperature

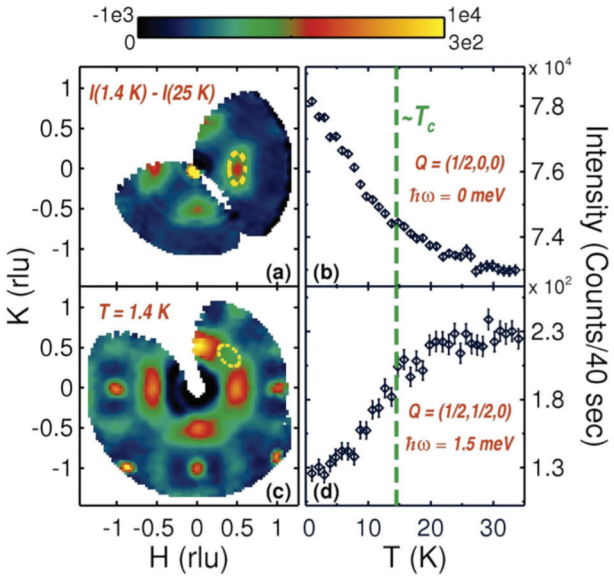

FIGURE 2: (a) and (b) are images of elastic and inelastic (1.5 meV) neutron scattering in $Fe_{1+y}Se_xTe_{1-x}$. The yellow dashed lines show the regions where temperature dependent magnetic scattering is probed versus temperature in (b) and (d). The dashed line in (b) and (d) indicates the superconducting T_c determined by susceptibility measurements.

close to the superconducting critical temperature, T_c (dashed line), the elastic scattering at Q = (0.5,0,0) shows no such anomaly. This provides an interesting link to the copper oxides where a spin glass unfazed by superconductivity was also found in under-doped YBCO [5]. More specific information about the spin glass order is obtained by analyzing cuts extracted from complete maps of the difference between low and high temperature elastic scattering in the (hk0) and (h0l) planes. Figure 3a shows that the in-plane correlation length is just 2.6 (1) Å, and of the same order as the lattice parameter. The out of plane correlations are accounted for by near neighbor Ising spin correlations with spins oriented along the tetragonal *c*-axis (Fig. 3b). There is a satisfying consistency here in that a spin glass is plausible in two dimensions only for Ising spins. It is also pleasing to see that high quality quantitative information can be extracted from the colorful maps of scattering produced by MACS. The relation of the spin glass to superconductivity is however, far from clear. Possible scenarios include phase separation into Te and Se rich regions with spin glass like magnetism and superconductivity respectively. A homogeneous multi-critical state with spin glass and superconducting phases decoupled by segregation in momentum space is also possible. Further experiments including detailed electron microscopy will be needed to distinguish.

Whether homogeneous or heterogeneous, the close proximity of superconductivity and magnetism in $Fe_{1+y}Se_xTe_{1-x}$ and the strong coupling to magnetic fluctuations with a wave vector that connects electron and hole pockets of the Fermi surface, indicate a central role for magnetic fluctuations in promoting superconductivity. In non-metallic frustrated magnets lattice strain can develop spontaneously to relieve magnetic frustration [6]. Fig. 1a indicates that magnetic frustration also occurs in metallic $Fe_{1+y}Se_xTe_{1-x}$. However, rather than a lattice distortion, superconductivity may in this case be needed to relieve frustration and lower the energy of the interacting spin system.

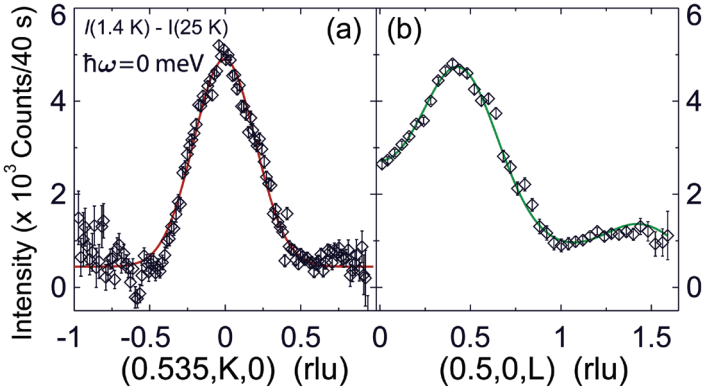

FIGURE 3: cuts extracted from complete maps of elastic difference intensity (1.4 K data minus 25 K data) in the (hk0) and (h0l) reciprocal lattice planes. The line in (a) is a Gaussian indicating an in-plane 2.6(1) Å correlation length. The line in (b) is the calculated intensity for nearest neighbor only correlations of *c*-axis spin components.

As these and other explanations are explored to further our understanding and control of magnetic superconductors, the unique mapping capabilities of MACS will be a key tool for new insight.

References

[1] C. Broholm, Nucl. Instr. and Meth. in Physics Res. , A **369**, 169 (1996); J. A. Rodriguez *et al.*, Measurement Science & Technology, **19**, 034023 (2008).

[2] T. J. Liu, *et al.*, Nature Materials, **9**, 716 (2010).

[3] Y. M. Qiu *et al.*, Phys. Rev. Lett., **103**, 067008 (2009).

[4] W. Bao W, *et al.*, Phys. Rev. Lett., **102**, 247001 (2009).

[5] C. Stock *et al.*, Phys. Rev., B **73**, 100504(R) (2006).

[6] S.-H. Lee, *et al.*, Phys. Rev. Lett., **84**, 3718 (2000).

Lattice distortion and magnetic quantum phase transition in $CeFeAs_{1-x}P_xO$

C. de la Cruz[1,2], W. Z. Hu[3], S. Li[2,3], Q. Huang[4], J. Lynn[4], M. Green[4], G. F. Chen[3,5], N. L. Wang[3], H. Mook[1], Q. Si[6], P. Dai[2,1,3]

Since the initial discovery of superconductivity in the oxypnictide LaFeAsO in 2008, several other families of the Fe-based materials have been studied. The discovery of ubiquitous antiferromagnetic (AFM) order in the parent compounds of iron arsenide superconductors has renewed interest in understanding the interplay between magnetism and high-transition temperature (high-T_c) superconductivity in these and related superconducting materials [1]. Superconductivity in the Fe-based arsenides can be induced either via charge carrier doping or application of pressure to their semimetal parent compounds. Similar to the considerations made for the copper oxides, these properties make it possible that superconductivity is being influenced by a magnetic quantum critical point (QCP) located in the not-yet accessed part of the overall phase diagram. The tunability of quantum fluctuations in these compounds, leading to a quantum phase transition, has been theorized as a result of the unusual property of the parent compound as an incipient Mott insulator, and consequently being located near the boundary of itinerancy and localization [2]. To understand how the AFM ground state itself can be suppressed by quantum fluctuations, it is important to isoelectronically tune the crystal lattice structure to avoid the influence of charge carrier doping and superconductivity. We have used neutron scattering to show that replacing the larger arsenic with smaller phosphorus in $CeFeAs_{1-x}P_xO$ simultaneously suppresses the AFM order and orthorhombic distortion near $x = 0.4$, providing the first evidence for a magnetic quantum critical point in these materials. Furthermore, we find that the pnictogen height in iron arsenide is an important controlling parameter for their electronic and magnetic properties, and also may play an important role in the electron pairing and superconductivity [3].

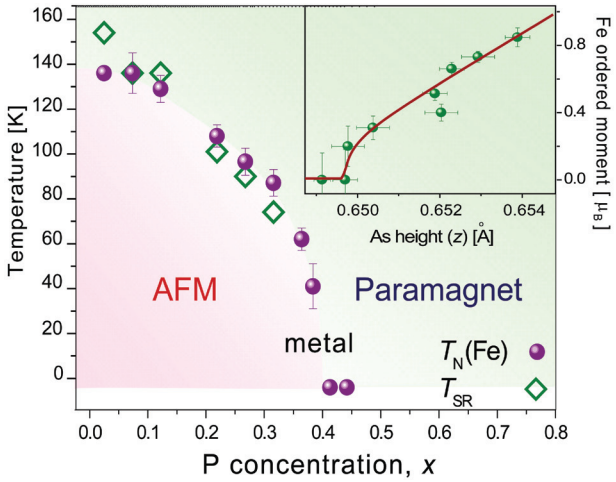

FIGURE 1: Experimentally obtained structural (T_{SR}) and magnetic phase transition temperatures (T_N(Fe) for the onset of Fe AMF order) as a function of P substitution for As, indicating the presence of a quantum critical point at $x \approx 0.4$. The inset shows the dependence of the Fe long range ordered moment on the pnictogen height (As(z)), suggesting it plays an important role in tuning the electronic and magnetic correlations in the system.

In the undoped state, the parent compounds of the iron arsenide superconductors have an orthorhombic lattice distortion and collinear AFM structure. Applying a magnetic field to suppress the influence of superconductivity is a common means to unmask any potential quantum critical point, but this approach is difficult to implement here because of the large superconducting critical field for the iron pnictides (a valuable property for applications, however). We instead achieve the same result by using an isoelectronic phosphorus substitution for arsenic in CeFeAsO, recognizing that superconductivity appears neither in CeFeAsO nor in CeFePO, a paramagnet with a tetragonal structure. Our systematic neutron scattering studies of the structural and magnetic phase transitions in $CeFeAs_{1-x}P_xO$ demonstrate that the pnictogen height [the average Fe-As(P) distance] and orthorhombicity of the FeAs(P) tetrahedron critically control the iron AFM ordered moment and Néel temperature of the system. These results expose a magnetic quantum critical point, thereby

[1]Oak Ridge National Laboratory, Oak Ridge, Tennessee 37831, USA
[2]The University of Tennessee, Knoxville, Tennessee 37996-1200, USA
[3]Beijing National Laboratory for Condensed Matter Physics, Institute of Physics, Chinese Academy of Sciences, Beijing 100190, China
[4]NIST Center for Neutron Research, National Institute of Standards and Technology, Gaithersburg, Maryland 20899-6012 USA
[5]Renmin University of China, Beijing 100872, China
[6]Rice University, Houston, TX 77005, USA

suggesting the importance of collective magnetic quantum fluctuations for both the electronic properties in the normal state and the origin of superconductivity.

The parent compound CeFeAsO undergoes the tetragonal (space group *P4/nmm*) to orthorhombic (space group *Cmma*) structural transition below ≈ 158 K followed by a long range commensurate AFM order with a collinear spin structure below ≈ 135 K. Similar to electron doping of CeFeAsO via fluorine substitution of oxygen, we find that phosphorus replacement of arsenic in CeFeAsO also results in decreasing both the structural and magnetic phase transition temperatures, despite having no charge carriers doped into the FeAs layer. The ordered Fe moment was also observed to smoothly decrease with increasing P content and tracked the distortion, vanishing at $x \approx 0.4$, suggesting the presence of a lattice-distortion-induced magnetic quantum phase transition through phosphorus doping. In addition, our demonstration of the pnictogen height as a parameter to systematically tune the electronic and magnetic properties of $CeFeAs_{1-x}P_xO$ provides new insight that is likely of broad relevance to all families of the iron pnictides. In principle, the changing pnictogen height can affect both the superconducting gap function and the strength of the electron pairing.

For a complete determination of the phosphorus doping evolution of the low temperature crystal structure, the high resolution full powder diffraction patterns at low temperatures were obtained from the BT-1 neutron powder diffractometer. The outcome of the detailed Rietveld analysis, displayed in Fig. 2, shows the P-doping effect on the crystal structure of $CeFeAs_{1-x}P_xO$. Substitution of the smaller P ion on the arsenic site reduces all three lattice parameters with the system becoming tetragonal for $x > 0.37$. The decreased c-axis lattice constant is achieved via a reduction of the As(P)-Fe-As(P) block distance [through reducing the FeAs(P) height], while the CeAs(P) and CeO block distances remain essentially unchanged with increasing P-doping. Remarkably, these trends are completely different from that of $CeFeAsO_{1-x}F_x$, where the c-axis lattice contraction is achieved via a large reduction of the Ce-As distance, while the Ce-O/F and As-Fe-As block distances actually increase with increasing F-doping. These fundamental differences reflect the fact that adding electrons into the system via F-doping brings the Ce-O/F charge transfer layer closer to the superconducting As-Fe-As block and facilitates electron transfer, while P-doping is a pure geometrical lattice effect without charge carrier transfer. Furthermore, since the Fe-As distance decreases rapidly with increasing P-doping which saturates at ≈ 2.36 Å for $CeFeAs_{1-x}P_xO$, the reduced Fe-As(P) distance may induce strong hybridization between the Fe 3d and the As 4*p* orbitals and thus quench the ordered Fe magnetic moment in CeFeAsO. More generally, the P-doping increases the electronic kinetic energy thereby weakening the magnetic order.

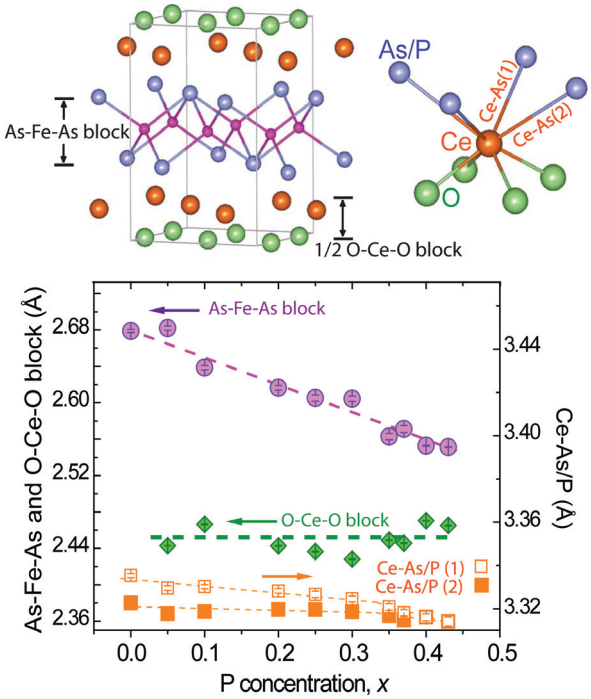

FIGURE 2: Low temperature structural evolution of $CeFeAs_{1-x}P_xO$ as a function of P -concentration obtained from analysis of BT-1 data. The effect of the smaller P substitution to the larger As is to contract the Fe-As-Fe block and reduce the average Fe-As distance, while keeping the O-Ce-O block size essentially constant. This implies an increase in the Fe-As hybridization which in turn directly influences the Fe spin interaction.

In summary, we have mapped out the structural and magnetic phase transitions of $CeFeAs_{1-x}P_xO$. We showed that superconductivity does not appear in the magnetic phase diagram over the entire measured doping and temperature ranges, and found the surprising property that the lattice distortion and the static Fe AF order are gradually suppressed by isoelectronic phosphorus substitution of arsenic. These results indicate the presence of a magnetic quantum critical point near phosphorus concentration of $x \approx 0.4$, thereby establishing that the phosphorous substitution for arsenic in this class of materials is an ideal tuning parameter to explore the magnetic quantum critical behavior of the iron pnictides.

References

[1] J. W. Lynn and P. Dai, Physica C **469**, 469 (2009).

[2] J. Dai, Q. Si, J-X. Zhu and E. Abrahams, Proc. Natl. Acad. Sci. U.S.A. **106**, 4118 (2009).

[3] C. de la Cruz, W. Z. Hu, S. Li, Q. Huang, J. W. Lynn, M. A. Green, G. F. Chen, N. L. Wang, H. A. Mook, Q. Si, and P. Dai, Phys. Rev. Lett. **104**, 017204 (2010).

Tuning the magnetic and structural properties of $Fe_{1+x}Te$

E. E. Rodriguez[1], P. Zavalij[2], P.-Y. Hsieh[1,2] and M. A. Green[1,2]

Precise control of chemical composition is proving to be as important in understanding the structural and electronic properties of the new iron based high temperature superconductors as it was for cuprates. In both cases, neutron diffraction has played a pivotal role in characterizing the evolution of their structural and magnetic phase diagrams. We have recently shown that by reacting iron telluride, a parent material to the new iron-based superconductors, with iodine vapor at low temperatures, the amount of excess iron in the crystal lattice (*i.e.*, the x in the chemical formula $Fe_{1+x}Te$) can be tuned, thus modifying both the magnetic ordering and the nature of the crystallographic phase transition at low temperatures [1]. This deintercalation process, or removal of the interstitial iron, leaves the central FeTe framework intact, thus allowing access to new $Fe_{1+x}Te$ compositions. It is an example of a "soft chemistry" approach, which is illustrated in the schematic of Fig. 1, and can be equally applied to single crystal as well as powdered samples.

Since the discovery of superconductivity in $LaO_{1-x}F_xFeAs$ at a critical temperature of 26 K [2], this phenomenon has been revealed in several structural families that possess two-dimensional layers of $(FeAs)^-$ separated by positively charged ions (*e.g.*, Ba^{2+}). In contrast to these strong ionic solids, the simple compounds of Fe*Ch*, where *Ch* = sulfur, selenium, or tellurium, possess layers that are only held together by relatively weak van der Waals forces. Nevertheless, the phase diagrams of both systems universally exhibit a close proximity between superconductivity and an ordered magnetic regime, the border between the two being controlled by chemical composition or externally applied pressure. The Fe*Ch* system has been shown to be particularly sensitive to stoichiometry. For example, β-$Fe_{1.01}Se$ is superconducting at temperatures below 8.5 K, whereas β-$Fe_{1.03}Se$ is neither magnetic nor superconducting, demonstrating that the excess interstitial iron is detrimental to the superconducting properties [3].

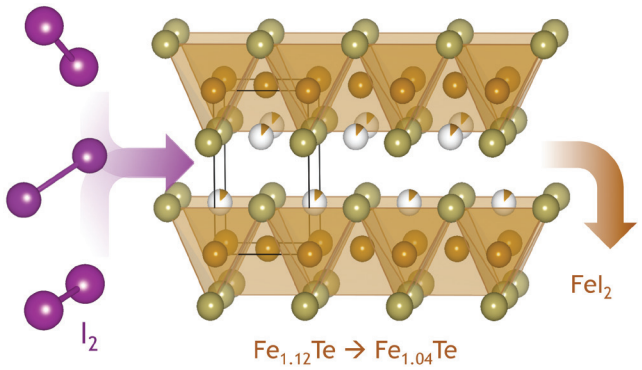

FIGURE 1: Schematic diagram illustrating how iodine molecules react with the iron atom interstitials, which are displayed as the partially occupied white atoms between the orange $FeTe_4$ tetrahedra. The presumed side product, FeI_2, was washed from the deintercalated $Fe_{1.04}Te$ with methanol as the solvent.

$Fe_{1+x}Te$ has only been reported for $0.067 < x < 0.17$, with the excess interstitial iron located between the layers composed of edge-sharing FeTe4 tetrahedral units (See Fig. 1). The amount of interstitial Fe controls the material's structure and magnetism. At low temperature for $x < 0.11$ the crystal lattice is orthorhombic and has magnetic ordering that is commensurate with the iron lattice; for materials at higher values of interstitial iron ($x > 0.11$), the lattice is monoclinic and has an incommensurate magnetic ordering. $Fe_{1+x}Te$ becomes superconducting upon substitution of selenium or sulfur for tellurium, but this substitution also affects the iron stoichiometry. Thus, studying how these two parameters contribute to changes in the properties of these materials remains unknown. To better illuminate these issues, the ability to exactly control the composition is essential.

A comparison of neutron powder diffraction patterns for the I_2-reacted and unreacted samples revealed significant differences in relative intensities of Bragg reflections between the two. In particular, accurate determination of the iron content was due to the large coherent neutron scattering length of 9.45 fm for iron. Least-squares refinement of the neutron diffraction data gave a crystal structure of the unreacted sample with a composition of $Fe_{1.118(5)}Te$, compared to $Fe_{1.042(5)}Te$ for a sample deintercalated by iodine.

[1]NIST Center for Neutron Research, National Institute of Standards and Technology, Gaithersburg, MD 20899
[2]University of Maryland, College Park, MD 20742

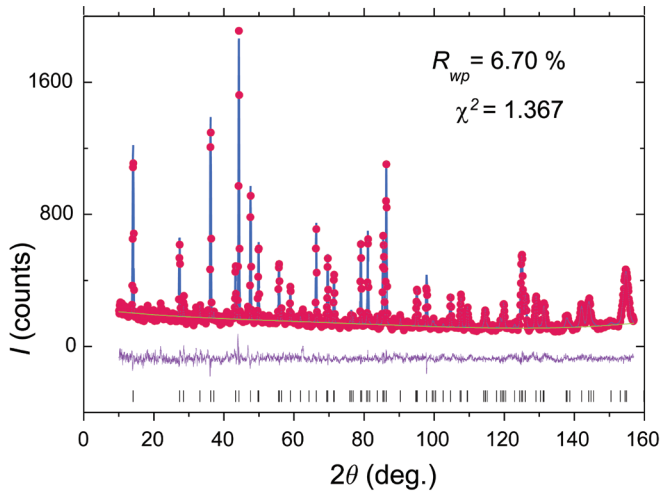

FIGURE 2: Observed (red), calculated (blue) and difference (purple) intensity of the neutron powder diffraction patterns of $Fe_{1.04}Te$. Data were obtained from the BT-1 instrument using the Cu311 monochromator (λ = 1.540 Å). The residual of the fit was R_{wp} = 6.7 % and the χ^2 = 1.367.

Figure 2 shows the neutron diffraction patterns, observed and calculated, for the $Fe_{1.042(5)}Te$ sample. In all samples, the refinement yielded atomic sites within the $FeTe_4$ tetrahedra at full occupancy, suggesting that the I_2 was preferentially removing iron from the interstitial site only. Further inspection of the structural parameters revealed that the deintercalation of the powders is associated with a small expansion of the tetragonal crystal lattice in both the *a* and *c* directions, implying that the interstitial Fe bonding, within and between the layers, has the effect of drawing the lattice together.

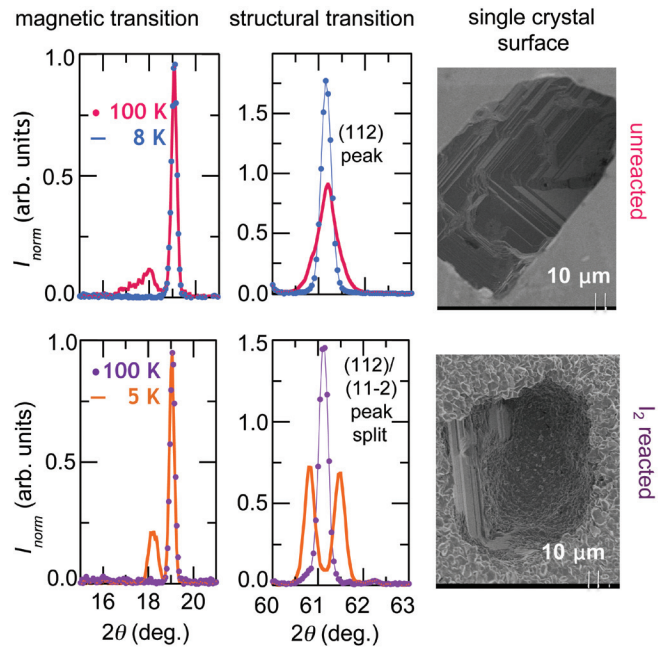

FIGURE 3: Magnetic and structural transitions for the unreacted $Fe_{1.118(5)}Te$ and I_2-reacted $Fe_{1.051(5)}Te$ compounds. On far left, the low 2θ scattering is due to the magnetic ordering at base temperatures. Splitting of the (112) Bragg peak is also shown for the I_2-reacted sample. On far right, SEM photographs of the surfaces of unreacted single crystal and I_2-reacted single crystal.

The structural changes upon iron extraction resulted in interatomic distances between the iron atoms increasing while the Fe–Te bond distance actually decreased. Likewise, the variance of the Te–Fe–Te tetrahedral angles also decreased. Here, bond angle variance is an average of the differences of the $FeTe_4$ tetrahedral bond angles from the ideal 109.5°, a value that has been shown to be correlated with the superconducting critical temperature [5].

Figure 3 shows a comparison of part of the neutron data for unreacted and I_2-reacted powder samples at base temperature and 100 K as well as the effect of the reaction on the surface of single crystal samples. Figure 3 demonstrates that at low temperatures, the unreacted sample has an incommensurate magnetic propagation vector and is orthorhombic, whereas the I_2-reaction sample has a commensurate propagation vector and is monoclinic. These observations are consistent with the change in stoichiometry.

In summary, we have demonstrated that the amount of interstitial iron in the layered structure of $Fe_{1+x}Te$ can be diminished by reaction with iodine. It has previously been reported that substitution of Te with Se or S to produce superconductivity has two effects. First, there is suppression of the low temperature structural and magnetic phase transitions. Second, there is a reduction of the interstitial iron content such that the optimal superconducting composition $FeTe_{0.5}Se_{0.5}$ has little or no excess iron [6]. The capability of controlling iron content through our technique will allow for the investigation of larger regions of the superconducting Fe_{1+x}(S,Se,Te) phase diagrams, as well as allow for the two factors upon substitution to be controlled and evaluated independently.

References

[1]. E. E. Rodriguez, P. Zavalij, P. –Y. Hsieh, M. A. Green, J. Am. Chem. Soc., DOI: 10.1021/ja104004t (in press).

[2]. Y. Kamihara, T. Watanabe, M. Hirano, H. Hosono, J. Am. Chem. Soc., **130**, 3296 (2008).

[3]. T. M. McQueen, Q. Huang, V. Ksenofontov, C. Felser, Q. Xu, H. Zandbergen, Y. S. Hor, J. Allred, A. J. Williams, D. Qu, J. Checkelsky, N. P. Ong, R. J. Cava, Phys. Rev. B **79**, 014522 (2009).

[4]. W. Bao, Y. Qiu, Q. Huang, M. A. Green, P. Zajdel, M. R. Fitzsimmons, M. Zhernenkov, S. Chang, M. Fang, B. Qian, E. K. Vehstedt, J. Yang, H. M. Pham, L. Spinu, Z. Q. Mao, Phys. Rev. Lett. **102**, 247001 (2009).

[5]. C. de la Cruz, Q. Huang, J. W. Lynn, J. Y. Li, W. Ratcliff, J. L. Zarestky, H. A. Mook, G. F. Chen, J. L. Luo, N. L. Wang, P. C. Dai, Nature **453**, 899 (2008).

[6]. B. C. Sales, A. S. Sefat, M. A. McGuire, R. Y. Jin, D. Mandrus, Y. Mozharivskyj, Phys. Rev. B **79**, 094521, (2009).

Neutron reflectometry study of the conformation of HIV Nef bound to lipid membranes

M. S. Kent[1], J. K. Murton[1], D.Y. Sasaki[1], S. Satija[2], B. Akgun[2], H. Nanda[2], F. Heinrich[2,3], J. E. Curtis[2], J. Majewski[4], C. R. Morgan[5] and J. R. Engen[5]

A particularly challenging problem in structural biology is to characterize changes in protein structure that result upon interaction with a lipid membrane. Neutron reflectometry (NR) can resolve structural details of membrane-associated proteins in physiological conditions, and may be unique in its ability to directly resolve details of the full membrane-bound protein structure. For a protein bound to a planar lipid membrane, NR determines the in-plane averaged distribution of amino acid residues normal to the membrane, and is sensitive to any changes in that distribution. In the work highlighted here NR was used to resolve the first details of the conformation of Nef from HIV upon binding to lipid membranes [1]. Nef is an HIV-1 accessory protein that directly contributes to AIDS progression and its effects only occur when it associates with membranes [2]. It is believed to undergo a transition from a solution conformation to a membrane-associated conformation that enables it to interact with cellular proteins. Despite its medical relevance, there is no direct information about the conformation of membrane-bound Nef. Understanding how the membrane-bound conformations of Nef relate to its ability to bind to cellular proteins under different conditions could lead to drug therapies to counteract its harmful effects.

Naturally occurring Nef has an amine-terminated arm (N-terminus) which is myristoylated (myr). Purified deuterated myr-Nef was not available for this study. Therefore a Histidine (6xHis) tag on the N-terminus was used to bind full-length, unmyristoylated deuterated Nef to a planar lipid membrane (in this case, a Langmuir monolayer). The monolayer was composed of mixtures of dipalmitoylphosphatidylcholine (DPPC) and 1,2-distearylglycero-3-triethyleneoxideiminodiacetic acid (DSIDA). The N-terminal 6xHis tag on d-Nef was spatially located where the naturally occuring myristic acid moiety would be found in Nef. The His tag adsorbed to Cu^{2+} in the headgroups of DSIDA to localize Nef to the membrane. This system represents one of the possible limiting states of membrane-bound myr-Nef, namely the open form in which the N-terminus is unassociated with the core domain but associates specifically with lipid membranes. The experimental system is illustrated in Fig. 1, which shows the two size extremes of Nef and their relationship to the membrane and the neutron beam. For the most extended form, the dimensions of Nef from the model of Geyer and Peterlin [3] were used and the protein was attached to the membrane by its N-terminus with no insertion. Figure 1 also shows the dimensions of the two lipids and a very highly compact form of Nef.

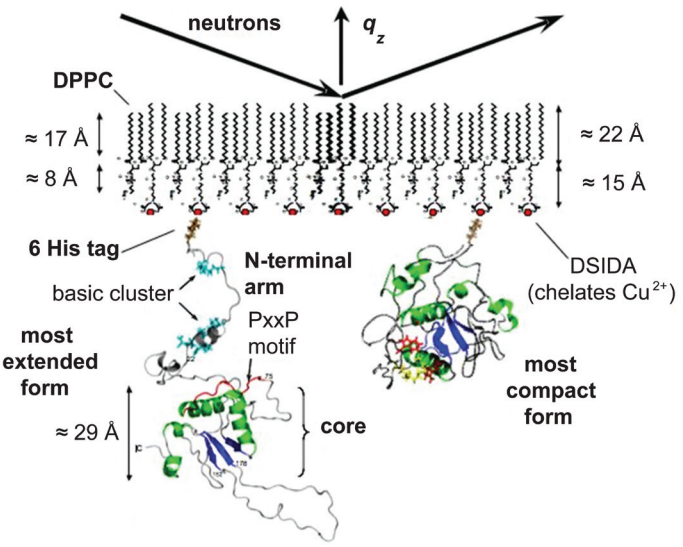

FIGURE 1: Illustration of the experimental system. Neutrons strike the opposite face of the lipid monolayer from where Nef interacts. The dimensions of Nef from the most extended form of the Geyer and Peterlin model [3] are shown at the left, along with the dimensions of the two lipids. For the purpose of size comparison, a model of a highly compact form of Nef is shown on the right. This figure is meant to be illustrative of the experimental setup and not necessarily to show the true conformations of Nef at the membrane.

[1]Sandia National Laboratories, Albuquerque, NM 87123
[2]NIST Center for Neutron Research, National Institute of Standards and Technology, Gaithersburg, MD 20899
[3]Carnegie Mellon University, Pittsburgh, PA 15213
[4]Los Alamos National Laboratories, Los Alamos, NM 87545
[5]Northeastern University, Boston, MA 02115

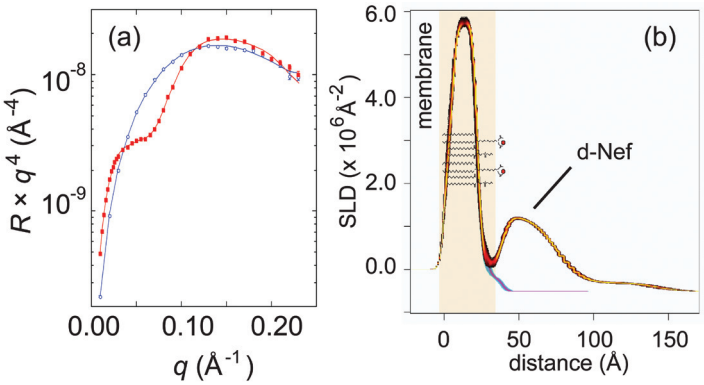

FIGURE 2: a) NR data for the d-DPPC/h-DSIDA monolayer alone (○) and with bound d-Nef (■) adsorbed. Adsorption was arrested after 2.0 h. b) SLD profiles corresponding to the data in (a) (with uncertainty limits determined from a Monte Carlo resampling procedure [5]). The lipid tail profile (large peak) continues into the blue/pink region for the monolayer alone. Adsorption of d-Nef gives rise to a second peak adjacent to the DSIDA headgroups.

Fig. 2a shows reflectivity data collected after allowing d-Nef to adsorb to a monolayer of 65 % d-DSIDA/Cu^{2+} 35 % d-DPPC for 2.0 h from solution at 0.5 μmol/L, and then flushing the subphase with 50 ml of Tris buffer. The reflectivity data were collected over a period of 6 h after subphase exchange. The profiles with uncertainty limits from simultaneous fits to the data in Fig. 2a before and after adsorption of d-Nef are shown in Fig. 2b. The profiles for the lipids alone are denoted by a blue/pink/yellow color scheme, and the profiles with d-Nef are denoted by a black/red/yellow color scheme. The model-independent profile of d-Nef is comprised of a ≈ 40 Å layer dense in residues that is directly adjacent to the lipid headgroups followed by a very slight tail extending into the subphase. The dense layer is asymmetric with the maximum skewed toward the membrane. Conformations in which the core domain is significantly displaced from the membrane such as depicted on the left in Fig. 1 can be ruled out. Certain protein binding sites on Nef appear to be blocked in this conformation, including a polyproline-rich segment on the core domain that is known to be a binding site for SH3 domains of tyrosine kinases [2]. Indeed, no binding of d-SH3 was detected upon introducing it into the subphase at 1.5 μmol/L.

The profiles also show that the SLD of the lipid headgroup region increases upon adsorption due to the insertion of d-Nef residues into the lipid headgroups. This is consistent with the fact that, for the present conditions, adsorption of the d-Nef containing monolayers is always accompanied by an increase in the area per molecule of ≈ 5 %. An example is shown in Fig. 3. The increase in area per molecule observed upon membrane binding of 6xHis Nef through the His tag provides direct evidence of insertion of residues. Prior work by others involving mutants of Nef has demonstrated that Nef interacts with membranes through the N-terminus and also with residues on the N-terminal arm that are able to form an amphiphilic helix [4]. We conclude that insertion of a portion of the N-terminal arm positions the core domain directly against the lipid headgroups.

This work provides the first structural data for membrane-associated Nef. Both good resolution and a strong neutron scattering signal were achieved with the use of deuterated lipids and d-Nef against an H_2O subphase. The reflectivity data and area per molecule data both indicated insertion of residues into the membrane

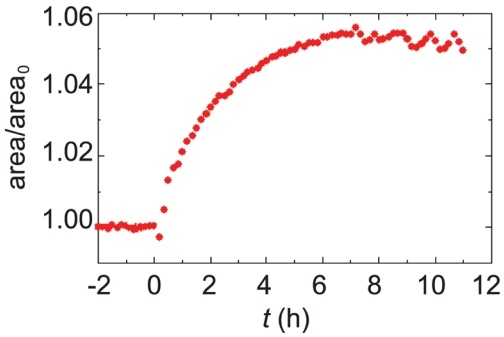

FIGURE 3: Change in area per molecule upon adsorption of 6xHis d-Nef to a monolayer of 35 % DPPC, 65 % DSIDA/Cu^{2+}. Time $t = 0$ corresponds to the first detection of absorption in the reflectivity data.

upon binding through the N-terminal His tag. When interpreted in light of the results of prior studies, this strongly suggests that a portion of the N-terminal arm inserts into the membrane. Binding of Nef to the same membrane also occurred at a much lower level in absence of the interaction through the His tag, however, in that case no insertion of residues into the membrane was detected. We conclude that binding through the N-terminus contributes to N-terminal arm insertion. Upon insertion of a portion of the N-terminal arm, the core domain of Nef is located directly against the lipid headgroups and forms a layer approximately 40 Å thick. The binding site for SH3 domains appears to be inaccessible in this conformation. In the future, further studies will focus on the conformation of membrane-bound Nef under different conditions and its ability to bind to a variety of other cellular proteins.

References

[1] M.S. Kent, J. K. Murton, D. Y. Sasaki, S. Satija, B. Akgun, H. Nanda, J. E. Curtis, J. Majewski, C. R. Morgan, and J. R. Engen, Biophysical Journal (submitted).

[2] S. T.Arold, and A. S. Baur, Trends Biochem Sci **26**, 356 (2001).

[3] M. Geyer, and B. M. Peterlin, FEBS Lett **496**, 91 (2001).

[4] H. Gerlach, V. Laumann, S. Martens, C. F. W. Becker, R. S. Goody, and M. Geyer, Nature Chemical Biology **6**,46 (2009).

[5] F. Heinrich, T. Ng, D. J. Vanderah, P. Shekhar, M. Mihailescu, H. Nanda, and M. Losche, Langmuir **25** 4219 (2009).

How does the stiffness of lipid vesicles change as they interact with pore-forming peptides?

J.-H. Lee[1], S.-M. Choi[1], C. Doe[1], A. Faraone[2,3], S. R. Kline[3], P. A. Pincus[4,1]

Cell membranes, which consist of lipid bilayers, play important roles in cells as walls to maintain intracellular fluid concentrations and as matrices to host membrane proteins. During cellular processes such as the releasing and absorption of vesicles, cell fission and cell fusion, the cell membranes undergo various morphological changes governed by the interplay between proteins and lipid membranes. Yet, just how membrane elastic properties are affected by protein-lipid interactions remains only partially understood. Antimicrobial peptides are one of the most common examples of proteins that modify membrane morphology. A typical antimicrobial peptide consists of 20 to 40 amino acids with a length comparable to the lipid bilayer thickness. Depending on the peptide to lipid molar ratio, P/L, the peptides associate with the membrane in two distinct ways (Fig. 1(a)). When P/L is low, the peptides insert into the headgroup region (depicted as purple bars lying horzontally on the membrane surface) and cause thinning of the chain region, creating an internal membrane tension. Upon reaching a critical value of P/L (P/L^*), the peptides start to perforate, forming trans-membrane pores to relieve the internal membrane tension [1]. While the pore-forming mechanisms of antimicrobial peptides in lipid membranes have been widely investigated, the effects of pore formation on the membrane fluctuation and corresponding elastic properties have not yet been reported.

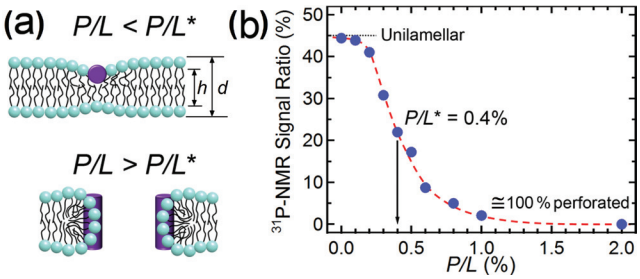

FIGURE 1: (a) Schematics for bound melittin and pores in lipid membranes. (b) ^{31}P NMR signal ratio (with/without Mn^{2+}) of DOPC LUV/melittin vs. P/L.

In the study highlighted here [2], the thermal fluctuation and elasticity of dioleoyl-phosphocholine (DOPC) large unilamellar vesicle (LUV) membranes interacting with antimicrobial peptides (melittins) were investigated using neutron spin-echo spectroscopy (NSE). Melittin is known to form toroidal pores in a DOPC bilayer. Suspensions of 6 mmol/L DOPC LUV in D_2O buffer with different concentrations of melittin were prepared. The ratios of ^{31}P-NMR signals of the suspensions with and without adding relaxation agent indicate that P/L^*, defined as P/L at which the half of LUVs are perforated, is ≈ 0.4 % (Fig. 1(b)).

The normalized intermediate dynamic structure factor, $I(q,t)/I(q,0)$, of the DOPC LUV/melittin in D_2O buffer at different values of P/L was measured at 30 °C using neutron spin echo (NSE) spectroscopy, where q is the magnitude of scattering vector and t is the Fourier time. Measured $I(q,t)/I(q,0)$ values were analyzed using the extended Zilman-Granek model [3,4] which describes the single membrane dynamics including the effects of internal dissipation within the membrane. If $qR \gg 1$, where R is the radius of the LUV, $I(q,t)/I(q,0)$ of a thermally fluctuating bilayer membrane is expressed as $I(q,t)/I(q,0) = \exp[-(\Gamma(q)t)^{2/3}]$ where the relaxation rate $\Gamma(q)$ is given as $\Gamma(q) = 0.025\gamma(k_BT/\tilde{\kappa})^{1/2}(k_BT/\eta)q^3$. Here, $\tilde{\kappa}$ is an effective bending modulus of membrane, γ is a function of k_BT and approaches unity for large bending modulus, k_B is the Boltzmann constant, T is the absolute temperature, and η is the viscosity of the solvent. At the length and time scales relevant to NSE measurements, $\tilde{\kappa}$ has contributions from the bending modulusof the membrane and from the internal dissipation within the membrane expressed by the bilayer compressibility modulus k, *i.e.*, $\kappa = \tilde{\kappa} + kd^2$, where d is the thickness of the undeformed bilayer (see Fig. 1a). It is known that κ and k of bilayers are coupled as $\kappa = \beta h^2 k$, where β is a constant prefactor and h is the thickness of the chain region (Fig. 1a). The measured values of $I(q,t)/I(q,0)$ agree well with the extended ZG model, resulting in $\Gamma(q)$ which follows the q^3-dependence as expected by the model (Fig. 2).

[1]Korea Advanced Institute of Science and Technology, Daejeon, Korea, 305-701
[2]University of Maryland,, College Park, MD 20742
[3]NIST Center for Neutron Research, National Institute of Standards and Technology, Gaithersburg, MD 20899
[4]University of California, Santa Barbara, CA 93106

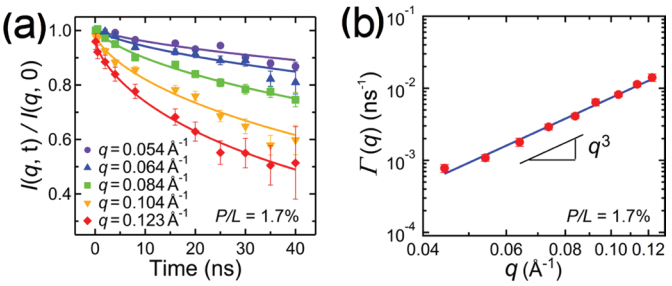

FIGURE 2: (a) $I(q,t)/I(q,0)$ of DOPC LUV/melittin at different values of q. The solid lines are fits using the extended ZG model. (b) Relaxation rate $\Gamma(q)$ vs. q. The solid line is a fit using the expression for $\Gamma(q)$ described in the text.

The effective bending moduli $\tilde{\kappa}$ of DOPC/melittin membranes are determined by fitting the measured $\Gamma(q)$ with the extended ZG model, from which the bending modulus κ and the bilayer compressibility modulus are estimated (Fig. 3(a)). In region I where melittin is adsorbed horizontally on the membrane surface, both κ and k decrease with P/L and reach a minimum around P/L^*. In region II and III where melittin forms pores, and k increase slightly until $P/L \approx 1.7$ % (region II) and increase rapidly from $P/L \approx 2.4$ % (region III). Since the relative change of the chain region thickness with P/L is fairly small, it cannot explain the rather large change of measured elasticity. When a peptide is adsorbed between lipid headgroups, perturbation of the chain packing occurs together with membrane thinning. A statistical thermodynamic analysis of chain packing in bilayers showed that could be dramatically decreased by the increase of chain conformational entropy in the membranes. Therefore, the decrease of κ (and k) in region I may be dominated by the perturbation of chain packing by peptide adsorption. Since melittin forms a rigid α-helix on a membrane, the pores formed by 4 to 7 melittins may be rather rigid and dominantly contribute to the increase of κ and k in region II. In region III, the rate of increase of κ and k with P/L becomes much larger near $P/L = 2$ %. To explain this, the inter-pore interaction needs to be considered because the population of pores is high in region III.

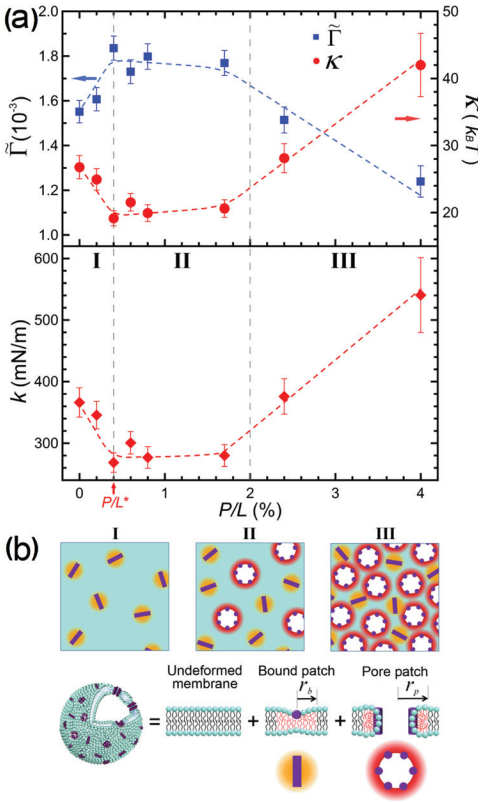

FIGURE 3: (a) Reduced relaxation rate $\tilde{\Gamma} = \Gamma(q)\eta_0/(k_BTq^3)$, bending modulus κ and bilayer compressibility modulus k of DOPC/melittin in D_2O buffer at different peptide/lipid ratios, P/L. (b) Scaled schematics of the distributions of bound melittin and pores on the membrane at P/L = 0.4 % (I), P/L = 1.7 % (II) and P/L = 4.0 % (III). In the DOPC bilayer, the bound patch radius r_b is ≈ 25 Å and the pore radius r_p is ≈ 38.5 Å.

Theoretical and experimental studies indicate that the interaction between nearby inclusions in a membrane is mediated through the local perturbation of lipid chain packing near the inclusions. Therefore, when inclusions are far apart, the inter-inclusion interaction is zero or negligibly small. However, when the two regions deformed by inclusions begin to overlap, a repulsive inter-inclusion interaction sets in. In the DOPC LUV/melittin system, there are two types of membrane regions deformed by a bound peptide (bound patch) and a peptide-induced pore (pore patch) (Fig. 3(b)). At P/L^*, the average inter-bound melittin distance is calculated to be ≈ 100 Å which is 2 times larger than the contact distance of bound patches in DOPC bilayer ($2r_b = 50$ Å). Therefore, the inter-patch interaction in region I may be negligible. Above P/L^*, the average inter-pore patch distances at $P/L = 2$ % and 4 % are calculated to be ≈ 120 Å and ≈ 80 Å, respectively. Since the contact distance of pore patches is 77 Å ($2r_p$), the inter-pore interaction may be small or negligible in region II but it becomes appreciable in region III, especially near P/L = 4 %. It should be noted that κ and k begin to increase rapidly from $P/L \approx 2$ % where the inter-patch interaction is expected to become significant.

The thermal fluctuation and elasticity of DOPC LUV membranes interacting with pore-forming peptides, melittins, has been investigated for the first time by *in-situ* NSE measurements. The results of this study are expected to play an important role in understanding the elastic behavior and morphological changes of cell membranes induced by protein-membrane interactions,and may provide new insights for developing new theoretical models for membrane fluctuations which include the membrane-mediated interactions between protein patches.

References

[1] H. W. Huang et al. Phys. Rev. Lett. **92**, 198304 (2004).

[2] J.-H. Lee, S.-M. Choi, C. Doe, A. Faraone, P. A. Pincus, and S. R. Kline, Phys. Rev. Lett. **105**, 038101 (2010).

[3] A. G. Zilman and R. Granek, Phys. Rev. Lett. **77**, 4788 (1996).

[4] M. C. Watson and F. L. H. Brown, Biophys. J. **98**, L9 (2010).

Bilayer membrane dynamics in NSAID-phospholipid adducts

M.B. Boggara[1,4], A. Faraone[2,3], R. Krishnamoorti[4]

The bending modulus (κ) of a lipid bilayer, a model for a cell membrane, is a key parameter in understanding its viscoelastic behavior and stability and a key determinant in a number of membrane processes. From a biophysical viewpoint, κ governs the thermal undulations that could determine short-range interactions between membranes and substrates. Most drug molecules interact with cell membranes to exert their therapeutic action. This is especially so in the case of amphiphilic drug molecules such as nonsteroidal anti-inflammatory drugs (NSAIDs) [1]. Understanding the behavior of membrane κ is thus potentially useful in developing drug-bilayer adducts for applications such as targeted drug delivery.

Here we highlight our study of κ as a function of pH in the physiologically relevant range of 2 to 8 focusing on the effect of ibuprofen, a popular NSAID, on bilayers made of 1,2-dimyristoyl-*sn*-glycero-3-phosphatidyl-choline (DMPC) [2]. Changing pH is likely to change the lipid-lipid, lipid-water and drug-lipid electrostatic interactions and the charge states of both protonated and deprotonated ibuprofen. Moreover, since such lipid–NSAID adducts have been suggested as a safer means of delivery of anti-inflammatory drugs [3], it is important to understand the potential impact of changes in pH on the mechanical properties of the membranes and therefore long-term stability of such adducts.

Neutron spin echo (NSE) is an excellent tool to directly probe the dynamics of lipid bilayer membranes by measuring the dynamics of height-height correlations in the plane of the membrane which is related to the bilayer κ (Fig. 1). Although, intercalation of phospholipid bilayers by small molecules is expected to lead to significant changes in the bilayer κ, these changes are known to be a complex interplay of many factors. Several studies have indicated that the drug-effect on the membrane mechanical properties can range from lowering κ, the elimination of micro/nano domains in mixed lipid bilayer systems, vesicle fusion, and influence on the drug's therapeutic or side effects.

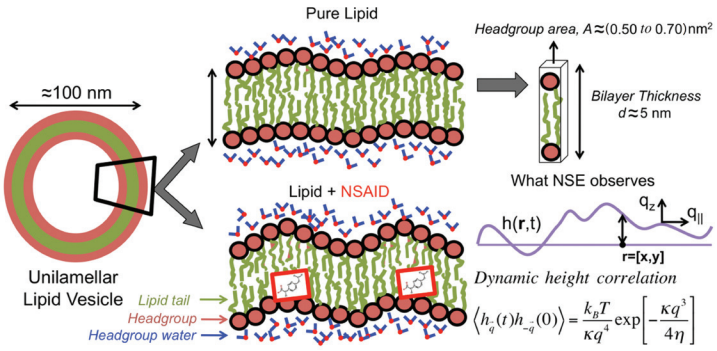

FIGURE 1: Left: Small unilamellar lipid vesicles used for experiments. Middle: Fluctuations for pure lipid and drug-incorporated bilayers. Above right: bilayer physical parameters obtained using SANS. Below right: NSE-measured membrane fluctuations expressed as the height-height dynamic correlation function.

NSE connects the dynamics of height-height correlations to the intermediate structure factor, $S(q,t) = I(q,t)/I(q,0) = Ae^{-(\Gamma t)^{2/3}}$, which is related to κ via the decay constant given by $\Gamma = (0.025\gamma k_BT/\eta)(k_BT/\kappa)^{1/2}\, q^3$, according to Zilman and Granek [4]. The plots of $S(q,t)$ at various q values in Fig. 2a are combined in the inset to Fig. 2a to give a master curve, $\ln[S(q,t)]$ vs. $q^2t^{2/3}$ by substituting for Γ in $S(q,t)$, which is then used to determine κ. The factor $\gamma = (1 - 3\ln(q\xi)\, k_BT/4\pi\kappa)$ is ≈ 1 for $\kappa \gg k_BT$

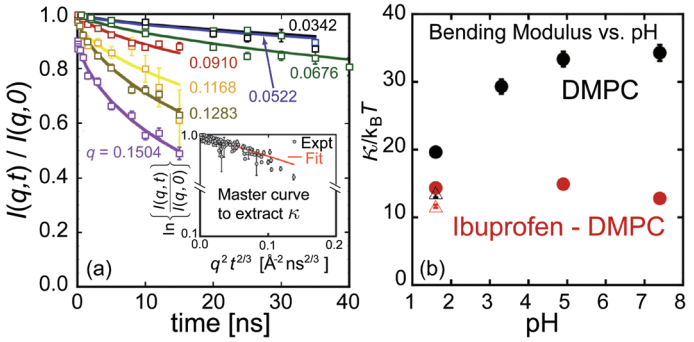

FIGURE 2: (a) Intermediate structure factor for DMPC at pH ≈ 7.4 and 30 ˚C. The number next to each curve is the value of q in Å^{-1}. The inset shows Zilman-Granek scaling to produce a master curve allowing the extraction of the membrane bending modulus, κ. (b) κ as a function of pH for DMPC and ibuprofen–DMPC (31 % mole fraction) at 30 ˚C (solid circles). Also shown are the data for pH ≈ 1.6 and 37 ˚C (open triangles).

[1]Current Address: Rensselaer Polytechnic Institute, Troy, New York 12180.
[2]NIST Center for Neutron Research, National Institute of Standards and Technology, Gaithersburg, Maryland 20899
[3]University of Maryland, College Park, Maryland 20742
[4]University of Houston, Houston, Texas 77204

which is valid for lipid bilayers. η is the solvent viscosity experienced by the bilayer and is usually taken as $\approx 3\eta_{D2O}$ to capture the effect of the local aqueous environment on the viscous dissipation of membrane undulations, as validated by atomistic molecular dynamics simulations. The inferred bending modulus for the lipid bilayer as a function of pH with and without ibuprofen is shown in Fig. 2b.

Figure 2b shows that at 30 ˚C the bending modulus of DMPC membranes, κ_{DMPC}, decreases significantly at low pH values while being roughly constant at high pH. On the other hand, $\kappa_{ibuprofen\text{-}DMPC}$ remains unchanged with varying pH and is lower than κ_{DMPC}. At a pH of ≈ 2 and at 37 ˚C, above any gel to fluid transitions for the lipid, the values of κ for the membranes with and without ibuprofen are roughly identical. The inferred κ values result from a combination of various deformation modes such as bending, area deformation, shear, thickness fluctuations, and molecular protrusion. The bilayer κ is further influenced by both the hydrophobic chains (*via* bilayer thickness) and the hydrophilic headgroup (*via* surface charge density or area compressibility). Since the bilayer surface charge density, σ, changes with pH, our qualitative estimates suggest that the contribution due to the electrostatic component κ_{el} to κ is $\approx k_BT$ at low pH and therefore insignificant. For pH > 4 κ_{el} is at least two orders of magnitude higher than at low pH, and potentially a significant fraction of κ.

The bilayer thickness d impacts κ through $\kappa \approx K_A d^2/c$, where K_A is the area compressibility modulus and $c \approx 12$ to 48. For DMPC, κ decreases by ≈ 32 % with a pH change from 8 to 2 at 30 ˚C. Further, at a pH of ≈ 2, κ decreases by ≈ 18% when the temperature is raised from 30 °C to 37 °C. Along with d decreasing from (4.7 ± 0.1) nm at 30 ˚C to (4.3 ± 0.1) nm at 37 ˚C, this decrease in κ with temperature is due to the lipid chain undergoing a gel-like to fluid-like transition. Moreover, the headgroup hydration is slightly lowered at low pH, suggesting that the decrease in κ with pH has origins in the structural and electrostatic perturbations to the headgroup. Addition of ibuprofen decreases κ by ≈ 53 % at high pH, where the drug is anionic, and locates in the headgroup/chain interfacial region [5]. On the other hand, ibuprofen leaves κ almost unaffected at low pH when it is neutral and locates deeper in the chains.

The effect of ibuprofen on κ can be understood by considering structural and hydration changes. Using κ obtained from spin echo [2] and $d \approx 4.3$ nm for DMPC in fluid phase and ≈ 4 nm for ibuprofen–DMPC from SANS [6], values of K_A were estimated (Table 1). At low pH and high temperature, the decrease in headgroup hydration and protonation of phosphate in the headgroup in the case of DMPC, leads to a headgroup region with low σ. Thus the bilayer presents low resistance to undulations as well as changes in local area. In the case of ibuprofen–DMPC, as the drug partitions into already fluid-like chains, the resulting K_A is comparable to that of DMPC. Thus, the values of κ_{DMPC} and $\kappa_{ibuprofen\text{–}DMPC}$ are similar at pH ≈ 2. At high pH, the headgroup is well hydrated and zwitterionic for DMPC, resulting in higher values of K_A. On the other hand, ibuprofen partitions into the headgroup region leading to a reduction in headgroup hydration. This results in a much smaller value of K_A, nearly half that of DMPC as has been observed in SOPC lipid systems in the presence of drug-like salicylate or short-chain alcohols, and which needs direct experimental confirmation for ibuprofen-DMPC system.

pH	DMPC		Ibuprofen – DMPC (mole ratio 0.31/1)	
	κ/k_BT	K_A(mN/m)	κ/k_BT	K_A(mN/m)
1.6	18.0 ± 0.5 (13.2 ± 0.3)	163 ± 8 (147 ± 8)	12.2 ± 0.3 (12.0 ± 0.2)	153 ± 8 (154 ± 7)
3.3	24.6 ± 0.8	267 ± 15		
4.9	26.8 ± 0.9	291 ± 17	12.8 ± 0.3	161 ± 9
7.4	26.2 ± 0.8	285 ± 16	12.3 ± 0.3	154 ± 8

Table 1. Membrane bending (κ) and area compressibility (KA) modului as a function of pH at 30 °C (data in parenthesis correspond to T = 37 °C).

To summarize, using a combination of NSE along with structural studies based on SANS and MD simulations, we have examined the changes in the bending modulus for DMPC-based membranes with pH and addition of ibuprofen. Significantly, we observe that κ decreases by ≈ 40 % going from pH ≈ 8 to pH ≈ 2 and attribute the decrease to changes in lipid interactions and headgroup hydration. Further, ibuprofen lowers κ at all pH values due to a combination of bilayer thinning, reduction in headgroup hydration and a lower area compression modulus. These studies provide a unified understanding of the role of electrostatics and membrane additives in cellular membranes. As well as adding to understanding useful in creating lipid-based systems for targeted delivery of such NSAIDs to the sites of inflammation, this work further signifies an important first step in an attempt to understand at a molecular level how NSAIDs might be causing ulcers.

References

[1] H. Chakraborty, S. Mondal, M. Sarkar, Biophys. Chem. **28**, 137 (2008).

[2] M.B. Boggara, A. Faraone, R. Krishnamoorti, J. Phys. Chem. B **114**, 8061 (2010).

[3] L.M. Lichtenberger, J.J. Romero, W.M.J. de Ruijter, F. Behbod, R. Darling, A.Q. Ashraf, S.K. Sanduja, J. Pharmacol. Exp. Ther. **279**, 298 (2001).

[4] A.G. Zilman, R. Granek, Chem. Phys. **284**, 195 (2002).

[5] M.B. Boggara, R. Krishnamoorti, Biophys. J. **98**, 586 (2010).

[6] M.B. Boggara, R. Krishnamoorti, Langmuir **26**, 5734 (2010).

A method for the measurement of retained austenite content in steels

T. Gnäupel-Herold[1,2], A. Creuziger[3]

With the recent emergence of transformation induced plasticity (TRIP) – with more than a century of development behind it – steel has seen a major developmental milestone bringing new levels of combined strength and ductility. Because of this, TRIP steels are seen as an important structural material for future car bodies. The key property responsible for this advance is the deformation induced transformation of the minority phase austenite (face centered cubic – fcc) into martensite (body centered tetragonal – bct), both embedded in the majority ferrite phase (body centered cubic – bcc). Therefore, the retained austenite (RA) content is intimately related to the strength, the formability and deformation history of TRIP steels.

Considering the importance of this property it is astounding that the measurement of the RA content through diffraction – seen as both accurate and precise – is based at least in part on heuristic principles that have rarely been questioned. The principle in question is the presumed randomness of grain orientations or, rather, the lack thereof. This presumption is never justified because there is no steel without some degree of preferred orientation. Even loose powders generally exhibit some degree of non-random grain orientation [1]. The consequences of non-random grain orientations – called preferred orientation – on any diffractive phase content determination are straightforward. Diffracted intensity is proportional to the phase content but now it becomes dependent on the specimen orientation.

What is the most efficient way to measure the retained austenite content in steel by diffraction? The apparently exhaustive answers provided by both ASTM standards and SAE recommendations reveal weaknesses when examined critically. The question of how to deal with the orientation dependence is crucial because preferred orientation is the greatest source of uncertainty for RA measurements. One can a) presume complete randomness; b) prescribe varying orientation averaging schemes or c), determine the orientation density function and use it as a correction. Option a) is never justified because there is no steel without some degree of preferred orientation. The dangers of option a) are best illustrated by the withdrawal of a previous NIST austenite standard reference material whose production was based on the premise of sufficient randomness. Option c) in the context of Rietveld refinement is deemed the best but also the costliest way in terms of instrumental and time requirements. Option b) is left as the most sensible approach because of modest instrumental requirements, and it is, together with some procedural recommendations, part of the two standard measurement procedures for RA content. Therein lies the rub: the averaging procedures described do not withstand a critical examination (sample orientations do not have equal weight, which is disregarded; only a small fraction of orientation space is used), and the error estimation is incorrect.

How is orientation averaging performed correctly? This has been answered already, albeit for a different context – the determination of the grain orientation density function (ODF) [2]. The most efficient way to determine the ODF is to measure intensities at specimen orientations that form an equidistant net on the pole sphere (where the specimen orientation in spherical polar coordinates

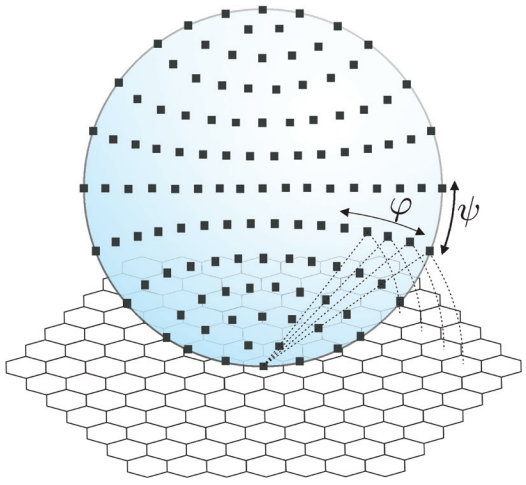

FIGURE 1: Regular hexagonal grid and the reverse equal-area projection of the centers of the hexagons onto a sphere. The locations on the sphere are the spherical coordinates of sample tilt ψ and sample rotation φ.

[1]University of Maryland, College Park MD 20742
[2]NIST Center for Neutron Research, National Institute of Standards and Technology, Gaithersburg MD 20899-6102
[3]Metallurgy Division, National Institute of Standards and Technology, Gaithersburg MD 20899-8553

(φ,ψ) meets the unit sphere). However, it is not possible to divide the surface of a sphere into equal, regular polygons. On the other hand, coverage through equal hexagons is straightforward for a plane. One can achieve a near-equidistant mesh on the pole sphere through the following procedure: project the sphere on a plane in equal-area projection, then sample the projected sphere with a regular hexagonal grid of chosen resolution, and "back-project" the grid into true spherical space.

Added up, the same mesh of specimen orientations also forms a complete orientation average which requires neither any corrections nor the ODF itself because ultimately only the sum peak is needed for a RA content measurement [1]. Note that the complete orientation average is most easily achieved with neutron diffraction. Due to the high penetration there are no inaccessible orientations and the only corrections necessary is the subtraction of background. X-ray diffraction is surface limited, (exception: high energy synchrotron diffraction) thus limiting the possible tilt range and the accessible region of orientation space (called partial averaging in the following). The method of complete orientation averaging with neutron diffraction addresses these problems and it establishes simple conditions for the minimum of necessary measurements to determine the austenite content.

The method of complete orientation averaging provides only a partial answer to the problem of measuring a phase fraction in a textured material. The remaining questions concern which and how many reflections to measure, and what number of orientations to choose for the mesh shown in Fig. 1. The selection of reflections follows in a straightforward manner from basic statistical principles. In order to get any measure on the accuracy of the orientation average for one reflection it needs to be compared with a suitable quantity. As there are no standard reference materials available this quantity can only be a different reflection measured on the same material with the same orientation averaging. Both reflections are divided by their respective theoretical intensities after which they become comparable – and the difference between the two values gives a direct measure of the deviation from the mean both of the averaging procedure and indirectly, the number of orientations used. The analysis of the latter is revealing because it sheds some light on the relationship between precision of the RA content measurement and number of orientations in the average (Fig. 2). The measurements were performed with sufficient counting time such that uncertainties stemming from the counting statistics became negligible.

The most significant result to be taken from Fig. 2 is that, depending on the averaging scheme the relative standard deviation of the measured RA fraction f_γ reaches a stable value ($\sigma_{rel} \approx 10$ %) spanning a range from $f_\gamma = 1.6$ % up to $f_\gamma = 14.1$ %. However, precision is not to be confused

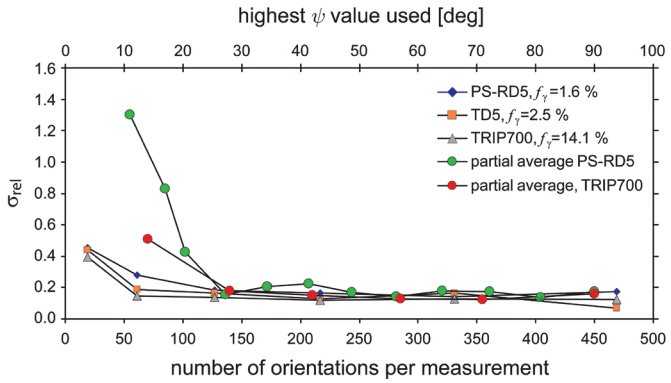

FIGURE 2: Relative standard deviations of f_γ for the complete averaging scheme (bottom axis) and for partial averaging in limited ψ-tilt (top axis). Low values on the top axis mean fewer orientations just as on the bottom axis.

with accuracy. Whereas σ_{rel} for partial averaging appears to reach the same stable value as the complete averaging scheme at $\psi \approx 30°$ - a value easily possible for most x-ray equipment – the absolute values for f_γ draw a different picture. The complete averaging method fares well with stable values reached at >100 orientations (Fig. 3) but partial averaging needs tilt angles > 60° to reach the same value, thus becoming essentially a complete average itself.

In summary, we can state that for the more than 40 different samples investigated here the most efficient way of measuring the retained austenite content - while providing both accuracy and precision - consists of using at least four reflections (two for ferrite / martensite, two for austenite), each with at least 100 orientations in the complete averaging scheme described here. The most severe preferred orientation will require more orientations to be included in the averaging. This is best judged by the standard deviation where $\sigma_{rel} \approx 10$ % appeared as the achievable limit.

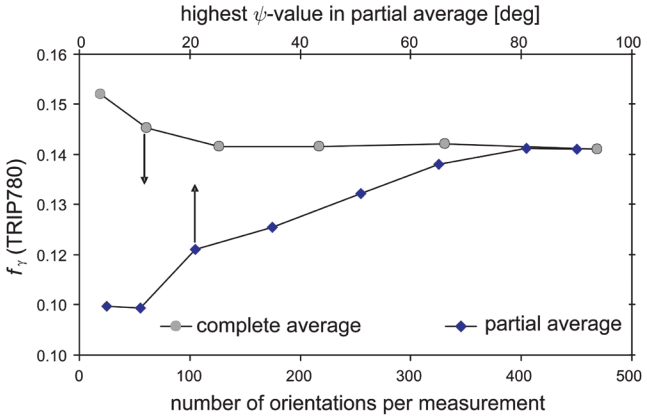

FIGURE 3: Comparison of the retained austenite content f_γ as obtained from complete and partial averaging schemes for undeformed TRIP700. The partial averaging is typically used in surface limited x-ray diffraction. For the standard deviations, see Fig. 2. Note that at psi- angle of 90° partial average becomes complete.

References

[1] T. Gnäupel-Herold, A. Creuziger, submitted to Mat. Sci Eng. A.

[2] S. Matthies, H.-R. Wenk, Phys. Stat. Sol. A **133,** 253 (1992).

Probing artificial muscles with neutrons

J. K. Park[1], R. B. Moore[1], P. J. Jones[2], C. Sahagun[2], S. E. Morgan[2], K. A. Page[3], D. S. Hussey[4], D. L. Jacobson[4], M. Arif[4]

Ionic polymer metal composites (IPMCs) are a class of materials with similarities to biological muscles that exhibit actuation due to electrical stimulation, and are often referred to as artificial muscles [1]. Although IPMCs have been studied for more than ten years, the exact actuation mechanism is still not well understood. IPMCs are based on a solid polymer electrolyte, which is plated on both surfaces by dense layers of metal nanoparticles (*e.g.*, platinum or gold) to serve as conductive electrodes.

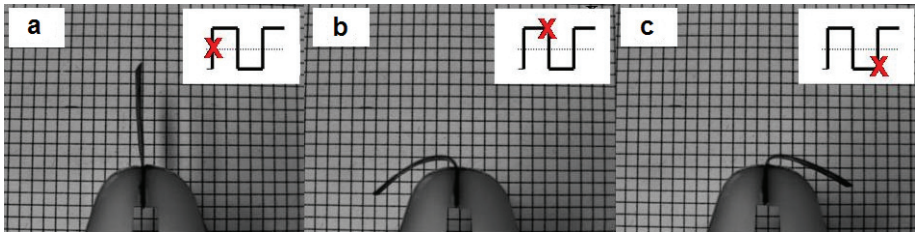

FIGURE 1: IPMC actuation under applied electrical voltage. Each image was captured at the position of X on the excitation square wave.

This structure resembles the membrane electrode assemblies (MEAs) used in fuel cells. Under the stimulus of a relatively low electric field (2 V to 3 V), IPMCs are capable of undergoing significant mechanical bending motion; an example of this is shown in Fig. 1. Conversely an external mechanical force applied to the surface of an IPMC can stimulate a detectable electrical response [2].

The vast majority of work on IPMCs has utilized the perfluorosulfonate ionomer (PFSI) Nafion, a copolymer of tetrafluroethylene with perfluorovinylether units terminated with sulfonic acid functionalities. This material has received considerable attention due to the unique nanophase-separated morphology observed upon aggregation of the polar, ionic moeities within the hydrophobic polytetrafluoroethylene (PTFE) matrix. There have been numerous small angle x-ray and neutron scattering studies performed to elucidate the morphology of Nafion and to propose detailed models for this technologically important material as an ionic conductor. From this body of work, it is generally accepted that there are continuous pathways that allow transport of ions and water [3,4] and recent studies have suggested that these pathaways may be elongated, locally parallel water channels [4,5].

One proposed mechanism for IPMC actuation that has commonly been discussed in the literature is an electrophoresis-like counterion and water redistribution within the nanostructured ionomer membrane [6-8]. Since the ionic polymer is negatively charged with protons or alkali-metal cations as the counterions, these mobile cations in the hydrated membrane readily redistribute in response to an applied electric field to create cation-rich and cation-poor boundary layers near the electrode/membrane interfacial regions as is shown if Fig. 2. As cations migrate toward the cathode, they drag along

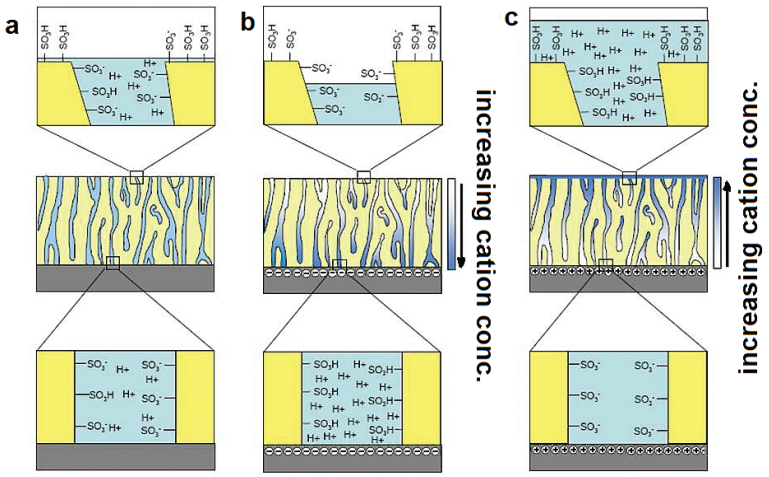

FIGURE 2: (a) Illustration of the equilibrium state between sulfonate groups and protons in the PFSI membrane with no applied bias, (b) illustration of proton and water migration to the negatively charged substrate and formation of isolated sulfonate-rich domains and dehydration on the top surface of the PFSI membrane, and (c) illustration of proton and water migration away from the positively-charged substrate forming a cationic film on the top surface of the PFSI membrane and neutralization of the positively charged substrate by non-mobile sulfonate ions.

[1]Virginia Polytechnic Institute and State University, Blacksburg, VA 24061
[2]The University of Southern Mississippi, Hattiesburg, MS 39406
[3]Polymers Division, National Institute of Standards and Technology, Gaithersburg, MD 20899
[4]Physics Laboratory, National Institute of Standards and Technology, Gaithersburg, MD 20899

water molecules. This hydraulic action results in swelling near the cathode and contraction near the anode due to dehydration, leading to the bending force that curves the IPMC towards the anode. Other models of the bending are electrostatic in nature, due to local cation redistribution which leads to polymer chain relaxation or dipole-dipole interactions [9,10].

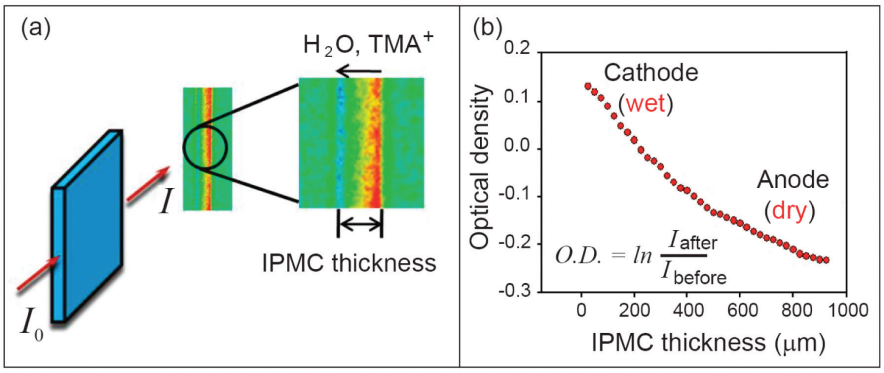

FIGURE 3: (a) Colorized images showing water/counterion -depleted zones represented by red pixels and water/counterion -rich areas represented by blue pixels. IPMC was subjected to 3 V DC. (b) Relative neutron optical density due to water/counterion gradient profile across the IPMC thickness.

Experimental studies to validate/invalidate actuation models have utilized magnetic resonance imaging (MRI) [11] and nuclear magnetic resonance (NMR) [12] methods, which showed greater proton density (PD) and higher water diffusion coefficients near the cathode, respectively. In this study high resolution neutron radiography was used to directly measure the the water/counterion redistribution under electrical stimulation predicted by the hydraulic model [1]. Recent improvements in neutron detectors allowed spatial resolution of 25 μm to be achieved. In addition to neutron imaging, this work also performed *in situ* atomic force microscopy studies of the IPMC surface to monitor changes in the morphological and surface characteristics that result from electrical stimulation.

The results of the neutron imaging are shown in Fig. 3. Here the IPMC was oriented to allow neutrons to travel parallel to the anode and cathode surfaces. The resulting neutron transmission allows the mapping of water distributed through the plane of the IPMC from anode to cathode. In the figure, the image of the unstimulated state is compared to the state after an electrical stimulus of 3 V was applied for 30 s. The resulting change in neutron attenuation showed a rapid redistribution of water/conterions in the IPMC when the electrical stimulus was applied. When the polarization of the applied electric field is reversed the corresponding water/counterion distribution is also rapidly reversed, in direct support of the hydraulic model for the deformation of the IPMC due to the applied electric potential. Additional measurements were made using D_2O swollen IPMCs neutralized to contain sodium and tetramethylammonium counterions were also studied to separate the cation motion from the hydraulic motion. These results showed that both the cations and water migrate under electrical stimulation.

In further support of the bulk redistribution of water/counterions obtained from neutron radiography, high resolution AFM studies were performed. These studies showed the hydration of the anode and dehydration of the cathode with the appearance of liquid pore like structures on the surface of negative polarity (cathode) of the IPMC and absence of liquid pores for the surface of positive polarity (anode).

The true mechanism of actuation for IPMCs remains under debate. However, the two methods used here, neutron radiography and atomic force microscopy, provide direct evidence that the actuation response involves a strong hydraulic contribution. After the application of an electrical field between the IPMC electrode layers, the mobile cations and the hydraulic sheath rapidly move toward the negatively charged cathode. This gradient in water and counterion concentration across the ionic polymer membrane creates swelling on the cathode side and contraction on the anode side that results in a bending force that curves the IPMC toward the anode. When the polarity is switched, both water and ions move rapidly across the ionic polymer film reversing the gradient and reversing the curvature of the IPMC.

References

[1] J.K. Park, P.J. Jones, C. Sahagun, K.A. Page, D.S. Hussey, D.L. Jacobson, S.E. Morgan and R.B. Moore. Soft Matter, **6**, 1444 (2010). DOI: 10.1039/b922828d.

[2] M. Shahinpoor, Electrochim. Acta, **48**, 2343 (2003).

[3] K. A. Mauritz and R. B. Moore, Chem. Rev., **104**, 4535 (2004).

[4] K. Schmidt-Rohr and Q. Chen, Nat. Mater., **7**, 75 (2008).

[5] M.-H. Kim, C. J. Glinka, S. A. Grot and W. G. Grot, Macromolecules, **39**, 4775 (2006).

[6] M. Shahinpoor, Y. Bar-Cohen, J. O. Simpson and J. Smith, Smart Mater. Struct., **7**, R15 (1998).

[7] P. G. De Gennes, K. Okumura, M. Shahinpoor and K. J. Kim, Europhys. Lett., **50**, 513 (2000).

[8] M. Shahinpoor, Smart Mater. Struct., **3**, 367 (1994).

[9] L. M. Weiland and D. J. Leo, Smart Mater. Struct., **13**, 323 (2004).

[10] S. Nemat-Nasser and J. Y. Li, J. Appl. Phys., **87**, 3321 (2000).

[11] L. Naji, J. A. Chudek and R. T. Baker, Soft Matter, **4**, 1879 (2008).

[12] L. Naji, J. A. Chudek and R. T. Baker, J. Phys. Chem. B, **112**, 9761 (2008).

'Molecular headphones', SANS and MD modeling of protein denaturing

P. E. Mason[1], C. E. Dempsey[2], G. W. Neilson[3], S. R. Kline[4], J. W. Brady[1]

Proteins are chains of amino acids that in aqueous media typically fold up into shapes with specific and very efficient biological functions. For decades now we have had a broad brush understanding of the forces that cause such folding: the interaction of the charged groups, hydrophilic and hydrophobic groups of the protein with both itself and with water, but a detailed understanding of these mechanisms has proved elusive. Our current research aims to gain a greater insight into the forces that cause proteins to fold up in solution by studying model systems that are easier to understand and quantify [1].

Broadly speaking, there are two types of hydrophobic groups in proteins, those that have a relatively high degree of curvature relative to the size of water ('knobbly' hydrophobic groups such as valine) and those with a relatively flat surface such as the indole group of tryptophan. In order to gain better insight into how these types of hydrophobic groups interact with each other, and how this interaction could be disrupted by denaturants (agents that cause a protein to lose its 3-D solution structure), we chose to examine some soluble analogues of these archetypal motifs. This solubility poses a bit of a problem as the hydrophobic systems we would ideally wish to study, just like oil and water are immiscible and if you attempt to mix them, they tend to simply phase separate into two layers. This led to the compromise of choosing molecules which were somewhat hydrophobic, but not hydrophobic enough to actually phase separate. The systems of isopropyl alcohol (rubbing alcohol) and pyridine in water were chosen as models for the 'knobbly' and 'flat' hydrophobic groups respectively, and guanidinium chloride was chosen as the denaturant (Fig. 1). A multidisciplinary approach was taken with all of the systems being studied by both molecular dynamics (MD) and small angle neutron scattering (SANS), a method capable of gaining information about association of solutes in solutions.

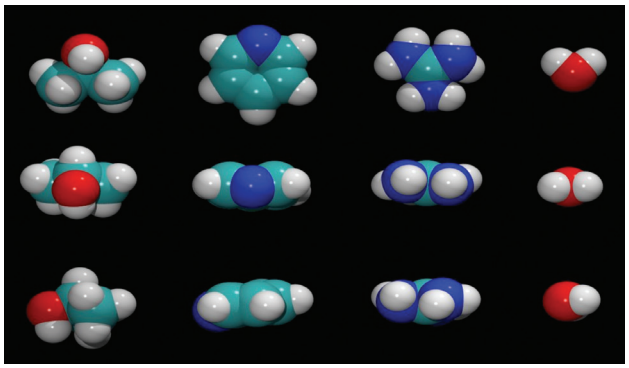

FIGURE 1: The size and shape of the molecules in this study, from left to right: isopropyl alcohol (knobbly) , pyridine (flat), guanidinium (as a denaturant), and water.

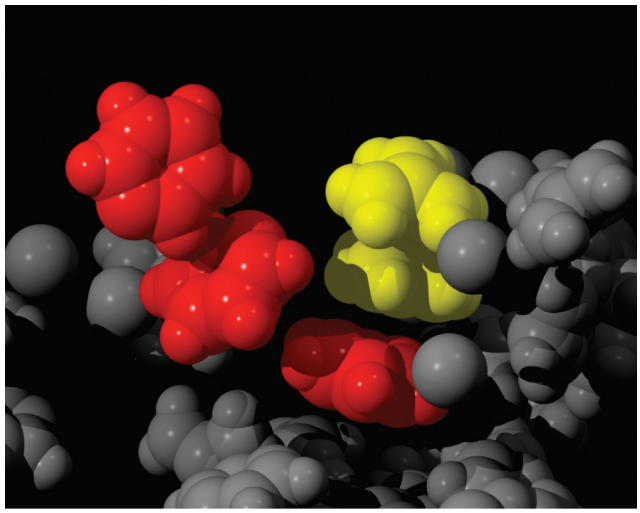

FIGURE 2: highlighted are the T-type interactions of the pyridine (red) and the stacking interaction of guanidinium (yellow) and pyridine (red). Guanidinium also interacts with itself in a stacking fashion (both yellow).

In the molecular dynamics simulations of these systems it can be seen that the molecules preferentially associate with each other, showing that they are hydrophobic, although not hydrophobic enough to phase separate. Further examination of the pyridine system reveals that the main mechanism by which these flat aromatic groups interact with each other is by a T-type interaction, but when

[1]Cornell University, Ithaca, NY 14853
[2]University of Bristol, Department of Biochemistry, Bristol BS8 1TD, Avon England
[3]University of Bristol, HH Wills Physics Lab, Bristol BS8 1TL, Avon England
[4]NIST Center for Neutron Research, National Institute of Standards and Technology, Gaithersburg, MD 20899 USA

the denaturant is added, it competes with this interaction, somewhat dispersing the aggregation of the hydrophobic groups. Interestingly, the denaturant, which is also a flat molecule, interacts with pyridine in a similar stacking type interaction to that found between two guanidinium ions (Fig. 2).

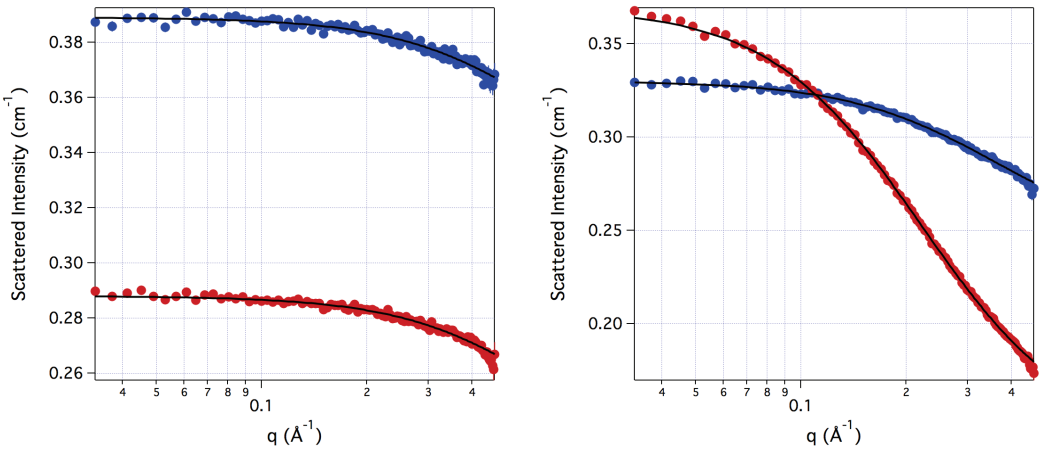

FIGURE 4: Blue data points are the small angle neutron scattering data for 3 mol/kg (molal) isopropyl alcohol/water (left) and 3 mol/kg pyridine/water (right) solutions, while the red data points are the same solutions after the addition of the denaturant guanidinium chloride, at an equal concentration of 3 mol/kg guanidinium chloride /water. It is clear that the addition of denaturant has no effect on the clustering of the knobbly hydrophobic group (isopropyl alcohol), while the clustering of the flat, hydrophobic group (pyridine) is significantly reduced.

This stacking interaction can be further quantified by the examination of 'density maps', which are an average spatial representation of atoms around a central molecule. Here the earlier finding is re-enforced, with the exception that the hydrogen bond interaction between the denaturant and the polar nitrogen of pyridine can be seen, giving the density map of guanidinium around pyridine the appearance of 'molecular headphones' (Fig. 3).

It was found in the simulations that the knobbly hydrophobic group of isopropyl alcohol did not interact with itself as strongly as the flat hydrophobic group of pyridine, nor was this interaction particularly disrupted by the addition of the flat denaturant guanidinium.

The average coordination number of the hydrophobic solute gives a measure of the aggregation of these species. Again the MD simulations showed that pyridine displayed a greater aggregation than isopropyl alcohol, and also that the clustering of pyridine was significantly dispersed by the flat denaturant guanidinium, while the clustering of isopropyl alcohol was relatively unaffected by its presence.

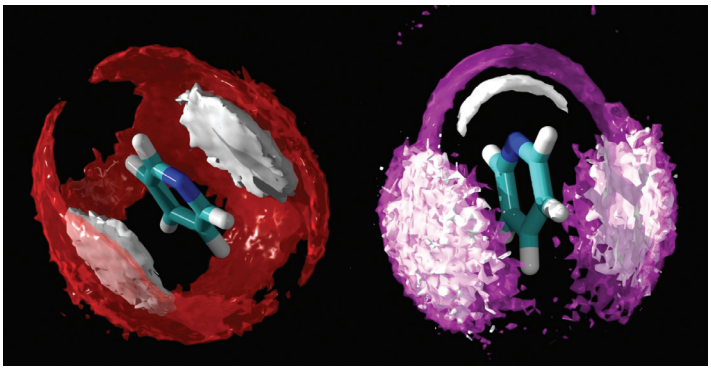

FIGURE 3: Left, the density maps of pyridine around pyridine (white is hydrogen on pyridine, red, carbon on pyridine) showing the T-type interaction (the white cloud closer to the pyridine than the red cloud), and right, the 'molecular headphones' of the density of guanidinium around pyridine (white is H on guanidinium, purple, nitrogen on guanidinium) showing the stacking type interaction (the white cloud within the purple cloud).

SANS at the NIST Center for Neutron Research allows the possibility to test the predictions of this model directly. SANS is sensitive to both the size and density of the clustering, in this case of the hydrogen rich hydrophobic molecules, and hence offers direct structural insight into these solutions.

A correlation length model was fitted to the data of Fig. 4 (black lines), yielding a small correlation length (1.4 ± 0.1) Å for the isopropanol aggregates, and a larger length (4.5 ± 0.02) Å for the pyridine aggregates. This directly confirms the MD prediction that the flat, aromatic groups associate much more strongly than the knobbly ones. Also, as predicted by the simulations, the SANS data confirms that the addition of denaturant has essentially no effect on the association of the knobbly hydrophobics, but significantly disrupts the aggregation of flat hydrophobic groups, reducing the correlation length to (2.7 ± 0.05) Å.

This combination of simulations and experiment confirms the geometry-dependent interactions of hydrophobic molecules with both each other and with a protein denaturant, yielding a valuable insight into the details of the driving forces that cause proteins to fold as they do.

Reference

[1] P. E. Mason, C. E. Dempsey, G. W. Neilson, S. R. Kline, J. W. Brady, J. Am. Chem. Soc. **131** , 16689 (2009).

Coordinatively-unsaturated metal-organic frameworks for hydrogen storage

W.L. Queen[1,2], C.M. Brown[1], K. Sumida[3], J.R. Long[3]

One of the greatest obstacles in the pursuit of a hydrogen-based economy is how to store enough gas on board a vehicle to achieve driving ranges similar to those observed with gasoline powered automobiles. Although a gram of hydrogen gas has three times the energy content of a gram gasoline, a liter of hydrogen gas at one atmosphere has only a third the energy content of a liter of gasoline. One solution to this problem has been the development of new materials that physisorb H_2 molecules. Metal-organic frameworks (MOFs) are currently under intense investigation for gas storage and separation applications, due to their high internal surface areas, convenient modular synthesis, and chemical tunability. These materials typically exhibit low binding energies ranging from −5 kJ/mol to −7 kJ/mol due to weak dispersive-type interactions between the adsorbed H_2 and framework. As a result, at room temperature they provide little to no improvement over the current storage densities achieved through the simple compression of hydrogen into holding tanks. An effective strategy to improve binding energy (optimal projected values are −15 kJ/mol to −25 kJ/mol for storage at room temperature) and enhance surface packing density of adsorbates is through the generation of new MOFs that, upon solvent removal, contain high concentrations of coordinatively unsaturated metal centers (UMC) on the framework surface [1,2]. In this report, we show that crucial gas adsorption properties, such as binding energy and selectivity can be further improved through chemical substitution of the UMC [3]. It is thought that the addition of UMC's with higher charge densities can induce larger dipoles in the adsorbed gas creating an overall increase in the binding strength.

$Fe_3[(Fe_4Cl)_3(BTT)_8(MeOH)_4]_2$ (Fe-BTT) a sodalite-type MOF having exposed Fe^{2+} sites and a Brunauer, Emmett and Teller (BET) surface area of 2010 m^2/g, has proven to be efficient at storage of H_2. Although Cu^{2+} and Mn^{2+} derivatives have previously been studied by us [4,5], the iron analog has shown a significant improvement in the binding enthalpy of H_2, −12 kJ/mol compared to −10.1 kJ/mol and −9.5 kJ/mol for Mn^{2+} and Cu^{2+} cations, respectively. In fact, at room temperature, this new material has H_2 binding that is among the strongest reported to date, a property that is directly reflected in the observed room temperature uptake equal to 1.1 % mass fraction and 8.4 g/L at 100 bar.

In order to understand more about the framework/gas interactions in Fe-BTT, we have performed neutron diffraction experiments, using the high resolution neutron diffractometer (BT-1). Data for the bare sample reveals nuclear scattering density near the open Fe^{2+} site corresponding to 30 % occupancy of methanol due to incomplete solvent removal. This number indicates that Fe-BTT has a similar concentration of UMCs compared to its Mn counterpart. Low temperature neutron diffraction data were collected again after the sample was sequentially dosed with (4, 8, 20, 33, 65, and 98) D_2 per formula unit. The strongest adsorption site, **I**, found in close proximity to the unsaturated Fe^{2+} is the first site occupied at low gas loadings, Fig.1. There is a remarkably short Fe^{2+}-D_2 distance of 2.17(5) Å, the shortest metal–D_2 distance yet observed in a MOF. This observation is consistent with significantly stronger binding energy compared to Mn-BTT and Cu-BTT, which exhibited metal–D_2 distances of

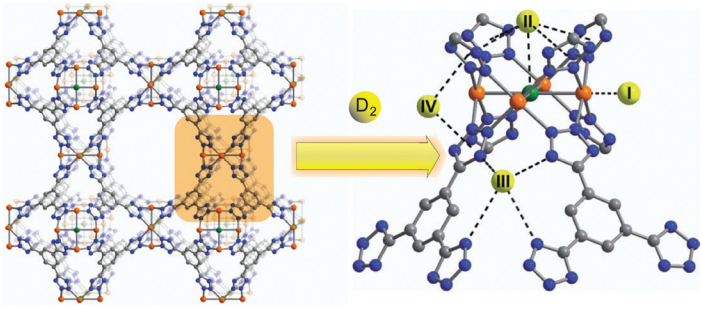

FIGURE 1: Atomic structure of Fe-BTT consists of chlorine centered $[Fe_4Cl]^{7+}$ units linked by BTT^{3-} ligands. Orange, green, gray, and blue spheres represent Fe, Cl, C, and N atoms, respectively. Solvent molecules, H atoms, and charge-balancing cations are omitted for clarity. A close up view of the portion of the framework highlighted in orange is shown on the right. The D_2 binding sites (yellow) within Fe-BTT were determined from Rietveld analysis of the powder neutron diffraction data. At higher D_2 loadings there were 6 additional occupied sites (not shown). While these additional sites were all localized, their binding strengths are typical for weak dispersive interactions, as reflected in a framework–D_2 distances which are all greater than 3.6 Å.

[1]NIST Center for Neutron Research, National Institute of Standards and Technology, Gaithersburg, MD, 20899
[2]University of Maryland, College Park, MD, 20742
[3]University of California, Berkeley, CA, 94720

2.27 Å and 2.47 Å, respectively [4,5]. The close approach of the adsorbed gas to the framework surface is essential for achieving a high storage density at cryogenic temperatures.

At higher D_2 loadings, additional adsorption sites become evident. The next strongest binding position, **II** in Fig. 1, is situated approximately 3.44 Å above the chloride ion of the $[Fe_4Cl]^{7+}$ unit with four tetrazolate rings within 3.60 Å of the site, forming a bowl-like adsorption pocket with a negative surface charge. Up to a loading of 8 D_2 molecules per formula unit, only sites **I** and **II** are occupied, suggesting that they have much higher binding enthalpies than the subsequently occupied sites. At higher loadings, site **III** D_2 molecules are found in the openings of the sodalite-type cages, with a 3.45 Å distance from the N_2 atoms of four tetrazolate ligands, while site **IV** is located in the channels of the structure, with the D_2 centroid 3.16 Å from the plane of two tetrazolate rings. Although it is not further discussed here, comparison of the D_2 adsorption sites of Fe-BTT and its Mn and Cu analogs reveals several differences related to the binding strengths of sites **III** and **IV**, presumably due to slight differences in unit cell dimensions and the distinct position of the extra-framework metal cations.

To complement our neutron diffraction studies, we collected inelastic neutron scattering data to probe the rotational spectra of Fe-BTT as a function of H_2 loading, Fig. 2. The peaks represent neutron energy loss due to transitions in the H_2 rotational levels. For free hydrogen, a single peak corresponding to the first rotational transition from J = 0→1 is expected at 14.7 meV; however, when H_2 strongly interacts with the surface of an adsorbent there is a hindrance to rotation causing changes in the position and splitting of the J = 1 level. At the lowest loading, there is a lack of a distinct peak at or below 14.7 meV, which could indicate a extremely strong interaction of H_2 with the Fe^{2+} ion, pushing the transition out of the available spectral window, Fig. 2(a), with phonon-rotation combination peaks at higher energies. At loadings up to 0.5 % mass fraction we observe two additional rotational lines at approximately 13.2 and 19.7 meV corresponding to a 1-dimensional rotational barrier of ≈ 15 meV, indicative of a moderate barrier for H_2 on site II. As sites III and IV become more populated in the 1.25 % and 2.0 % mass fraction data, there are rotational lines that appear close to free H_2, indicating an even lower rotational barrier. The highest loadings, 4.0 % and 6.0 % mass fraction, exhibit very broad indistinct features at higher energy (> 20 meV), characteristic of molecular recoil from weakly bound hydrogen. Also, at 6 % mass fraction, there is the appearance of a shoulder on the most intense peak, which is at a frequency characteristic of bulk hydrogen.

The two spectra of Fe-BTT loaded with 0.1 % mass fraction normal-H_2 (n-H_2) and para-H_2 (p-H_2), where only site **I** is occupied, are superimposible indicating a full

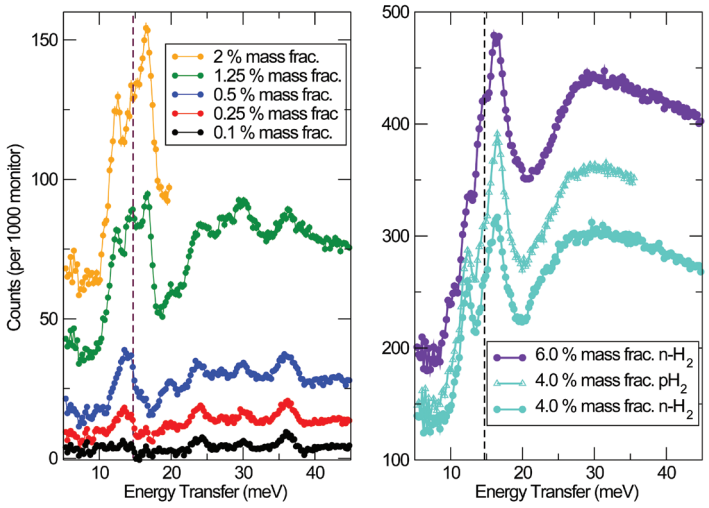

FIGURE 2: Inelastic neutron spectra at several hydrogen loadings following subtraction of the spectrum of evacuated Fe-BTT. **(a):** lowest n-H_2 data up to 2.0 % mass fraction. **(b)** higher n-H_2 loadings up to 6 % mass fraction, and p-H_2 at 4 % mass fraction. In both panels, the dashed line represents the expected energy transfer of 14.7 meV corresponding to the first rotational transition (J = 0→1) for free hydrogen.

interconversion of n-H_2 (25 % para-H_2, and 75 % ortho-H_2 at room temperature) to p-H_2, a process catalyzed by the paramagnetic high-spin Fe^{2+} centers. At the 4 % mass fraction loading, the scaling factor of p-H_2/n-H_2 is 1.2, Fig 2(b), indicative of an incomplete conversion. It is thought that there is an initial conversion occurring as the gas is loaded at 50 K because H_2 can gain access to Fe^{2+}, but as the sample is cooled to collect data, the gas becomes localized in sites that are distant from the metal, reducing H_2-Fe^{2+} interactions and freezing the para–ortho ratio.

This study features a sodalite-type MOF whose properties, such as binding energy, can be systematically tuned through chemical substitution. The Fe-BTT framework has a high initial isosteric heat of adsorption, −12 kJ/mol, and enhanced storage capacity at 298 K, both of which are directly related to the coordinatively unsaturated Fe^{2+} cation as determined by neutron diffraction and inelastic neutron scattering. Gas adsorption measurements combined with neutron diffraction data and inelastic neutron scattering spectroscopy have provided us a clearer understanding of the adsorption process that will be useful for the future optimization of storage/separation materials.

References

[1] S. K. Bhatia, A. L. Myers, Langmuir, **22**, 1688 (2006).

[2] Y. Liu, H. Kabbour, C. M. Brown, D. A. Neumann, C. C. Ahn, Langmuir, **24**, 4772 (2008).

[3] K. Sumida, S. Horike, S.S. Kaye, Z.R. Herm,W.L. Queen, C.M. Brown, F. Grandjean, G.J. Long, A. Dailly, J.R. Long, Chem. Sci, In press (2010).

[4] M. Dincă, A. Dailly, Y. Liu, C. M. Brown, D. A. Neumann, J. R. Long, J. Am. Chem. Soc., **128**, 16876 (2006).

[5] M. Dincă, W. S. Han, Y. Liu, A. Dailly, C. M. Brown and J. R. Long, Angew. Chem., Int. Ed., **46**, 1419 (2007).

Graphite oxide framework (GOF) materials for hydrogen storage

J. W. Burress[1], S. Gadipelli[1,2], J. Ford[1,2], J. M. Simmons[1], W. Zhou[1,3], T. Yildirim[1]

Vehicles and other systems powered by hydrogen fuel cells emit only water as a waste product. Thus, adoption of this technology would reduce greenhouse gas emissions by reducing dependency on fossil fuels. An important challenge, however, is storing enough hydrogen on board to provide a range comparable to that of a vehicle powered by fossil fuels. Unfortunately, current materials still lack the ability to store necessary amounts of hydrogen under technologically useful conditions. Hence, there is urgent need for new ideas and materials to solve the hydrogen storage problem.

In this study [1], we show that graphene oxide (GO), a substance known for more than a century, can be easily turned into a potentially useful gas storage material. GO is a sheet of carbon atoms with many hydroxyl, epoxide and carboxyl surface groups. In principle, hydrogen can be stored between layers of this lightweight material. However, the challenge is to separate the layers without filling the space between them. Here we show that by using the well-known chemistry between boronic acids and hydroxyl groups, GO layers can be linked together to form a new layered structure (see Figs. 1 and 2). Such GOF structures can have tunable pore widths, volumes, and binding sites depending on the linkers chosen, and could exhibit interesting gas sorption properties.

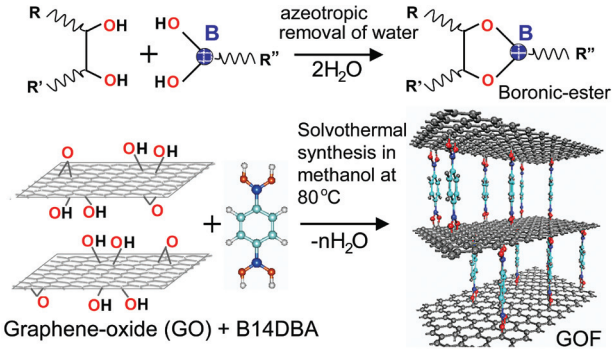

FIGURE 1: A schematic view of boronic-ester (top) and GOF formation (bottom). Idealized graphene-oxide framework (GOF) materials proposed in this study are formed of layers of graphene oxide connected by benzene-diboronic acid (B14DBA) pillars.

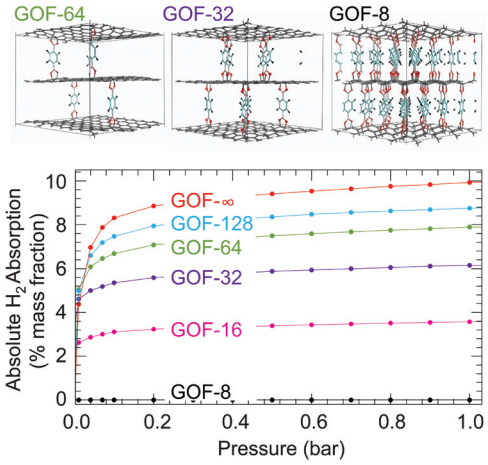

FIGURE 2: The GCMC simulations for ideal GOF-n structures with n-graphene carbons per linker.

To evaluate the potential of GOF materials for H_2 storage, we performed theoretical Grand Canonical Monte Carlo (GCMC) simulations. A series of idealized, model systems with various diboronic acid linker concentrations were examined. Structural optimization yielded ≈ 1.1 nm interlayer separations for these ideal structures. The simulated absolute hydrogen adsorption isotherms at 77 K for several representative GOF structures are shown in Fig. 2. When the linker concentration is too high, the GOF structure is too dense and contains no accessible pores. Consequently, there is no H_2 uptake. As the linker concentration decreases, the GOF specific pore volume increases and eventually reaches the limit of no linker present. Naturally, a GOF structure with lower linker concentration would possess higher H_2 adsorption capacity. However, low linker concentration will lead to low structural stability and reduced graphene interlayer separation. Therefore, these factors must be balanced to optimize the linker concentration. The GOF-32 structure with one linker per 32 graphene-carbons (Fig. 2) appears to be one reasonable choice, as it is structurally stable (according to density functional theory lattice dynamics calculation), while possessing an H_2 adsorption capacity (≈ 6.1 % mass fraction H_2 uptake at 77 K and 1 bar) that is predicted to be higher than any other porous material known. Overall, our simulation results were quite

[1]NIST Center for Neutron Research, National Institute of Standards and Technology, Gaithersburg MD 20899
[2]University of Pennsylvania, Philadelphia PA 19104
[3]University of Maryland,, College Park, MD 20742

encouraging and strongly motivated us to experimentally pursue these materials.

We synthesized samples containing varying amounts of linker and characterized them with powder x-ray diffraction. As shown in Fig. 3, we observed a controllable, monotonic increase in the interlayer spacing in the GOF samples, from 0.75 nm to 1.05 nm. This, combined with neutron prompt gamma activation analysis (PGAA) shown in Fig. 4(b), indicates that the boronic acid is intercalated in the GO and that the sample prepared with a 1:1 ratio of GO:linker roughly corresponds to GOF-33.

As shown in Fig. 4(a) the inelastic neutron scattering (INS) spectra of GOF differs significantly from the INS spectra of GO and resembles the calculated INS spectra of GOF-32, further supporting that the synthesized materials are structurally similar to our ideal GOF systems shown in Figs. 1 and 2. The x-ray photoelectron spectroscopy (XPS) normalized to the graphitic carbon peak at 285 eV is shown in Fig. 4(c). It indicates that the O/C ratio of 0.43 in GO is reduced down to ≈ 0.33 in the GOF materials. The peak near 287 eV corresponds to carbon with singly-bonded C-O chemistries and its intensity increases with linker concentration as expected for boron-ester cross-linked graphene layers. Thermogravimetric analysis revealed a 100 °C increase in the exfoliation temperature with the GOFs, again supporting interlinking of GO planes.

The porosity and gas storage capacity of GOF samples were measured with nitrogen and hydrogen and CO2 sorption isotherms. The nitrogen Brunauer, Emmett and Teller (BET) surface area reaches a maximum for the 1:1 GO:linker GOF at 470 m^2/g as compared to ≈ 20 m^2/g for the GO-control. Despite this low surface area, GOF exhibits a H_2 uptake of 1 % mass fraction at 1 bar at 77 K compared to 0.2 % mass fraction for the GO-control. The initial isosteric heat of hydrogen adsorption was determined to be Q_{st} ≈ 9 kJ/mol, twice as large as for a graphene sheet and typical metal-organic framework (MOF) materials such as MOF-5 and comparable to MOFs with open metal centers. The INS spectra of H_2-loaded GOF shows a peak around

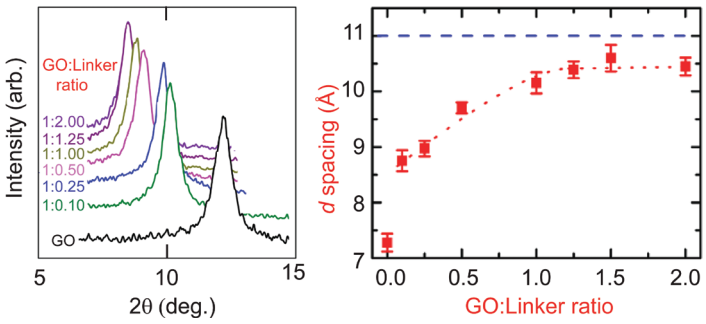

FIGURE 3: X-ray diffraction and the corresponding interlayer *d*-spacing versus linker concentration. The dashed-line indicates the optimized *d*-spacing of 11 Å that was calculated for GOF-32 shown in Fig. 2.

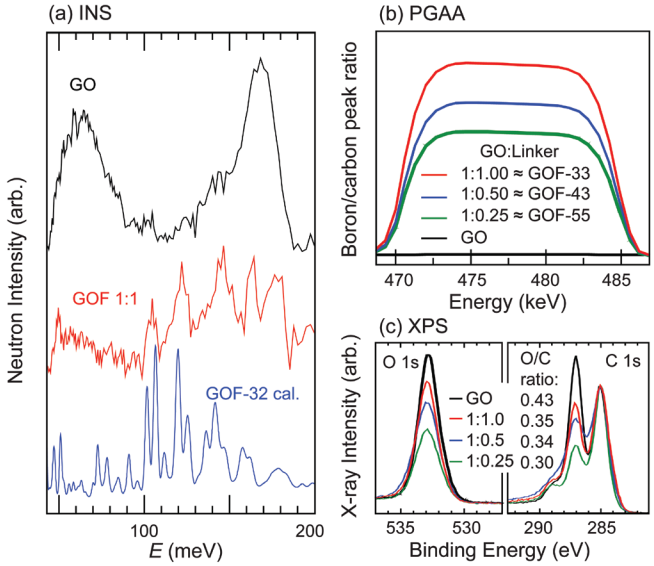

FIGURE 4: (a) INS spectra of GO and GOF 1:1 sample and a model calculation based on GOF-32 structure. (b) The major boron peaks normalized to carbon peak in PGAA spectra, indicating the approximate relations between GO:Linker samples and the ideal GOF-n structures. (c) XPS O 1s and C 1s core level spectra for GO and three different GOFs.

10 meV, suggesting very strong hindered rotation due to a strong binding potential which confirms the large Q_{st}. Compared to the simulation results, the experimental H_2 uptake achieved so far in our GOF material is less than expected for an ideal GOF structure and only 30 % greater than that typical for activated carbons. This is most probably due to presence of unreacted functional groups in our initial GOF materials. This is supported by the large O/C ratio that we obtained from XPS data shown in Fig. 4(c). The O/C ratio for our ideal GOF-32 is 4/32 ≈ 0.13, significantly smaller than the current experimental ratio of 0.35. Clearly, there is significant room for optimization.

In conclusion, we have successfully shown that graphene oxide layers can be used as building blocks for new nanoporous materials by interlinking them with diboronic acid. Considering the rich boron chemistry and large number of different types of boronic acids, it is quite possible that there are other linkers that will perform better than the B14DBA used in this study. We hope that our theoretical predictions and the first experimental results reported here will start a new research direction based on cheap and environmentally friendly GO as a building block for new nanoporous materials with better gas adsorption properties.

References

[1] J. W. Burress, S. Gadipelli, J. Ford, J. M. Simmons, W. Zhou, T. Yildirim, Angew. Chem. Int. Ed. **49**, 1 (2010).

New insight into the crystal structure of highly piezoelectric PZT: a single crystal diffraction study

D. Phelan[1], P. M. Gehring[1], X. Long[2], Y. Xie[2], Z. -G. Ye[2], A. M. Glazer[3], H. Yokota[4], P. A. Thomas[5]

$PbZr_{1-x}Ti_xO_3$ (PZT) exhibits exceptional piezoelectricity (the production of a voltage when a material is squeezed) even though the parent piezoelectric compounds $PbZrO_3$ and $PbTiO_3$ do not. For this reason, PZT ceramics have long been the material of choice for use in device applications that require the conversion between mechanical and electrical energy, common examples being medical ultrasound imaging, sonar, and microphonics. Any fundamental understanding of this phenomenon requires a detailed knowledge of how the PZT crystal structure changes when the two parent compounds are mixed. In particular, scientists wish to understand why the piezoelectricity in PZT is optimal for Ti contents close to $x = 0.5$. Yet for decades such efforts have been stymied because researchers have had to rely on x-ray and neutron powder diffraction methods, and subtle differences between certain crystal structures cannot be resolved through powder diffraction alone. As a result no consensus exists on the detailed phase diagram of PZT over a very wide range of Ti concentration. Recently, chemists at Simon Fraser University (SFU) achieved a major breakthrough by growing the first high quality single crystal specimens of PZT. Here we highlight our neutron diffraction measurements on them, the first ever on single crystal PZT, which provide new insights into the crystal structures in the region of interest.

The structural phase diagram of PZT, along with some of its unresolved features, is depicted in Fig. 1(a). The nearly vertical line near $x = 0.5$ is the well-known morphotropic phase boundary (MPB) that separates Ti-rich (tetragonal) from Ti-poor regions; it is also the compositional range that displays the best piezoelectric properties. Knowing how the crystal structure evolves across this phase boundary is widely regarded as being of the utmost importance in order to understand the piezoelectric mechanism. In particular, one of the unresolved issues is whether the room temperature structures for Ti-poor compounds are rhombohedral or monoclinic. This is important because the direction of the electric polarization is directly related to the crystal symmetry. If the symmetry is rhombohedral, then the polarization is restrained uniaxially; but if the symmetry is monoclinic, then the Pb-atom is free to move within a mirror plane, which allows the polarization to rotate within that plane. This seemingly minor detail becomes significant when the crystal is perturbed by an electric field or external stress, and it has important implications for the piezoelectricity.

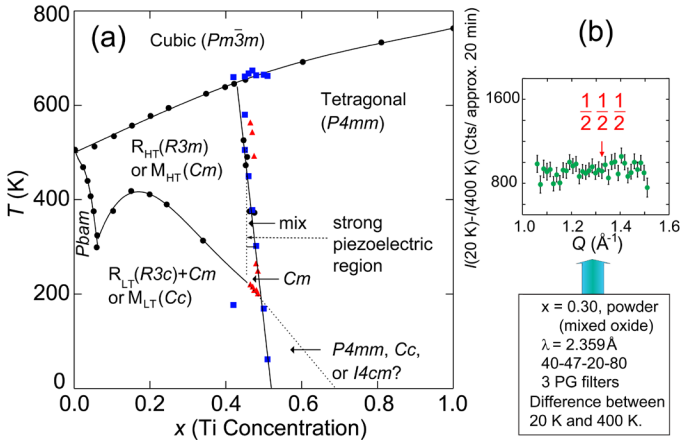

FIGURE 1: (a) The PZT phase diagram and its ambiguities as currently understood. Data are taken from Ref. 3 (black circles), Ref. 4 (blue squares), and Ref. 1 (red triangles). R_{HT}, M_{HT} and R_{LT}, M_{LT} represent possible rhombohedral and monoclinic high- and low-temperature phases, respectively. The possibility of an *I4cm* superlattice phase is suggested in Ref 5. (b) The difference diffraction pattern (20 K to 400 K) for a 20 g PZT $x = 0.3$ powder sample measured on BT-9.

One of the problems with Rietveld refinement of highly pseudosymmetric materials like PZT is that many models refine to very similar agreement factors, which makes it difficult to choose between them. A different approach is based on the search for superlattice peaks that appear when the primitive unit cell is doubled, for instance in the presence of oxygen octahedra rotations; observations of such peaks (or the lack thereof) place severe constraints on the allowed symmetries. An important model of the PZT structure proposes a monoclinic ground-state structure (space group *Cc* [1]) that should generate a very weak superlattice reflection at the reciprocal lattice position ½ ½ ½. (Indexing throughout is given with respect to a primitive cubic unit cell.) However, it has proven impossible to prove

[1]NIST Center for Neutron Research, National Institute of Standards and Technology, Gaithersburg, Maryland 20899, USA
[2]Simon Fraser University, Burnaby, BC, V5A 1S6, Canada
[3]University of Oxford, Parks Road, Oxford OX1 3PU, UK
[4]University of Tokyo, Tokyo 113-8656, Japan
[5]University of Warwick, Coventry CV4 7AL, UK

or rule out this model using powder diffraction, even though no such peak was observed by powder neutron diffraction (see Fig. 1b) due to the fact that the model predicts a very weak structure factor.

Neutron diffraction measurements were performed on two PZT crystals with compositions far from ($x = 0.325$) and close to ($x = 0.460$) the MPB using thermal (BT-9) and cold (SPINS) triple-axis spectrometers located at the NCNR. We attempted to determine the phase symmetry by searching for weak superlattice peaks. Fig. 2 shows data taken at variety of reciprocal lattice positions, and only peaks corresponding to a rhombohedral symmetry (space group *R3c*) due to octahedral tilting were observed. No Bragg peak was seen at ½ ½ ½; instead, we can say with 99 % confidence that any ½ ½ ½ peak intensity is less than 0.002 % of the fundamental 100 Bragg peak. This extremely restrictive upper bound effectively proves that the ground state crystal symmetry for PZT cannot be monoclinic *Cc*.

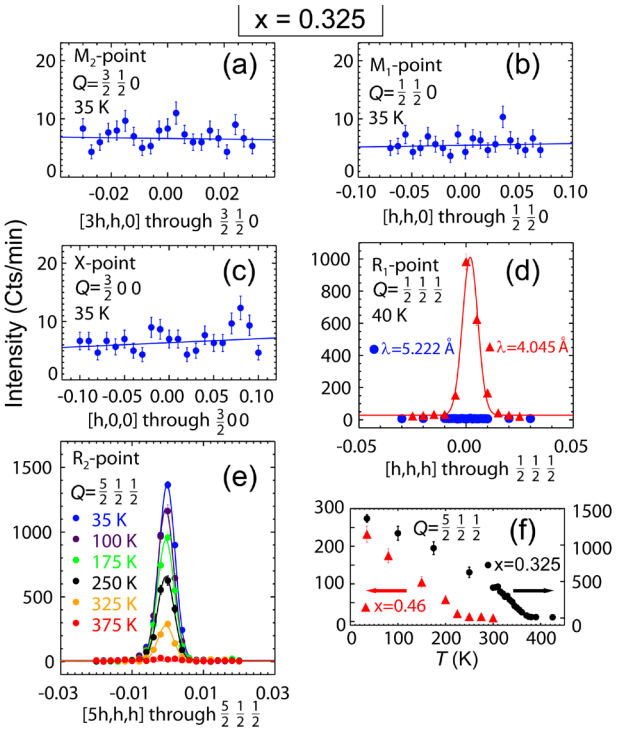

FIGURE 2: All panels are for $x = 0.325$ except (d) which includes $x = 0.460$: (a-c) Radial scans through the M and X points reveal no superlattice reflections at 35 K. (d) Scans performed using two different wavelengths through an R_1 point. The dependence of the peak on wavelength is indicative of a multiple-scattering effect. (e) Scans through one R_2 point at various temperatures are consistent with a rhombohedral distortion. (f) Order parameters of the superlattice phases at two concentrations.

A second monoclinic phase (*Cm*) that generates no superlattice reflections has also been proposed for PZT [2]. In order to search for the presence of the *Cm* phase, the radial linewidth of the 200 Bragg reflection was measured as a function of temperature because it should remain a resolution-limited singlet under rhombohedral symmetry but should split if there is a monoclinic distortion. To observe very subtle changes in the linewidth, the best

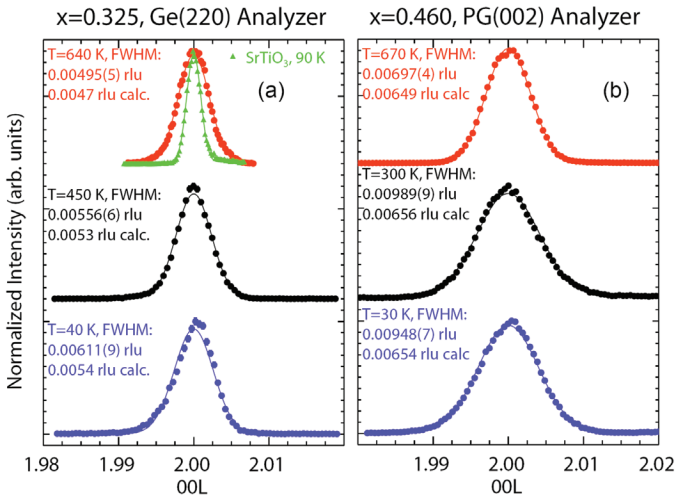

FIGURE 3: Radial scans through the 200 Bragg reflection at selected temperatures. Data from Ref. [6] on single crystal $SrTiO_3$ are represented by green triangles.

possible wave-vector resolution was needed. The 220 reflection from a perfect Ge single crystal was employed as an analyzer because the near perfect matching of the 200 and 220 d-spacings from PZT and Ge provides an almost optimal resolution condition. Fig. 3 shows the results of radial scans through 200 as a function of temperature. Although small, a significant change in the linewidth was observed at the lowest temperature along with a slight peak asymmetry, which is consistent with a very small monoclinic distortion. Thus, as we have observed a broadening of 200, but at the same time superlattice reflections consistent with *R3c*, the most likely ground-state is a two-phase mixture of *R3c* and *Cm*.

We have performed the first single-crystal neutron diffraction measurements on PZT. Our measurements effectively eliminate one of the two major models, which proposes a monoclinic *Cc* ground-state, and instead suggests that the ground state structure of PZT consists of coexisting *R3c* and *Cm* phases, and that such phase coexistence may play an important role in the piezoelectricity. The availability of single crystals will also allow us to study other aspects of PZT; in particular, we have already begun to investigate the lattice dynamics (phonons) and diffuse scattering of these crystals at the NCNR.

References

[1] D. Pandey, A. K. Singh and S. Baik, Acta Crystallogr. A**64**, 192 (2008).

[2] H. Yokota and N. Zhang and A. E. Taylor and P. A. Thomas and A. M. Glazer, Phys. Rev. B **80**, 104109 (2009).

[3] B. Jaffe, W. R. Cook, and H. Jaffe *Piezoelectric Ceramics* (Academic Press, London and New York, 1971).

[4] B. Noheda *et al.* Phys. Rev. B **63**, 014103 (2000).

[5] I. A. Kornev, L. Bellaiche, P.E. Janolin, B. Dkhil, and E. Suard, Phys. Rev. Lett. **97**, 157601 (2006).

[6] G. Xu, P. M. Gehring, V. J. Ghosh, and G. Shirane, Acta Cryst. **A60**, 598 (2004).

Multiple filling of voids improves thermoelectric efficiency of skutterudites

J.R.D. Copley[1], J.B. Leão[1], J.J. Rush[1,2], X. Shi[3,4], Jihui Yang[3], H. Wang[5], M. Chi[5], J.R. Salvador[3], Jiong Yang[6], S. Bai[6], W. Zhang[6], and L. Chen[6]

In a thermoelectric device, a temperature difference is induced by the flow of electric current across the material. It follows that those materials favoring the flow of electricity while offering resistance to the flow of heat are preferred for such devices. This idea is incorporated in the concept of a Phonon-Glass-Electron-Crystal (PGEC) [1]. The types of materials that possess PGEC properties are usually open structure compounds, such as skutterudites and clathrates, containing large crystallographic voids. The idea is that the crystal-like electrical properties (favoring electrical flow) are provided by the framework atoms, whereas the very low lattice thermal conductivity (κ_L) (or resistance to heat flow) is realized by introducing guest atoms (or "fillers") into the nanometer-size voids. Indirect evidence of phonon-glass behavior in cage-structured materials has come from observations such as strongly temperature-dependent atomic displacement parameters of the fillers, low values of κ_L, and sharp filler atom peaks in the phonon density of states. The inelastic neutron scattering study of single- and multiple-filled skutterudites highlighted in this article was undertaken to look for direct evidence in support of the phonon-glass concept.

The atomic structures of our samples were first examined using high resolution Scanning Transmission Electron Microscopy (STEM). Figure 1 shows high angle annular dark-field (HAADF) STEM images in the [001] direction for the multiple-filled skutterudite $Ba_{0.08}La_{0.05}Yb_{0.04}Co_4Sb_{12}$, using a beam size of ≈ 0.6 Å. The population of guest atoms is directly probed along the [001] direction, since filler-only atomic columns can be identified. The obvious intensity variation among the filler columns suggests that the guest atoms are randomly distributed within the voids of the host material.

The validity of the mechanism of multiple independent fillers scattering a broad range of host lattice phonons, leading to significant reductions

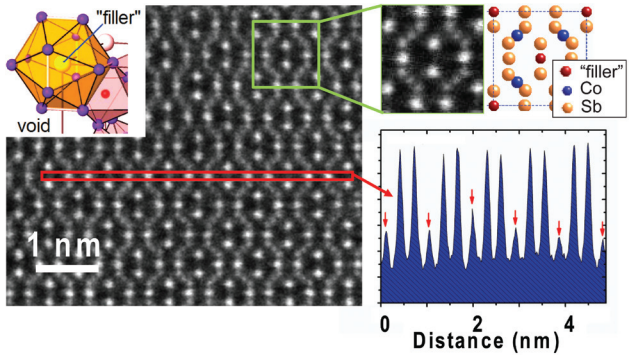

FIGURE 1: A typical HAADF-STEM image of a Ba, La, and Yb-filled skutterudite sample along the [001] direction. The intensity profile shows fluctuations in filler concentration among the atomic columns. The left inset shows the filler in the void concept.

in κ_L, hinges upon the phase incoherence of the filler vibrations, and inelastic neutron scattering is a unique tool to study such incoherence. It measures the scattering function $S(Q,E)$, where Q and E are the wave vector transfer and energy transfer respectively. If the filler vibrations are phase incoherent, the difference function $\Delta S(Q,E_0)$, which is the difference between the scattering functions for the filled and unfilled materials evaluated at E_0, the energy of one of the localized filler modes, is expected to vary as Q^2.

Room temperature inelastic neutron scattering spectra were obtained using the Disk Chopper Spectrometer (DCS). Most of the measurements were performed using 2.35 Å incident neutrons with an energy resolution of ≈ 0.7 meV at 5 meV energy loss. The complicated spectrum for the unfilled structure (Fig. 2), particularly between

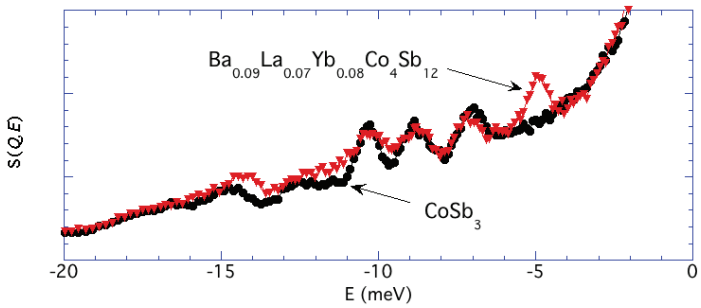

FIGURE 2: A comparison of 4.8 Å neutron energy gain data for the normalized unfilled $CoSb_3$, and for $Ba_{0.09}La_{0.07}Yb_{0.08}Co_4Sb_{12}$.

[1]NIST Center for Neutron Research, National Institute of Standards and Technology, Gaithersburg, MD 20899
[2]University of Maryland, College Park, MD 20742
[3]Materials and Processes Laboratory, General Motors R&D Center, Warren, MI 48090
[4]Optimal Inc., Plymouth, MI 48170
[5]Oak Ridge National Laboratory, Oak Ridge, TN 37831
[6]Chinese Academy of Sciences, Shanghai 200050, China

6 meV and 16 meV, precludes unambiguous identification of resonant modes in this range of energies. On the other hand the Yb mode is clearly identifiable in the triple-filled sample spectrum at about 5 meV. The La and Ba modes overlap significantly with the measured optical modes of the skutterudite framework. In order to better reveal the filler modes, Fig. 3 shows $\Delta S(Q,E)$ differences between the partially filled skutterudites $La_{0.2}Co_4Sb_{12}$, $Yb_{0.2}Co_4Sb_{12}$, and $Ba_{0.09}La_{0.07}Yb_{0.08}Co_4Sb_{12}$, and the host material $CoSb_3$. Localized La and Yb modes are clearly identified near 6 meV and 5 meV in $La_{0.2}Co_4Sb_{12}$ and $Yb_{0.2}Co_4Sb_{12}$, respectively, whereas for $Ba_{0.09}La_{0.07}Yb_{0.08}Co_4Sb_{12}$ only the Yb mode is clearly visible. The La mode is much weaker because of its much smaller scattering cross section, and due to partial overlap with the Yb mode and with the host optical modes. The different types of filler atoms in the triple-filled skutterudites also have different resonant frequencies, further adding to the phase incoherence.

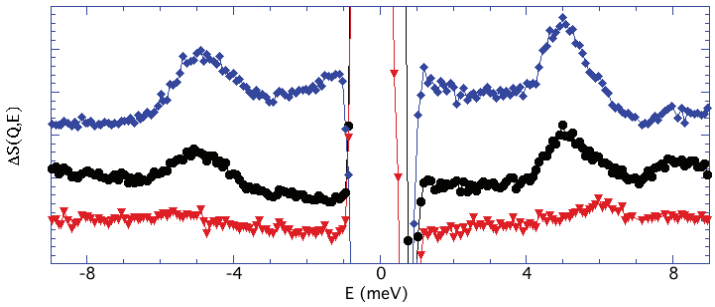

FIGURE 3: Difference functions $\Delta S(Q,E)$, relative to unfilled $CoSb_3$, for $Yb_{0.2}Co_4Sb_{12}$ (top), $Ba_{0.09}La_{0.07}Yb_{0.08}Co_4Sb_{12}$ (middle), and $La_{0.2}Co_4Sb_{12}$ (bottom).

The difference function $\Delta S(Q,E)$ for the partially filled skutterudites varies as Q^2 [2], indicating that cage fillers in skutterudites with filling fractions up to ≈ 24 % are vibrationally phase incoherent, and that these materials are indeed akin to phonon glasses. Our neutron scattering measurements for partially filled skutterudites suggest that there is a characteristic length L such that the vibrations of the guest atoms are largely phase-incoherent when the average nearest inter-filler distance is greater than L, and largely phase-coherent when that distance is less than L. In partially filled skutterudites, the filler-filler interaction is a screened Coulomb interaction with an effective screening length of ≈ 12.6 Å, which corresponds to 29 % occupancy. For smaller occupancies (inter-filler distances > 12.6 Å) relatively weak interactions exist between fillers.

The multiple filler modes, discussed above, scatter a broad range of acoustic phonons, resulting in very low values of κ_L. The lattice thermal conductivity κ_L may be written as κ-κ_e, where κ is the total thermal conductivity and κ_e is the electronic thermal conductivity; the latter quantity is obtained using $\kappa_e = L_0\sigma T$, where L_0 is the Lorenz number (approximately 2.0×10^{-8} V^2/K^2 in filled skutterudites), σ is the electrical conductivity, and T is the absolute

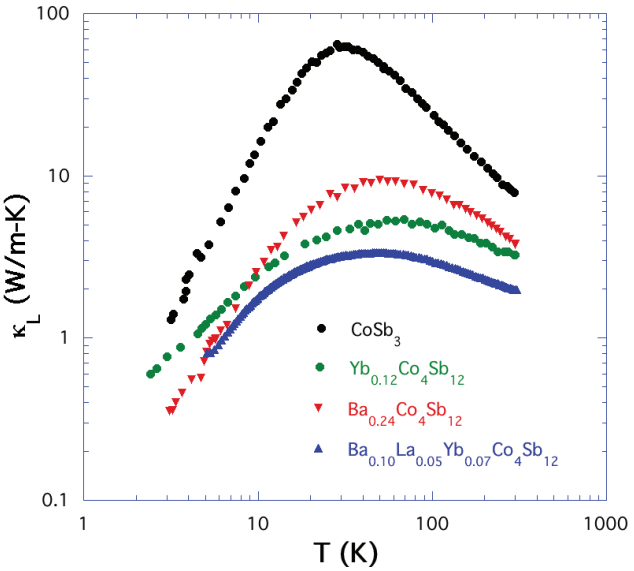

FIGURE 4: Low temperature lattice thermal conductivity for $CoSb_3$-based skutterudites.

temperature. Low temperature lattice conductivities are shown in Fig. 4. Partial filling of the voids, especially filling with multiple types of atoms, transforms the thermal conductivity from crystal-like toward glass-like behavior. For multiple-filled skutterudites a broad peak is observed above 30 K, which is totally unlike typical crystal behavior. The value of κ_L in multiple-filled skutterudites is roughly 2 W/m-K at room temperature, much less than that of the unfilled skutterudite $CoSb_3$. Above 700 K, κ_L is reduced to about 0.20 W/m-K, 7 times lower than for the Yb-filled system and nearly 20 times lower than for $CoSb_3$. As the temperature approaches 700 K κ_L becomes comparable with the theoretical minimum κ_{min}.

Due to the combined effects of sufficiently random filler distribution, phase-incoherent localized vibrations, and the broad spectrum of guest resonant frequencies that leads to κ_L being ≈ κ_{min}, we conclude that phonon-glass behavior is realized in multiple-filled skutterudites. Although single- and double-filled skutterudites exhibit similar random filler distributions and incoherent filler rattling, their κ_L values are still higher than κ_{min} at elevated temperatures.

The efficiency of thermoelectric materials is described by the dimensionless figure of merit $ZT = \alpha^2\sigma T/\kappa$, where α is the thermopower. A very high ZT value of 1.7 at 850 K has been achieved due to the realization of κ_{min}. This represents a more than 100 % improvement over current state-of-the-practice thermoelectric bulk materials. Such improvements make these phonon-glass materials very attractive for power generation applications.

References

[1] G. A. Slack, in *CRC Handbook of Thermoelectrics,* edited by D. M. Rowe (CRC, Boca Raton, FL, 1995), pp. 407.

[2] X. Shi, *et al.*, submitted.

Observation of thickness fluctuations in surfactant membranes

M. Nagao

Surfactant membranes are flexible objects with thermally activated dynamics around room temperature. As shown schematically in Fig. 1, membrane dynamics has been investigated in terms of single surfactant molecular motion such as rotation, lateral diffusion, or vibration, and in terms of collective movements of surfactant molecules like bending, thickness, and protrusion fluctuations. The bending motion, which is known to be observed at length scales larger than the membrane thickness, has been well described by the Helfrich bending energy [1], and many experimental investigations have been focused on understanding this motion. Helfrich proposed that the mechanical free energy functional of a membrane is increased by its resistance to bending, $\delta H = \kappa \delta C^2/2$, where κ is the bending modulus and δC is a change in curvature. At length scales smaller than the membrane thickness, thickness fluctuations and protrusion motions are expected to be relevant [2,3]. However, these dynamics are difficult to investigate experimentally since the membrane thickness is too small to be accessed using visible light. It is known that when a film is very thin (less than 100 nm), the shapes of the fluctuations in the two surfaces become correlated and thickness fluctuations become important [4] and hence are a relevant topic for the investigation of film dynamics [5]. In solutions, however, while there has been related work, no detailed investigations of thickness fluctuations have been reported. Here we highlight our recent work providing evidence of thickness fluctuations in a surfactant solution as observed by neutron spin echo (NSE) [6]. NSE can probe membrane dynamics at length scales from below 1 nm to tens of nanometers and time scales ranging from a few ps to hundreds of ns.

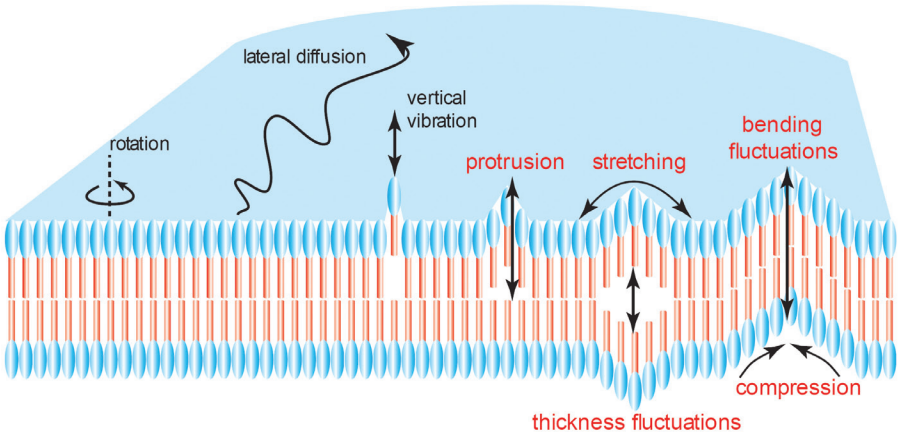

FIGURE 1: Schematic model of dynamics of surfactant membranes. Depending on the length scale of the measurement, various motions may be observed: single molecular motions such as rotation, lateral diffusion and vertical vibration; collective motions such as, protrusion, stretching, and compression; and in thin films correlated motions of the top and bottom layer such as thickness and bending fluctuations.

A swollen lamellar structure composed of surfactant pentaethylene glycol dodecyl ether ($C_{12}E_5$), deuterated water (D_2O), and an oil, deuterated octane (C_8D_{18}), was used as a model system. The volume fractions of $C_{12}E_5$, D_2O, and C_8D_{18} were $\phi_s = 0.041$, $\phi_w = 0.9385$, and $\phi_o = 0.0205$, respectively. This sample contained a small amount of oil, so that the $C_{12}E_5$ bilayers were slightly swollen by it and dispersed in D_2O. Here, we call "membrane" the two $C_{12}E_5$ surfactant monolayers with the oil layer in between. The membrane thickness in this case can be calculated from the composition of the sample as $d_m = 2(1+\phi_o/\phi_s)ds = 4.65$ nm, where $d_s = 1.55$ nm is the length of the surfactant molecule. The temperature was kept at 30 °C for small-angle neutron scattering (SANS) and 29 °C for NSE with a temperature accuracy of ± 0.1 °C. At both temperatures the system is in the lamellar phase as confirmed by a SANS measurement.

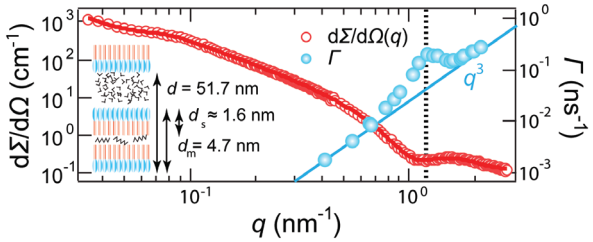

FIGURE 2: SANS profile $d\Sigma/d\Omega(q)$ observed from the swollen lamellar sample at $T = 30$ °C together with the decay rate Γ observed by the NSE measurement at $T = 29$ °C. The inset gives a schematic idea of the structure of the system. The solid red line shows the result of the fit to a model scattering function of a lamellar structure, the solid blue line guides the eyes to show the $\Gamma \sim q^3$ relation, and the dashed black line shows the peak position in Γ, which almost coincides with the dip position in the SANS profile.

NIST Center for Neutron Research, National Institute of Standards and Technology, Gaithersburg, MD 20899 and Indiana University, Bloomington, IN 47408

Shown in Fig. 2 is the SANS profile at $T = 30$ °C. A correlation peak due to the stacking of the lamellae is observed at $q \approx 0.09$ nm^{-1} and the internal structure of the swollen lamellar membranes gives rise to another peak around $q = 1.5$ nm^{-1}. The scattering profile is reproduced using a model scattering function [7] as shown by the solid red line. The membrane thickness was estimated from the fit as $d_m = (4.7 \pm 1.5)$ nm, which is excellent agreement with the calculation from the sample composition. The inset in Fig. 2 indicates the structure of the present system with the parameters estimated by SANS.

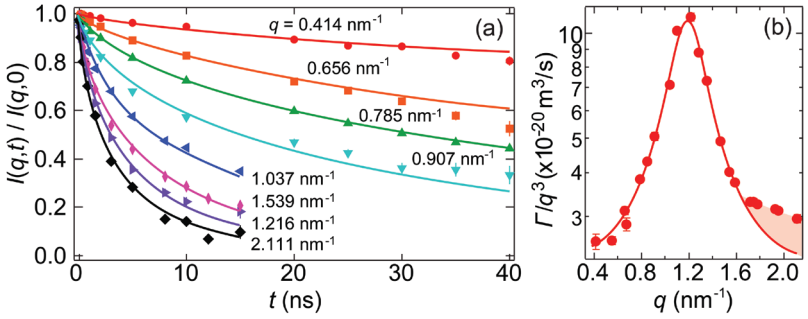

FIGURE 3: Intermediate scattering function $I(q,t)/I(q,0)$ observed by NSE and q-dependence of Γ/q^3.

Figure 3 presents the intermediate scattering function, $I(q,t)/I(q,0)$, showing the membrane dynamics measured by NSE spectroscopy. Solid lines in the figure indicate fit results according to the single membrane fluctuation model, a stretched exponential decay function given by $I(q,t)/I(q,0) = \exp[-(\Gamma t)^{2/3}]$, where Γ is the decay rate [8]. In this model, the decay rate Γ_b is expressed as [8], $\Gamma_b = 0.025\gamma\left(\frac{\kappa_B T}{\kappa}\right)^{1/2}\left(\frac{\kappa_B T}{\eta}\right)q^3$, where γ is a pre-factor originating from averaging the q vector, k_BT the thermal energy, and η the solvent viscosity. Therefore, if the system shows only single membrane fluctuations, Γ_b should follow a q^3 relation. However, as shown in Fig. 2, the q-dependence of Γ deviates from the q^3 relation around the dip position in the SANS profile. In addition to the bending mode, the present result shows that an excess motion appears near the length scale of the membrane thickness. Enhancement of the decay rate at length scales similar to the membrane thickness was first reported and related to the thickness fluctuations by Farago and co-workers [9]. However, their work did not show a relationship between the bending and the thickness fluctuations.

So far, we do not have a good theory to analyze the NSE data quantitatively. Thus we employ a phenomenological approach. Figure 3(b) shows the q variation of G/q^3, which should be a constant for the case of pure bending motion. A clear peak-like behavior centered at $q \approx 1.2$ nm^{-1} indicates that beyond bending there are also thickness fluctuations. The data are well reproduced by the following relation: $\Gamma/q^3 = \Gamma_b/q^3 + \frac{A}{1+(q-q_0)^2\xi^2}$, where the first term corresponds to the bending motion and the second term to the thickness fluctuations. The q-dependence of the thickness fluctuations is expressed by the Lorentz function in order to include a finite distribution of the fluctuation lengths. The fitting parameters relate to the physical characteristics of the motion as follows; A relates to the damping frequency of the motion, q_0 is the momentum transfer value corresponding to the membrane thickness, and ξ gives an indication of the amplitude of the fluctuations. The best fit parameters are $\Gamma_b/q^3 = (19.7 \pm 0.8) \times 10^{-21}$ m^3/s, $A = (89.0 \pm 1.5) \times 10^{-21}$ m^3/s, $q_0 = (1.186 \pm 0.002)$ nm^{-1}, and $\xi = (5.13 \pm 0.16)$ nm. The term Aq_0^3 corresponds to the decay rate of the thickness fluctuations.

From the fits, $Aq_0^3 = (1.48 \pm 0.03) \times 10^8$ s^{-1}, which decreases with temperature (data not shown) and is close to the decay rate of the shape fluctuations in pentaethylene glycol decyl ether, water, and octane droplet microemulsion [10]. This result suggests that the thickness fluctuations in the swollen lamellar phase yield the shape fluctuations in the droplet phase, which exists in the lower-temperature region. The estimated bending modulus $\kappa = (2.6 \pm 0.1)\ k_BT$ is about twice that of $C_{12}E_5$ monolayers, indicating that the present membrane behaves like a $C_{12}E_5$ bilayer.

Figure 3(b) shows a clear deviation of the experimental data from the fit result at high q. Although the Lorentz function employed here is rather phenomenological, the deviation shows a possibility of another intra-membrane dynamics, such as protrusion motion.

In summary, the membrane dynamics of a swollen lamellar phase was investigated using NSE. The surfactant bilayers are swollen by a small amount of oil, and thickness fluctuations are observed. The q dependence of the relaxation rate of the thickness fluctuations is reproduced using a Lorentz function, and the relations between fit and dynamical mode parameters are proposed. At the length scale around the membrane thickness, the bending, thickness, and perhaps protrusion fluctuations are observable by the NSE technique. It would be also possible to observe these modes in lipid vesicles containing membrane proteins and/or cholesterol. Such investigations will improve the understandings of membrane dynamics.

References

[1] W. Helfrich, Z. Naturforsch. C **28**, 693 (1973).

[2] J. N. Israelachvili, H. Wennerström, Langmuir **6**, 873 (1990).

[3] G. Brannigan, F. L. H. Brown, Biophys. J. **90**, 1501 (2006).

[4] A. Vrij, J. Th. G. Overbeek, J. Am. Chem. Soc. **90**, 3074 (1968).

[5] See the following review E. D. Manev, A. V. Nguyen, Adv. Coll. Int. Sci. **114-115**, 133 (2005) and references therein.

[6] M. Nagao, Phys. Rev. E **80**, 031606 (2009).

[7] J. Lemmich, K. Mortensen, J. H. Ipsen, T. Hønger, R. Bauer, O. G. Mouritsen, Phys. Rev. E **53**, 5169 (1996).

[8] A. G. Zilman, R. Granek, Phys. Rev. Lett. **77**, 4788 (1996).

[9] B. Farago, M. Monkenbusch, K. D. Goecking, D. Richter, J. S. Huang, Physica B **213&214**, 712 (1995).

[10] T. Hellweg, D. Langevin, Phys. Rev. E **57**, 6825 (1998).

Neutron transmission measurements of concentration profiles in non-homogeneous shear flows

M. E. Helgeson[1], N. J. Wagner[2], L. Porcar[3]

Many complex fluids exhibit non-homogeneous flows under certain conditions, in which the flow field separates into regions of different local deformation rate. For example, wormlike micelles (WLMs), comprised of long thread-like surfactant aggregates, are a well-studied class of materials that exhibit this "shear banding" [1, 2]. These flows can be accurately modeled using non-monotonic rheological constitutive relations between the local shear stress and shear rate [1-3], which are unstable between two critical shear rates $\dot{\gamma}_{1c}$ and $\dot{\gamma}_{2c}$ (Fig. 1, dotted line). Because these models qualitatively resemble thermodynamic phase separation, this has spurred debate as to whether or not inhomogeneous flow is accompanied by macroscopic concentration gradients within the fluid. However, validation of this "flow-concentration coupling" has proven difficult because no methods currently exist to make local composition measurements within the shear banded flow field. Thus the direction, and even existence of, shear-induced concentration gradients remains a hotly contested theoretical problem.

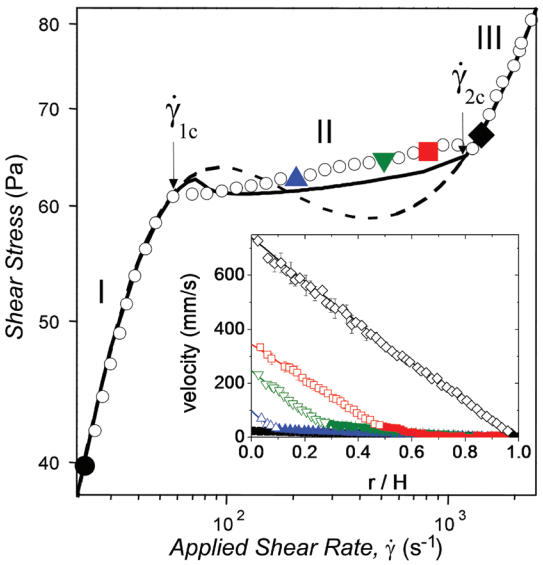

FIGURE 1: Steady state rheology of shear banding CTAB wormlike micelles [3, 5]. Open circles: data, curves: model. Inset: velocity profiles vs. relative position (r/H) for region (II), $\dot{\gamma}_{1c} < \dot{\gamma}_0 < \dot{\gamma}_{2c}$, are characteristic of shear banding. The data point colors and shapes correspond to points in the outer graph. Closed and open symbols represent points in the low-shear band (I) and high-shear band (III), respectively.

We have recently devised a method to directly measure the local concentration of fluids under shear using neutron transmission profiling [4]. Because the neutron attenuation is an absolute quantity, it can be generally applied to any fluid with sufficient neutron contrast. To review, the neutron transmission, T, of a two-component fluid is given by $T = \exp\{-t[\Delta\sigma_{s12}\phi + \Sigma'_a]\}$ where t is the sample thickness, $\Delta\sigma_{s12}$ is the difference in coherent cross-section between components 1 and 2, ϕ is the volume fraction of component 2, and Σ'_a is the total incoherent cross-section. Thus, spatially-resolved transmission measurements enable direct determination of the concentration profile of material within the flow field.

In order to carry out these measurements, we use a recently developed Taylor Couette shear cell for small angle scattering measurements in the flow-gradient shear plane (Fig. 2a). The cell is equipped with a translating slit aperture to allow for translation of the incident neutron beam across the Couette gap, yielding position-dependent scattering and transmission measurements [6]. Because the measured transmission can often be convoluted by forward scattering in ordinary SANS measurements, we have modified the experiments to be compatible with ultra-small angle neutron scattering (USANS). The resulting technique, scanning narrow aperture flow-USANS (SNAFUSANS), yields accurate transmission measurements with precise spatial resolution.

To test the existence of flow-concentration coupling, we have made SNAFUSANS measurements on a model shear banding WLM fluid comprised of CTAB, a cationic surfactant, in D_2O near an equilibrium isotropic-nematic phase boundary [3, 5]. Our previous flow-SANS measurements have shown that shear banding in this system is due to a shear-induced, first-order phase

[1]Massachusetts Institute of Technology, Cambridge, MA 02139
[2]University of Delaware, Newark, DE 19716
[3]Institute Laue-Langevin, Grenoble, France

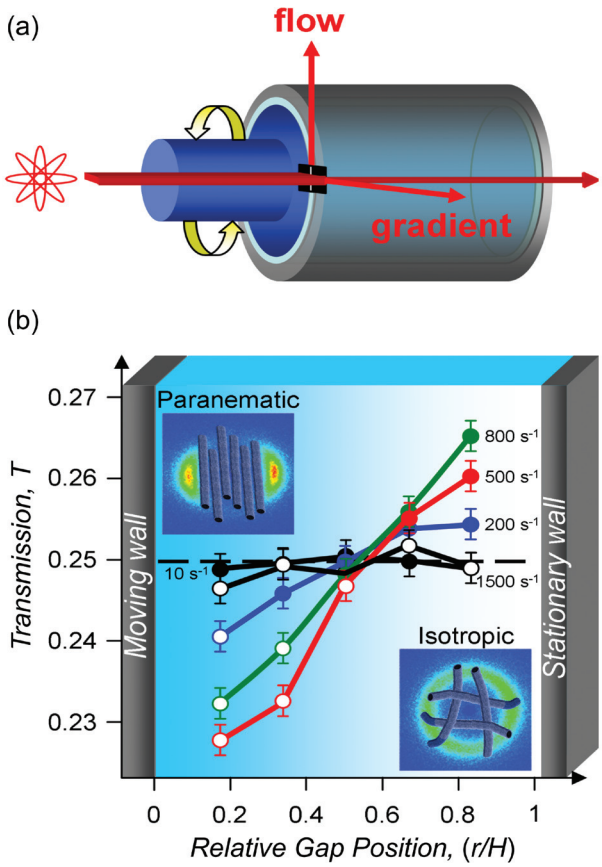

FIGURE 2: (a) Schematic of the SNAFUSANS shear cell, indicating the incident beam direction relative to the beam slit (black). (b) Absolute neutron transmission (T) profiles for shear banding CTAB wormlike micelles confirm the existence of flow-concentration coupling. Insets show 2D SANS profiles for positions in the high-shear (paranematic) and low-shear (isotropic) bands.

transition to a highly-aligned paranematic state in the high-shear band which coexists with a poorly-aligned isotropic state in the low-shear band [3, 5].

The measured transmission profiles for applied shear rates, $\dot{\gamma}_0$, spanning $\dot{\gamma}_{1c}$ and $\dot{\gamma}_{2c}$ and beyond confirm the existence of flow-concentration coupling during shear banding (Fig. 2b). For $\dot{\gamma}_0 < \dot{\gamma}_{1c}$ the transmission profile, and thus the surfactant concentration, is uniform with gap position, r/H, as expected for a homogeneously flowing fluid. However, for $\dot{\gamma}_{1c} < \dot{\gamma}_0 < \dot{\gamma}_{2c}$ where shear banding occurs, the transmission exhibits a significant gradient, with T decreasing for points in the high-shear band and increasing for points in the low-shear band. Finally, a uniform transmission profile returns for $\dot{\gamma}_0 > \dot{\gamma}_{2c}$, where the fluid is entirely paranematic in structure.

These results provide the first conclusive evidence for flow-concentration coupling in a shear banding fluid. Specifically, we find that the surfactant volume fraction increases in the high-shear band at the expense of the low-shear band (Fig. 3), and at significantly high γ_0 reaches that required for the formation of a single nematic phase at rest, further confirming the mechanism previously proposed for shear banding in the CTAB/D_2O system [5]. Combination of this local composition information with local microstructure and flow kinematic data has allowed for the construction of non-equilibrium phase diagrams, which serve as a quantitative "fingerprint" for the process of shear banding as it relates to the thermodynamics of the fluid [4].

In conclusion, the SNAFUSANS technique demonstrates unparalleled ability to interrogate both the structure and composition of complex fluids under shear. This initial study has, for the first time, confirmed flow-concentration coupling in a shear banding fluid, and provides a complete data set with which to test emerging theories. More generally, the method should be readily applicable to the growing number of materials that exhibit non-homogeneous flow, enabling significant advances in understanding the intricate relationships between composition, microstructure, and flow in complex fluids.

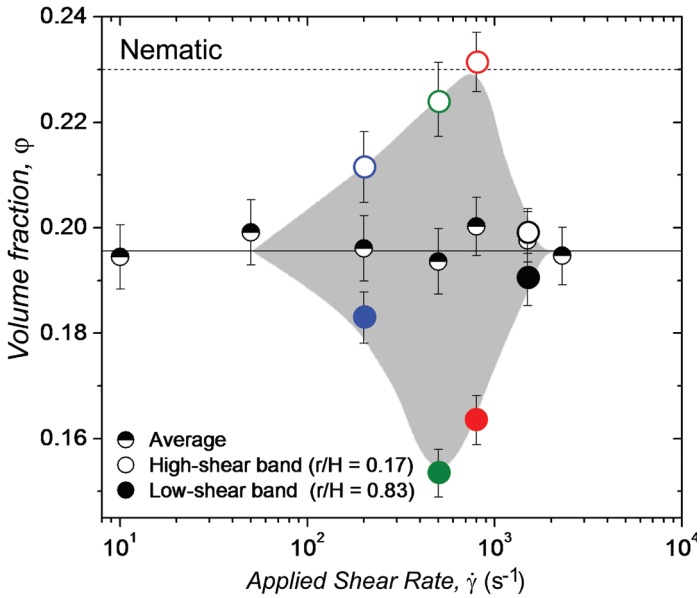

FIGURE 3: Measured CTAB volume fractions for the gap positions, r/H, indicated, indicating flow-concentration coupling during shear banding (shaded region). Solid and dashed lines give the concentration of the fluid at rest and that of an equilibrium nematic phase, respectively. Symbol colors correspond to the applied shear rates in previous figures.

References

[1] P. D. Olmsted, Rheologica Acta **47**, 283 (2008).

[2] J. K. G. Dhont and W. J. Briels, Rheologica Acta **47**, 257 (2008).

[3] M. E. Helgeson *et al.*, Journal of Rheology **53**, 727 (2009).

[4] M.E. Helgeson, L. Porcar, C. Lopez-Barron, and N.J. Wagner, Phys. Rev. Lett. **105**, 084501 (2010).

[5] M. E. Helgeson *et al.*, Soft Matter **5**, 3858 (2009).

[6] M. W. Liberatore *et al.*, Physical Review E **73** (2006).

Mechanism of molecular exchange in copolymer dispersions

S-H Choi,[1] T. P. Lodge[1,2] and F. S. Bates[1]

Self-assembly of block copolymers provides considerable advantages over that of low molecular weight surfactants, including mechanical robustness, versatility in targeting media, and multiple functionality. The static structure and properties of block copolymer dispersions in aqueous and organic media has been extensively investigated [1]. However, much less attention has been paid to the kinetics of block copolymer dispersions, and particularly the mechanism governing molecular exchange between aggregates or micelles. The common difficulty in attaining equilibrium stems from the strong incompatibility between the core-forming blocks and the solvent, coupled with the relatively large length of the core blocks. Potentially, molecular exchange kinetics, studied with suitably designed block copolymer solutions, can provide fundamental understanding on the time required for attainment of thermodynamically equilibrated structures.

In this highlight, we report the mechanism of single molecule exchange in block copolymer spherical micelles dispersed in oil, using the time-resolved small-angle neutron scattering (TR-SANS). In this model system, two pairs of structurally matched diblock copolymers of poly(styrene) (PS) and poly(ethylene-*alt*-propylene) (PEP) were prepared and designated PS-PEP-1 ($<N_{PS}>$ = 255 and $<N_{PEP}>$ = 978) and PS-PEP-2 ($<N_{PS}>$ = 412 and $<N_{PEP}>$ = 952), where the numbers denote the average number of repeat units. Each pair includes perdeuterated PS (*d*PS-PEP) and protonated PS (*h*PS-PEP). All four PS-PEP diblock copolymers form well-defined spherical micelles with a PS core and a PEP corona when dispersed in squalane at lower concentration. The characteristics of the diblock copolymers and corresponding dispersions have been well documented elsewhere [2,3].

TR-SANS measurements were performed with the NG-7 30 m instrument at NIST, with a neutron wavelength of 7 Å. Specimens were prepared by dispersing the copolymers in a mixture of perdeuterated and protonated squalane to contrast match a statistical 50:50 mixture of *d*PS and *h*PS in the micelle cores. Dispersions of pure *h*PS-PEP and *d*PS-PEP in the isotopic squalane mixture were blended to produce "postmixed" specimens, and stored at room temperature where the molecular exchange is completely suppressed due to the glassy PS core. Subsequently, the postmixed specimens were heated to a target temperature and monitored by SANS every 5 min (the experimental scheme is illustrated in Fig. 1). The SANS intensity is a proportional to the square of the core contrast ($I(t) \sim [\rho_{core}(t) - \rho_{solvent}]^{½}$, where ρ_x is the scattering length density of x). The scattering length density of the cores in turn is directly related to the fraction of *h*PS (or *d*PS) chains in the cores, and is thus time dependent. Accordingly, the SANS intensity decreases with time as chains are exchanged, as shown in Fig. 2. The instantaneous state of exchange can be represented by the normalized relaxation function,

$R(t) = \{[I(t) - I(\infty)] / [I(0) - I(\infty)]\}^{½}$, in which $I(0)$ and $I(\infty)$ are the scattering intensities at $t = 0$ and $t \to \infty$. Consequently, the values of $R(t)$ are plotted versus a logarithmic time scale in Fig. 3. Consistent with results reported by Lund *et al.*, $R(t)$ is nearly linear on a logarithmic time scale, indicating a very broad distribution of characteristic times [4].

Since the results include two parameters (temperature and the core degree of polymerization N_{core}), we applied the time-temperature superposition principle to account

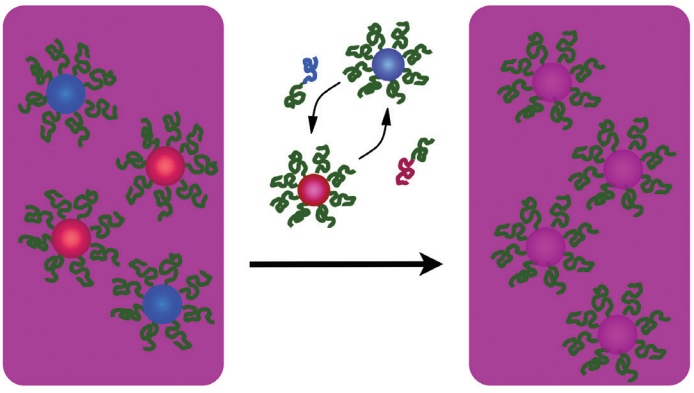

FIGURE 1: Experimental scheme of time-resolved small-angle neutron scattering.

Department of Chemical Engineering and Materials Science[1], and Department of Chemistry[2], University of Minnesota, Minneapolis, MN 55455

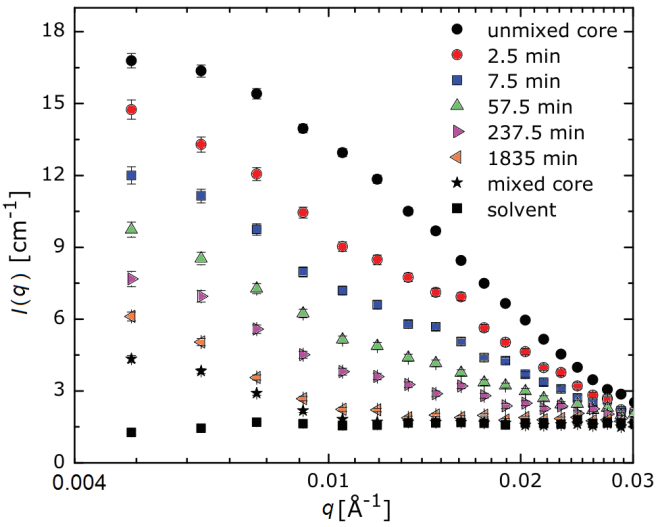

FIGURE 2: Time dependence of SANS patterns obtained from a 1 % volume fraction *d*PS-PEP-2/*h*PS-PEP-2 50/50 mixture at 135 °C. Initial measurements were made at 30 °C (black filled circles) and followed by the acquisition of SANS data every 5 min (shown in the legend).

for the effect of temperature based on the shift factors a_T. Figure 4 illustrates that each set of data can be shifted onto individual master curves with a reference temperature T_{ref} of 125 °C. It is noteworthy that $R(t)$ is strongly sensitive to N_{core}, which is one crucial piece of evidence to resolve the exchange mechanism.

We set up a kinetic model to explain experimental data and details of the model has been documented elsewhere [2]; a brief summary follows. Merging and splitting of dispersions (also known as fusion/fission), one of two primary mechanism in exchange kinetics, was not considered due to the concentration independence of $R(t)$ observed at multiple concentrations. Single molecule exchange, the other primary mechanism, includes extraction of a core block, transportation through medium, and insertion into another micelle. Here, the extraction of the core block is assumed to be rate-limiting. When a single molecule pulls out, the PS core block is governed by Rouse dynamics and must overcome the unfavorable interaction at the interface. Subsequently, the polydisperse

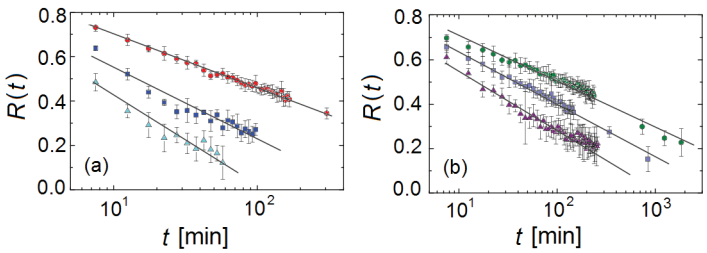

FIGURE 3: Decay of reduced SANS intensity (normalized relaxation function) as a function of time for (a) *d*PS-PEP-1/*h*PS-PEP-1 at 100 °C (red circle), 110 °C (blue square), and 115 °C (cyan triangle) and (b) *d*PS-PEP-2/*h*PS-PEP-2 at 135 °C (green circle), 140 °C (gray square), and 145 °C (purple triangle). These results are nearly linear over the measurement range on a logarithmic time scale.

nature of the core blocks is considered. We observed reasonable agreement between the experimental data and estimated $R(t)$ by our model as illustrated in Fig. 4. Therefore, we propose that the exchange kinetics of block copolymer dispersions is governed by hypersensitivity to Ncore, therefore polydispersity, associated with the incompatibility between core forming blocks and media.

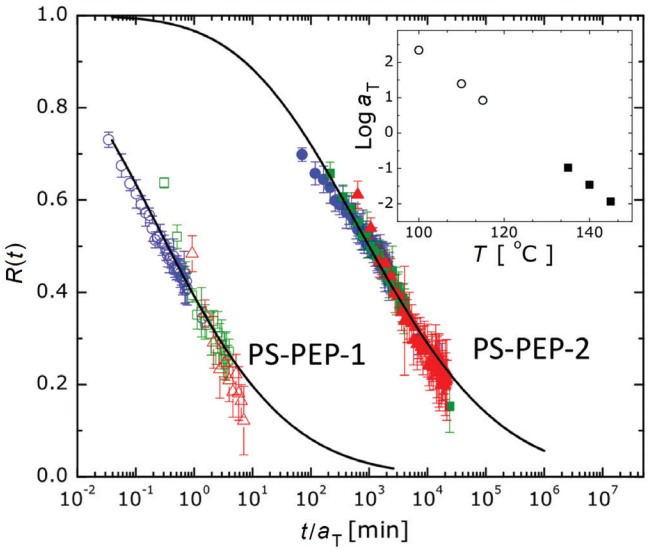

FIGURE 4: Time-temperature superposed TR-SANS results with T_{ref} = 125 °C. Shift factors a_T are shown in the inset. Master curves for chain exchange kinetics for PS-PEP-1 (unfilled, originally measured at 100 °C (blue), 110 °C (green), and 115 °C (red)) and PS-PEP-2 (filled, originally measured at 135 °C (blue), 140 °C (green), and 145 °C (red). Solid curves are best fit to our model.

In conclusion, we have addressed the fundamental understanding of single molecular exchange kinetics in block copolymer dispersions using TR-SANS measurement. Good agreement between experimental data and our model provides key parameters controlling the single molecular exchange. This work also highlights the power of contrast matching technique in small-angle neutron scattering to investigate equilibrium kinetics without any additional chemical attachment but deuterium.

References

[1] G. Riess, Prog. Polym. Sci. **28**, 1107 (2003).

[2] S. Choi, F. S. Bates, T. P. Lodge, J. Phys. Chem. B **113**, 13840 (2009).

[3] S. Choi, T. P. Lodge, F. S. Bates, Phys. Rev. Lett. **104**, 047802 (2010).

[4] R. Lund, L. Willner, J. Stellbrink, P. Lindner, D. Richter, Phys. Rev. Lett. **96**, 068302 (2006).

How does ionic liquid distribute between microphase-separated domains of a block copolymer?

J. M. Virgili, A. J. Nedoma, R. A. Segalman, and N. P. Balsara

Electrolytes based on mixtures of block copolymers and ionic liquids show promise in decoupling mechanical and ion-conducting properties critical for applications such as battery electrolytes and fuel cells. Block copolymers are made up of different kinds of polymers connected together (blocks). By carefully selecting the polymer blocks, copolymer materials can be engineered combining the properties of the individual blocks. The block copolymers in this work contain a polar block that is miscible, and a non-polar block that is immiscible, with the ionic liquid. The blocks have been chosen such that the miscible block favors ion transport while the immiscible block promotes mechanical stability. Knowledge of the distribution of ionic liquids in block copolymer microphases is crucial for application development because high concentrations of the ionic liquid in the non-polar microphases may decrease the efficiency of ion transport and plasticize the microphases that are intended to provide mechanical stability.

The phase behavior of mixtures of an AB block copolymer with an ionic liquid has been studied previously in the dilute [1] and concentrated [2, 3] copolymer limits. These studies have revealed a selective solvent-like behavior of the ionic liquid, in which the higher solubility of the A block in ionic liquid compared to that of the B block results in the formation of micelles in the dilute copolymer limit and preferential swelling of the A microphases in the concentrated copolymer limit. While these studies have improved our understanding of the phase behavior of AB block copolymer mixtures in an ionic liquid, quantitative characterization of the distribution of ionic liquid between A and B copolymer microphases has yet to be established. Here we highlight our recent work using contrast-matching neutron scattering techniques to obtain a quantitative measure of ionic liquid distribution in these microphases [4].

We conducted small-angle neutron scattering (SANS) experiments on the NG-7 instrument at the NCNR to characterize the distribution of ionic liquid between copolymer domains. The block copolymer used was poly(styrene-*block*-2-vinylpyridine) (S2VP) and the ionic liquid was imidazolium bis(trifluoromethane) sulfonimide ([Im][TFSI]). Both [*h*Im][TFSI] (*h*-liquid) and [*d*Im][TFSI] (*d*-liquid), where the prefix *h* or *d* indicates a protonated or deuterated imidazolium cation, were utilized. We could also vary the deuterated fraction of S2VP by using blends of S2VP in which the PS component was either deuterated (*d*PS) or protonated (*h*PS). f_d is the deuterated fraction of such a copolymer blend before adding any ionic liquid. In the experiment *h*-liquid was mixed with a certain volume fraction of copolymer, $\phi_{POLYMER}$, and SANS measurements were made for various values of f_d.

An example is shown in Fig. 1a for $\phi_{POLYMER} = 0.86$ at 30 °C. The Bragg peaks correspond to a lamellar structure of liquid-rich polar P2VP microphase regions separated from liquid-poor non-polar PS microphase regions. Near

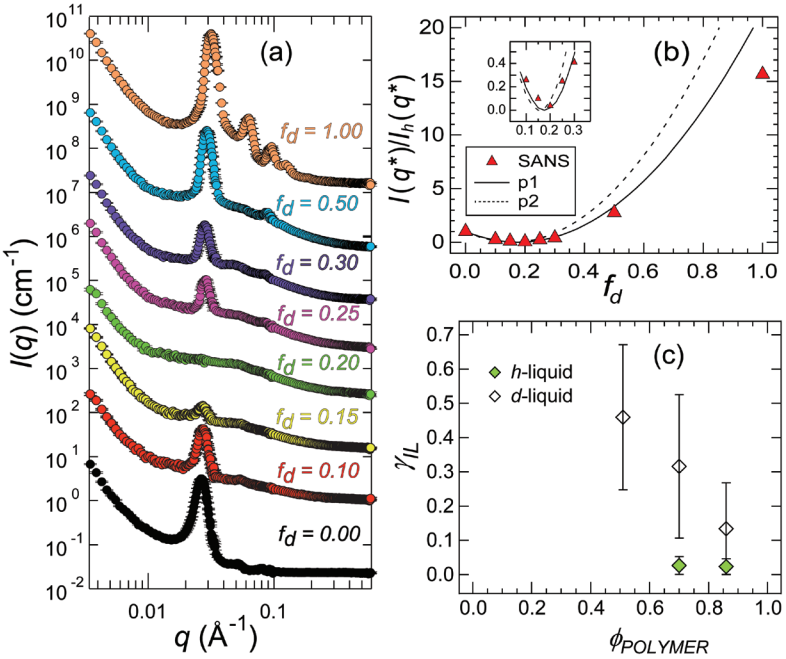

FIGURE 1: (a) SANS intensity profiles (offset for clarity) for various values of deuterated copolymer volume fraction f_d as a function of q for polymer volume fraction $\phi_{POLYMER} = 0.86$ mixtures in *h*-liquid at 30 °C. (b) Experimentally measured and modeled normalized peak intensities of the data in Fig. 1a as a function of f_d. Inset shows detail near the contrast match composition. (c) Ionic liquid partition coefficient, γ_{IL}, for partitioning into PS blocks for varying copolymer to *h*-liquid and *d*-liquid mixture compositions as a function of copolymer volume fraction $\phi_{POLYMER}$.

University of California, Berkeley, Berkeley, CA 94720

$f_d = 0.2$ one can see that the major peak visible in all the other curves disappears, rendering the lamellae invisible at the contrast-matching condition. In this way one can get a measure of the *h*-liquid concentration in the deuterium-containing PS microphase, because the scattering length density there now matches that in the liquid-swollen P2VP microphase regions.

In order to extract the ionic liquid concentration in the PS microphase, the intensity of the major Bragg peak at q^*, $I(q^*)$, must be modeled, making assumptions about the mixtures in the microphases. In effect, the models contain γ_{IL}, the ionic liquid microphase partition coefficient, as a parameter. This parameter measures the fraction of ionic liquid in the PS microphase divided by the fraction of ionic liquid in the P2VP microphase. Fig. 1b plots the $I(q^*)$ normalized to the $f_d = 0$ (undeuterated) value versus f_d for the case shown in Fig. 1a. The data are compared to the results of two model profiles, *p*1 and *p*2, which are described in detail in Ref. 4. Profile *p*1 assumes complete partitioning of ionic liquid into P2VP blocks with moderate mixing of PS and P2VP phases, while profile *p*2 results from the same degree of PS and P2VP mixing as *p*1, but some of the liquid is allowed to pervade the PS phase. Clearly, *p*1 gives the better fit, both to the value of f_d and the peak intensity, as shown in detail in the inset to Fig. 1b.

We repeated the experiment and analysis described above for various $\phi_{POLYMER}$ values, and also performed a similar experiment using *d*-liquid. The results are summarized in Fig. 1c where we plot γ_{IL} versus $\phi_{POLYMER}$ for both copolymer/*h*-liquid and copolymer/*d*-liquid mixtures. The analysis indicates that γ_{IL} for *d*-liquid ranges from 0 to 0.67 while that of *h*-liquid is in the vicinity of 0 to 0.10. In spite of the large error bars, it is evident that γ_{IL} increases with increasing ionic liquid concentration in the case of *d*-liquid. The difference in partitioning of the deuterated and protonated ionic liquid in the PS- and P2VP-rich phases seen in Fig. 1c is unexpected. The error bars in Fig. 1c mainly reflect our inability to ascertain the extent of inter-mixing of the PS and P2VP chains under these scattering contrast conditions and the fact that the calculations are thus constrained to the *h*-liquid based values of $0 \le \phi_{PS,\,P2VP} \le 0.15$ and $0 \le \phi_{P2VP,\,PS} \le 0.15$, where $\phi_{PS,\,P2VP}$ is the fraction of P2VP in the PS microphase and $\phi_{P2VP,\,PS}$ is the fraction of PS in the P2VP microphase.

The unexpected result for the difference in partitioning of the deuterated and protonated ionic liquid in the PS- and P2VP-rich phases seen in Fig. 1c prompted us to look for corroborating evidence. Glass transition temperatures of the PS-rich microphase ($T_{g,PS}$) were determined using differential scanning calorimetry (DSC) and are plotted in Fig. 2 as a function of the ionic liquid partitioning coefficient in the PS-rich microphase determined by SANS. The error bars in Fig. 2 correspond to the range of γ_{IL} values

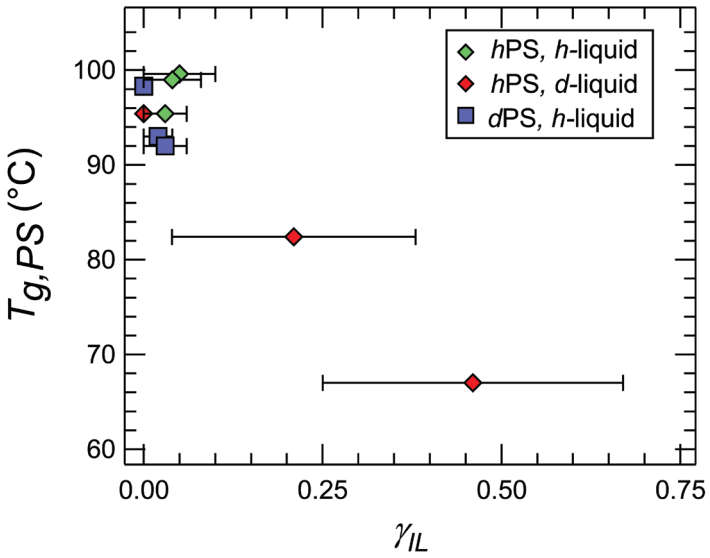

FIGURE 2: Glass transition temperature, $T_{g,PS}$, versus ionic liquid partition coefficient, γ_{IL}, for various copolymer/liquid mixture compositions and deuterium labeling. Error bars for γ_{IL} correspond to Fig. 1c.

shown in Fig. 1c. For the *h*-copolymer/*h*-liquid mixtures, $T_{g,PS}$ is in the vicinity 100 °C, due to the near-complete partitioning of ionic liquid in the P2VP-rich microphase. In contrast, mixtures containing *d*-liquid exhibit a lower $T_{g,PS}$. This finding is consistent with the SANS data that reveal a significant concentration of *d*-liquid in the PS-rich microphase. Based on measurements of the Flory-Huggins polymer-solvent interaction parameter, χ, of protonated versus deuterated polymers we anticipate variations of order 0.001 for $\chi_{PS/P2VP}$ caused by deuterium labeling. It is thus not surprising that deuteration of the copolymers has little effect on the glass transition temperature. Much less is known about the effect of deuteration on ionic interactions and hydrogen bonding, and hence what effect using deuterated ionic liquid has on thermodynamic properties.

We have examined the distribution of an ionic liquid within microphase-separated S2VP copolymer domains in concentrated mixtures of the two components. Using SANS contrast matching and DSC we established that the ionic liquid selectively partitions into P2VP domains for mixtures in the composition range $0.51 \le \phi_{POLYMER} \le 0.86$. The strong partitioning seen for *h*-liquid demonstrates the potential for block copolymer/ionic liquid electrolytes to allow the variation of mechanical properties necessary for real-world applications while maintaining the necessary ion-conducting properties.

References

[1] Y. Y. He, Z. B. Li, P. Simone, T. P. Lodge, J. Am. Chem. Soc. **128** (8), 2745 (2006).

[2] P. M. Simone, T. P. Lodge, Macromolecules **41** (5), 1753 (2008).

[3] J. M. Virgili, A. Hexemer, J. A. Pople, N. P. Balsara, R. A. Segalman, Macromolecules **42** (13), 4604 (2009).

[4] J. M. Virgili, A. J. Nedoma, R. A. Segalman, N. P. Balsara, Macromolecules **43** (8), 3750 (2010).

Decoherence-free neutron interferometry

D. A. Pushin[1], M. G. Huber[2], M. Arif[2], D. G. Cory[1,3,4]

Matter wave optics provides deep insights into quantum mechanics, and in particular matter wave interferometers have served as important examples of macroscopic quantum coherence. In general, matter wave interferometers are extremely sensitive to environmental noise such as mechanical vibrations, and as a result are not widely used. Just as the neutron interferometer assisted in the development of our current understanding of foundational issues in quantum mechanics, it is well suited to leading the practical implementation of improved coherent control using quantum information theory. Here we demonstrate how quantum error correcting codes may be used to improve experimental designs of quantum devices in order to achieve noise suppression. In particular, neutron interferometry is used as a testbed to show the potential for adding quantum error correction to quantum measurements.

A two-level quantum system is considered to be coherent if precise knowledge of the relative phase between the two basis states is obtainable. For measurements that involve averaging over multiple instances of the system, the phase for each element of the ensemble must be the same in order to maintain coherence. Dephasing occurs when a physical process causes the development of a random relative phase between the two basis states for each member of the ensemble.

In the case of a neutron interferometer, we are obtaining an expectation value measurement by averaging over many experiments consisting of interactions of individual neutrons with the device. The physical process leading to the development of the random relative phase for each neutron is mechanical vibrations. The two-level system is defined by the two possible paths a neutron can take from the first blade of the interferometer to the detectors (see Fig. 1b). Neutrons interact with the blades of the interferometer via Bragg scattering to produce two coherent beams of neutrons. The results of Bragg scattering may be modeled as a single neutron undergoing no interaction with the blade (transmission), or scattering (reflection), resulting in a single component of the neutron's momentum being inverted [1]. For a standard Mach- Zehnder (MZ) interferometer (Fig. 1b) the middle blade serves as a mirror that redirects the two paths to a third blade where they recombine and interfere. For the 4-blade Decoherence-Free (DF) configuration (Fig. 1b), the situation is nearly identical, except that the two paths are redirected twice with no mixing of states in the center of the interferometer.

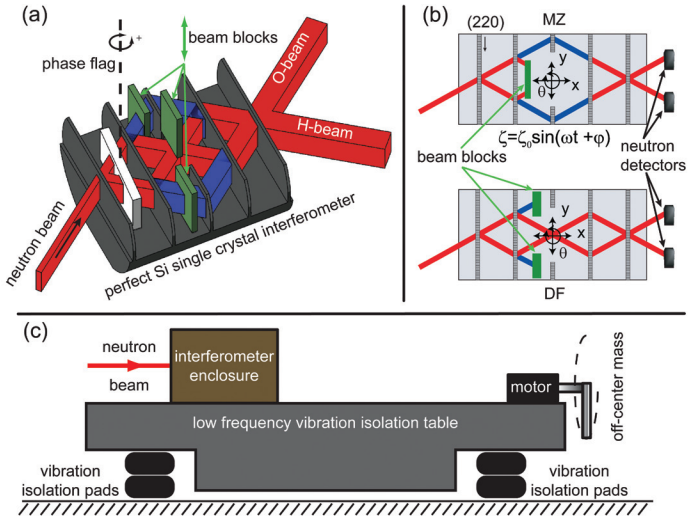

FIGURE 1: (a) A diagram of the 5-blade neutron interferometer. By moving cadmium shields up or down we can *in situ* select the three (MZ) or four (DF) blade interferometer configuration. (b) A schematic top-view representation of the five blade beam paths. The upper diagram represents the MZ setup. When we block the outer paths only we have the four blade (DF) setup, as shown in the lower diagram. (c) A schematic diagram of the neutron interferometer facilities at the NIST. This facility has several vibration isolation stages to remove vibrations above 1 Hz. To test the robustness of the interferometers to mechanical vibrations we introduced vibrations by a motor with an off-center mass attached to the table. We controlled the frequency of this noise through the speed of the motor. Vibrations were monitored by a seismometer [2].

Mechanical vibrations may be considered as sinusoidal oscillations around the center of mass of the single crystal, which we write as $\zeta(t) = \zeta_0 \sin(\omega t + \phi)$, where ϕ is a random phase that corresponds to a variation of neutron arriving times on the first blade. This variable can take any value between 0 and 2π. For ζ we can specify any coordinates x, y, z, or any angles (such as θ - rotation around z axis). In order to motivate the discussion we adopt a simple model for the neutron/blade interaction that includes all of the necessary physics [1]. Vibrations modify the velocity and path length of reflected neutrons relative to transmitted

[1]Massachusetts Institute of Technology, Cambridge, MA 02139
[2]Physics Division, National Institute of Standards and Technology, Gaithersburg, MD 20899
[3]Perimeter Institute for Theoretical Physics, Waterloo, Ontario, Canada N2L 2Y5
[4]University of Waterloo, Ontario, Canada N2L 3G1

neutrons, introducing a relative phase difference between the two paths. For low frequency noise we may consider the interferometer as moving with a constant velocity for the time a neutron is in the device. For different arrival times of neutrons at the first blade, this velocity will be different. Thus, the phase difference between the two paths will be randomly distributed based on the time of arrival. When averaging over multiple measurements, we must average over the random phase, which leads to decoherence and a loss of contrast. The advantage of the DF interferometer is that these phases will be much smaller, with significantly less variance than for the MZ interferometer.

The interferometer contrast is a measure of interferometer quality and is ≤ 1. Figure 2 represents numerical simulations of changes in the interferometer contrast due to vibrations along *x* and *y* axes and rotational vibrations about *z* [1]. From these numerical simulations we can see that 4-blade (DF) design is far less sensitive to low frequency vibrations. Thus a solution to robust interferometry could be based on a four-blade single-crystal geometry that reduces errors introduced by vibrations.

In order to test our idea and compare MZ and DF designs we built a five blade neutron interferometer that incorporates both a standard Mach-Zender configuration and a decoherence-free configuration based on a decoherence-free subspace (DFS) [2]. The switch between designs occurs *in situ* by moving cadmium (Cd) beam blocks. In Fig. 3a we show a drawing of the five blade interferometer used in this study. It was cut out of a single crystal Si ingot at the University of Missouri machine shop. The incoming neutron beam coherently splits at the blades by Bragg scattering. In order to preserve crystallographic registration of the blades each blade remains attached to the common base.

As shown in Fig. 1, the neutron beam enters the single crystal interferometer from the left and is split coherently by the first blade over two paths. Blades 2, 3, and 4 direct the beams through four different paths and recombine them at the last (fifth) blade. Interference of these paths is observed by ^{3}He detectors placed in the O- and H-beams. As shown in Fig. 1b, by placing Cd blocks we can choose either the MZ (3-blade, upper schematic diagram) or DF (4-blade, lower diagram) setups.

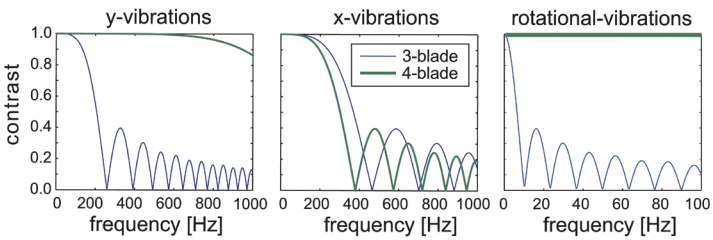

FIGURE 2: Calculation of contrast change due to applied vibrations for 3-blade (MZ) and 4-blade (DF) interferometers show on Fig. 1b. From the left: vibrations along the *y*-axis, the *x*-axis, and due to rotational vibrations around *z*-axis and the center of mass. Note that the scale of the frequency for rotational vibrations is a factor of 10 lower than those shown for vibrations along the *y*- and *x*-axes [1].

Figure 1c outlines the experimental setup of the Neutron Interferometer and Optic Facilities at the National Institute of Standards and Technology, Gaithersburg, MD. The interferometer is placed inside an enclosure with a temperature stability of a few mK to maintain its phase stability [3]. The enclosure is isolated from external vibrations by a high position stability (< 1μm) vibration isolation system. We add controlled vibrations to the system through a motor with an off-center shaft. Vibrations were monitored by a short-period seismometer.

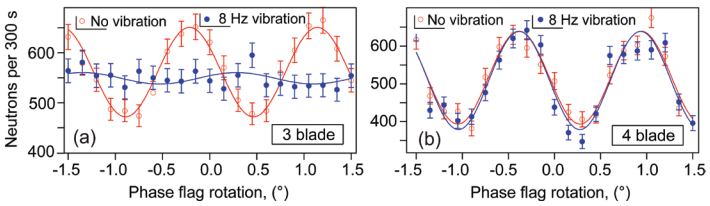

FIGURE 3: (a) Interferograms from the three blade (MZ) interferometer without vibrations (open circles) and with 8 Hz vibrations (closed circles). We observe a complete loss of contrast with 8 Hz vibrations. (b) Interferograms from the four blade (DF) setup at the same conditions as in 3a. Within experimental errors there is no loss of contrast from the added vibrations.

To measure the contrast we introduce a phase difference between the two interferometer paths and measure the phase dependence on the output intensity at both the O- and H- beams. In neutron interferometry it is convenient to introduce this phase difference through a fused silica phase flag placed between the first and the second blades (see Fig. 1a). Figure 3a shows the intensity dependence for the 3-blade (MZ) configuration with and without added noise. The vibrations were artificially introduced with a fundamental frequency of 8 Hz. Without vibrations the interferometer has a 12 % contrast while with vibrations there is no detectable contrast.

Figure 3b shows the contrast for the four blade (DF) interferometer under the same conditions used for the three blade MZ setup [2]. Here there is no measurable loss of contrast with added noise. As expected, the DF configuration is substantially more robust to the applied noise than is the MZ configuration [1].

Experiments verify that the decoherence-free interferometer is protected against low frequency mechanical vibrations that significantly degrade the performance of the standard design. We anticipate that these improvements will increase the range of applications for matter wave interferometry, such as in soft condensed matter and spintronics.

References

[1] D. A. Pushin, M. Arif, and D. G. Cory, Phys. Rev. A **79**, 053635 (2009).

[2] D. A. Pushin, M. G. Huber, M. Arif, and D. G. Cory, (submitted)

[3] D. A. Pushin, M. Arif, M. G. Huber, and D. G. Cory, Phys. Rev. Lett. **100**, 250404 (2008).

Software for biological soft condensed matter science

J. E. Curtis and S. Krueger

Proteins, nucleic acids, and lipids are the key components that carry out the structural and catalytic roles enabling complex biological systems to function. Atomic level structural knowledge of such systems has relied upon x-ray diffraction and nuclear magnetic resonance (NMR) spectroscopy. Increasingly, the biological research community acknowledges that understanding the structure of homogeneous and heterogeneous protein, protein-nucleic acid complexes in solution and on lipid membranes is an important problem that is not generally accessible using x-ray diffraction or NMR. Many of these systems have unstructured or disordered regions that have important functional roles that complicate the interpretation of experimental data.

We are developing software for the NCNR user community to aid the design and interpretation of neutron scattering data for biological soft condensed matter systems. The software aims to lower the barrier experienced by non-experts to handle the technical details (coordinates, force-fields) of manipulating atomic information and to accurately calculate neutron observables that can be compared to experimental data. The platform-independent open-source software is designed such that the atomic coordinates are accessible by other state of the art molecular dynamics and molecular modeling software suites. We have condensed the modeling, structure generation, and analysis algorithms into a software suite called SASSIE. The development of the software has been guided by a variety of collaborative research projects with NCNR users. We have used the software to design and interpret various small-angle neutron (SANS) and neutron reflectivity (NR) experiments of homogeneous and heterogeneous biological systems [1, 2].

As an example, in collaboration with scientists from the Center for Advanced Research in Biotechnology (CARB), we have used SASSIE to model the structure of the *Methanobacterium thermoautotrophicum* (mtMCM) minichromosome maintenance protein complex in solution. The mechanism of DNA unwinding during the replication process is not completely understood. However, it is thought that the flexible domains present in the mtMCM play an important role. While some partial x-ray crystal structures are available and cryo-EM has provided several different structures of the full protein, no solution structures have been reported. Figure 1 shows the SANS data obtained for the N-terminal portion of mtMCM in solution. A family of structures that best fit the SANS data was found by using SASSIE to explore the range of possible conformations of the flexible regions of the protein and then comparing the resultant structures to the SANS data. These structures will be compared to those obtained from mtMCM with DNA bound in order to ascertain if there are inherent structural differences between mtMCM with and without DNA. If so, then these differences could be important in ascertaining the mechanism of DNA unwinding during DNA replication.

In summary, we have developed open-source software to aid in the design and analysis of neutron scattering experiments of complex biological systems. The software is available to the scientific community at (www.smallangles.net).

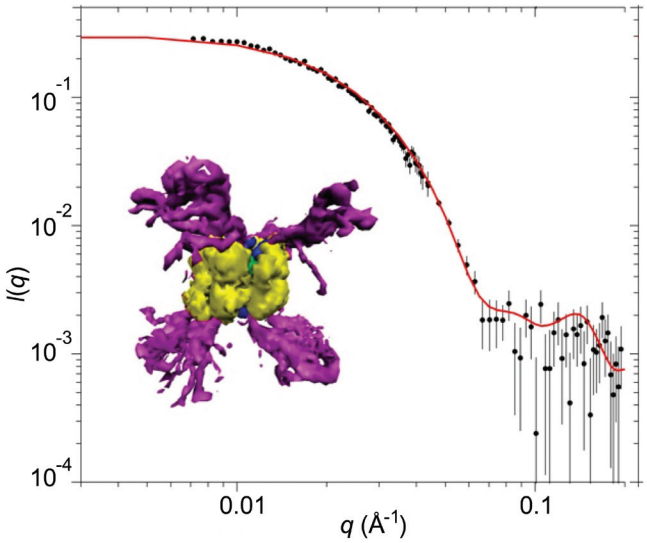

FIGURE 1: Determination of the structure of MCM helicase. SANS data for mtMCM in solution are shown along with the model SANS curve for one of these structures (solid red line). The family of best-fit structures, depicted as a density plot of configuration space, is shown in the inset. The yellow area maps out the space that is occupied by one of the flexible regions in the protein while the magenta area represents the space occupied by the other flexible region. The blue and green areas, barely seen in the figure, represent the static regions of the protein.

References

[1] S. A. K. Datta, *et al.*, J. Mol. Bio. **365**, 812 (2007), D. Lee, *et al.*, Mol. Cell, **22**, 423 (2006), J. VanOudenhove *et al.*, J. Mol. Bio. 387, 910 (2009).

[2] H. Nanda *et al.*, Biophys. J (in press), M. S. Kent *et al.* Biophys. J (in press), J. E. Curtis and S. Krueger, Chem. Phys. Comm. (submitted), H. Nanda *et al.* J. Mol. Bio. (submitted).

NIST Center for Neutron Research, National Institutes of Standards and Technology, Gaithersburg, MD 20899

Following lithium through battery components and functioning prototypes

H. Wang[1] and R. G. Downing[2]

Energy storage systems such as batteries play an increasingly significant role in our daily routine as they power personal electronics, tools, and a variety of vehicles. Longer lasting and more powerful batteries are in ever greater demand in today's mobile society. Companies, universities and federal laboratories are using NIST facilities to develop powerful and longer lasting lithium ion batteries. Neutron Depth Profiling (NDP) is a nondestructive analytical technique used to determine the quantity and the depth distribution of lithium, as well as several additional elements in solid films (Fig. 1). It is among the effective neutron techniques that give researchers a faster and clearer perception of lithium's behavior in existing and new battery designs.

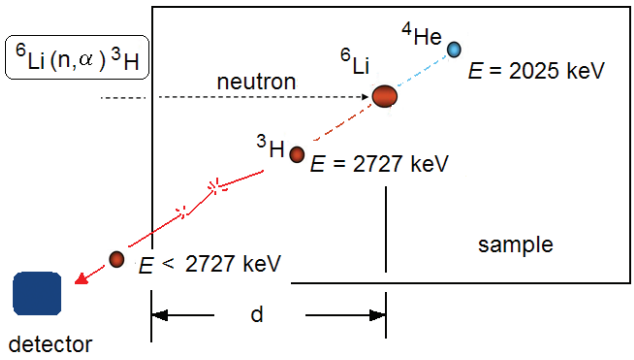

FIGURE 1: In NDP, as the nuclear decay particles course through the sample they lose energy by collisions, giving a measure of the depth below the surface from which they originated.

Lithium ion batteries permanently lose a significant portion of the electrical storage capacity upon first use and sustain incremental losses in each subsequent charge-discharge cycle. So where is the unavailable lithium and why does it stop contributing to the available energy? An NDP analysis locates the total lithium inventory and its distribution across the entire battery thickness. Furthermore, since the NDP technique is nondestructive; analyses are conducted on a fully functioning battery. Neutrons are electrically neutral particles that flow through the sample and react with a small number of lithium atoms to produce energetic alpha and triton particles. As those particles emerge from all depths of the cell the number of particles of a given energy define both the Li atom density and the depth of origin across the cell. The battery remains undisturbed in the instrument over multiple charge-discharge cycles while cold neutrons flow through the cell generating the NDP signal. Researchers observe the migration of the lithium as devices age through repeated charge and discharge cycle. The "frozen" lithium is eventually spotted.

Migration of lithium is shown through a time series of NDP measurements in Fig. 2. The top group shows 5 NDP individual spectra taken during the charge cycle of a thin film lithium ion battery. Lithium ions are shown migrating from the $LiCoO_2$ cathode (decreasing in Li content at the high energy plateau) to the Li metal anode (increasing in lithium content at the low energy peaks) through a LiPON electrolyte (relatively invariant at the intermediate energy). As expected, when the battery is discharged, the anode gives up Li ions that migrate back to the cathode (lower group of spectra). The NDP spectra capture the systematic drop in Li atom density from the anode and the gain of Li at the cathode. This process has been repeated under different conditions and for extended charge-discharge cycles. In summary, NDP that allows charge-discharge cycles to be followed systematically and the lithium quantified without destroying the cells or exposing the air-sensitive lithium to the atmosphere is a powerful tool in the quest for long-lived lithium batteries.

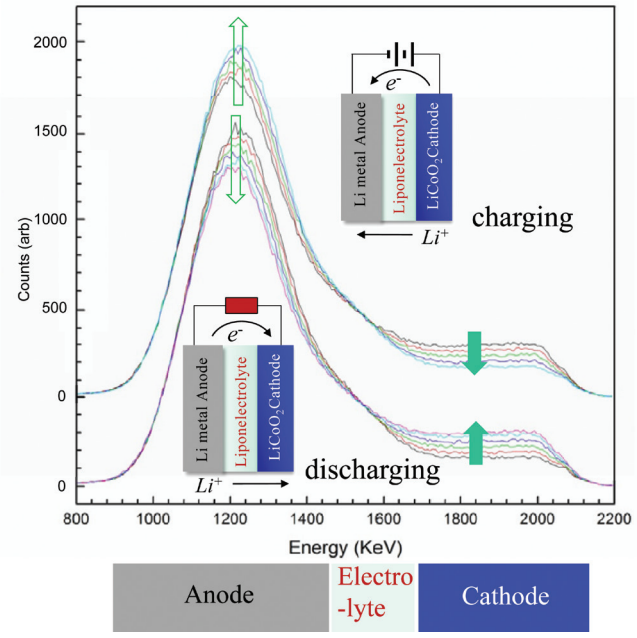

FIGURE 2: NDP spectra of the lithium distribution in a thin film battery. (The discharge spectra are displaced 500 units.) The large arrows depict the time sequence of Li depth profiles captured as the battery is charged and discharged. The inset diagrams illustrate the lithium ion and electron flow and battery composition and construction. Below, the colored strip shows the approximate positions of the battery components.

[1]State University of New York, Binghamton, NY 13902
[2]Analytical Chemistry Division, National Institute of Standards and Technology, Gaithersburg, MD 20899

Peering inside: imaging an object's interior while clarifying its elemental makeup

R. Bindel[1], E. Korobkina[2], T. Mahale[3]

Somewhere between prompt gamma activation analysis (PGAA) and neutron imaging, a hybrid tool dubbed "scanning PGAA" produces images of a sample's interior structure while elucidating its elemental composition. This technology is uniquely positioned to evaluate new materials, particularly those for which non-destructive analyses are needed. Recently, 3D fabrication techniques capable of complex freeform geometries have been of increasing interest to the medical community as a way of producing customized bone replacement implants out of titanium alloys. However, there is uncertainty in the homogeneity of the alloy within samples produced by such processes, and this is unacceptable for medical purposes. Scanning PGAA was used to look at an interior cross section of a non-stochastic foam made of a Ti-6Al-4V. The feasibility of examining the spatial homogeneity of the alloy was assessed.

The instrument configuration for scanning PGAA is similar to the typical PGAA setup. PGAA is a tool for measuring the presence and amount of many different elements, but it has no inherent imaging ability. In the usual arrangement at the NG-7 beam guide, a sample is placed in a uniform, collimated neutron beam. A shielded gamma-ray spectrometer views the sample through a long lead collimator perpendicular to the neutron beam. In the scanning PGAA configuration, the neutron beam is focused using a polycapillary neutron optic [1], and the field of view of the spectrometer is reduced to a few millimeters before and after the focal spot. A system of precision stages is used to move the sample in a raster pattern through the neutron beam to produce a multidimensional image.

The sample was manufactured using an Electron Beam Melting (EBM) process in which 2D layers of powdered Ti-6Al-4V are sequentially melted to produce a 3D part. This layered approach is capable of producing complex geometries; however, the powdered starting material is recycled between layers, possibly exacerbating the buildup of contaminants or fractionated evaporation and deposition of the constituent elements.

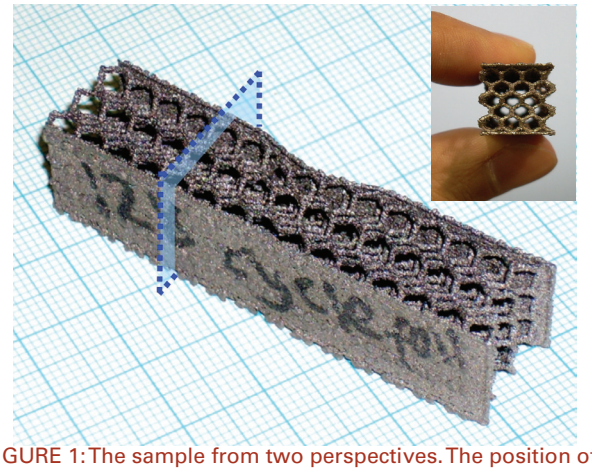

FIGURE 1: The sample from two perspectives. The position of the slice imaged by scanning PGAA is superimposed in blue.

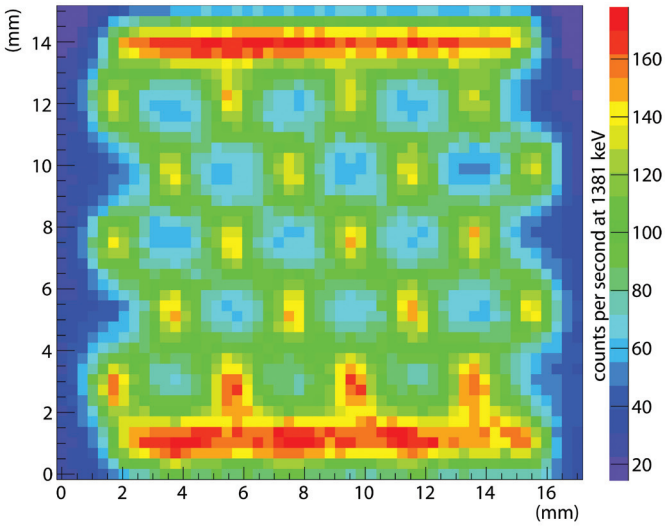

FIGURE 2: An interior cross-sectional image produced by mapping the intensity of the titanium peak at 1381 keV.

Figure 1 presents photographs of the sample with the location of the cross-sectional slice superimposed. Figure 2 shows a map representing the intensity of the titanium signal at 1381 keV, where a PGAA spectrum was acquired for 10 s at each pixel. Figure 3 shows a PGAA spectrum obtained over a 90 minute period at just one position. In this spectrum, the weak aluminum and vanadium peaks can be quantified. Using multiple long acquisitions at different spots, homogeneity of the titanium alloy sample can be assessed. The combination of imaging along with the multi-element analytical properties of PGAA make scanning PGAA a good candidate for examining the homogeneity of Ti-6Al-4V forms produced with additive manufacturing techniques.

Reference

H. H. Chen-Mayer, D. F. R. Mildner, V. A. Sharov, Q. F. Xiao, Y. T. Cheng, R. M. Lindstrom, R. L. Paul, Rev. Sci. Instrum. **658** (10), 3744 (1997).

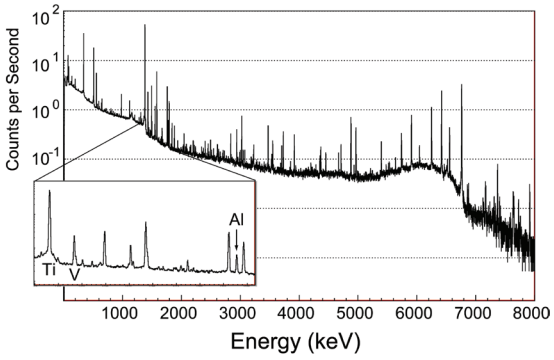

FIGURE 3: A long PGAA count at a single location featuring titanium, aluminum, and vanadium peaks.

[1]Chemical Science and Technology Laboratory, National Institute of Standards and Technology, Gaithersburg, MD 20899
[2]North Carolina State University, Raleigh, NC 27606
[3]Telos Medtech LLC, Raleigh, NC 27606

Time-resolved SANS with sub-millisecond resolution (t-SANS)

C.J. Glinka[1,2], J.G. Barker[1], J. Moyer[1], N. Maliszewskyj[1], P.Tsai[1], X. Wang[3], A. Wiedenmann[4]

Changes in nanoscale structure that occur on time scales in the micro- to millisecond regime in response to some stimulus are critical to the function and performance of materials as varied as muscle tissue, membranes, superconductors, 'smart' gels, electrorheological fluids, domains in ferroelectrics and ferromagnets, and photosensitive macromolecules. Using neutrons to probe this time regime has been difficult for intensity reasons but has recently become more viable due to the successful demonstration [1] of a novel technique proposed a decade ago by Gähler [2]. Now the first permanent installation of equipment enabling the technique has been completed at the NG-7 30 m SANS instrument. The capability provided to follow changes in nanostructure and macromolecular conformations on relevant time scales is expected to have a major impact on materials and biological research at the NCNR.

The main modification to the NG-7 SANS instrument to implement Gähler's technique has been the incorporation of a high speed disk chopper within the initial collimation section of the instrument, some 15 m from the sample position. The 10 μs to 20 μs neutron pulses from the chopper have a broad band of wavelengths (10 % < $\Delta\lambda/\lambda$ < 30 % depending on the setting of the instrument's upstream velocity selector) and thus spread in time with several pulses overlapping when they reach the sample. This so-called frame overlap is normally to be avoided in time-of-flight measurements, but here is essential to the intensity gain inherent in Gähler's technique. With the proper choice of neutron pulsing frequency, depending on the given sample stimulus frequency and sample-to-detector distance, neutrons from multiple pulses that scattered at equivalent times, relative to the sample stimulus period, arrive at the detector at the same time. With this technique, which we refer to as t-SANS, the effective duty cycle of the measurements is typically ≈10 % rather than 1 % to 2 %, which is what it would be if the pulses had to be spread far enough apart to avoid any frame overlap. A time-distance diagram illustrating the principle of the technique is shown in Fig. 1.

To demonstrate the technique, t-SANS measurements have been made on a rapidly-solidified amorphous Fe (with 4 % Si) sample as a function of the frequency of an applied sinusoidal magnetic field. The scattering is isotropic in zero field and increases perpendicular to an applied field, presumably due to the alignment of magnetic precipitates along the field direction. The orientational response of the precipitates is what is directly probed with t-SANS. Shown in Fig. 2 is the ratio of the scattering perpendicular and parallel to a sinusoidal field of with amplitude 0.011 T and a frequency of 1560 Hz. For the conditions of this measurement the calculated time resolution is 60 μs full width at half maximum which is more than adequate to confirm that the precipitates align along the field with little or no phase lag at this frequency.

With the apparatus installed on the NG-7 SANS changes in nanostructure that occur in as little as 30 μs in response to a periodic stimulus can be detected and characterized. This capability is expected to greatly expand the scope of SANS studies on a wide range of materials.

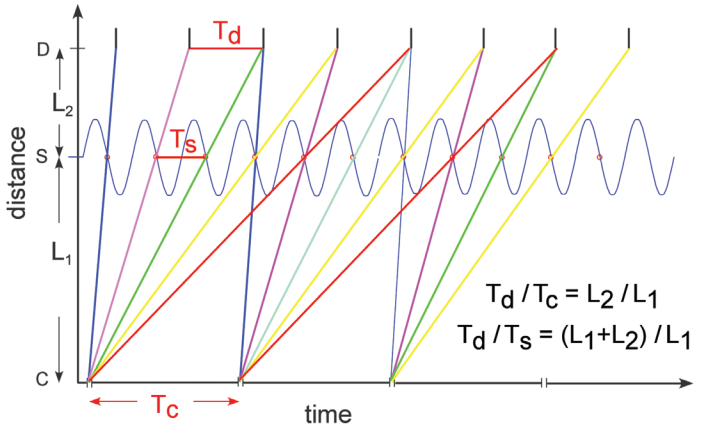

FIGURE 1: A time-distance diagram showing the trajectories of neutrons from successive chopper openings (C) resulting in frame overlap at the sample (S). Neutrons from different chopper pulses which probe the same oscillation state are observed at the same time equivalent channel at the detector (D), if the equations in the diagram are satisfied.

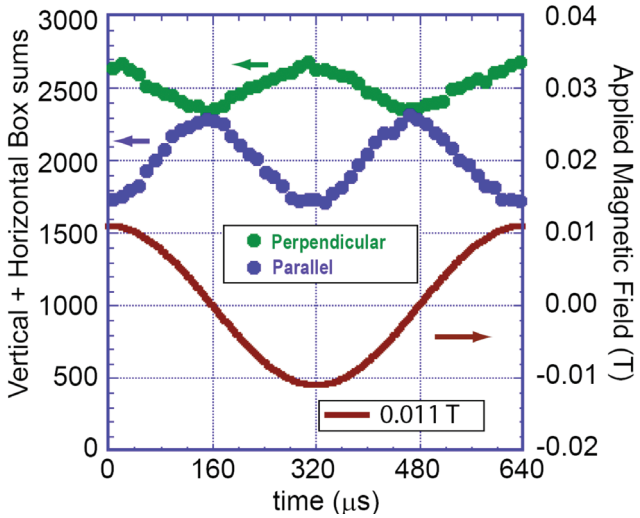

FIGURE 2: The integrated SANS (0.008 Å^{-1} < Q < 0.033 Å^{-1}) parallel and perpendicular to a time varying magnetic field (solid line). These data show that the magnetic moments in the sample are able to follow the field reversals at this frequency.

References

[1] A. Wiedenmann, U. Keiderling, K. Habicht, M. Russina, R. Gähler, Phys. Rev. Lett. **97**, 057202 (2006).

[2] D. Kipping, R. Gähler, K. Habicht, Physics Letters A **372**, 1541 (2008). Gähler's acronym for the technique described herein is TISANE.

[1]NIST Center for Neutron Research, National Institute of Standards and Technology, Gaithersburg, MD 20899
[2]University of Delaware, Newark, DE 19716
[3]Brown University, Providence, RI 02912
[4]Institut Laue-Langevin, 38042 Grenoble Cedex 9, France

Elemental analysis of a single-wall carbon nanotube candidate reference material

R. Zeisler[1], R. L. Paul[1], R. O. Spatz[1], L. L. Yu[1], J. L. Mann[1], W.R. Kelly[1], S. D. Leigh[2], and J. Fagan[3]

Carbon nanotubes (CNTs) are one of the first major nanoscale manufactured products to enter the market. Reliable and reproducible quantitative measurement and characterization of CNT samples is important not only for progress in the understanding and development of new applications incorporating these materials, but also for the development of an information base for CNT toxicology. The characterization of CNTs containing residual catalyst and impurity metals represents a broad analytical challenge. The metals may be present as major constituents or at trace and ultra-trace levels, and may be loosely adducted to the matrix, firmly incorporated, or chemically bound. Common analytical techniques such as inductively coupled plasma optical emission or mass spectrometry (ICP-OES or ICP-MS) may be hampered by problems if nanoparticle-containing solutions are introduced directly into the plasma or if sample digestion is incomplete. Additionally, the need for sample dilution becomes an issue with only small amounts of CNT material available for analysis. Similar limitations exist for x-ray fluorescence spectrometry (XRF), which may not have the sensitivity to analyze small CNT amounts in dispersions or in bulk samples.

In response to the need for reliable measurement of CNTs, NIST has developed a single-wall CNT (SWCNT) reference material, Standard Reference Material (SRM) 2483 Carbon Nanotube Soot. This SRM, which contains SWCNTs together with other carbon species, catalyst residues, and trace element contaminants, has been characterized by a combination of neutron activation analysis (NAA) and inductively coupled plasma mass spectrometry (ICP-MS). Instrumental neutron activation analysis (INAA) was carried out on 25 mg to 40 mg samples of the SRM. Prompt gamma-ray activation analysis (PGAA) was performed on approximately 100 mg samples using both the NIST thermal and cold neutron PGAA spectrometers. Both methods are fully instrumental and require no sample dissolution. All measurements were carried out using pure elements or compounds as standards and appropriate control materials. ICP-MS measurements were performed on 25 mg to 160 mg samples of the SRM following Carius Tube digestion in hydrochloric and nitric acids. Calibration was performed using NIST single element spectrometric solutions.

PGAA, INAA, and ICP-MS procedures complemented each other in elemental coverage and provided independent results for the catalyst elements and some trace contaminants. These results were combined to assign mass fraction values for the Certificate of Analysis (COA). Table 1 lists the measurement results together with the proposed certified values and their statistically evaluated uncertainties for the COA.

NAA procedures were found to be well-suited for the characterization of the SWCNT materials because of their extensive dynamic range. Percent level elements were determined in the same test portions as the trace elements. PGAA provided results for CNT matrix elements such as hydrogen and carbon, the catalyst residue elements and some trace elements. ICP-MS provided results chiefly for the rare earth elements allowing for the first time the assignment of certified values for this group. This work demonstrated that analysts may find in the characterization of CNT materials a new domain for NAA applications.

Table 1. Measurement and certified values reported for SRM 2483.

Element / Nuclide	INAA	PGAA	ICP-MS	Certificate Value
	Average (SD) n = 44	Average (SD) n = 10	Average (SD) n=9	Value (U) k=2
Ba mg/kg	120.2 (9.6)		116.6 (2.5)	**118.4 (3.6)**
Ce mg/kg	189 (17)		196.3 (2.3)	**192.6 (5.4)**
Cl mg/kg	2080 (74)	2170 (40)		**2125 (54)**
Co %	0.954 (0.028)	0.971 (0.012)		**0.963 (0.011)**
Dy mg/kg	8.44 (0.31)		8.27 (0.07)	**8.36 (0.13)**
Eu mg/kg	2.34 (0.18)		2.207 (0.020)	**2.274 (0.084)**
Gd mg/kg		10.05 (0.11)	11.05 (0.09)	**10.58 (0.56)**
La mg/kg	102.2 (3.0)		106.2 (1.2)	**104.2 (2.7)**
Mo %	3.39 (0.11)	3.42 (0.05)		**3.406 (0.029)**
Sm mg/kg	12.36 (0.39)	13.86 (0.15)	13.00 (1.5)	**13.09 (0.90)**

[1]Analytical Chemistry Division, National Institute of Standards and Technology, Gaithersburg, MD 20899
[2]Statistical Engineering Division , National Institute for Standards and Technology, Gaithersburg, MD 20899
[3]Polymers Division, National Institute for Standards and Technology, Gaithersburg, MD 20899

Neutron Source Operations

The NIST reactor (NBSR) operated for 267 full power (20 MW) days or a 99 % availability during FY10. A typical operational year consists of seven cycles of approximately 38 days followed by 11 days of shutdown maintenance and refueling activities. The shutdown periods are carefully scheduled and choreographed by the Reactor Operations and Engineering (ROE) Group to assure the maximum preventative and corrective maintenance is efficiently performed during this limited time. The ROE routine maintenance program is a significant contributor to the outstanding record of safe and reliable NBSR operation.

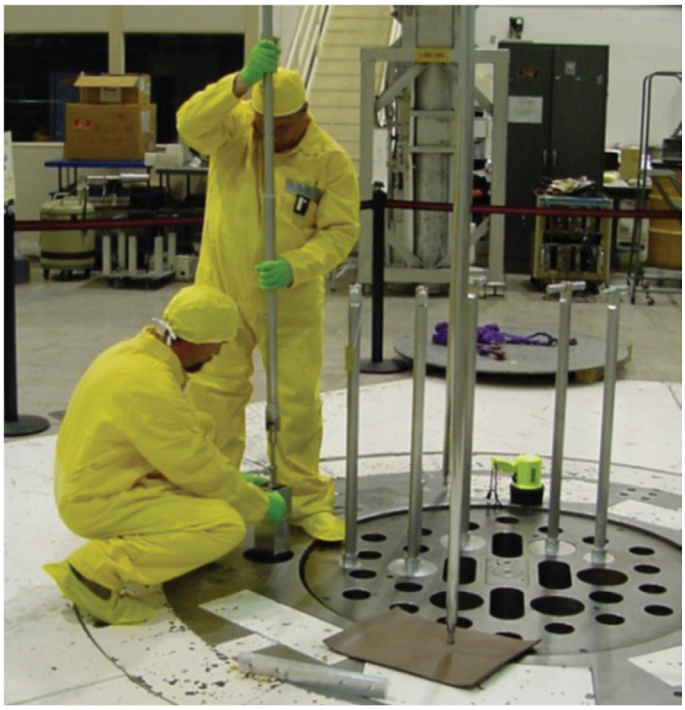

FIGURE 1: Senior Reactor Operators Paul Bobik and Jim Moody add new fuel to the NBSR during a routine maintenance shutdown.

Beyond routine and corrective maintenance activities, much of the ROE staff efforts this past year involved a coordinated NBSR Age Management program that focused on the replacement or upgrade of systems nearing the end of their useful lifetime. Planning for these large projects began several years ago and the opportunity of an extended facility shutdown in 2011 will allow several essential NBSR systems to be upgraded or replaced.

The NBSR power level is controlled by four neutron absorbing shim arms that must be replaced approximately every four years. Over this reporting year, the ROE Group contracted for the design and manufacture of a replacement set of shim arms. Following the receipt of a first set to qualify the shim arm manufacturing process, the NCNR will purchase sufficient spares to last well past the current license expiration date of July 2029. New technology was utilized to manufacture the new shim arms and a prototype was received in August for inspection by the ROE Group.

Sean O'Kelly has now become the Chief of the ROE Group following the retirement of Wade Richards and a Quality Engineer, Bill Schuster, was hired to provide configuration management oversight. Finally, two new senior reactor operator licenses were received by Andrew Blazek and Jeff Burmeister.

FIGURE 2: Senior Reactor Operators Bill Mueller and Jeff Burmeister remove prototype NBSR shim arm for examination.

Expansion Initiative

The NCNR is now midway through an Expansion Initiative to increase its cold neutron measurement capability by more than 25 percent by installing a new cold source and new beamlines, and set the foundation for a new generation of world-class instruments directly supporting the needs of science and industry. The Initiative is a complex multi-year project that includes the co-ordination of civil construction works for new buildings to house the expanded instrument suite in addition to refurbishment projects for facility improvements to the neutron source. The Initiative is proceeding on a schedule that will require a 10½ month shutdown of the reactor beginning in April 2011. During this outage period new cold neutron guides will be run from the reactor confinement building in readiness to serve new and relocated instrumentation in the expanded guide hall. And over the past year the Facility's engineering and technical staff have been working hard to reach a series of major milestones required for the outage and this first phase of installation work.

Civil Construction

Construction work on the guide hall addition and new technical services and administrative building (TSB) is now complete (Fig. 1). The guide hall extension provides an additional 16,000 sq ft to the 20,000 sq ft area of the current building for the new guides, shielding and instrumentation envisaged through the Initiative. The two-story TSB will house the Facility User Office and includes shop space and a conference facility along with some 40 new offices. Staff began moving into this new accommodation during the summer of 2010. The availability of new office space is a key component in the ongoing program to improve and renovate the NCNR laboratories used by both visitors and staff, enabling a number of the rooms vacated to be refurbished and returned to laboratory space as originally purposed. A second 18 month construction phase is scheduled for the autumn of 2010 and will deliver new buildings to house support infrastructure for the neutron source and, during the outage period, core bore holes from the confinement building through to the guide hall,

FIGURE 1: Panoramic view showing the completed TSB (foreground, left side,) with a new walkway connecting to the guide hall in the back. The guide hall extension (slightly different wall pattern) can be seen on the right-hand side.

FIGURE 2: – Inside the recently completed guide hall extension. As part of the second construction phase, the dividing wall (shown on the left) between the existing guide hall and the extension will be removed.

marking the start of the guide installation program.

Outage activities: Guide and shielding installation

The central tenet of the Expansion Initiative is the installation of five new supermirror guides (outlined below) to service new and re-located cold-neutron instruments in the guide hall extension. The MACS spectrometer will be relocated to a new cold source at BT-9, thereby opening a viewport on the current facility cold source to accommodate the new guides. During the reactor outage period the first stage of a carefully choreographed and multi-phase installation sequence begins with the installation of new guide sections running from the reactor confinement building and through the D-wing (Fig. 2). All guide components for this first phase have been delivered and are undergoing characterization and pre-alignment. Staff members have also been working to complete the huge inventory of engineered ancillary components required to install the guides including main shutters, shielding, and vacuum jackets. Close to the reactor face the guides are housed in large monolith assemblies and detailed installation sequences have been established to guarantee that there is clearance to maneuver the assemblies in place and also to ensure appropriate access to re-check guide alignment.

Guide Specifications

The new guides utilize the latest in supermirror coating technology, yet must conform to existing installations and have only a restricted viewing angle of the cold source.

FIGURE 3: Design drawing showing the current layout of the confinement building and D-wing (on the left). The MACS at NG-0 (kidney-shaped analyzer) and the Double Focusing Triple Axis spectrometer at BT-7 to MACS' right can be seen in the center of the figure. To the right of BT-7 is the residual stress facility at BT-8, and beyond that (circular gray object) is BT-9, to which MACS will be moved.

FIGURE 4: Design drawing showing the planned layout of the confinement building and D-wing post-outage in early 2012 with the new guides installed. MACS (analyzer not shown) is in place at BT-9.

Extracting five new beams presented an engineering and neutronics design challenge solved through judicious use of curved sections close to the source followed by straight sections:

NG-A – is a 41 m long guide earmarked for the Neutron Spin Echo instrument. To restrict beam divergence lower critical angle, high reflectivity coatings are used on the straight portions and inner radii of the guides.

NG-B – is also a low divergence guide for use by small angle neutron scattering (SANS) instruments. At a distance of just under a meter from the cold source, the guide divides into discrete upper (48 m long) and lower (52 m long) sections designed for 30 m and 10 m SANS instruments, respectively.

NG-C – is also a high-flux high reflectivity guide and will service a "reflectometer village" comprising the current vertical polarized beam reflectometer plus the new instruments MAGIk and CANDoR. The end station of NG-D will be the new location for the chemistry Prompt Gamma Activation Analysis and Neutron Depth Profiling stations.

Second cold source installation

The displacement of MACS has necessitated the design and building of a second cold source dedicated to the instrument. The new 'PeeWee' source has disk geometry, optimized for MACS subject to the geometric constraints imposed at BT-9 (Fig. 5), and will provide a factor two gain in brightness for the spectrometer. PeeWee follows the same

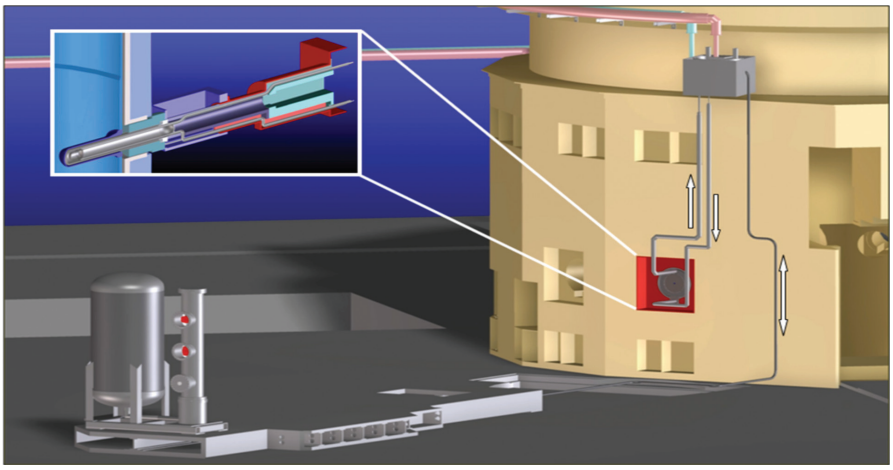

FIGURE 5: Design drawing showing the location of major components of the BT-9 cold source. The H_2 condenser is seen above the beam port; warm H_2 gas lines run through a support structure for MACS to a ballast tank seen on the left. The in-pile assembly is shown inset.

Post-outage period

Reactor operations are scheduled to re-start early in 2012 at which time the Facility instrumentation will be configured as shown in Fig. 6. During the first half of 2012, the remaining sections of the new supermirror guides will be installed into the new guide hall addition. New experimental capabilities will be achieved at the end of the expansion project in late 2012 (Fig. 7), after which time the NCNR will continue its program of instrument development, based around the new guide infrastructure.

design philosophy applied to the existing cold source and utilizes a thermosiphon as the simplest means to supply liquid hydrogen to the source. The new source operates with half a liter of liquid hydrogen, as compared to five liters in the existing cold source, and so the additional heat load is readily handled by the current refrigerator unit.

Source facility developments

Reactor operations and engineering personnel will take the opportunity of the outage period to schedule a number of projects serving to enhance reactor reliability. As part of the Initiative, the reactor control room is the subject of a program to replace obsolete components and a new liner for the fuel storage pool is to be fitted. Funding through the American Recovery and Reinvestment Act (ARRA) will improve further source operations through replacement of the thermal shield system. The thermal shield reduces radiation heating in the reactor pressure vessel and biological shield by means of water flow through a series of pipes and ring headers located between the vessel and biological shield and its replacement is the third and final major evolution of work undertaken in the confinement building during the outage period.

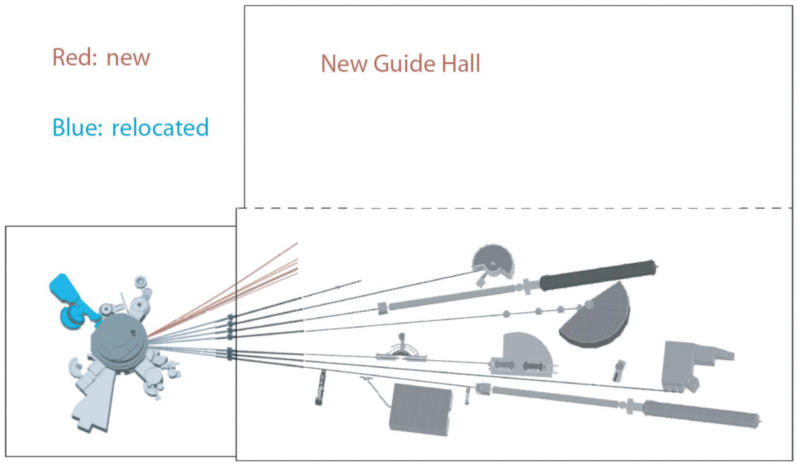

FIGURE 6: Expected facility configuration post outage, early 2012.

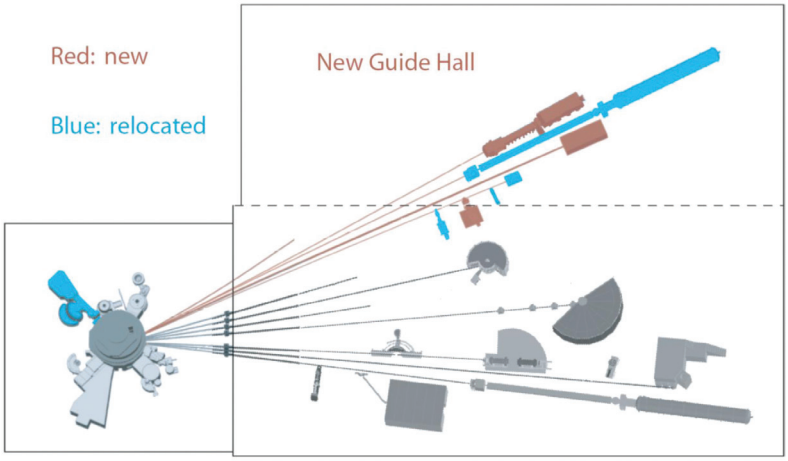

FIGURE 7: Expected Facility configuration at the end of the Expansion Initiative, late 2012.

Facility Development

Running in parallel with Expansion Initiative activities (ref. to pages containing the Expansion article) and construction of new instruments, is a continuous process of development and evolution of existing instrumentation, software, and sample environment equipment.

Instrument Development

The past year saw the Multi-Axis Crystal Spectrometer (MACS) enter the Facility's user program and staff have engaged in a number of activities designed to both enhance the performance and improve the reliability of this newly commissioned spectrometer. Installation of a new substrate for the air pad floor has reaped benefits of improved reproducibility and faster repositioning of the analyzer. Outfitting the twenty double-crystal analyzers with new drive trains and absolute multi-turn encoders has also resulted in increased precision of movement. And a new computer controlled pre-sample optics package now permits remote adjustment of beam size and attenuation.

First experiments using the TISANE time-resolved small angle scattering technique and equipment installed at the NG-7 SANS instrument have been performed this year (reference to tSANS article). The TISANE project, funded through the Center for High Resolution Neutron Scattering (CHRNS), permits dynamic studies of phenomena occurring on time scales of 50 μs to 150 μs by time-resolved stroboscopic SANS. In-house designed and built dedicated timing electronics and histogramming software have been used to initiate this program and comparisons of this system with the Wiedemann implementation (phase locked loop synchronized function generators) demonstrate the performance to be indistinguishable whilst offering a faster experiment setup is faster that it is less sensitive to drifts in chopper frequency.

A program to develop and commission new detector systems has been established to address the needs of the new instrument in the Expansion Initiative. The design of the Very Small Angle Neutron Scattering (vSANS) spectrometer calls for two types of detectors: a high resolution area detector typical of most instruments of this type and arrays of linear position sensitive tubes. A contract for the full complement of the latter has been awarded to GE Reuter Stokes, who will manufacture 8 panels of tube detectors based on a variant of the SNS EQ-SANS 8-pack design and electronics conforming to the SNS data acquisition standard. Testing and commissioning of the first of these panels is underway.

Motivated in equal parts by the ^{3}He shortage and spatial constraints, a detector system based on scintillator technologies is in design for the CANDoR white-beam reflectometer. A sliver of ^{6}LiF/ZnS(Ag) impregnated plastic will produce visible light when struck by neutrons. This light is then conducted via wavelength-shifting fibers to silicon photomultiplier devices (SiPMs), rather than conventional photomultiplier tubes. The SiPMs are compact, rugged, and inexpensive and have the useful characteristic that charge produced by a captured photon mimics the charge produced in neutron capture events in gas-filled detectors. Detectors so constructed can be very thin (≈ 1mm), permitting many more channels of crystal-analyzed neutron detection than a similar arrangement using conventional gas-filled pencil detectors. A prototype detector has been constructed and preliminary results are promising.

Instrument Control, Data Acquisition, and Software Development

The Instrument Control Environment (ICE) software system is now fully deployed on the SANS instruments in addition to the BT-7 and MACS spectrometers. Python scripting capability has now been introduced to increase the flexibility of ICE and enable scientists to

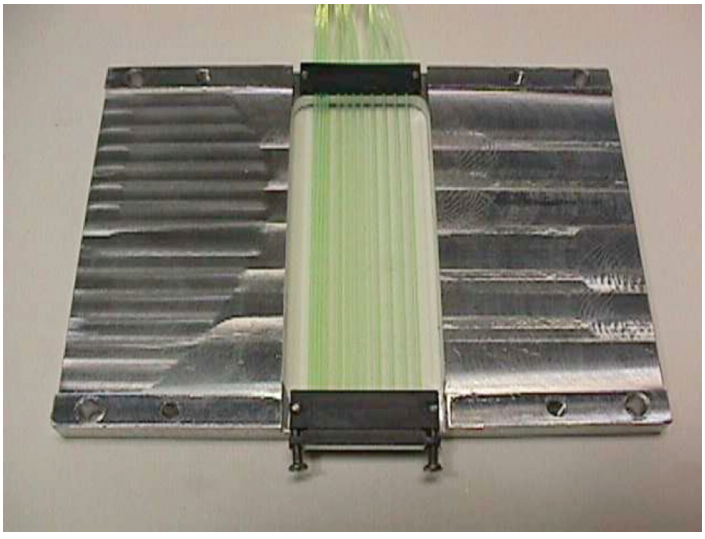

FIGURE 1: Prototype scintillator detector showing arrays of wavelength-shifting fibers set at various separations for test purposes.

customize the code particularly in cases of novel and developmental instrument setup and control scenarios. A code freeze will be implemented prior to the upcoming major facility outage to permit refactoring of ICE in preparation for its roll out on new instruments within the expansion initiative, and, ultimately, to new classes of instruments.

The NCNR raw data archive system has been revamped and expanded to include all instruments in the scattering suite. In addition to a highly available file server, the system has a searchable metadata catalogue which matches the raw data to the experiment responsible for its production. To promote better access of facility users to raw data, the archived data are mirrored to an externally facing web server (http://www.ncnr.nist.gov/ncnrdata). Users wishing to keep their experiment data private for the 18 month fair use period may opt out of the mirror process.

The user experience at the NCNR has also been improved by provision of a web application displaying live updates of the data being measured on each instrument. New data points are displayed automatically along with an estimate of completion time of the scan, based on the progress of each measurement, so that users can check remotely when their runs will be complete. The concept of live data on the web has also been extended to a prototype reduction suite for our triple axis spectrometers (TAS). This later project formed the core of a summer research project at NCNR for undergraduate and high school students. The reduction pipeline can include previous measurements such as background estimation scans so that the user can easily verify that the measurement is capturing the effects they expect. This project demonstrates the feasibility of creating rich web applications for data reduction, and other triple axis tools include an online UB matrix calculator and a resolution calculator.

Data Analysis Software Development

The Data Analysis and Visualization Environment (DAVE) project provides software solutions for a range of inelastic neutron scattering instruments at the NCNR and other facilities. It is widely used by scientists, particularly non-experts, to reduce, view and interpret their data. DAVE has been available for close to a decade and is now in its second major developmental phase that is based on the IDL iTool paradigm. This has resulted in improvements in many aspects of the application suite, especially with regards to usability and visualization functionality.

Many new capabilities were added during the past year. The most notable is data reduction and visualization support for MACS. Multiple datasets from MACS can now be read, corrected and readily viewed along constant planes in momentum and energy space as shown in the Figure below. Another new function included is the partial analysis of multiple triple-axis spectrometer datasets to identify and extract crystallographic reflections for subsequent use in other analysis programs such as FullProf. The FANS data reduction module has been overhauled using iTools hence incorporating benefits of the framework such as session management, better visualization, undo/redo functionality, indexed online help and much more. This will now serve as a prototypical iTool-based data reduction module in DAVE.

Full support and minor changes to existing functionality consume a good fraction of development time, typically in response to user feedback. Data reduction modules have evolved in tracking instrument upgrades and modifications and data analysis modules have been updated to include many new modeling functions. Work on Mslice focused on optimizing the algorithm used in manipulating multi-dimensional data and generating slices along a particular plane. The time taken to load and calculate projections of the data has been dramatically reduced, by up to a factor of x50, which is a significant and important gain particular for modern instrumentation capable of producing large data sets of the order of tens of gigabytes.

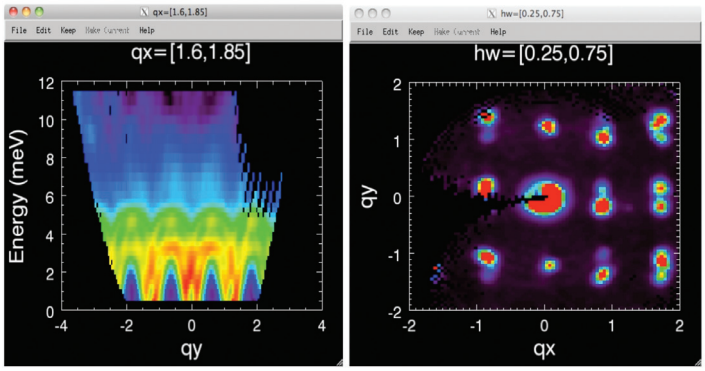

FIGURE 2: DAVE visualization of dispersion curves and continuum measured from an iron-based multiferroic compound on MACS.

Finally, IDL 8.0 was released recently with many language enhancements and upgrades to the iTool framework which will be of immediate benefit for DAVE. The intention is to release DAVE using IDL 8.0 in the near future and following an appropriate evaluation process.

The development of reflectometry analysis tools – REFLPAK - has continued over the past year with the emphasis on making techniques such as simultaneous fitting and direct inversion accessible to more users. New constrained optimizers are much more robust, allowing users to find better fits with to the model with less interaction with the program and new Markov chain Monte Carlo (MCMC) code incorporates a Bayesian approach to uncertainty analysis, allowing instrumental

effects to be properly reflected in the uncertainty of the fitted model. The resulting joint parameter probability function makes plain any hidden correlations in the model parameters. Also under development is general off-specular reflectometry modeling software to analyze data from MAGIk, the dedicated off-specular reflectometer instrument to be built as part of the Expansion Initiative, as well as the Liquids and Magnetic reflectometers at the SNS. As a first step, modeling of a substrate modified Born approximation including refraction effects has been implemented, and this will be extended to a more complete distorted wave Born approximation. This software can take advantage of modern graphics processors for fast calculation of arbitrary structures.

Sample Environment

NCNR personnel support a diverse range of sample environment equipment required for user research program. During the past year a number of new pieces of equipment have been acquired to support, in particular, the operational capacity and reliability of low-temperature operations. A non-magnetic dilution refrigerator provides sample temperatures down to 30 mK and is suitable for use on a number of instruments including DCS, Spin Echo, MACS, and all the triple-axis spectrometers. This new low-temperature capability complements the 11.5 Tesla superconducting magnet/dilution refrigerator, which was returned to service this year following repairs and refurbishment. Two new bottom-loading 4 K closed-cycle refrigerators (CCRs) were also added to the equipment roster. These new CCRs are fully compatible with existing tailsets and specialty vacuum cans, yet offer more sample space and a lower background signature. The NCNR received a new 10 Tesla cryogen-free magnet this year. Coupled with a cryogen-free 1.5 K insert that is currently on order, and optionally the non-magnetic dilution refrigerator received this year, this complete system will afford the researcher up to 10 Tesla and temperatures from 30 mK to 700 K in a completely "dry" system. NIST-developed safety venting mechanisms are currently being implemented across the top-loading CCRs and ILL orange cryostats to prevent the potentially explosive buildup of pressure possible below an ice blockage in the sample well.

A new SANS rheometer affords a much-needed upgrade to this popular choice, including new sample thickness and sample geometry options. The USANS instrument now has a new, dedicated refrigerated/heating circulator that operates from -40 ˚C to 200 ˚C and works in conjunction with a new multiple-position sample changer.

User demand for ^{3}He neutron spin filters (NSFs) continues to grow at a rapid rate. The NCNR's program to provide and develop NSFs is run in collaboration with the Physics Laboratory at NIST, and in the past year has serviced 30 user experiments totaling over 100 days of beam time.

Polarized beam experiments are routinely carried out on the thermal neutron triple-axis spectrometer BT-7, small-angle neutron scattering instruments, and reflectometers, along with preliminary commissioning experiments on MACS.

The user program is underpinned by a strong technical development program. Polarization of the NSFs is achieved by SEOP (spin-exchange optical pumping) and following a doubling of the laser power and modifications to the spectral narrowing scheme for each system the ^{3}He gas can now be polarized some 50 % faster. This improves significantly the time-averaged polarized neutronic performance of the cells and is particularly important for polarized beam experiments where the signal is low

There is a continued drive to develop user-friendly hardware and software to control ^{3}He NSFs that are readily incorporated into the instrument software. Programs to predict and monitor the polarized neutronic performance and flip the ^{3}He polarization during the user's experiment on each instrument have now been implemented. This represents the first steps toward full automation of flipping ^{3}He polarization, thus neutron polarization flipping, controlled by the instrument computer.

The performance of the filters continues to improve with notable advances in hardware for each instrument class. On BT-7, the relaxation time of the polarizer has been improved by an order of magnitude following the development of a new double-layer mu-metal end-compensated 'magic box' capable of providing a magnetic field of 3.9 mT - more than 3 times higher than the regular box. The high-field box makes the ^{3}He polarization decay less sensitive to the external stray field around the instrument and thus operation of polarized beam experiments much more reliable.

Development activity for SANS experiments has focused on a low-field magnetostatic cavity. In this case the aim once more is to provide a homogeneous field for maintaining the ^{3}He polarization, and one appropriate to cover the entire Q range of the instruments. This device has been tested offline and on NG-3 where it extends the Q range for loss-free neutron spins by at least a factor of two. The device will be ready for user experiments following implementation of the NMR based method for ^{3}He flipping. Envisaged is the integration of an *in-situ* spin-exchange optical pumping scheme into this device, improving further the polarized neutronic performance.

Finally, cells for reflectometry measurements now operate reliably with an initial flipping ratio of 50 % to 70 % and ^{3}He polarization relaxation of about 300 h. Therefore the time-averaged polarized neutronic performance over a two day period is comparable to that predicted for *in-situ* SEOP operation.

Serving the Science and Technology Community

The mission of the NIST Center for Neutron Research is to assure the availability of neutron measurement capabilities to meet the needs of U.S. researchers from industry, academia and from other U.S. government agencies. To carry out this mission, the NCNR uses several different mechanisms to work with participants from outside NIST, including a competitive proposal process, instrument partnerships, and collaborative research with NIST.

Proposal System

Most of the time on NCNR instruments is made available through a competitive, peer-review proposal process. The NCNR issues calls for proposals approximately twice a year. Proposals are reviewed at several different levels. First, expert external referees evaluate each proposal on merit and provide us with written comments and ratings. This is a very thorough process where several different referees review each proposal. Second, the proposals are evaluated on technical feasibility and safety by NCNR staff. Third, we convene our Beam Time Allocation Committee (BTAC) to assess the reviews and to allocate the available instrument time. Using the results of the external peer review and their own judgment, the BTAC makes recommendations to the NCNR Director on the amount of beam time to allocate to each approved experiment. Approved experiments are scheduled by NCNR staff members in consultation with the experimenters.

The current BTAC members are:

- Andrew Allen (NIST Ceramics Division)
- Jeffrey Allen (Michigan Technological University)
- Collin Broholm (Johns Hopkins University)
- Leslie Butler (Louisiana State University)
- Kalina Hristova (Johns Hopkins University)
- Ramanan Krishnamoorti (University of Houston)
- Valery Kiryukhin (Rutgers University)
- Raul Lobo (University of Delaware)
- Lee Magid (University of Tennessee, Knoxville)
- Janna Maranas (The Pennsylvania State University)
- Alan Nakatani (Rohm and Haas Company)
- Stephan Rosenkranz (Argonne National Laboratory)
- Lynn Walker (Carnegie-Mellon University)

Partnerships

The NCNR may form partnerships with other institutions to fund the development and operation of selected instruments. These partnerships, or "Participating Research Teams", may have access to as much as 75 % of the available beam time on the instrument depending on the share of total costs borne by the team. A minimum of 25 % of the available beam time is always made available through the NCNR proposal program to all users. Partnerships are negotiated for a fixed period (usually three years) and may be renewed if there is mutual interest and a continued need. These partnerships have proven to be an important and effective way to expand the research community's access to NCNR capabilities and have been very successful in developing new instruments.

Collaboration with Nist

Some time on all instruments is available to NIST staff in support of our mission. This time is used to work on NIST research needs, instrument development, and promoting the widespread use of neutron measurements in important research areas, particularly by new users. As a result of these objectives, a significant fraction of the time available to NIST staff is used collaboratively by external users, who often take the lead in the research. Access through such collaborations is managed through written beam time *requests*. In contrast to proposals, beam time requests are reviewed and approved internally by NCNR staff. We encourage users interested in exploring collaborative research opportunities to contact an appropriate NCNR staff member.

Research Participation at the NCNR

The NCNR continued its strong record of serving the U.S. research community this year. Over the 2010 fiscal year, 2290 research participants benefited from use of the NCNR. (Research participants include users who come to the NCNR to use the facility as well as active collaborators, including co-proposers of approved experiments, and co-authors of publications resulting from work performed at the NCNR.) Research participants represented 223 external institutions, including 146 U.S. universities, 32 national laboratories, and 45 U.S. industries. The NCNR is a national facility, with participants from 42 states, DC, and Puerto Rico.

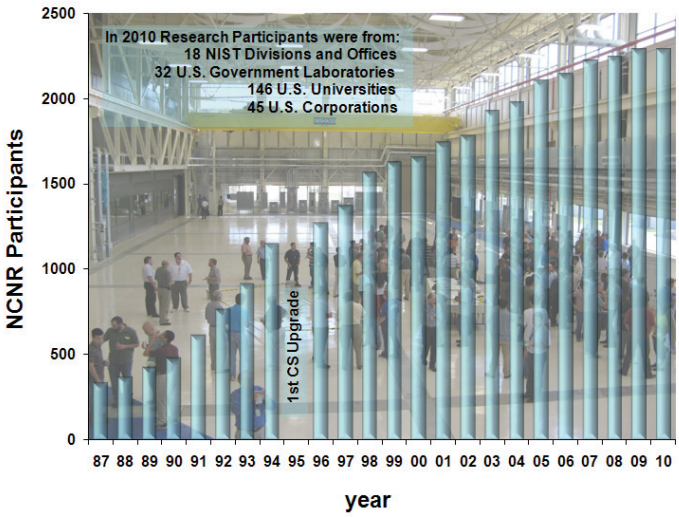

FIGURE 1: Research participants at the NCNR 1986-2010

2010 NCNR Proposal Program

Two calls in the past year resulted in the submission of 745 proposals, a record number, of which 392 were approved and received beam time. The oversubscription, i.e., the ratio of days requested on all proposals to the days available, was 2.5

on the average, but as high as 6 for specific instruments in one call. Proposal demand has grown constantly since the NCNR first began accepting proposals in 1991, and has doubled in the past eight years. The following table shows the data for several instrument classes.

Instrument class	Proposals	Days requested	Days allocated
SANS and USANS	255	947	406
Reflectometers	108	767	364
Spectrometers	334	2327	805
Diffraction	20	99	47
Imaging	28	134	61
Total	745	4269	1683

User Group Holds Third Election

The NCNR Users Group (NUG) provides an independent forum for all facility users to raise issues to NCNR management, working through its executive officers to carry out this function. In December 2009, the NUG conducted its third online election of officers, a process scheduled every other year The newly elected NUG Executive Committee members are Despina Louca (University of Virginia), Dale Schaefer (University of Cincinnati), John Katsaras (Oak Ridge National Laboratory), and Erik Watkins (University of California, Davis). Three members remain in office for two more years. They are Mark Dadmun (University of Tennessee, chair), Michel Kenzelmann (Paul Scherrer Institute, Switzerland), and Lynn Walker (Carnegie-Mellon University). In late 2010, the NUG will conduct a comprehensive survey of user satisfaction and concerns, addressing areas such as support from NCNR staff, proposal review, sample environments, instrument hardware and software, data analysis, and user laboratories.

Panel of Assessment

The major organizational components of NIST are evaluated periodically for quality and effectiveness by the National Research Council (NRC), the principal operating agency of both the National Academy of Sciences and the National Academy of Engineering. A panel appointed by the NRC reported on the NIST Center of Neutron Research in January 2009. Their findings are summarized in a document that may be viewed online at http://www.nap.edu/openbook.php?record_id=12765&page=R1.

The panel members included Tonya Kuhl of the University of California, Davis (chair), Frank Bates, University of Minnesota, C. W. (Paul) Chu, University of Houston, Donald Engelmann, Yale University, Christopher Gould, North Carolina State University, Alexander Grosberg, New York University, Russell Hemley, Carnegie Institution of Washington, Herbert Mook, Oak Ridge National Laboratory, Sunil Sinha, University of California, San Diego, and Barbara Wyslouzil, the Ohio State University.

The Center for High Resolution Neutron Scattering (CHRNS)

The CHRNS is a national user facility that is jointly funded by the National Science Foundation and the NCNR. Its primary goal is to maximize access to state-of-the-art neutron scattering instrumentation for the research community. It operates six neutron spectrometers and diffractometers at the NCNR, enabling users from around the nation and the world to observe dynamical phenomena involving energies from ≈ 30 neV to ≈ 100 meV, and to obtain structural information on length scales from 1 nm to ≈ 10 μm. A more detailed account of CHRNS activities may be found on pp 60-62 of this report.

Partnerships for Specific Instruments

NG-7 SANS Consortium

A consortium that includes NIST, the Industrial Partnership for Research in Interfacial and Materials Engineering (IPRIME) led by the University of Minnesota, and the ExxonMobil Research and Engineering Company, operates, maintains, and conducts research at the NG-7 30 m SANS instrument. The consortium uses 65 % of the beam time on this instrument, with the remaining 35 % allocated to the general scientific community through the NCNR's proposal system. Consortium members conduct independent research programs primarily in the area of large-scale structure in soft matter. For example, ExxonMobil has used this instrument to deepen their understanding of the underlying nature of ExxonMobil's products and processes, especially in the fields of polymers, complex fluids, and petroleum mixtures.

NIST / General Motors – Neutron Imaging

An ongoing partnership and collaboration between General Motors and NIST has resulted in an exciting use of neutron imaging to visualize the operation of fuel cells and lithium-ion batteries for automotive vehicle applications. Neutron imaging is an ideal method for visualizing both hydrogen and lithium, the fuel of electric vehicles engines. With a newly developed 10 μm spatial resolution detector, studies of the transport phenomena from the anode to the cathode in fuel cells and batteries have been conducted. These unique, fundamental measurements, provide valuable material characterizations that will help improve the performance, increase the reliability, and reduce the time to market introduction of the next generation electric car engines.

Interagency Collaborations

The Smithsonian Institution's Nuclear Laboratory for Archeological Research is part of the Anthropology Department at the National Museum of Natural History. It has had a productive 32 year partnership with the NCNR, during which time it has chemically analyzed over 41 000 archaeological artifacts by Instrumental Neutron Activation Analysis (INAA), drawing extensively on the collections of the Smithsonian, as well as on those of many other institutions in this country and abroad. Such chemical analyses provide a means of linking these diverse collections together in order to study continuity and change involved in the production of ceramic and other artifacts.

The Center for Food Safety and Applied Nutrition, U.S. Food and Drug Administration (FDA), directs and maintains a multi-laboratory facility at the NCNR that provides agency-wide analytical support for food safety and food defense programs. Neutron activation (instrumental, neutron-capture prompt-gamma, and radiochemical), x-ray fluorescence spectrometry, and low-level gamma-ray detection techniques provide diverse multi-element and radiological information about foods and related materials. Ongoing work includes studies of cryogenic homogenization of foods, preparation of an in-house swordfish reference material, improved detection capabilities for toxic and nutritional elements in foods, and rapid screening of food products for dangerous levels of cadmium, lead, and mercury in beverages and residual bromine in baked goods. Recent studies include the investigation of possible procedural losses from foods of several elements, including mercury, bromine, and selenium.

The Center for High Resolution Neutron Scattering (CHRNS)

The Center for High Resolution Neutron Scattering (CHRNS) is a national user facility that is jointly funded by the National Science Foundation through its Division of Materials Research (grant numbers DMR-0454672 and DMR-0944772), and by the NCNR. The primary purpose of this partnership is to maximize access to state-of-the-art neutron scattering instrumentation for the research community using the NCNR's proposal system. Proposals to use the CHRNS instruments are critically reviewed on the basis of scientific merit and/or technological importance.

The core mission of CHRNS is fourfold: (i) to develop and operate neutron scattering instrumentation, with broad application in materials research, for use by the general scientific community; (ii) to promote the effective use of the CHRNS instruments by having an identifiable staff whose primary function is to assist users; (iii) to conduct research that advances the capabilities and utilization of CHRNS facilities; and (iv) to contribute to the development of human resources through educational and outreach efforts.

Scattering Instruments and Research

CHRNS supports operation of the 30-meter Small Angle Neutron Scattering (SANS) instrument, the Ultra-Small Angle Neutron Scattering (USANS) instrument, the Spin-Polarized Inelastic Neutron Scattering (SPINS) spectrometer, the Multi-Angle Crystal Spectrometer (MACS), the Disk Chopper Spectrometer (DCS), the High Flux Backscattering Spectrometer (HFBS), and the Neutron Spin-Echo (NSE) spectrometer.

The small angle scattering instruments supported by CHRNS provide structural information over length scales from ≈ 1 nm to ≈ 10 μm. The spectrometers collectively yield dynamical information over time scales from ≈ $3x10^{-14}$ s to ≈ 10^{-7} s (energy scales from ≈ 100 meV to ≈ 30 neV). These wide ranges of accessible distances and times support a very diverse scientific program, allowing researchers in materials science, chemistry, biology, and condensed matter physics to investigate materials such as polymers, metals, ceramics, magnetic materials, porous media, fluids and gels, and biological molecules.

In the most recent Call for Proposals (call 26), 227 of the 391 proposals received were for the six CHRNS-operated instruments. There were also 14 proposals for MACS. Of the 227 proposals, 122 received awarded beam time (as well as 7 for MACS). Of the 1262 days requested, the Beam Time Allocation Committee approved 537. Roughly half of the users of neutron scattering techniques at the NCNR use CHRNS-funded instruments, and more than one third of NCNR publications (see the "Publications" section on p. 65) over the current one-year period are based on

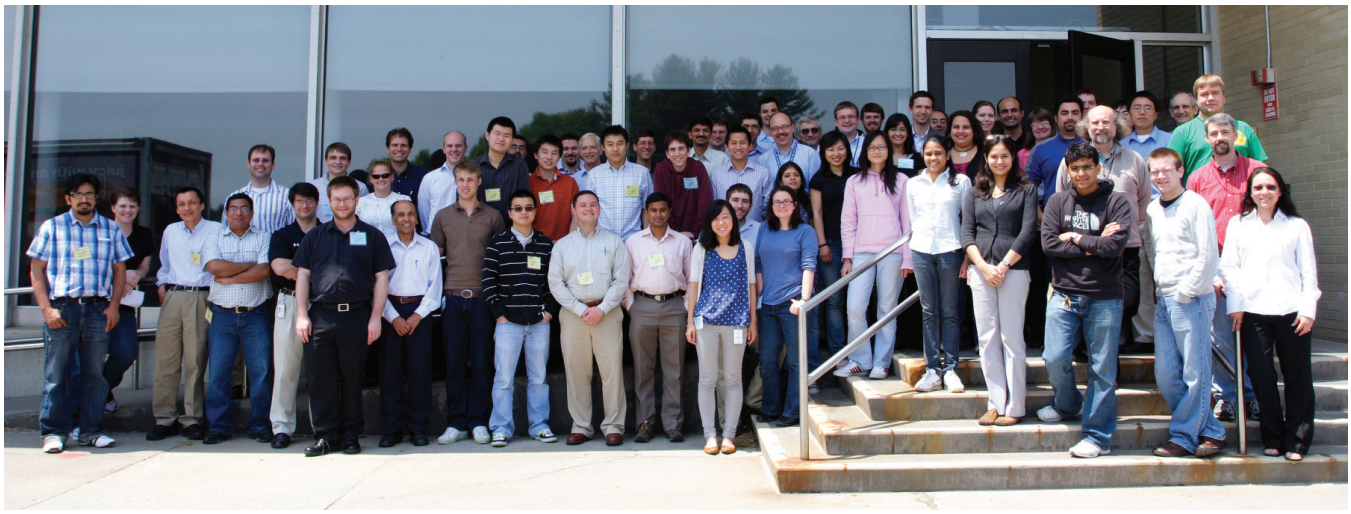

FIGURE 1: NCNR 2010 Summer School participants

FIGURE 2: The 2010 SURF students, NCNR advisors, and other staff

research performed using these instruments. In 2009 more than 25 Ph.D. theses were completed using results from CHRNS-sponsored instruments.

Scientific Support Services

An important ingredient of the CHRNS operation is its support of staff whose responsibility is to provide services that are essential to the success of neutron scattering investigations. One such service is the provision and operation of an expanding range of sample environment equipment. The sample environment team often takes on projects to expand the range of existing equipment, enhance its safety, improve its reliability, and even develop entirely new capabilities. For example, a new ten Tesla magnet and a new dilution refrigerator were added to our suite of equipment.

Other services include the maintenance of several well-equipped user laboratories, and the development, documentation and maintenance of data reduction, visualization, and analysis software through the DAVE project; DAVE is a suite of programs that enables users to rapidly reduce, examine and display their experimental data. It may be downloaded free of charge from the website http://www.ncnr.nist.gov/dave/, either as a binary executable with an embedded runtime license or as the complete source code.

A major addition to DAVE over the past year has been data reduction and visualization support for the new Multi-Axis Crystal Spectrometer (MACS). This provides users with a useful and easy way of decomposing the large and intricate data generated by the instrument.

Education and Outreach

One of the missions of the CHRNS program is to contribute to the development of human resources through education and outreach, thereby fostering future generations of scientists and neutron scatterers.

This was the 16th annual CHRNS sponsored neutron scattering summer school. The 2010 school, devoted to small angle neutron scattering and neutron reflectometry, attracted 90 applicants for the 36 available places. The CHRNS summer schools are very effective in educating potential new users of neutron scattering as more than 70 % of the participants return to the NCNR for their own research. Course materials have been placed on the Web at http://www.ncnr.nist.gov/programs/CHRNS/outreach_ssmaterials.html.

We also offered a series of tutorial demonstrations based on the experiments and lectures presented at the 2009 Summer School on Neutron Spectroscopy. Ten participants, from US universities and from six NIST divisions other than the NCNR, attended the tutorials. Tutorial course materials may be found on the Web, at http://www.ncnr.nist.gov/programs/CHRNS/outreach_tutorialmaterials.html.


FIGURE 3: Middle school science teachers and NCNR/CHRNS staff

FIGURE 4: Participants and NCNR/CHRNS staff at the HFBS/DCS tutorial

This was the fourth year that NIST organized a "Summer Institute" for middle school science teachers. This year we had twenty-one teachers from three Maryland counties, and from the state of Florida. They toured the NCNR and attended lectures and demonstrations that described how neutrons are used to probe matter. They were also provided the opportunity to interact with facility users, SURF students and the scientific staff. The neutron scattering component of the Summer Institute gave teachers a greater appreciation of what can be accomplished using neutron scattering.

CHRNS once again participated in NIST's Summer Undergraduate Research Fellowship (SURF) program, hosting seven undergraduate students who worked with staff members studying topics such as frustrated magnetism, magnetic recording materials, superconductors, and data analysis software development. The students enthusiastically agreed that their summer research experiences were productive and worthwhile, and their advisors benefited from their efforts, expanding their understanding of the scientific process.

Other education and outreach activities included "Bring your Kids to Work Day", and tours for middle school and high school students. During the "Bring your Kids to Work Day", held every year in the month of April, NIST opens its doors to more than 250 students ranging from 6th through 12th grades. Within this site-wide yearly program, the NCNR prepares tours of the facility, lectures and demonstrations specially designed for middle school age children on how neutrons are used to probe matter.

This year the NCNR participated in the new NIST Summer High School Internship Program, known as the SHIP. Four students from Montgomery County Schools participated in the program. Alex Yee and Ophir Lifshitz, advised by William Ratcliff worked on a project called WRED: Data fitting and calculation in a web-based environment. Pavan Bhargava and his advisor Joseph Dura worked on the production of novel Nafion thin films for the development of lipid bilayers. Jonathan Shear, with advisor Efrain Rodriguez, worked on Neutron Studies of Magnetism and the Crystal Structure of Chromium Tellurides and their Potential for Magnetic Refrigeration.

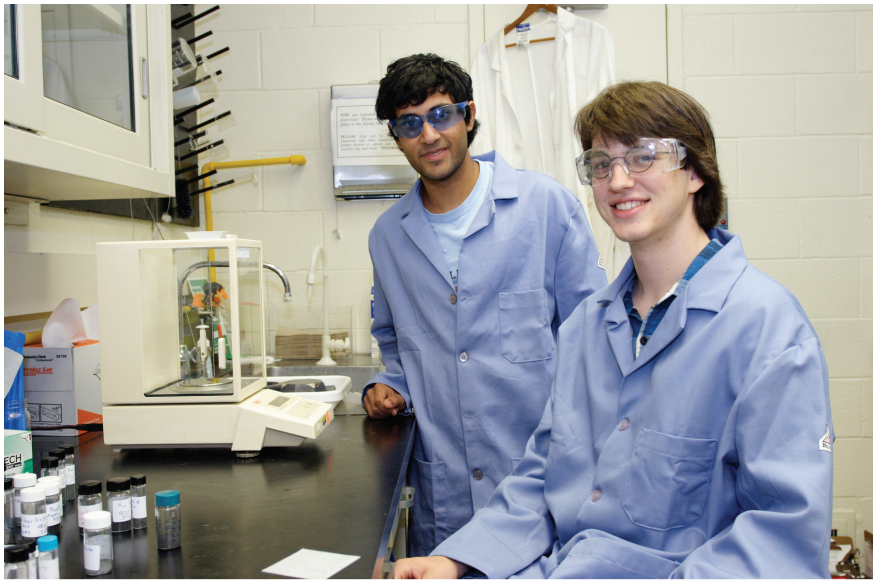

FIGURE 5: left to right: Vikas Bhatia (SURF) and Jonathan Schear (SHIP)

Awards 2010

Turkish president Abdullah Gül awards **Taner Yildirim** (right) of the NCNR the **Special Award** for 2009 from **Tubitak**, the Scientific and Technological Research Council of Turkey. The award is reserved for Turkish scientists working abroad, and is **among Turkey's highest awards for scientific achievement.**

Collin Broholm of Johns Hopkins University and the NCNR has been awarded the **NSSA Sustained Research Prize by the Neutron Scattering Society of America** (NSSA) for *"outstanding neutron scattering studies of correlated electron physics in magnets, metals and superconductors, and for science-driven development ofneutron scattering techniques"*. Broholm was also selected as a Fellow by the NSSA for *"outstanding neutron scattering studies of correlated electron physics in magnets, metals and superconductors, and for science-driven development of neutron scattering techniques."*

Craig Brown of the NCNR has been awarded the **2010 Science Prize** by the **Neutron Scattering Society of America** for *"For outstanding neutron scattering studies of hydrogen-framework interactions in metal-organic frameworks."*

Jeff Lynn of the NCNR has been selected as a **Fellow** by the **Neutron Scattering Society of America** for *"seminal studies of the colossal magneto- resistance effect and his many contributions to our understanding of the interplay of magnetism and superconductivity."*

Chuck Majkrzak of the NCNR has been selected as a **Fellow** by the **Neutron Scattering Society of America** for *"fundamental contributions to the development of neutron reflectivity."*

Dan Neumann of the NCNR has been selected as a **Fellow by the Neutron Scattering Society of America** for *"outstanding research using inelastic and quasielastic neutron scattering on carbon containing and other diverse materials and exceptional leadership in serving and expanding the American neutron community."*

Wen-Li Wu of the NIST Polymers Division has been selected as a **Fellow** by the **Neutron Scattering Society of America** for *"important contributions to a broad range of problems in polymer science and in its industrial application using neutron scattering.*

Tom Gentile of the Ionizing Radiation Division at the NCNR has been appointed **Fellow** of the **American Physical Society** *"For his extensive contributions to diverse precision measurements, particularly in the development of neutron spin filters using polarized 3He and in the application of polarized 3He to precision measurements in neutron science."*

NCNR's **William Ratcliff** was named a **Minority Research Trailblazer** for his work on frustrated magnetic systems and was recognized at the 24th annual **BEYA Science, Technology, Engineering, and Math Global Competitiveness Conference.**

William Kamitakahara of the NCNR was given the NIST **Colleague's Choice Award for "***creating and designing the NCNR proposal system, which is the backbone of the scientific operations of the NCNR and is broadly hailed by the user community as among the best…in the world."*

Muhammad Arif and **David Jacobson** the Ionizing Radiation Division at the NCNR were awarded the **DOC Gold Medal** for scientific/engineering achievement in *"developing the world's most advanced neutron imaging station and for applying cutting-edge neutron tomography techniques to study water transport in hydrogen fuel cells."*

Qingzhen Huang of the NCNR was awarded the **DOC Silver Medal** for scientific/engineering achievement. He is recognized for *"his pioneering use of neutron diffraction to reveal key relationships between the bulk magnetic and structural properties that led directly to the development of an entirely new class of magnetocaloric materials which exhibit superior performance."*

Yiming Qiu of the NCNR is the recipient of the **2010 Award for Scientific Support** by the NIST chapter of **Sigma Xi.** As an instrument scientist for the Disk Chopper Spectrometer, Dr. Qiu assists visiting scientists in all aspects of their experiments, from proposal writing through planning, execution, and interpretation, to write-up for publication. Yiming is an internationally recognized expert in the application of neutron scattering techniques to condensed matter physics.

Juscelino Leão of the NCNR was awarded the **DOC Bronze Medal** for *"his development of new pressure cells which enable NCNR facility users to study samples under hydrostatic pressures as high as 1 GPa and at temperatures between 1.1 K and 400 K."*

Muhammad Arif, Patrick Hughes, Alan K. Thompson of the Ionizing Radiation Division at the NCNR along with Charles W. Clark and Robert E. Vest of the Physics Division were awarded the **DOC Bronze Medal** for developing a novel approach for *"detecting neutrons using Lyman alpha light produced by the hydrogen atoms generated in the absorption of neutrons by helium-3."*

Andrew Allen of the MSEL was awarded the **DOC Bronze Medal** for his *"exceptional leadership in the design, assembly, testing, and commissioning of a best-in-the-world ultra-small-angle x-ray scattering instrument"*. Allen has also often used small angle neutron scattering facilities at the NCNR.

Kathryn Krycka of the NCNR was selected by the NIST chapter of **Sigma Xi** for a **2010 outstanding poster award** for her presentation: *"Core-Shell Magnetic Morphology within Fe_3O_4 Nanoparticles."*

Chris Metting of the University of Md and the NCNR took 2nd place in the **ACNS Poster Competition** for his poster entitled *"Characterization and modeling of off-specular neutron scattering for analysis of two dimensional ordered structures"* at the **2010 American Conference on Neutron Scattering.**

Ping-Yen Hsieh of the University of Md and the NCNR took 3rd place in the **ACNS Poster Competition** for his poster entitled *"The gas adsorption behaviors in chiral holmium metal-organic framework materials"* at the **2010 American Conference on Neutron Scattering.**

Wendy Queen of the NCNR was selected for an **Outstanding Graduate Researcher Award** by the Dept. of Chemistry at **Clemson University** upon receiving her Ph.D.

Herb Mook of Oak Ridge National Laboratory and a user at the NCNR has been awarded the **Clifford G. Shull Prize** by the **Neutron Scattering Society of America** for *"outstanding contributions to the study of magnetism, superconductivity, and quantum phenomena in matter with neutrons."*

Professor **Sang Wook Cheong** of Rutgers University was awarded the American Physical Society's **James C. McGroddy Prize** for New Materials by *"For groundbreaking contributions in theory and experiment that have advanced the understanding and utility of multiferroic oxides."* Cheong's group has collaborated with NCNR workers on measurements of $BiFeO_3$ at the BT-9 and BT-7 spectrometers.

Caltech Professor **Brent Fultz** was given the Minerals, Metals and Materials Society's Electronic, Magnetic & Photonic Materials Division **Distinguished Scientist/Engineer** award *"For his outstanding contribution to fundamental understanding of thermodynamics in materials using inelastic neutron scattering."* Fultz' group has conducted work at the NCNR.

David J. Lohse of ExxonMobil along with Nikos Hadjichristidis of the University of Athens, Greece, were selected by the Division of Polymer Materials of the American Chemical Society for the **2010 Cooperative Research Award in Polymer Science and Engineering** sponsored by the Eastman Kodak Company. Dr. Lohse's work has included use of the NG-7 SANS instrument at the NCNR.

Stony Brook University graduate student **Jinsheng Wen** has been named a winner of the 2009 **Chinese Government Award for Outstanding Self-Financed Students Studying Abroad.** Wen has conducted many of his neutron measurements on superconductors at the NCNR.

Publications: August 1, 2009 to July 31, 2010

Abdurashitov, J.N., Gavrin, V.N., Gorbachev, V.V., Gurkina, P.P., Ibragimova, T.V., Kalikhov, A.V., Khairnasov, N.G., Knodel, T.V., Mirmov, I.N., Shikhin, A.A., Veretenkin, E.P., Yants, V.E., Zatsepin, G.T., Bowles, T.J., Elliott, S.R., Teasdale, W.A., Nico, J.S., Cleveland, B.T., Wilkerson, J.F., "Measurement of the Solar Neutrino Capture Rate with Gallium Metal. III. Results for the 2002-2007 Data-taking Period," Phys. Rev. C **80**(1), 015807-1 (2009).

Adriano, C., Giles, C., Bittar, E.M., Coelho, L.N., de Bergevin, F., Mazzoli, C., Paolasini, L., Ratcliff, W., Bindel, R., Lynn, J.W., Fisk, Z., Pagliuso, P.G., "Cd Doping Effects in the Heavy-Fermion Compounds Ce_2MIn_8 (M=Rh and Ir)," Phys. Rev. B **81**(24), 245115-1 (2010).

Ainalem, M.-L., Kristen, N., Edler, K.J., Höök, F., Sparr, E., Nylander, T., "DNA Binding to Zwitterionic Model Membranes," Langmuir **26**(7), 4965 (2010).

Ainalem, M.-L, Campbell, R.A., Nylander, T., "Interactions between DNA and Poly(amido amine) Dendrimers on Silica Surfaces," Langmuir **26**(11), 8625 (2010).

Akgun, B., Uğur, G., Brittain, W.J., Majkrzak, C.F., Li, X., Wang, J., Li, H., Wu, D.T., Wang, Q., Foster, M.D., "Internal Structure of Ultrathin Diblock Copolymer Brushes," Macromol. **42**, 8411 (2009).

Alsmadi, A.M., Alyones, S., Mielke, C.H., McDonald, R.D., Zapf, V., Altarawneh, M.M., Lacerda, A., Chang, S., Adak, S., Kothapalli, K., Nakotte, H., "Complex Conductivity of U*TX* Compounds in High Magnetic Fields," J. Appl. Phys. **105**(7), 07E108-1 (2009).

Alsmadi, A.M., Alyones, S., Mielke, C.H., McDonald, R.D., Zapf, V., Altarawneh, M.M., Lacerda, A., Chang, S., Adak, S., Kothapalli, K., Nakotte, H., "Radio-Frequency Measurements of UNiX Compounds (X = Al, Ga, Ge) in High Magnetic Fields," J. Magn. Magn. Mater. **321**(22), 3712 (2009).

Altunbas, A., Sharma, N., Lamm, M.S., Yan, C., Nagarkar, R.P., Schneider, J.P., Pochan, D.J., "Peptide-Silica Hybrid Networks: Biomimetic Control of Network Mechanical Behavior," ACS Nano **4**(1), 181 (2010).

Anderson, D.L., "Analysis of Beverages for Hg, As, Pb, and Cd with a Field Portable X-Ray Fluorescence Analyzer," J. AOAC Int. **93**(2), 683 (2010).

Anderson, D.L., "Analytical Capabilities of Anticoincidence INAA for Biological Materials," J. Radioanal. Nucl. Chem. **282**, 75 (2009).

Anderson, D.L., "Screening of Foods and Related Products for Toxic Elements with a Portable X-Ray Tube Analyzer," J. Radioanal. Nucl. Chem. **282**(2), 415 (2009).

Anderson, D.L., "Use of L-Cysteine for Minimization of Inorganic Hg Loss during Thermal Neutron Irradiation," J. Radioanal. Nucl. Chem. **282**(1), 11 (2009).

Anovitz, L.M., Lynn, G.W., Cole, D.R., Rother, G., Allard, L.F., Hamilton, W.A., Porcar, L., Kim, M.-H., "A New Approach to Quantification of Metamorphism using Ultra-Small and Small Angle Neutron Scattering," Geochim. Cosmochim. Acta. **73**, 7303 (2009). **[CHRNS]**

Argyriou, D.N., Hiess, A., Akbari, A., Eremin, I., Korshunov, M.M., Hu, J., Qian, B., Mao, Z., Qiu, Y., Broholm, C., Bao, W., "Incommensurate Itinerant Antiferromagnetic Excitations and Spin Resonance in the $FeTe_{0.6}Se_{0.4}$ Superconductor," Phys. Rev. B **81**(22), 220503-1 (2010).

Ashkar, R., Stonaha, P., Washington, A.L., Shah, V.R., Fitzsimmons, M.R., Maranville, B., Majkrzak, C.F., Lee, W.T., Schaich, W.L., Pynn, R., "Dynamical Theory Calculations of Spin-Echo Resolved Grazing-Incidence Scattering from a Diffraction Grating," J. Appl. Crystallogr. **43**, 455 (2010).

Azuah, R.T., Kneller, L.R., Qiu, Y., Tregenna-Piggott, P.L.W., Brown, C.M., Copley, J.R.D., Dimeo, R.M., "DAVE: A Comprehensive Software Suite for the Reduction, Visualization, and Analysis of Low Energy Neutron Spectroscopic Data," J. Res. Natl. Inst. Stand. Technol. **114**(6), 341 (2009). **[CHRNS]**

Babcock, E., Boag, S., Becker, M., Chen, W.C., Chupp, T.E., Gentile, T.R., Jones, G.L., Petukhov, A.K., Soldner, T., Walker, T.G., "Effects of High-Flux Neutron Beams on ^{3}He Cells Polarized *in situ* with Spin-Exchange Optical Pumping," Phys. Rev. A **80**(3), 033414-1 (2009).

Babcock, E., Boag, S., Andersen, K.H., Becker, M., Beecham, C., Bordenave, F., Chastagnier, J., Chen, W.C., Chung, R., Chupp, T.E., Elmore, S., Fouilloux, P., Gentile, T.R., Jullien, D., Lelievre-Berna, E., Mouveau, P., Petoukhov, A., Revert, M., Soldner, T., "In-Situ SEOP Polarizer and Initial Tests on a High Flux Neutron Beam," Physica B **404**, 2655 (2009).

Barbour, A.M., Telling, M.T.F., Larese, J.Z., "Investigation of the Behavior of Ethylene Molecular Films Using High Resolution Adsorption Isotherms and Neutron Scattering," Langmuir **26**(11), 8113 (2010). **[CHRNS]**

Bass, C.D., Bass, T.D., Heckel, B.R., Huffer, C.R., Luo, D., Markoff, D.M., Micherdzinksa, A.M., Snow, W.M., Swanson, H.E., Walbridge, S.C., "A Liquid Helium Target System for a Measurement of Parity Violation in Neutron Spin Rotation," Nucl. Instrum. Meth. A **612**, 69 (2009).

Bay, D.C., Budiman, R.A., Nieh, M.-P., Turner, R.J., "Multimeric Forms of the Small Multidrug Resistance Protein EmrE in Anionic Detergent," Biochim. Biophys. Acta. **1798**, 526 (2010).

Beekman, M., Stefanoski, S., Wong-Ng, W., Kaduk, J.A., Huang, Q., Reeg, C., Bowers, C.R., Nolas, G.S., "Structure and Thermal Conductivity of $Na_{1-x}Ge_{3+z}$," J. Solid State Chem. **183**, 1272 (2010).

Ben, T., Ren, H., Ma, S., Cao, D., Lan, J., Jing, X., Wang, W., Xu, J., Deng, F., Simmons, J.M., Qiu, S., Zhu, G., "Targeted Synthesis of a Porous Aromatic Framework with High Stability and Exceptionally High Surface Area," Angew. Chem. Int. Edit. **48**, 9457 (2009).

Bhattacharya, S., Dai, Z., Li, J., Baxter, S., Callaway, D.J.E., Cowburn, D., Bu, Z., "A Conformational Switch in the Scaffolding Protein NHERF1 Controls Autoinhibition and Complex Formation," J. Biol. Chem. **285**(13), 9981 (2010).

Boag, S., Babcock, E., Andersen, K.H., Becker, M., Charlton, T.R., Chen, W.C., Dalgliesh, R.M., Elmore, S.D., Frost, C.D., Gentile, T.R., Lopez Anton, R., Parnell, S.R., Petoukhov, A.K., Skoda, M.W.A., Soldner, T., "In Situ SEOP Polarised ^{3}He Neutron Spin Filter for Incident Beam Polarisation and Polarisation Analysis on Neutron Scattering Instruments," Physica B **404**, 2659 (2009).

Bode, P., Greenberg, R.R., De Nadai F., Elisabete A., "Neutron Activation Analysis: A Primary (Ratio) Method to Determine Si-Traceable Values of Element Content in Complex Samples," CHIMA **63**(10), 678 (2009).

Boggara, M.B., Krishnamoorti, R., "Small-Angle Neutron Scattering Studies of Phospholipid-NSAID Adducts," Langmuir **26**(8), 5734 (2010).

Boggara, M.B., Faraone, A., Krishnamoorti, R., "Effect of pH and Ibuprofen on Phospholipid Bilayer Bending Modulus," J. Phys. Chem. B **114**, 8061 (2010). **[CHRNS]**

Boland, E.K., Liu, J., Maranas, J.K., "A Molecular Picture of Motion in Polyolefins," J. Chem. Phys. **132**(14), 144901-1 (2010). **[CHRNS]**

Borgmeyer, B., Wilson, C., Winholtz, R.A., Ma, H.B., Jacobson, D., Hussey, D., "Heat Transport Capability and Fluid Flow Neutron Radiography of Three-Dimensional Oscillating Heat Pipes," J. Heat Transfer **132**, 061502-1 (2010).

Bridges, C.A., Krishnamurthy, V.V., Poulton, S., Paranthaman, M.P., Sales, B.C., Myers, C., Bobev, S., "Magnetic Order in $CaMn_2Sb_2$ Studied via Powder Neutron Diffraction," J. Magn. Magn. Mater. **321**(22), 3653 (2009).

Brown, C.M., Sumida, K., Long, J.R., "Understanding Physisorbed Hydrogen Systems Using Neutrons," in "ACS Division Proceedings, Division of Fuel Chemistry," edited by unknown, (ACS, Fall National Meeting & Exposition 2009 Conf. Proc., August 2009, Washington, D.C.) **54**(2), (2009).

Caba, B.L., Zhang, Q., Carroll, M.R.J., Woodward, R.C., St. Pierre, T.G., Gilbert, E.P., Riffle, J.S., Davis, R.M., "Nanostructure of PEO-polyurethane-PEO Triblock Copolymer Micelles in Water," J. Colloid Interface Sci. **344**, 81 (2010).

Cabassi, R., Bolzoni, F., Gilioli, E., Bissoli, F., Prodi, A., Gauzzi, A., "Jahn-Teller-Induced Crossover of the Paramagnetic Response in the Singly Valent e_g System $LaMn_7O_{12}$," Phys. Rev. B **81**(21), 214412-1 (2010).

Cabrera, I., Kenzelmann, M., Lawes, G., Chen, Y., Chen, W.C., Erwin, R., Gentile, T.R., Leao, J.B., Lynn, J.W., Rogado, N., Cava, R.J., Broholm, C., "Coupled Magnetic and Ferroelectric Domains in Multiferroic $Ni_3V_2O_8$," Phys. Rev. Lett. **103**(8), 087201-1 (2009).

Cao, L.R., Hattrick-Simpers, J.R., Bindel, R., Tomlin, B.E., Zeisler, R., Paul, R., Bendersky, L.A., Downing, R.G., "Combinatorial Study of Thin Film Metal Hydride by Prompt Gamma Activation Analysis," J. Radioanal. Nucl. Chem. **283**, 63 (2010).

Cappelletti, R.L., editor, "2009 NIST Center for Neutron Research Accomplishments and Opportunities," NIST SP 1105 (2009).

Chambrier, M.-H., Ibberson, R.M., Goutenoire, F., "Structure Determination of α-$La_6W_2O_{15}$," J. Solid State Chem. **183**, 1297 (2010).

Chang, L.J., Huang, D.J., Li, W.-H., Cheong, S.-W., Ratcliff, W., Lynn, J.W., "Crossover from Incommensurate to Commensurate Magnetic orderings in $CoCr_2O_4$," J. Phys.: Condens. Matter **21**, 456008 (2009).

Chang, L.J., Prager, M., PerBon, J., Walter, J., Jansen, E., Chen, Y.Y., Gardner, J.S., "Magnetic Order in the Double Pyrochlore $Tb_2Ru_2O_7$," J. Phys: Condens. Matter **22**, 076003 (2010).

Chatjaroenporn, K., Baker, R.W., Fitzgerald, P.A., Warr, G.G., "Polymerizable Cationic Micelles Form Cylinders at Intermediate Conversions," Langmuir **26**(14), 11715 (2010).

Chen, S.H., Mallamace, F., Chu, X.Q., Kim, C., Lagi, M., Faraone, A., Fratini, E., Baglioni, P., "Neutron Scattering Studies of Dynamic Crossover Phenomena in a Coupled System of Biopolymer and its Hydration Water," J. Phys.: Conf. Ser. **177**(1), 021006 (2009). **[CHRNS]**

Chen, S.-H., Lagi, M., Chu, X.-Q., Zhang, Y., Kim, C., Faraone, A., Fratini, E., Baglioni, P., "Dynamics of a Globular Protein and its Hydration Water Studied by Neutron Scattering and MD Simulations," Spectroscopy **24**(1-2), 1 (2010). **[CHRNS]**

Chen, S.H., Zhang, Y., Lagi, M., Chong, S.H., Baglioni, P., Mallamace, F., "Evidence of Dynamic Crossover Phenomena in Water and Other Glass-Forming Liquids: Experiments, MD Simulations and Theory," J. Phys.: Condens. Matter **21**, 504102 (2009). **[CHRNS]**

Chen, S.-H., Zhang, Y., Lagi, M., Chu, X., Liu, L., Faraone, A., Fratini, E., Baglioni, P., "The Dynamic Response Function $X_T(Q,t)$ of Confined Supercooled Water and its Relation to the Dynamic Crossover Phenomenon," Z. Phys. Chem. **224**(1-2), 109 (2010). **[CHRNS]**

Chen, W.C., Erwin, R., McIver III, J.W., Watson, S., Fu, C.B., Gentile, T.R., Borchers, J.A., Lynn, J.W., Jones, G.L., "Applications of ^{3}He Neutron Spin Filters at the NCNR," Physica B **404**(17), 2663 (2009). **[CHRNS]**

Chen, Y.-S., Peng, H., "Studying the Water Transport in a Proton Exchange Membrane Fuel Cell by Neutron Radiography and Relative Humidity Sensors," J. Fuel Cell Sci. Technol. **6**, 031016-1 (2009).

Choi, S.-H., Lodge, T.P., Bates, F.S., "Mechanism of Molecular Exchange in Diblock Copolymer Micelles: Hypersensitivity to Core Chain Length," Phys. Rev. Lett. **104**(4), 047802-1 (2010).

Chu, X.-Q., Lagi, M., Mamontov, E., Fratini, E., Baglioni, P., Chen, S.-H., "Experimental Evidence of Logarithmic Relaxation in Single-Particle Dynamics of Hydrated Protein Molecules," Soft Matter **6**, 2623 (2010). **[CHRNS]**

Chung, J.-H., Ohgushi, K., Ueda, Y., "Magnetic Phase Diagrams of the Multicritical Olivine Mn_2SiS_4 and Mn_2GeS_4," J. Magn. Magn. Mater. **322**, 832 (2010).

Ciezak, J.A., Jenkins, T.A., Hemley, R.J., "Optical and Raman Microspectroscopy of Nitrogen and Hydrogen Mixtures at High Pressures," in "Shock Compression of Condensed Matter 2009: Proceedings of the American Physical Society Topical Group on Shock Compression of Condensed Matter," edited by Elert, M., Furnish, M. D., Anderson, W.W., Proud, W.G., and Butler, W.T., (AIP Conf. Proc., June 2009, Knoxville, TN) **1195**, 1291 (2009).

Ciezak, J.A., Trevino, S.F., "Analysis of the Vibrational Spectrum of Dihydrazinium 5,5′-Azotetrazolate Dihydrate by Electronic Structure Calculations," J. Mol. Struct. **975**, 23 (2010).

Cizas, P., Budvytyte, R., Morkuniene, R., Moldovan, R., Broccio, M., Lösche, M., Niaura, G., Valincius, G., Borutaite, V., "Size-Dependent Neurotoxicity of β-Amyloid Oligomers," Arch. Biochem. Biophys. **496**(2), 84 (2010).

Clover, B., Hammouda, B., "SANS from P85/Water-d Under Pressure," Langmuir **26**(9), 6625 (2010). **[CHRNS]**

Coffey, D., DeMarco, M., Ho, P.C., Maple, M.B., Sayles, T., Lynn, J.W., Huang, Q., Toorongian, S., Haka, M., "Absence of the Hyperfine Magnetic Field at the Ru Site in Ferromagnetic Rare-Earth Intermetallics," Phys. Rev. B **81**(18), 184404-1 (2010).

Cooper, R.L., Bass, C.D., Beise, E.J., Breuer, H., Byrne, J., Chupp, T.E., Coakley, K.J., Dewey, M.S., Fisher, B.M., Fu, C., Gentile, T.R., McGonagle, M., Mumm, H.P., Nico, J.S., Thompson, A.K., Wietfeldt, F.E., "An Experiment for the Precision Measurement of the Radiative Decay Mode of the Neutron," Nucl. Instrum. Meth. A **611**, 219 (2009).

Cooper, R.L., Chupp, T.E., Dewey, M.S., Gentile, T.R., Mumm, H.P., Nico, J.S., Thompson, A.K., Fisher, B.M., Kremsky, I., Wietfeldt, F.E., Beise, E.J., Kiriluk, K.G., Byrne, J., Coakley, K.J., Fu, C., "Radiative β Decay of the Free Neutron," Phys. Rev. C **81**(3), 035503-1 (2010).

Crompton, K.E., Forsythe, J.S., Horne, M.K., Finkelstein, D.I., Knott, R.B., "Molecular Level and Microstructural Characterisation of Thermally Sensitive Chitosan Hydrogels," Soft Matter **5**(23), 4704 (2009).

Cross, J.O., Newville, M., Maranville, B.B., Bordel, C., Hellman, F., Harris, V.G., "Evidence for Nanoscale Two-Dimensional Co Clusters in $CoPt_3$ Films with Perpendicular Magnetic Anisotropy," J. Phys.: Condens. Matter **22**, 146002 (2010).

Das, N.C., Upreti, S., Sokol, P.E., "Small Angle Neutron Scattering and Photoluminescence Property of Wet Chemistry Process Synthesised ZnO Nanoparticles," J. Exp. Nanosci. **5**(2), 180 (2010).

Das, N.C., Sokol, P.E., "Hybrid Photovoltaic Devices from Regioregular Polythiophene and ZnO Nanoparticles Compsites," Renewable Energy , in press.

Das, P., O'Brien, T., Laver, M., Dewhurst, C.D., Ni, N., Bud'ko, S.L., Canfield, P.C., Eskildsen, M.R., "Small- Angle Neutron Scattering Study of Vortices in Superconducting $Ba(Fe_{0.93}Co_{0.07})_2As_2$," Supercond. Sci. Technol. **23**, 054007 (2010). **[CHRNS]**

Davey, J.R., Mukundan, R., Spendelow, J.S., Mukherjee, P.P., Hussey, D.S., Jacobson, D.L., Arif, M., Borup, R., "Wetting and Drying Responses of Gas Diffusion Layers and Proton Exchange Membrane to Current Transients," ECS Trans. **25**(1), 971 (2009).

de la Cruz, C., Hu, W.Z., Li, S., Huang, Q., Lynn, J.W., Green, M.A., Chen, G.F., Wang, N.L., Mook, H.A., Si, Q., Dai, P., "Lattice Distortion and Magnetic Quantum Phase Transition in $CeFeAs_{1-x}P_xO$," Phys. Rev. Lett. **104**(1), 017204-1 (2010).

Decker, J.E., Walker, A.R.H., Bosnick, K., Clifford, C.A., Dai, L., Fagan, J., Hooker, S., Jakubek, Z.J., Kingston, C., Maker, J., Mansfield, E., Postek, M.T., Simard, B., Sturgeon, R., Wise, S., Vladar, A.E., Yang, L., Zeisler, R., "Sample Preparation Protocols for Realization of Reproducible Characterization of Single-Wall Carbon Nanotubes," Metrologia **46**, 682 (2009).

Dennis, C.L., Jackson, A.J., Borchers, J.A., Hoopes, P.J., Strawbridge, R., Foreman, A.R., van Lierop, J., Grüttner, C., Ivkov, R., "Nearly Complete Regression of Tumors via Collective Behavior of Magnetic Nanoparticles in Hyperthermia," Nanotechnology **20**, 395103 (2009). **[CHRNS]**

Dewey, M.S., Gilliam, D.M., Nico, J.S., Greene, G.L., Laptev, A., Yue, A., "Measuring ^{6}Li(n,t) and ^{10}B(n,α) Cross Sections Using the NIST Alpha-Gamma Device," in "Reactor Dosimetry State of the Art 2008," edited by Voorbraak, W., Debarberis, L., D'hondt, P., and Wagemans, J., (13th ASTEM-EWGRD, May 2008, Akersloot, Netherlands), 483 (2009).

Dewey, M., Coakley, K., Gilliam, D., Greene, G., Laptev, A., Nico, J., Snow, W., Wietfeldt, F., Yue, A., "Prospects for a New Cold Neutron Beam Measurement of the Neutron Lifetime," Nucl. Instrum. Meth. A **611**, 189 (2009).

Diallo, S.O., Azuah, R.T., Kirichek, O., Taylor, J.W., Glyde, H.R., "Limits on Bose-Einstein Condensation in Confined Solid ^{4}He," Phys. Rev. B **80**(6), 060504-1 (2009).

Doe, C., Jang, H.-S., Kline, S.R., Choi, S.-M., "SANS Investigation of Selectively Distributed Single-Walled Carbon Nanotubes in a Polymeric Lamellar Phase," Macromol. **43**, 5411 (2010).

Doe, C., Jang, H.-S., Kim, T.-H., Kline, S.R., Choi, S.-M., "Thermally Switchable One-and Two-Dimensional Arrays of Single-Walled Carbon Nanotubes in a Polymeric System," J. Am. Chem. Soc. **131**, 16568 (2009).

Domach, M.M., Walker, L.M., "Stabilizing BioMacromol. in Nontoxic Nano-Structured Materials," JALA **15**(2), 136 (2010). **[CHRNS]**

Dowling, M.B., Lee, J.-H., Raghavan, S.R., "pH-Responsive Jello: Gelatin Gels Containing Fatty Acid Vesicles," Langmuir **25**(15), 8519 (2009).

Eberle, A.P.R., Wagner, N.J., Akgun, B., Satija, S.K., "Temperature-Dependent Nanostructure of an End-Tethered Octadecane Brush in Tetradecane and Nanoparticle Phase Behavior," Langmuir **26**(5), 3003 (2010). **[CHRNS]**

Ehlers, G., Greedan, J.E., Stewart, J.R., Rule, K.C., Fouquet, P., Cornelius, A.L., Adriano, C., Pagliuso, P.G., Qiu, Y., Gardner, J.S., "High Resolution Neutron Scattering Study of $Tb_2Mo_2O_7$: A Geometrically Frustrated Spin Glass," Phys. Rev. B **81**(22), 224405-1 (2010). **[CHRNS]**

ElMassalami, M., Moreno, R., Takeya, H., Ouladdiaf, B., Lynn, J.W., Freitas, R.S., "Magnetic Structures of Quaternary Intermetallic Borocarbides RCo_2B_2C (R=Dy, Ho, Er)," J. Phys.: Condens. Matter **21**, 436006 (2009).

Ell, J.R., Mulder, D.E., Faller, R., Patten, T.E., Kuhl, T.L., "Structural Determination of High Density, ATRP Grown Polystyrene Brushes by Neutron Reflectivity," Macromol. **42**, 9523 (2009).

Ferguson, P.P., Todd, A.D.W., Dahn, J.R., "Importance of Nanostructure for High Capacity Negative Electrode Materials for Li-ion Batteries," Electrochem. Commun., in press.

Fratini, E., Faraone, A., Todea, A.M., Baglioni, P., "Hydrated $\{Mo_{72}Fe_{30}\}$ Clusters: Low-Frequency Hydrogen Modes and Self-Aggregation," Inorganica Chimica Acta., in press. **[CHRNS]**

Fredin, N.J., Berry, B.C., Yager, K.G., Karim, A., Satija, S.K., Pickel, D.L., Jones, R.L., "Application of Thermal Gradients to Achieve Orientational Order in Block Copolymer Thin Films," in "238th ACS National Meeting & Exposition, Fall 2009, Division of Polymer Materials: Science & Engineering," edited by unknown, (ACS, Fall National Meeting & Exposition 2009 Conf. Proc., August 2009, Washington, D.C.) **101**, 791 (2009).

Fu, R.S., Preston, J.S., Pasaogullari, U., Tabuchi, Y., Shiomi, T., Hussey, D.S., Jacobson, D.L., "An Investigation of Thermally-Induced Water Transport in Polymer Electrolyte Fuel Cells with Neutron Radiography Imaging Technique," in "Proton Exchange Membrane Fuel Cells 9," edited by Fuller, T., Hartnig, C., Ramani, V., Uchida, H., Gasteiger, H., Cleghorn, S., Strasser, P., Zawodzinski, T., Jones, D., Shirvanina, P., Jarvi, T., Zelenay, P., Lamy, C., and Bele, P., (216th ECS Meeting, October 2009, Vienna, Austria) **25**(1), 543 (2009).

Fullerton-Shirey, S.K., Maranas, J.K., "Structure and Mobility of PEO/$LiClO_4$ Solid Polymer Electrolytes Filled with Al_2O_3 Nanoparticles," J. Phys. Chem. C. **114**, 9196 (2010). **[CHRNS]**

Garcia Sakai, V., Mamontov, E., Neumann, D.A., "A Background Suppression Chopper for the High-Flux Backscattering Spectrometer at NIST," J. Neutron Res. **16**(3&4), 65 (2008). **[CHRNS]**

Gardner, J.S., Ehlers, G., "Magnetic Order and Crystal Field Excitations in $Er_2Ru_2O_7$: A Neutron Scattering Study," J. Phys.: Condens. Matter **21**, 436004 (2009).

Gardner, J.S., Gingras, M.J.P., Greedan, J.E., "Magnetic Pyrochlore Oxides," Rev. Mod. Phys. **82**(1), 53 (2010). **[CHRNS]**

Gardner, J.S., Stewart, J.R., Ehlers, G., "Phase Separation in the Heisenberg Spin System, $Gd_2Ti_2O_7$," in "Neutron and X-Ray Scattering in Advancing Materials Research" edited by Mohamed, B., and Aziz, A., (AIP Conf. Proc., June 2009, Kuala Lumpur, Malaysia) **1202**, 3 (2010).

Gardner, J.S., Kam, K.C., Ehlers, G., "New Relaxation Processes in Diluted $Ho_2Ti_2O_7$," Physica B **405**, 774 (2010). **[CHRNS]**

Geissler, E., Hecht, A.-M., Horkay, F., "Scaling Behavior of Hyaluronic Acid in Solution with Mono- and Divalent Ions," Macromol. Symp. **291-292**, 362 (2010). **[CHRNS]**

Gentile, T.R., Brown, S.W., Lykke, K.R., Shaw, P.S., Woodward, J.T., "Internal Quantum Efficiency Modeling of Silicon Photodiodes," Appl. Opt. **49**(10), 1859 (2010).

Gericke, M., Page, S., Ramsay, D., Alarcon, R., Balascuta, S., Barron, L., Bowman, J.D., Carlini, R.D., Chen, W., Chupp, T.E., Crawford, C., Covrig, S., Dabaghyan, M., Freedman, S.J., Gentile, T.R., Gillis, R.C., Greene, G.L., Hersman, F.W., Ino, T., Jones, G.L., Lauss, B., Leuschner, M., Losowki, B., Mahurin, R., Masuda, Y., Mei, J., Mitchell, G.S., Muto, S., Nann, H., Penttila, S.I., Salas-Bacci, A., Santra, S., Seo, P.-N., Sharapov, E., Sharma, M., Smith, T., Snow, W.M., Wilburn, W.S., Yuan, V., "Parity Violation in Neutron-Proton Capture - The NPDGamma Experiment," Nucl. Instrum. Meth. A **611**, 239 (2009).

Gilliam, D.M., Yue, A.T., Dewey, M.S., "Calibration of a Manganese Bath Relative to ^{252}CF Nu-Bar," in "Reactor Dosimetry State of the Art 2008," edited by Voorbraak, W., Debarberis, L., D'hondt, P., and Wagemans, J., (13th ASTEM-EWGRD, May 2008, Akersloot, Netherlands), 361 (2009).

Gnäupel-Herold, T.H., "Techniques for Neutron Stress Determination with High Spatial Resolution," J. Nondestruct. Eval. **28**, 149 (2009).

Gogotsi, Y., Portet, C., Osswald, S., Simmons, J.M., Yildirim, T., Laudisio, G., Fischer, J.E., "Importance of Pore Size in High-Pressure Hydrogen Storage by Porous Carbons," Int. J. Hydrogen Energy **34**(15), 6314 (2009).

Green, M.A., "Surface Attraction," Nat. Mater. **9**, 539 (2010).

Grünwald, A.T.D., Wildes, A.R., Schmidt, W., Tartakovskaya, E.V., Kwo, J., Majkrzak, C.F., Ward, R.C.C., Schreyer, A., "Magnetic Excitations in Dy/Y Superlattices as Seen via Inelastic Neutron Scattering," Phys. Rev. B **82**(1), 014426-1 (2010).

Hadjiantoniou, N.A., Krasia-Christoforou, T., Loizou, E., Porcar, L., Patrickios, C.S., "Alternating Amphiphilic Multiblock Copolymers: Controlled Synthesis via RAFT Polymerization and Aqueous Solution Characterization," Macromol. **43**, 2713 (2010). **[CHRNS]**

Hammouda, B., "The Mystery of Clustering in Macromolecular Media," Polymer **50**, 5293 (2009). **[CHRNS]**

Hammouda, B., "Insight into the Denaturation Transition of DNA," Int. J. Biol. Macromol. **45**, 532 (2009). **[CHRNS]**

Hammouda, B., "A New Guinier-Porod Model," J. Appl. Crystallogr., in press. **[CHRNS]**

Hammouda, B., "SANS from Polymers - Review of the Recent Literature," Polym. Rev. **50**(1), 14 (2010). **[CHRNS]**

Hao, J., Cheng, H., Butler, P., Zhang, L., Han, C.C., "Origin of Cononsolvency, Based on the Structure of Tetrahydrofuran-Water Mixture," J. Chem. Phys. **132**(15), 154902-1 (2010).

Harris, A.B., Yildirim, T., "Charge and Spin Ordering in the Mixed-Valence Compound $LuFe_2O_4$," Phys. Rev. B **81**(13), 134417-41 (2010).

Hattrick-Simpers, J.R., Wang, K., Cao, L., Chiu, C., Heilweil, E., Downing, R.G., Bendersky, L.A., "Observation of Phase Transitions in Hydrogenated Yttrium Films via Normalized Infrared Emissivity," J. Alloys Compd. **490**, 42 (2010).

He, C., El-Khatib, S., Eisenberg, S., Manno, M., Lynn, J.W., Zheng, H., Mitchell, J.F., Leighton, C., "Transport Signatures of Percolation and Electronic Phase Homogeneity in $La_{1-x}Sr_xCoO_3$ Single Crystals," Appl. Phys. Lett. **95**(22), 222511-1 (2009).

He, C., El-Khatib, S., Wu, J., Lynn, J.W., Zheng, H., Mitchell, J.F., Leighton, C., "Doping Fluctuation-Driven Magneto-Electronic Phase Separation in $La_{1-x}Sr_xCoO_3$ Single Crystals," Europhys. Lett. **87**(2), 27006-p1 (2009).

He, L., Fujimoto, C.H., Cornelius, C.J., Perahia, D., "From Solutions to Membranes: Structure Studies of Sulfonated Polyphenylene Ionomers," Macromol. **42**, 7084 (2009). **[CHRNS]**

Helgeson, M.E., Hodgdon, T.K., Kaler, E.W., Wagner, N.J., "A Systematic Study of Equilibrium Structure, Thermodynamics, and Rheology of Aqueous CTAB/$NaNO_3$ Wormlike Micelles," J. Colloid Interface Sci. **349**, 1 (2010).

Helgeson, M.E., Porcar, L., Lopez-Barron, C., Wagner, N.J., "Direct Observation of Flow-Concentration Coupling in a Shear-Banding Fluid," Phys. Rev. Lett., in press. **[CHRNS]**

Helgeson, M.E., Reichert, M.D., Hu, Y.T., Wagner, N.J., "Relating Shear Banding, Structure, and Phase Behavior in Wormlike Micellar Solutions," Soft Matter **5**, 3858 (2009). **[CHRNS]**

Helton, J.S., Matan, K., Shores, M.P., Nytko, E.A., Bartlett, B.M., Qiu, Y., Nocera, D.G., Lee, Y.S., "Dynamic Scaling in the Susceptibility of Spin-½ Kagome Lattice Antiferromagnet Herbertsmithite," Phys. Rev. Lett. **104**(14), 147201-1 (2010). **[CHRNS]**

Her, J.-H., Zhou, W., Stavila, V., Brown, C.M., Udovic, T.J., "Crystal Structure of $Na_2B_{12}H_{12}$ and the Role of Cation Size on the Structural Behavior of the Alkali-Metal Dodecahydro-Closo-Dodecaborates," in "ACS Division Proceedings, Division of Fuel Chemistry," edited by unknown, (ACS, Fall National Meeting & Exposition 2009 Conf. Proc., August 2009, Washington, D.C.) **54**(2) (2009).

Hernandez, Y., Brown, C.M., "User Facilities: The Education of New Neutron Users," in "8th International Conference on Methods and Applications of Radioanalytical Chemistry: MARC-VIII," edited by Ünlü, K., Heller-Zeisler, S., and Zeisler, R. (AIP Conf. Proc, April 2009, Kona, HI,) **1164**(1), 52 (2009).

Herrera, A.P., Barrera, C., Zayas, Y., Rinaldi, C., "Monitoring Colloidal Stability of Polymer-Coated Magnetic Nanoparticles using AC Susceptibility Measurements," J. Colloid Interface Sci. **342**, 540 (2010). **[CHRNS]**

Heuser, B.J., Ju, H., Trinkle, D.R., Udovic, T.J., "Hydrogen Trapping at Dislocations in Palladium at Low Temperature: Results From Inelastic Neutron Scattering and Advanced Computations," in "Effects of Hydrogen on Materials," edited by Somerday, B., Sofronis, P., and Jones, R., (ASM International Hydrogen 2008 Conference, September 2008, Grant Teton National Park, WY) 464 (2009).

Hickner, M.A., Hussey, D.S., "Neutron Radioscopy: Industrial and Scientific Applications," in "Encyclopedia of Analytical Chemistry," edited by Meyers, R.A., (Wiley, US) Chap. on Nuclear Methods (2010).

Hickner, M.A., Siegel, N.P., Chen, K.S., Hussey, D.S., Jacobson, D.L., "Observations of Transient Flooding in a Proton Exchange Membrane Fuel Cell Using Time-Resolved Neutron Radiography," J. Electrochem. Soc. **157**(1), B32 (2010).

Hong, T., Custelcean, R., Sales, B.C., Roessli, B., Singh, D.K., Zheludev, A., "Synthesis and Structural Characterization of 2Dioxane•2H_2O• $CuCl_2$: Metal-Organic Compound with Heisenberg Antiferromagnetic S= ½ Chains," Phys. Rev. B **80**(13), 132404-1 (2009). **[CHRNS]**

Horkay, F., Magda, J., Alcoutlabi, M., Atzet, S., Zarembinski, T., "Structural, Mechanical and Osmotic Properties of Injectable Hyaluronan-Based Composite Hydrogels," Polymer , in press. **[CHRNS]**

Horkay, F., Basser, P.J., Hecht, A.-M., Geissler, E., "Counterion and pH-Mediated Structural Changes in Charged Biopolymer Gels," Macromol. Symp. **291-292**, 354 (2010). **[CHRNS]**

Hould, N.D., Kumar, S., Tsapatsis, M., Nikolakis, V., Lobo, R.F., "Structure and Colloidal Stability of Nanosized Zeolite Beta Precursors," Langmuir **26**(2), 1260 (2010). **[CHRNS]**

Huang, S.X., Chien, C.L., Thampy, V., Broholm, C., "Control of Tetrahedral Coordination and Superconductivity in $FeSe_{0.5}Te_{0.5}$ Thin Films," Phys. Rev. Lett. **104**(21), 271002-1 (2010).

Huang, S.-L., Hsu, Y.-C., Wu, C.-M., Lynn, J.W., Hsien, W.-H., "Thermal Effects on the Activity and Structural Conformation of Catechol 2,3-Dioxygenase from *Pseudomonas Putida* SH1," J. Phys. Chem. B **114**, 987 (2010).

Huber, M.G., Wietfeldt, F.E., Gentile, T.R., Chen, W.C., Arif, M., Hussey, D.A., Pushin, D.A., Yang, L., Black, T., "Precision Measurement of the Neutron-^{3}He Spin- Dependent Scattering Length using Neutron Interferometry," Nucl. Instrum. Meth. A **611**, 235 (2009).

Huber, M.G., Arif, M., Black, T.C., Chen, W.C., Gentile, T.R., Hussey, D.S., Pushin, D.A., Wietfeldt, F.E., Yang, L., "Erratum: Precision Measurement of the *n*-^{3}He Incoherent Scattering Length Using Neutron Interferometry," Phys. Rev. Lett. **103**(17), 179903-1 (2009).

Hule, R.A., Nagarkar, R.P., Hammouda, B., Schneider, J.P., Pochan, D.J., "Dependence of Self-Assembled Peptide Hydrogel Network Structure on Local Fibril Nanostructure," Macromol. **42**, 7137 (2009). **[CHRNS]**

Hussey, D.S., Jacobson, D.L., "In Situ Neutron Imaging of Alkaline and Lithium Batteries," ECS Transactions **25**(35), 75 (2009).

Hussey, D.S., Jacobson, D.L., Arif, M., Coakley, K.J., Vecchia, D.F., "In Situ Fuel Cell Water Metrology at the NIST Neutron Imaging Facility," J. Fuel Cell Sci. Technol. **7**, 021024-1 (2010).

Hussey, D.S., Jacobson, D.L., "High-Resolution Neutron Radiography Analysis of Proton Exchange Membrane Fuel Cells," in "Modern Aspects of Electrochemistry, Vol. 49: Modeling and Diagnostics of Polymer Electrolyte Fuel Cells," edited by Pasaogullari, U. and Wang, C.-Y., (Springer) Chap. 5, 175 (2010).

Iannuzzi, M.A., Reber, III, R., Lentz, D.M., Zhao, J., Ma, L., Hedden, R.C., "USANS Study of Porosity and Water Content in Sponge-like Hydrogels," Polymer **51**, 2049 (2010). **[CHRNS]**

Inosov, D.S., Shapoval, T., Neu, V., Wolff, U., White, J.S., Haindl, S., Park, J.T., Sun, D.L., Lin, C.T., Forgan, E.M., Viazovska, M.S., Kim, J.H., Laver, M., Nenkov, K., Khvostikova, O., Kühnemann, S., Hinkov, V., "Symmetry and Disorder of the Vitreous Vortex Lattice in Overdoped $BaFe_{2-x}Co_xAs_2$: Indication for Strong Single-Vortex Pinning," Phys. Rev. B **81**(1), 014513-1 (2010). **[CHRNS]**

Inoue, R., Kanaya, T., Nishida, K., Tsukushi, I., Telling, M.T.F., Gabrys, B.J., Tyagi, M., Soles, C., Wu, W.-l., "Glass Transition and Molecular Mobility in Polymer Thin Films," Phys. Rev. E. **80**(3), 031802-1 (2009). **[CHRNS]**

Ivancic, T.M., Hwang, S.-J., Bowman, Jr., R.C., Birkmire, D.S., Jensen, C.M., Udovic, T.J., Conradi, M.S., "Discovery of a New Al Species in Hydrogen Reactions of $NaAlH_4$," J. Phys. Chem. Lett. **1**, 2412 (2010).

Janssen, Y., Kim, M.S., Park, K.S., Wu, L.S., Marques, C., Bennett, M.C., Chen, Y., Li, J., Huang, Q., Lynn, J.W., Aronson, M.C., "Determination of the Magnetic Structure of Yb_3Pt_4:k=0 Local-Moment Antiferromagnet," Phys. Rev. B. **81**(6), 064401-1 (2010).

Jeong, Y., Chung, T.C.M., "The Synthesis and Characterization of a Super-Activated Carbon Containing Subsitutional Boron (BC_x) and its Applications in Hydrogen Storage," Carbon, in press.

Ji, S., Kan, E.J., Whangbo, M.-H., Kim, J.-H., Qiu, Y., Matsuda, M., Yoshida, H., Hiroi, Z., Green, M.A., Ziman, T., Lee, S.-H., "Orbital Order and Partial Electronic Delocalization in a Triangular Magnetic Metal Ag_2MnO_2," Phys. Rev. B **81**(9), 094421-1 (2010). **[CHRNS]**

Jia, S., Chi, S.X., Lynn, J.W., Cava, R.J., "Magnetic and Structural Properties of $Ca(Fe_{1-x}Co_x)_2P_2$ and $Ca(Ni_{1-x}Co_x)_2P_2$," Phys. Rev. B **81**(21), 214446-1 (2010).

Johnson, M.E., Malardier-Jugroot, C., Head-Gordon, T., "Effects of Co-Solvents on Peptide Hydration Water Structure and Dynamics," Phys. Chem. Chem. Phys. **12**, 393 (2010). **[CHRNS]**

Jones, B.H., Lodge, T.P., "High-Temperature Nanoporous Ceramic Monolith Prepared from a Polymeric Bicontinuous Microemulsion Template," J. Am. Chem. Soc. **131**, 1676 (2009).

Jones, C.Y., Nevers, T.J., "Temperature-Dependent Distortions of the Host Structure of Propylene Oxide Clathrate Hydrate," J. Phys. Chem. C **114**, 4194 (2010).

Junghans, A., Köper, I., "Structural Analysis of Tethered Bilayer Lipid Membranes," Langmuir **26**(13), 11035 (2010).

Kadowaki, H., Doi, N., Aoki, Y., Tabata, Y., Sato, T.J., Lynn, J.W., Matsuhira, K., Hiroi, Z., "Observation of Magnetic Monopoles in Spin Ice," J. Phys. Soc. Jpn. **78**(10), 103706 (2009).

Kalman, D.P., Wagner, N.J., "Microstructure of Shear-Thickening Concentrated Suspensions Determined by Flow-USANS," Rheol. Acta **48**(8), 897 (2009). **[CHRNS]**

Kamazawa, K., Harada, M., Ikedo, Y., Sugiyama, J., Tyagi, M., Matsuo, Y., "Long Range Proton Diffusive Motion of $CsHSO_4$ and $CsHSeO_4$: - High Energy Resolution Quasielastic Neutron Scattering of Superprotonic Conductors-," J. Phys. Soc. Jpn. **79**, 7 (2010). **[CHRNS]**

Kang, S., Wu, W.-l., Choi, K.-W., De Silva, A., Ober, C.K., Prabhu, V.M., "Characterization of the Photoacid Diffusion Length and Reaction Kinetics in EUV Photoresists with IR Spectroscopy," Macromol. **43**, 4275 (2010).

Kawabata, Y., Nagao, M., "Neutron Spin Echo Studies on Dynamical Structures of Microemulsion," Hamon **20**(1), 80 (2010).

Kealley, C.S., Sokolova, A.V., Kearley, G.J., Kemner, E., Russina, M., Faraone, A., Hamilton, W.A., Gilbert, E.P., "Dynamical Transition in a Large Globular Protein: Macroscopic Properties and Glass Transition," Biochim. Biophys. Acta. **1804**, 34 (2010). **[CHRNS]**

Kent, B., Garvey, C.J., Lenné, T., Porcar, L., Garamus, V.M., Bryant, G., "Measurement of Glucose Exclusion from the Fully Hydrated DOPE Inverse Hexagonal Phase," Soft Matter **6**, 1197 (2010).

Kent, M.S., Murton, J.K., Sazaki, D.Y., Satija, S., Akgun, B., Nanda H., Curtis, J.E., Majewski, J., Morgan, C.R., Engen, J.R., "Neutron Reflectometry Study of the Conformation of HIV Nef Bound to Lipid Membranes," Biophys. J., in press.

Khan, A.S., Meredith, C.S., "Thermo-Mechanical Response of Al 6061 with and without Equal Channel Angular Pressing (ECAP)," Int. J. Plast. **26**, 189 (2010).

Khodadadi, S., Roh, J.H., Kisliuk, A., Mamontov, E., Tyagi, M., Woodson, S.A., Briber, R.M., Sokolov, A.P., "Dynamics of Biological Macromolecules: Not a Simple Slaving by Hydration Water," Biophys. J. **98**, 1321 (2010). **[CHRNS]**

Kiel, J.W., Kirby, B.J., Majkrzak, C.F., Maranville, B.B., Mackay, M.E., "Nanoparticle Concentration Profile in Polymer-based Solar Cells," Soft Matter **6**, 641 (2010).

Kiel, J.W., Mackay, M.E., Kirby, B.J., Maranville, B.B., Majkrzak, C.F., "Phase-Sensitive Neutron Reflectometry Measurements Applied in the Study of Photovoltaic Films," J. Chem. Phys., in press.

Kienzle, P.A., Patel, N., McKerns, M., "Parallel Kernels: An Architecture for Distributed Parallel Computing," in "Proceedings of the 8th Python in Science Conference (SciPy2009)," edited by Varoquaux, G., van der Walt, S., and Millman, K.J., (SciPy2009, August 2009, Pasadena, CA), 36 (2009).

Kilburn, D., Roh, J.H., Guo, L., Briber, R.M., Woodson, S.A., "Molecular Crowding Stabilizes Folded RNA Structure by the Excluded Volume Effect," J. Am. Chem. Soc. **132**, 8690 (2010).

Kim, S.-H., Halasyamani, P.S., Melot, B.C., Seshadri, R., Green, M.A., Sefat, A.S., Mandrus, D., "Experimental and Computational Investigation of the Polar Ferrimagnet $VOSe_2O_5$," Chem. Mater., in press.

King, G., Woodward, P.M., "Cation Ordering in Perovskites," J. Mater. Chem. **20**(28), 5785 (2010).

King, G., Garcia-Martin, S., Woodward, P.M., "Octahedral Tilt Twinning and Compositional Modulation in $NaLaMgWO_6$," Acta Crystallogr. Sect. B: Struct. Sci. **65**(6), 676 (2009).

Kiran, S.K., Acosta, E.J., "Predicting the Morphology and Viscosity of Microemulsions Using the HLD-NAC Model," Ind. Eng. Chem. Res. **49**, 3424 (2010).

Kirby, B.J., Davies, J.E., Liu, K., Watson, S.M., Zimanyi, G.T., Shull, R.D., Kienzle, P.A., Borchers, J.A., "Vertically Graded Anisotropy in Co/Pd Multilayers," Phys. Rev. Lett. **81**(10), 100405-1 (2010).

Koga, T., Wong, J., Endoh, M.K., Mahajan, D., Gutt, C., Satija, S.K., "Hydrate Formation at the Methane/Water Interface on the Molecular Scale," Langmuir **26**(7), 4627 (2010).

Kopetka, P., Middleton, M., Williams, R.E., Rowe, J.M., "A Second Liquid Hydrogen Cold Source for the NIST Reactor," in "Proceedings of the 12th Meeting of the International Group on Research Reactors," (IGORR-12, October 2009, Beijing, China) in press.

Krepkiy, D., Mihailescu, M., Freites, J.A., Schow, E.V., Worcester, D.L., Gawrisch, K., Tobias, D.J, White, S.H., Swartz, K.J., "Structure and Hydration of Membranes Embedded with Voltage-Sensing Domains," Nature **462**, 473 (2009).

Krycka, K.L., Booth, R.A., Hogg, C.R., Ijiri, Y., Borchers, J.A., Chen, W.C., Watson, S.M., Laver, M., Gentile, T.R., Dedon, L.R., Harris, S.A., Rhyne, J.J., Majetich, S.A., "Core-Shell Magnetic Morphology of Structurally Uniform Magnetite Nanoparticles," Phys. Rev. Lett. **104**(20), 207203-1 (2010). **[CHRNS]**

Krycka, K.L., Borchers, J.A., Booth, R.A., Hogg, C.R., Ijiri, Y., Chen, W.C., Watson, S.M., Laver, M., Gentile, T.R., Harris, S., Dedon, L.R., Rhyne, J.J., Majetich, S.A., "Internal Magnetic Structure of Magnetite Nanoparticles at Low Temperature," J. Appl. Phys. **107**(9), 09B525-1 (2010). **[CHRNS]**

Krycka, K.L., Booth, R., Borchers, J.A., Chen, W.C., Conlon, C., Gentile, T.R., Hogg, C., Ijiri, Y., Laver, M., Maranville, B.B., Majetick, S.A., Rhyne, J.J., Watson, S.M., "Resolving 3D Magnetism in Nanoparticles Using Polarization Analyzed SANS," Physica B **404**(17), 2561 (2009). **[CHRNS]**

Kumar, N., Chi, S.X., Chen, Y., Rana, K.G., Nigam, A.K., Thamizhavel, A., Ratcliff, II, W., Dhar, S.K., Lynn, J.W., "Evolution of the Bulk Properties, Structure, Magnetic Order, and Superconductivity with Ni Doping in $CaFe_{2-x}Ni_xAs_2$," Phys. Rev. B **80**(14), 144524-1 (2009).

Kumar, R., Raghavan, S.R., "Thermothickening in Solutions of Telechelic Associating Polymers and Cyclodextrins," Langmuir **26**(1), 56 (2010). **[CHRNS]**

Kumar, R., Ketner, A.M., Raghavan, S.R., "Nonaqueous Photorheological Fluids Based on Light-Responsive Reverse Wormlike Micelles," Langmuir **26**(8), 5405 (2010).

Lam, V.D., Walker, L.M., "A pH-Induced Transition of Surfactant-Polyelectrolyte Aggregates from Cylindrical to String-of-Pearls Structure," Langmuir **26**(13), 10489 (2010). **[CHRNS]**

Larson-Smith, K., Jackson, A., Pozzo, D.C., "Small Angle Scattering Model for Pickering Emulsions and Raspberry Particles," J. Colloid Interface Sci. **343**, 36 (2010). **[CHRNS]**

Lauw, Y., Rodopoulos, T., Gross, M., Nelson, A., Gardner, R., Horne, M.D., "Electrochemical Cell for Neutron Reflectometry Studies of the Structure of Ionic Liquids at Electrified Interface," Rev. Sci. Instrum. **81**(7), 074101-1 (2010).

Laver, M., Mudivarthi, C., Cullen, J.R., Flatau, A.B., Chen, W.-C., Watson, S.M., Wuttig, M., "Magnetostriction and Magnetic Heterogeneities in Iron-Gallium," Phys. Rev. Lett. **105**(2), 027202-1 (2010).

Lee, Jr., C.T., Smith, K.A., Hatton, T.A., "Small-Angle Neutron Scattering Study of the Micellization of Photosensitive Surfactants in Solution and in the Presence of a Hydrophobically Modified Polyelectrolyte," Langmuir **25**(24), 13784 (2009). **[CHRNS]**

Lee, H.-Y., Diehn, K.K., Ko, S.W., Tung, S.-H., Raghavan, S.R., "Can Simple Salts Influence Self-Assembly in Oil? Multivalent Cations as Efficient Gelators of Lecithin Organosols," Langmuir , in press. **[CHRNS]**

Lee, J.-H., Choi, S.-M., Doe, C., Faraone, A., Pincus, P.A., Kline, S.R., "Thermal Fluctuation and Elasticity of Lipid Vesicles Interacting with Pore-Forming Peptides," Phys. Rev. Lett. **105**(3), 038101-1 (2010). **[CHRNS]**

Lee, S.-H., Xu, G., Ku, W., Wen, J.S., Lee, C.C., Katayama, N., Xu, Z.J., Ji, S., Lin, Z.W., Gu, G.D., Yang, H.-B., Johnson, P.D., Pan, Z.-H., Valla, T., Fujita, M., Sato, T.J., Chang, S., Yamada, K., Tranquada, J.M., "Coupling of Spin and Orbital Excitations in the Iron-Based Superconductor $FeSe_{0.5}Te_{0.5}$," Phys. Rev. B **81**(22), 220502-1 (2010). **[CHRNS]**

Lee, W., Kofinas, P., Briber, R.M., "Small Angle Neutron Scattering Study of Deuterated Sodium Dodecylsulfate Micellization in Dilute Poly((2-dimethylamino)ethyl methacrylate) Solutions," Polymer **51**, 2872 (2010).

Levin, I., Karimi, S., Provenzano, V., Dennis, C.L., Wu, H., Comyn, T.P., Stevenson, T.J., Smith, R.I., Reaney, I.M., "Reorientation of Magnetic Dipoles at the Antiferroelectric-Paraelectric Phase Transition of $Bi_{1-x}Nd_xFeO_3$ ($0.15 \leq x \leq 0.25$)," Phys. Rev. B **81**(2), 020103-1 (2010).

Li, J., Callaway, D.J.E., Bu, Z., "Ezrin Induces Long-Range Interdomain Allostery in the Scaffolding Protein NHERF1," J. Mol. Biol. **392**, 166 (2009). **[CHRNS]**

Li, S.-L., Yao, D.-X., Qiu, Y.-m., Kang, H.J., Carlson, E.W., Hu, J.–P., Chen, G.-F., Wang, N.-L., Dai, P.-C., "Low-Energy Ce Spin Excitations in CeFeAsO and $CeFeAsO_{0.84}F_{0.16}$," Front. Phys. China **5**(2), 161 (2010). **[CHRNS]**

Li, X., Shew, C.-Y., Liu, Y., Pynn, R., Liu, E., Herwig, K.W., Smith, G.S., Robertson, J.L., Chen, W.-R., "Theoretical Studies on the Structure of Interacting Colloidal Suspensions by Spin-Echo Small Angle Neutron Scattering," J. Chem. Phys. **132**(17), 174509-1 (2010).

Lin-Gibson, S., Chatterjee, K., Cooper, J.A., Wallace, W.E., Becker, M.L., Simon, Jr., C.G., Horkay, F., "PEG-Hydrogels: Synthesis, Characterization, and Cell Encapsulation," in "238th ACS National Meeting & Exposition," edited by unknown, (ACS Fall National Meeting & Exposition, August 2009 Washington, DC) (2009).

Lindstrom, R.M., "Errors, PGAA, and Metrology," J. Radioanal. Nucl. Chem. **282**, 5 (2009).

Lindstrom, R.M., "Routine Gamma-Ray Peak Integration: How Good Can It Be?," Trans. Am. Nucl. Soc. **101**, 99 (2009).

Lindstrom, R.M., Fischbach, E., Buncher, J.B., Greene, G.L., Jenkins, J.H., Krause, D.E., Mattes, J.J., Yue, A., "Study of the Dependence of ^{198}Au Half-Life on Source Geometry," Nucl. Instrum. Meth. A, in press.

Linegar, K.L., Adeniran, A.E., Kostko, A.F., Anisimov, M.A., "Hydrodynamic Radius of Polyethylene Glycol in Solution Obtained by Dynamic Light Scattering," Colloid J. **72**(2), 279 (2010).

Linton, P., Rennie, A.R., Alfredsson, V., "Evolution of Structure and Composition During the Synthesis of Mesoporous Silica SBA-15 Studied by Small-Angle Neutron Scattering," Solid State Sci., in press. **[CHRNS]**

Lister, S.E., Soleilhavoup, A., Withers, R.L., Hodgkinson, P., Evans, J.S.O., "Structures and Phase Transitions in $(MoO_2)_2P_2O_7$," Inorg. Chem. **49**, 2290 (2010).

Liu, D.M., Huang, Q.Z., Yue, M., Lynn, J.W., Liu, L.J., Chen, Y., Wu, Z.H., Zhang, J.X., "Temperature, Magnetic Field, and Pressure Dependence of the Crystal and Magnetic Structures of the Magnetocaloric Compound $Mn_{1.1}Fe_{0.9}(P_{0.8}Ge_{0.2})$," Phys. Rev. B **80**(17), 174415-1 (2009).

Liu, H.-T., Gnäupel-Herold, T., Hovanski, Y., Dahl, M.E., "Fatigue Performance Enhancement of AWJ-Machined Aircraft Aluminum with Dry-Grit Blasting," in "Proceedings for the 2009 American WJTA Conference and Expo," edited by Hashish, M., (AM WJTA Conf. Proc., August 2009, Houston, TX). (2009).

Liu, L.J., Liu, D.M., Huang, Q.Z., Zhang, T.L., Zhang, L., Yue, M., Lynn, J.W., Zhang, J.X., "Neutron Diffraction Study of the Magnetic Refrigerant $Mn_{1.1}Fe_{0.9}P_{0.76}Ge_{0.24}$," Powder Diffr., in press.

Liu, T.J., Hu, J., Qian, B., Fobes, D., Mao, Z.Q., Bao, W., Reehuis, M., Kimber, S.A.J., Prokes, K., Matas, S., Argyriou, D.N., Hiess, A., Rotaru, A., Pham, H., Spinu, L., Qiu, Y., Thampy, V., Savici, A.T., Rodriguez, J.A., Broholm, C., "From (π,O) Magnetic Order to Superconductivity with (π,π) Magnetic Resonance in $Fe_{1.02}Te_{1-x}Se_x$," Nat. Mater., in press. **[CHRNS]**

Liu, Y., Porcar, L., Hong, K., Shew, C.-Y., Li, X., Liu, E., Butler, P.D., Herwig, K.W., Smith, G.S., Chen, W.-R., "Effect of Counterion Valence on the pH Responsiveness of Polyamidoamine Dendrimer Structure," J. Chem. Phys. **132**(12), 124901-1 (2010). **[CHRNS]**

Liu, Y., Chen, C.-Y., Chen, H.-L., Hong, K., Shew, C.-Y., Li, X., Liu, L., Melnichenko, Y.B., Smith, G.S., Herwig, K.W., Porcar, L., Chen, W.-R., "Electrostatic Swelling and Conformational Variation Observed in High-Generation Polyelectrolyte Dendrimers," J. Phys. Chem. Lett. **1**(13), 2020 (2010). **[CHRNS]**

Loizou, E., Porcar, L., Schexnailder, P., Schmidt, G., Butler, P., "Shear-Induced Nanometer and Micrometer Structural Responses in Nanocomposite Hydrogels," Macromol. **43**, 1041 (2010). **[CHRNS]**

Lokitz, B.S., Messman, J.M., Hinestrosa, J.P., Alonzo, J., Verduzco, R., Brown, R.H., Osa, M., Ankner, J.F., Kilbey, II, S. M., "Dilute Solution Properties and Surface Attachment of RAFT Polymerized 2-Vinyl-4,4-dimethyl Azlactone (VDMA)," Macromol. **42**, 9018 (2009). **[CHRNS]**

Long, Y.W., Huang, Q., Yang, L.X., Yu, Y., Lv, Y.X., Lynn, J.W., Chen, Y., Jin, C.Q., "Low-Temperature Neutron Diffraction Study of the Crystal and Magnetic Phase Transitions in $DyCrO_4$," J. Magn. Magn. Mater. **322**, 1912 (2010).

Louca, D., Kamazawa, K., Proffen, T., "Formation of Local Electric Dipoles with No Unique Polar Axis in $Tb_3Fe_5O_{12}$," Phys. Rev. B **80**(21), 214406-1 (2009). **[CHRNS]**

Lucas, G.E., "An Evolution of Understanding of Reactor Pressure Vessel Steel Embrittlement" J. Nucl. Mater., in press. **[CHRNS]**

Lumata, L.L., Besara, T., Kuhns, P.L., Reyes, A.P., Zhou, H.D., Wiebe, C.R., Balicas, L., Jo, Y.J., Brooks, J.S., Takano, Y., Case, M.J., Qiu, Y., Copley, J.R.D., Gardner, J.S., Choi, K.Y., Dalal, N.S., Hoch, M.J.R., "Low-Temperature Spin Dynamics in the Kagome System $Pr_3Ga_5SiO_{14}$," Phys. Rev. B **81**(22), 224416-1 (2010). **[CHRNS]**

Luzin, V., Prask, H.J., Gnäupel-Herold, T., Sampath, S., "Use of Neutron Diffraction for Stress Measurements in Thin and Thick Thermal Sprayed Coatings," Int. Heat Treat. Surf. Eng **4**(1), 17 (2010).

Luzin, V., Matejicek, J., Gnäupel-Herold, T.H., "Through-Thickness Residual Stress Measurement by Neutron Diffraction in Cu+W Plasma Spray Coatings," Mater. Sci. Forum **652**, 50 (2010).

Lynn, J.W., "Iron Based Superconductors," in "McGraw-Hill Yearbook of Science and Technology 2010," edited by unknown, (McGraw-Hill) 204 (2010).

Lynn, J.W., "Book review of *Neutron Scattering in Condensed Matter Physics,* by A. Furrer, et al." Neutron News **21**, 59 (2010).

Mackey, E.A., Paul, R.L., Spatz, R.O., Tomlin, B.E., Zeisler, R., "Quality Assurance in Homogeneity Assessment of Soil Standard Reference Materials," Trans. Am. Nucl. Soc. **101**, 114 (2009).

Mackey, E.A., Christopher, S.J., Lindstrom, R.M., Long, S.E., Marlow, A.F., Murphy, K.E., Paul, R.L., Popelka-Filcoff, R.S., Rabb, S.A., Sieber, J.R., Spatz, R.O., Tomlin, B.E., Wood, L.J., Yu, L.L., Zeisler, R., Yen, J.H., Wilson, S.A., Adams, M.G., Brown, Z.A., Lamothe, P.L., Taggart, J.E., Jones, C., Nebelsick, J., "Certification of Three NIST Renewal Soil Standard Reference Materials for Element Content: SRM 2709a San Joaquin Soil, SRM 2710a Montana Soil I, and SRM 2711a Montana Soil II," NIST Special Publication **260-172**, 2 (2010).

Mahabir, S., Wan, W., Katsaras, J., Nieh, M.-P., "Effects of Charge Density and Thermal History on the Morphologies on Spontaneously Formed Unilamellar Vesicles," J. Phys. Chem. B **114**, 5729 (2010). **[CHRNS]**

Malardier-Jugroot, C., Bowron, D.T., Soper, A.K., Johnson, M.E., Head-Gordon, T., "Structure and Water Dynamics of Aqueous Peptide Solutions in the Presence of Co-Solvents," Phys. Chem. Chem. Phys. **12**, 382 (2010). **[CHRNS]**

Mallamace, F., Branca, C., Corsaro, C., Leone, N., Spooren, J., Stanley, H.E., Chen, S.-H., "Dynamical Crossover and Breakdown of the Stokes-Einstein Relation in Confined Water and in Methanol-Diluted Bulk Water," J. Phys. Chem. B **114**, 1870 (2010). **[CHRNS]**

Mang, J.T., Hjelm, R.P., Francois, E.G., "Measurement of Porosity in a Composite High Explosive as a Function of Pressing Conditions by Ultra-Small-Angle Neutron Scattering with Contrast Variation," Propellants Explos. Pyrotech. **35**, 7 (2010). **[CHRNS]**

Manson, J.L., Lancaster, T., Blundell, S.J., Qiu, Y., Singleton, J., Sengupta, P., Pratt, F.L., Kang, J., Lee, C., Whangbo, M.-H., "Spin Gluctuations and Orbital Ordering in Quasi-One-Dimensional α-$Cu(dca)_2(pyz)$ {dca = Dicyanamide = $N(CN)_2$ -; pyz = Pyrazine}, a Molecular Analogue of $KCuF_3$," Polyhedron **29**, 514 (2010). **[CHRNS]**

Marcus, M.S., Simmons, J.M., Baker, S.E., Hamers, R.J., Eriksson, M.A., "Predicting the Results of Chemical Vapor Deposition Growth of Suspended Carbon Nanotubes," Nano Lett. **9**(5), 1806 (2009).

Marinenko, R.B., Turner, S., Simons, D.S., Rabb, S.A., Zeisler, R.L., Yu, L.L., Newbury, D.E., Paul, R.L., Ritchie, N.W.M., Leigh, S.D., Winchester, M.R., Richter, L.J., Meier, D.C., Scott, K.C.K., Klinedinst, D., Small, J.A., "Characterization of SiGe Films for Use as a National Institute of Standards and Technology Microanalysis Reference Material (RM8905)," Microsc. Microanal. **16**, 1 (2010).

Mason, P.E., Dempsey, C.E., Neilson, G.W., Kline, S.R., Brady, J.W., "Preferential Interactions of Guanidinum Ions with Aromatic Groups over Aliphatic Groups," J. Am. Chem. Soc. **131**, 16689 (2009). **[CHRNS]**

Matan, K., Ibuka, S., Morinaga, R., Chi, S.X., Lynn, J.W., Christianson, A.D., Lumsden, M.D., Sato, T.J., "Doping Dependence of Spin Dynamics in Electron-doped $Ba(Fe_{1-x}Co_x)_2As_2$," Phys. Rev. B, in press.

Mayumi, K., Nagao, M., Endo, H., Osaka, N., Shibayama, M., Ito, K., "Dynamics of Polyrotaxane Investigated by Neutron Spin Echo," Physica B **404**, 2600 (2009). **[CHRNS]**

Mayumi, K., Endo, H., Osaka, N., Yokoyama, H., Nagao, M., Shibayama, M., Ito, K., "Mechanically Interlocked Structure of Polyrotaxane Investigated by Contrast Variation Small-Angle Neutron Scattering," Macromol. **42**, 6327 (2009).

Mayumi, K., Ito, K., "Structure and Dynamics of Polyrotaxane and Slide-ring Materials," Polymer **51**, 959 (2010). **[CHRNS]**

McMullan, J.M., Wagner, N.J., "Directed Self-Assembly of Colloidal Crystals by Dielectrophoretic Ordering Observed with Small Angle Neutron Scattering (SANS)," Soft Matter , in press. **[CHRNS]**

Meli, L., Santiago, J.M., Lodge, T.P., "Path-Dependent Morphology and Relaxation Kinetics of Highly Amphiphilic Diblock Copolymer Micelles in Ionic Liquids," Macromol. **43**, 2018 (2010).

Melnichenko, Y.B., Mayama, H., Cheng, G., Blach, T., "Monitoring Phase Behavior of Sub- and Supercritical Co_2 Confined in Porous Fractal Silica with 85% Porosity," Langmuir **26**(9), 6374 (2010). **[CHRNS]**

Mikel, S.E., Biernacki, J.J., Gnäupel-Herold, T., "A Neutron Diffraction-Based Technique for Determining Phase-Resolved Strains in Portland Cement," ACI Mater. J. **106**(5), 455 (2009).

Mildner, D.F.R., Gubarev, M.V., "Wolter Optics for Neutron Focusing," Nucl. Instrum. Methods Phys. Res. A, in press.

Mirarefi, P., Lee, Jr., C.T., "Photo-Induced Unfolding and Inactivation of Bovine Carbonic Anhydrase in the Presence of a Photoresponsive Surfactant," Biochim. Biophys. Acta. **1804**, 106 (2010).

Mrozek, R.A., Cole, P.J., Cole, S.M., Schroeder, J.L., Schneider, D.A., Hedden, R.C., Lenhart, J.L., "Design of Nonaqueous Polymer Gels with Broad Temperature Performance: Impact of Solvent Quality and Processing Conditions," J. Mater. Res. **25**(6), 1105 (2010).

Mudivarthi, C., Laver, M., Cullen, J., Flatau, A.B., Wuttig, M., "Origin of Magnetostriction in Fe-Ga," J. Appl. Phys. **107**(9), 09A957-1 (2010). **[CHRNS]**

Mukherjee, P.P., Mukundan, R., Spendelow, J.S., Borup, R.L., Hussey, D.S., Jacobson, D.L., Arif, M., "High Resolution Neutron Imaging of Water in the Polymer Electrolyte Fuel Cell Membrane," ECS Trans. **25**(1), 505 (2009).

Mukundan, R., Lujan, R.W., Davey, J.R., Spendelow, J.S., Hussey, D.S., Jacobson, D.L., Arif, M., Borup, R.L., "Ice Formation in PEM Fuel Cells Operated Isothermally at Sub-Freezing Temperature," ECS Trans. **25**(1), 345 (2009).

Murray, L.J., Dinca, M., Yano, J., Chavan, S., Bordiga, S., Brown, C.M., Long, J.R., "Highly-Selective and Reversible O_2 Binding in Cr_3(1,3,5-Benzenetricarboxylate)$_2$," J. Am. Chem. Soc. **132**, 7856 (2010).

Nagao, M., Seto, H., "Full Fitting Analysis of the Relative Intermediate Form Factor Measured by Neutron Spin Echo," Physica B **404**(17), 2603 (2009). **[CHRNS]**

Nagao, M., "Observation of Local Thickness Fluctuations in Surfactant Membranes using Neutron Spin Echo," Phys. Rev. E. **80**(3), 031606-1 (2009). **[CHRNS]**

Nagao, M., Kawabata, Y., Seto, H., "High-Pressure SANS and NSE Experiments in Microemulsion Systems," Rev. High Pres. Sci. Tech. **19**(1), 52 (2009).

Nakatsuji, S., Nambu, Y., Onoda, S., "Novel Geometrical Frustration Effects in the Two-Dimensional Triangular-Lattice Antiferromagnet $NiGa_2S_4$ and Related Compounds," J. Phys. Soc. Jpn. **79**(1), 011003-1 (2010).

Nanda, H., Datta, S.A.K., Heinrich, F., Losche, M., Rein, A., Krueger, S., Curtis, J.E., "Electrostatic Interactions and the Binding Orientation of HIV-1 Matrix Studied by Neutron Reflectivity," Biophys. J., in press.

Nedoma, A.J., Lai, P., Jackson, A., Robertson, M.L., Wanakule, N.S., Balsara, N.P., "Phase Behavior of Asymmetric Multicomponent A/B/A-C Blends with Unequal Homopolymer Molecular Weights," Macromol. **43**, 3549 (2010). **[CHRNS]**

Nico, J.S., "Neutron Beta Decay," J. Phys. G: Nucl. Part. Phys. **36**, 104001 (2009).

Obrzut, J., Page, K.A., "Electrical Conductivity and Relaxation in Poly(3-hexylthiophene)," Phys. Rev. B **80**(19), 195211-1 (2009). **[CHRNS]**

O'Shaughnessy, C.M., Golub, R., Schelhammer, K.W., Swank, C.M., Seo, P.-N., Huffman, P.R., Dzhosyuk, S.N., Mattoni, C.E.H., Yang, L., Doyle. J.M., Coakley, K.J., Thompson, A.K., Mumm, H.P., Lamoreaux, S.K., McKinsey, D.N., Yang, G., "Measuring the Neutron Lifetime using Magnetically Trapped Neutrons." Nucl. Iustrum. Methods Phys. A **611**, 171 (2009).

Pabst, G., Kŭcerka, N., Nieh, M.P., Rheinstädter, M.C., Katsaras, J., "Applications of Neutron and X-ray Scattering to the Study of Biologically Relevant Model Membranes," Chem. Phys. Lipids **163**, 460 (2010).

Pafiti, K.S., Loizou, E., Patricklos, C.S., Porcar, L., "End-Linked Semifluorinated Amphiphilic Polymer Conetworks: Synthesis by Sequential Reversible Addition-Fragmentation Chain Transfer Polymerization and Characterization," Macromol. **43**, 5195 (2010).

Park, J.K., Jones, P.J., Sahagun, C., Page, K.A., Hussey, D.S., Jacobson, D.L., Morgan, S.E., Moore, R.B., "Electrically Stimulated Gradients in Water and Counterion Concentrations within Electroactive Polymer Actuators," Soft Matter **6**, 1444 (2010).

Park, M.J., Balsara, N.P., Jackson, A., "Order-Disorder Transitions in Block Copolymer Electrolytes at Equilibrium with Humid Air," Macromol. **42**, 6808 (2009). **[CHRNS]**

Paul, R.L., Hossain, T., Wu, L., Downing, R.G., "Determination of Trace Boron in Bulk High-Purity Silicon," Trans. Am. Nucl. Soc. **101**, 112 (2009).

Paul, R.L., Mackey, E.A., Zeisler, R., Spatz, R.O., Tomlin, B.E., "Determination of Elements in SRM Soil 2709a by Neutron Activation Analysis," J. Radioanal. Nucl. Chem. **282**(3), 945 (2009).

Peri, S.R., Kim, H., Akgun, B., Enlow, J., Jiang, H., Bunning, T.J., Li, X., Foster, M.D., "Structure of Copolymer Films Created by Plasma Enhanced Chemical Vapor Deposition," in press.

Peri, S.R., Habersberger, B., Akgun, B., Jiang, H., Enlow, J., Bunning, T.J., Majkrzak, C.F., Foster, M.D., "Variations in Cross-link Density with Deposition Pressure in Ultrathin Plasma Polymerized Benzene and Octafluorocyclobutane Films," Polymer , in press.

Perriman, A.W., Williams, D.S., Jackson, A.J., Grillo, I., Koomullil, J.M., Ghasparian, A., Robinson, J.A., Mann, S., "Synthetic Viruslike Particles and Hybrid Constructs Based on Lipopeptide Self-Assembly," Small **6**(11), 1191 (2010). **[CHRNS]**

Petorak, C., Ilavsky, J., Wang, H., Porter, W., Trice, R., "Microstructural Evolution of 7 wt.% Y_2O_3-ZrO_2 Thermal Barrier Coatings due to Stress Relaxation at Elevated Temperatures and the Concomitant Changes in Thermal Conductivity," Surf. Coat. Technol. in press.

Phelan, D., Millican, J.N., Gehring, P.M., "Dissimilarity of Polar Displacements in Barium and Lead Based Relaxors," Appl. Phys. Lett. , in press.

Porcar, L., Falus, P., Chen, W.-R., Faraone, A., Fratini, E., Hong, K., Baglioni, P., Liu, Y., "Formation of the Dynamic Clusters in Concentrated Lysozyme Protein Solutions," J. Phys. Chem. Lett. **1**, 126 (2010). **[CHRNS]**

Porcar, L., Hong, K., Butler, P.D., Herwig, K.W., Smith, G.S., Liu, Y., Chen, W.-R., "Intramolecular Structural Change of PAMAM Dendrimers in Aqueous Solutions Revealed by Small Angle Neutron Scattering," J. Phys. Chem. B **114**, 1751 (2010). **[CHRNS]**

Posen, I.D., McQueen, T.M., Williams, A.J., West, D.V., Huang, Q., Cava, R.J., "Geometric Magnetic Frustration in the *R*-Type Ferrite $SrSn_2Ga_{1.3}Cr_{2.7}O_{11}$ and the Spinel-Based Chromates," Phys. Rev. B **81**(13), 134413-1 (2010).

Preston, J.S., Fu, R.S., Pasaogullari, U., Hussey, D.S., Jacobson, D.L., "An Updated Look at the Role of Micro-Porous Layer on Liquid Water Distribution in Polymer Electrolyte Fuel Cells," ECS Trans. **25**(1), 311 (2009).

Pynn, R., Fitzsimmons, M.R., Lee, W.T., Stonaha, P., Shah, V.R., Washington, A.L., Kirby, B.J., Majkrzak, C.F., Maranville, B.B., "Birefringent Neutron Prisms for Spin Echo Scattering Angle Measurement," Physica B **404**, 2582 (2009).

Qiu, Y., Bao, W., Zhao, Y., Broholm, C., Stanev, V., Tesanovic, Z., Gasparovic, Y.C., Chang, S., Hu, J., Qian, B., Fang, M., Mao, Z., "Spin Gap and Resonance at the Nesting Wave Vector in Superconducting $FeSe_{0.4}Te_{0.6}$," Phys. Rev. Lett. **103**(6), 067008-1 (2009). **[CHRNS]**

Quan, P., Lai, M.-C., Hussey, D.S., Jacobson, D.L., Kumar, A., Hirano, S., "Time-Resolved Water Measurement in a PEM Fuel Cell Using High-Resolution Neutron Imaging Technique," J. Fuel Cell Sci. Technol., in press.

Raman, K.V., Watson, S.M., Shim, J.H., Borchers, J.A., Chang, J., Moodera, J.S., "Effect of Molecular Ordering on Spin and Charge Injection in Rubrene," Phys. Rev. B **80**(19), 195212-1 (2009).

Ramirez-Cuesta, A.J.T., Ryan, K., Brown, C.M., "AB-Initio Calculations of the Dynamics of Select Hydrogen Storage Materials, Compared to Inelastic Neutron Scattering Spectra," in "ACS Division Proceedings, Division of Fuel Chemistry," edited by unknown, (ACS, Fall National Meeting & Exposition 2009 Conf. Proc., August 2009, Washington, D.C.) **54**(2), (2009).

Ratcliff, II, W., Lima Sharma, A.L., Gomes, A.M., Gonzalez, J.L., Huang, Q., Singleton, J., "The Magnetic Ground State of $CaMn_2Sb_2$," J. Magn. Magn. Mater. **321**(17), 2612 (2009).

Ratcliff, II W., Kienzle, P.A., Lynn, J.W., Li, S., Dai, P., Chen, G.F., Wang, N.L., "Magnetic Form Factor of $SrFe_2As_2$: Neutron Diffraction Measurements," Phys. Rev. B **81**(14), 140502-1 (2010).

Ren, S., Laver, M., Wuttig, M., "Nanolamellar Magnetoelectric $BaTiO_3$-$CoFe_2O_4$ Bicrystal," Appl. Phys. Lett. **95**(15), 153504-1 (2009).

Rexeisen, E.L., Fan, W., Pangburn, T.O., Tarbagil, R.R., Bates, F.S., Lodge, T.P., Tsapatsis, M., Kokkoli, E., "Self-Assembly of Fibronectin Mimetic Peptid-Amphiphile Nanofibers," Langmuir **26**(3), 1953 (2010).

Rikkou, M.D., Loizou, E., Porcar, L., Butler, P., Patrickios, C.S., "Degradable Amphiphilic End-linked Conetworks with Aqueous Degradation Rates Determined by Polymer Topology," Macromol. **42**, 9412 (2009). **[CHRNS]**

Rikkou, M.D., Loizou, E., Patrickios, C.S., Porcar, L., "Structural Characterization of Amphiphilic Polymer Conetworks End-Linked with the Optimal Amount of Cross-Linker," Eur. Polym. J. **46**, 441 (2010). **[CHRNS]**

Rodriguez, E.E., Zavalij, P., Hsieh, P.-Y., Green, M.A., "Iodine as an Oxidant in the Topotactic Deintercalation of Interstitial Iron in $Fe_{1+x}Te$," J. Am. Chem. Soc. **132**, 10006 (2010).

Roh, J.H., Guo, L., Kilburn, J.D., Briber, R.M., Irving, T., Woodson, S.A., "Multistage Collapse of a Bacterial Ribozyme Observed by Time-Resolved Small-Angle X-ray Scattering," J. Am. Chem. Soc. **132**, 10148 (2010).

Ross, K.A., Ruff, J.P.C., Adams, C.P., Gardner, J.S., Dabkowska, H.A., Qiu, Y., Copley, J.R.D., Gaulin, B.D., "Two-Dimensional Kagome Correlations and Field Induced Order in the Ferromagnetic XY Pyrochlore $Yb_2Ti_2O_7$," Phys. Rev. Lett **103**(22), 227202-1 (2009). **[CHRNS]**

Rubinson, K.A., Krueger, S., "Poly(ethylene glycol)s 2000-8000 in Water May be Planar: A Small-Angle Neutron Scattering (SANS) Structure Study," Polymer **50**(20), 4852 (2009).

Rule, K.C., Ehlers, G., Gardner, J.S., Qiu, Y., Moskvin, E., Kiefer, K., Gerischer, S., "Neutron Scattering Investigations of the Partially Ordered Pyrochlore $Tb_2Sn_2O_7$," J. Phys.: Condens. Matter **21**, 486005 (2009). **[CHRNS]**

Russo, D., Copley, J.R.D., Ollivier, J., Teixeira, J., "On the Behaviour of Water Hydrogen Bonds at Biomolecular Sites: Dependences on Temperature and on Network Dimensionality," J. Mol. Struct. **972**, 81 (2010). **[CHRNS]**

Sahin,I., Yilmazer,N., "A Discrete Fourier Transform for Alignment of Visual Evoked Potentials," in "Computational Intelligence in Bioinformatics and Computational Biology - CIBCB," edited by unknown, (IEEE CIBCB, May 2010, Montreal, Canada) 1 (2010).

Sahoo, P., Adarsh, N.N., Chacko, G.E., Raghavan, S.R., Puranik, V.G., Dastidar, P., "Combinatorial Library of Primaryalkylammonium Dicarboxylate Gelators: A Supramolecular Synthon Approach," Langmuir **25**(15), 8742 (2009).

Sahoo, P.P., Gaudin, E., Darriet, J., Row, T.N.G., "Synthesis, Characterization, and Crystallographic Study in PbO-Bi_2O_3-V_2O_5 System: $Pb_{3-x}Bi_{2x/3}V_2O_8$ ($0.20 \leq x \leq 0.50$)," Inorg. Chem. **49**, 5603 (2010).

Sasai, K., Kofu, M., Ibberson, R.M., Hirota, K., Yamaura, J.-I., Hiroi, Z., Yamamuro, O., "A Novel Isomorphic Phase Transition in β-Pyrochlore Oxide KOs_2O_6: A Study using High Resolution Neutron Powder Diffraction," J. Phys.: Condens. Matter **22**, 015403 (2010).

Savici, A.T., Granroth, G.E., Broholm, C.L., Pajerowski, D.M., Brown, C.M., Talham, D.R., Meisel, M.W., Schmidt, K.P., Uhrig, G.S., Nagler, S.E., "Neutron Scattering Evidence for Isolated Spin-½ Ladders in $(C_5D_{12}N)_2CuBr_4$," Phys. Rev. B **80**(9), 094411-1 (2009). **[CHRNS]**

Segawa, K., Kofu, M., Lee, S.-H., Tsukada, I., Hiraka, H., Fujita, M., Chang, S., Yamada, K., Ando, Y., "Zero-Doping State and Electron-Hole Asymmetry in an Ambipolar Cuprate," Nat. Phys., in press. **[CHRNS]**

Shane, D.T., Corey, R.L., McIntosh, C., Rayhel, L.H., Bowman, Jr., R.C., Vajo, J.J., Gross, A.F., Conradi, M.S., "$LiBH_4$ in Carbon Aerogel Nanoscaffolds: An NMR Study of Atomic Motions," J. Phys. Chem. C **114**, 4008 (2010).

Sharpless, K.E., Lindstrom, R.M., Nelson, B.,C., Phinney, K.W., Rimmer, C.A., Sander, L.C., Schantz, M.M., Spatz, R.O., Thomas, J.B., Turk, G.C., Wise, S.A., Wood, L.J., Yen, J.H., "Preparation and Characterization of Standard Reference Material 1849Infant/Adult Nutritional Formula," J. AOAC Int. **93**(4), 1262 (2010).

Shenoy, S., Moldovan, R., Fitzpatrick, J., Vanderah, D.J., Deserno, M., Lösche, M., "In-Plane Homogeneity and Lipid Dynamics in Tethered Bilayer Lipid Membranes (tBLMs)," Soft Matter, in press.

Shibayama, M., Matsunaga, T., Nagao, M., "Evaluation of Incoherent Scattering Intensity by Transmission and Sample Thickness," J. Appl. Crystallogr. **42**(4), 621 (2009).

Shlyk, L., Ueland, B.G., Lynn, J.W., Huang, Q., De Long, L.E., Parkin, S., "Magnetic Structure, Magnetization and Magnetotransport Properties of (Ba,Sr)Md$_{2\pm x}T_{4\pm x}$O$_{11}$ (M=Fe, Co; T=Ru, Ti)," Phys. Rev. B **81**(18), 184415-1 (2010).

Shoenfelt, J., Mitkus, R.J., Zeisler, R., Spatz, R.O., Powell, J., Fenton, M.J., Squibb, K.A., Medvedev, A.E., "Involvement of TLR2 and TLR4 in Inflammatory Immune Responses Induced by Fine and Coarse Ambient Air Particulate Matter," J. Leukocyte Biol. **86**, 303 (2009).

Simmons, J.M., Yildirim, "Thermally Activated Pore Opening in a Metal Organic Framework", in "ACS Division Proceedings, Division of Fuel Chemistry," edited by unknown, (ACS, Fall National Meeting & Exposition 2009 Conf. Proc., August 2009, Washington, D.C.) **54**(2), (2009). **[CHRNS]**

Singh, S., Basu, S., Gupta, M., Majkrzak, C.F., Kienzle, P.A., "Growth Kinetics of Intermetallic Alloy Phase at the Interfaces of Ni/Al Multilayer using Polarized Neutron and X-ray Reflectometry," Phys. Rev. B **81**(23), 235413-1 (2010).

Singh, Y., Green, M.A., Huang, Q., Kreyssig, A., McQueeney, R.J., Johnston, D.C., Goldman, A.I., "Magnetic Order in $BaMn_2As_2$ from Neutron Diffraction Measurements," Phys. Rev. B **80**(10), 100403-1 (2009).

Siritanon, T., Laurita, G., Macaluso, R.T., Millican, J.N., Sleight, A.W., Subramanian, M.A., "First Observation of Electronic Conductivity in Mixed-Valence Tellurium Oxides," Chem. Mater. **21**, 5572 (2009).

Sitepu, H., "Texture and Structural Refinement Using Neutron Diffraction Data from Molybdite (MoO_3) and Calcite ($CaCO_3$) Powders and a Ni-Rich $Ni_{50.7}Ti_{49.30}$ Alloy," Powder Diffr. **24**(4), 315 (2009).

Smith, M.B., McGillivray, D.J., Genzer, J., Lösche, M., Kilpatrick, P.K., "Neutron Reflectometry of Supported Hybrid Bilayers with Inserted Peptide," Soft Matter **6**, 862 (2010).

Spernjak, D., Prasad, A.K., Advani, S.G., "In Situ Comparison of Water Content and Dynamics in Parallel, Single-Serpentine, and Interdigitated Flow Fields of Polymer Electrolyte Membrane Fuel Cells," J. Power Sources **195**(11), 3553 (2010).

Stavila, V., Her, J.-H., Zhou, W., Hwang, S.-J., Kim, C., Ottley, L.A.M., Udovic, T.J., "Probing the Structure, Stability and Hydrogen Storage Properties of Calcium Dodecahydro-*Closo*-Dodecaborate," J. Solid State Chem. **183**, 1133 (2010).

Stock, C., Jonas, S., Broholm, C., Nakatsuji, S., Nambu, Y., Onuma, K., Maeno, Y., Chung, J.-H., "Neutron-Scattering Measurement of Incommensurate Short-Range Order in Single Crystals of the $S = 1$ Triangular Antiferromagnet $NiGa_2S_4$," Phys. Rev. Lett. **105**(3), 037402-1 (2010). **[CHRNS]**

Stock, C., Chapon, L.C., Adamopoulos, O., Lappas, A., Giot, M., Taylor, J.W., Green, M.A., Brown, C.M., Radaelli, P.G., "One-Dimennsional Magnetic Fluctuations in the Spin-2Triangular Lattice α-$NaMnO_2$," Phys. Rev. Lett. **103**(7), 077202-1 (2009). **[CHRNS]**

Stock, C., Van Eijck, L., Fouquet, P., Maccarini, M., Gehring, P.M., Xu, G., Luo, H., Zhao, X., Li, J., Viehland, D., "Interplay Between Static and Dynamic Polar Correlations in Relaxor $Pb(Mg_{1/3}Nb_{2/3})O_3$," Phys. Rev. B **81**(14), 144127-1 (2010). **[CHRNS]**

Stoltz, C.A., Mason, B.P., Hooper, J., "Neutron Scattering Study of Internal Void Structure in RDX," J. Appl. Phys. **107**(10), 103527-1 (2010). **[CHRNS]**

Sumida, K., Horike, S., Kaye, S.S., Herm, Z.R., Queen, W.L., Brown, C.M., Grandjean, F., Long, G.J., Dailly, A., Long, J.R., "Hydrogen Storage and Carbon Dioxide Capture in an Iron-Based Sodalite-Type Metal-Organic Framework (Fe-BTT) Discovered *via* High-Throughput Methods," Chem. Sci., in press.

Sun, D., Ma, S., Simmons, J.M., Li, J.-R., Yuan, D., Zhou, H.-C., "An Unusual Case of Symmetry-Preserving Isomerism," Chem. Commun. **46**, 1329 (2010).

Sun, K., Raghavan, S.R., "Thermogelling Aqueous Fluids Containing Low Concentrations of Pluronic F127 and Laponite Nanoparticles," Langmuir **26**(11), 8015 (2010).

Taribagil, R.R., Hillmyer, M.A., Lodge, T.P., "Hydrogels from ABA and ABC Triblock Polymers," Macromol. **43**, 5396 (2010). **[CHRNS]**

Thomas, J.J., Allen, A.J., Jennings, H.M., "Hydration Kinetics and Microstructure Development of Normal and $CaCl_2$-Accelerated Tricalcium Silicate Pastes," J. Phys. Chem. C **113**, 19836 (2009).

Thomas, J.J., Jennings, H.M., Allen, A.J., "Relationships between Composition and Density of Tobermorite, Jennite, and Nanoscale $CaO\text{-}SiO_2\text{-}H_20$," J. Phys. Chem. C **114**, 7594 (2010). **[CHRNS]**

Thompson, A.J., Sharp, J.W., Rawn, C.J., "Microstructure and Crystal Structure in TAGS Compositions," J. Electron. Mater. **38**(7), 1407 (2009).

Thompson, S.M., Ma, H.B., "Effect of Localized Heating on Three-Dimensional Flat-Plate Oscillating Heat Pipe," Adv. Mech. Eng. **2010** Article ID 465153, 1 (2010).

Todd, A.D.W., Ferguson, P.P., Barker, J.G., Fleischauer, M.D., Dahn, J.R., "Comparison of Mechanically Milled and Sputter Deposited Tin-Cobalt-Carbon Alloys using Small Angle Neutron Scattering," J. Electrochem. Soc. **156**(12), A1034 (2009).

Tominaga, T., Osada, Y., Gong, J.P., "Structural Approaches on the Toughness in Double Network Hydrogels," in "Chemomechanical Instabilities in Responsive Materials," edited by Borckman, P., De Kepper, P., Kholehlov, R., and Métens, S., (NATO Science for Peace and Security Series A: Chemistry and Biology), 117 (2009). **[CHRNS]**

Tomlin, B.E., Zeisler, R., "Improvements in Determinations Using the Cu-64 Annihilation Gamma Rays," Appl. Radiat. Isot. **67**(12), 2075 (2009).

Tristram-Nagle, S., Kim, D.J., Akhunzada, N., Kŭcerka, N., Mathai, J.C., Katsaras, J., Zeidel, M., Nagle, J.F., "Structure and Water Permeability of Fully Hydrated DiphytanoylPC," Chem. Phys. Lipids **163**, 630 (2010). **[CHRNS]**

Tsao, C.-S., Liu, Y., Li, M., Zhang, Y., Leao, J.B., Chang, H.-W., Yu, M.-S., Chen, S.-H., "Neutron Scattering Methodology for Absolute Measurement of Room-Temperature Hydrogen Storage Capacity and Evidence for Spillover Effect in a Pt-Doped Activated Carbon," J. Phys. Chem. Lett. **1**(10), 1569 (2010).

Tu, R.S., Marullo, R., Pynn, R., Bitton, R., Bianco-Peled, H., Tirrell, M.V., "Cooperative DNA Binding and Assembly by a bZip Peptide-Amphiphile," Soft Matter **6**, 1035 (2010).

Ueland, B.G., Gardner, J.S., Williams, A.J., Dahlberg, M.L., Kim, J.G., Qiu, Y., Copley, J.R.D., Schiffer, P., Cava, R.J., "Coexisting Magnetic Order and Cooperative Paramagnetism in the Stuffed Pyrochlore $Tb_{2+x}Ti_{2-2x}Nb_xO_7$," Phys. Rev. **81**(6), 060408-1 (2010). **[CHRNS]**

Ueland, B.G., Lynn, J.W., Laver, M., Choi, Y.J., Cheong, S.-W., "Origin of Electric-Field-Induced Magnetization in Multiferroic $HoMnO_3$," Phys. Rev. Lett. **104**(14), 147204-1 (2010). **[CHRNS]**

van der Zaag, P. J., Borchers, J.A., "Antiferromagnetic-Ferromagnetic Oxide Multilayers: Fe_3O_4-Based Systems as a Model," in "Magnetic Properties of Antiferromagnetic Oxide Materials,"edited by Duò, L., Finazzi, M., and Ciccacci, F, (Wiley-VCH Verlag GMBH & Co. KGaA, Weihheim) Chap. 7, 239 (2010).

Verdal, N., Hartman, M.R., Jenkins, T., DeVries, D.J., Rush, J.J., Udovic, T.J., "Reorientational Dynamics of $NaBH_4$ and KBH_4," J. Phys. Chem. C **114**, 10027 (2010). **[CHRNS]**

Verdal, N., Hartman, M.R., Bacon, M., Jenkins, T.A., Rush, J.J., Udovic, T.J, "Hydorgen Dynamics of Alkali-Metal Borohydrides," in "ACS Division Proceedings, Division of Fuel Chemistry," edited by unknown, (ACS, Fall National Meeting & Exposition 2009 Conf. Proc., August 2009, Washington, D.C.) **54**(2), (2009). **[CHRNS]**

Virgili, J.M., Nedoma, A.J., Segalman, R.A., Balsara, N.P., "Ionic Liquid Distribution in Ordered Block Copolymer Solutions," Macromol. **43**, 3750 (2010).

Wang, B., Tchessalov, S., Cicerone, M.T., Warne, N.W., Pikal, M.J., "Impact of Sucrose Level on Storage Stability of Proteins in Freeze-Dried Solids: II. Correlation of Aggregation Rate with Protein Structure and Molecular Mobility," J. Pharm. Sci. **98**(9), 3145 (2009). **[CHRNS]**

Wang, B., Cicerone, M.T., Aso, Y., Pikal, M.J., "The Impact of Thermal Treatment on the Stability of Freeze-Dried Amorphous Pharmaceuticals: II. Aggregation in an IgG1Fusion Protein," J. Pharm. Sci. **99**(2), 683 (2010).

Wang, B., Pikal, M.J., "The Impact of Thermal Treatment on the Stability of Freeze Dried Amorphous Pharmaceuticals: I. Dimer Formation in Sodium Ethacrynate," J. Pharm. Sci. **99**(2), 663 (2010).

Wang, C.-W., Wu, C.-M., Li, C.-Y., Karna, S.K., Hsu, C.-K., Li, C.H.C., Li, W.-H., Yu, C.-C., Wu, C.-P., Chou, H., Lynn, J.W., "Short Range Magnetic Correlations Induced by La Substitution in $Ho_{1-x}La_xMn_2O_5$," J. Phys.: Condens. Matter **22**, 246002 (2010).

Wang, H., "Dispersing Carbon Nanotubes Using Surfactants," Curr. Opin. Colloid Interface Sci. **14**, 364 (2009). **[CHRNS]**

Wang, M., Luo, H., Zhao, J., Zhang, C., Wang, M., Marty, K., Chi, S., Lynn, J.W., Schneidewind, A., Li, S., Dai, P., "Electron-Doping Evolution of the Low-Energy Spin Excitations in the Iron Arsenide Superconductor $BaFe_{2-x}Ni_xAs_2$," Phys. Rev. B **81**(17), 174524-1 (2010).

Wang, X., Yakovlev, S., Beers, K.M., Park, M.J., Mullin, S.A., Downing, K.H., Balsara, N.P., "On the Origin of Slow Changes in Ionic Conductivity of Model Block Copolymer Electrolyte Membranes in Contact with Humid Air," Macromol. **43**, 5306 (2010). **[CHRNS]**

Wang, Y., Mukherjee, P.P., Mishler, J., Mukundan, R., Borup, R.L., "Cold Start of Polymer Electrolyte Fuel Cells: Three-Stage Startup Characterization," Electrochim. Acta **55**, 2636 (2010).

Weck, P.F., Kim, E., Poineau, F., Rodriguez, E.E., Sattelberger, A.P., Czerwinski, K.R., "Structural and Electronic Trends in Rare-Earth Technetate Pyrochlores," Dalton Trans., in press.

Weigandt, K. M., Pozzo, D.C., Porcar, L., "Structure of High Density Fibrin Networks Probed with Neutron Scattering and Rheology," Soft Matter **51**(21), 4321 (2009). **[CHRNS]**

Wen, J., Xu, G., Xu, Z., Lin, Z.W., Li, Q., Chen, Y., Chi, S., Gu, G., Tranquada, J.M., "Effect of Magnetic Field on the Spin Resonance in $FeTe_{0.5}Se_{0.5}$ as seen via Inelastic Neutron Scattering," Phys. Rev. B **81**(10), 100513-1 (2010).

Wen, J., Xu, G., Gu, G., Shapiro, S.M., "Robust Charge and Magnetic Orders under Electric Field and Current Multiferroic $LuFe_2O_4$," Phys. Rev. B **81**(14), 144121-1 (2010).

Wen, J., Xu, G., Xu, Z., Lin, Z.W., Li, Q., Ratcliff, W., Gu, G., Tranquada, J.M., "Short-Range Incommensurate Magnetic Order Near the Superconducting Phase Boundary in $Fe_{1+\delta}Te_{1-x}Se_x$," Phys. Rev. B **80**(10), 104506-1 (2009).

West, D.V., Posen, I.D., Huang, Q., Zandbergen, H.W., McQueen, T.M., Cava, R.J., "$PbMn(SO_4)_2$: A New Chiral Antiferromagnet," J. Solid State Chem. **182**(9), 2461 (2009).

Whitney, S.M., Biegalski, S.R.F., Downing, G., "Benchmarking and Analysis of ^{6}Li Neutron Depth Profiling of Lithium Ion Cell Electrodes," J. Radioanal. Nucl. Chem. **282**, 173 (2009).

Wietfeldt, F.E., Byrne, J., Collett, B., Dewey, M.S., Jones, G.L., Komives, A., Laptev, A., Nico, J.S., Noid, G., Stephenson, E.J., Stern, I., Trull, C., Yerozolimsky, B.G., "aCORN: An Experiment to Measure the Electron-Antineutrino Correlation in Neutron Decay," Nucl. Instrum. Meth. A **611**, 207 (2009).

Williams, R.E., Richards, W.J., O'Kelly, S., Rowe, J.M., Diamond, D.J., Hanson, A.L., Cheng, L.-Y., Cuadra, A., "LEU Conversion of the NIST Research Reactor: Maintaining Core Geometry to Avoid a Startup Core," in "Proceedings of the Conference on the Physics of Reactors," (PHYSOR, Pittsburg, PA, May 2010) CD-ROM (2010).

Wu, H., Zhou, W., Pinkerton, F.E., Meyer, M.S., Srinivas, G., Yildirim, T., Udovic, T.J., Rush, J.J., "A New Family of Metal Borohydride Ammonia Borane Complexes: Synthesis, Structures, and Hydrogen Storage Properties," J. Mater. Chem., in press.

Wu, H., Simmons, J.M., Liu, Y, Brown, C.M., Wang, X.-S., Ma, S., Peterson, V.K., Southon, P.D., Kepert, C.J., Zhou, H.-C., Yildirim, T., Zhou, W., "Metal-Organic Frameworks with Exceptionally High Methane Uptake: Where and How is Methane Stored?," Chem. Eur. J. **16**, 5205 (2010).

Wu, H., Skripov, A.V., Udovic, T.J., Rush, J.J., Derakhshan, S., Kleinke, H., "Hydrogen in Ti_3Sb and Ti_2Sb: Neutron Vibrational Spectroscopy and Neutron Diffraction Studies," J. Alloys Compd. **496**, 1 (2010). **[CHRNS]**

Wu, H., Zhou, W., Udovic, T.J., Rush, J.J., Yildirim, T., "Crystal Chemistry and Dehydrogenation/Rehydrogenation Properties of Perovskite Hydrides $RbMgH_3$ and $RbCaH_3$," J. Phys. Chem. C **113**(33), 15091 (2009).

Wu, H., Simmons, J.M., Srinivas, G., Zhou, W., Yildirim, T., "Adsorption Sites and Binding Nature of CO_2 in Prototypical Metal-Organic Frameworks: A Combined Neutron Diffraction and First-Principles Study," J. Phys. Chem. Lett. **1**(13), 1946 (2010).

Wu, Y., Yu, B., Jackson, A., Zha, W., Lee, L.J., Wyslouzil, B.E., "Coaxial Electrohydrodynamic Spraying: A Novel One-Step Technique to Prepare Oligodeoxynucleotide Encapsulated Lipoplex Nanoparticles," Mol. Pharm. **6**(5), 1371 (2009).

Xiang, S., Zhou, W., Gallegos, J.M., Liu, Y., Chen, B., "Exceptionally High Acetylene Uptake in a Micro-porous Metal-Organic Framework with Open Metal Sites," J. Am. Chem. Soc. **131**(34), 12415 (2009).

Xiang, S., Zhou, W., Zhang, Z., Green, M.A., Liu, Y., Chen, B., "Open Metal Sites within Isostructural Metal-Organic Frameworks for Differential Recognition of Acetylene and Extraordinarily High Acetylene Storage Capacity at Room Temperature," Angew. Chem. Int. Edit. **49**(27), 4615 (2010).

Xie, W., He, J., Kang, H.J., Tang, X., Zhu, S., Laver, M., Wang, S., Copley, J.R.D., Brown, C.M., Zhang, Q., Tritt, T.M., "Identifying the Specific Nanostructures Responsible for the High Thermoelectric Performance of $(Bi,Sb)_2Te_3$ Nanocomposites," Nano Letters , in press. **[CHRNS]**

Yamada, N.L., Endo, H., Osaka, N., Kawabata, Y., Nagao, M., Takeda, T., Seto, H., Shibayama, M., "Dector Area Expansion at iNSE Neutron Spin Echo Spectrometer," Physica B **404**(17), 2607 (2009).

Yang, C.-C., Li, W.-H., Wu, C.-M., Li, C.H.C., Sun, J., Lynn, J.W., "Interplay Between the Crystalline and Magnetic Structures in Lightly Cr-Doped $Bi_{0.37}Ca_{0.63}Mn_{0.96}Cr_{0.04}O_{2.99}$," Inorg. Chem. **49**, 3297 (2010).

Yang, H., Shin, K., Tae, G., Satija, S.K., "Structure of a Monolayer of Poly(Ethylene Glycol) End-Capped with a Fluoroalkyl Group and its Relationship with Protein Adsorption at the Aqueous Interface," Soft Matter **5**(14), 2731 (2009).

Yang, K.X., Kitto, M.E., Orsini, J.P., Swami, K., Beach, S.E., "Evaluation of Sample Pretreatment Methods for Multiwalled and Single-walled Carbon Nanotubes for the Determination of Metal Impurities by ICPMS, ICPOES, and Instrument Neutron Activation Analysis," J. Anal. At. Spectrom., in press.

Yao, J., Wang, Z., van Tol, J., Dalal, N.S., Aitken, J.A., "Site Preference of Manganese on the Copper Site in Mn-Substituted $CuInSe_2$ Chalcopyrites Revealed by a Combined Neutron and X-ray Powder Diffraction Study," Chem. Mater. **22**(5), 1647 (2010).

Ye, F., Chi, S., Fernandez-Baca, J.A., Moreo, A., Dagotto, E., Lynn, J.W., Mathieu, R., Kaneko, Y., Tokura, Y., Dai, P., "Electronic Self-Organization in the Single-Layer Manganite $Pr_{1-x}Ca_{1+x}MnO_4$," Phys. Rev. Lett. **103**(16), 167202-1 (2009).

Yoonessi, M., Dang, T.D., Heinz, H., Wheeler, R., Bai, Z., "Investigation of Nanostructures and Properties of Sulfonated Poly(arylenethioethersulfone) Copolymer as Proton Conducting Materials by Small Angle neutron Scattering," Polymer **51**, 1585 (2010).

Yu, J., Louca, D., Phelan, D., Tomiyasu, K., Horigane, K., Yamada, K., "Uncharacteristic Phase Separation Trends with the Ionic Size in Cobaltites," Phys. Rev. B **80**(5), 052402-1 (2009). **[CHRNS]**

Yuan, G., Li, C., Satija, S.K., Karim, A., Douglas, J.F., Han, C.C., "Observation of a Characteristic Length Scale in the Healing of Glassy Polymer Interfaces," Soft Matter , in press.

Yue, M., Li, Z.Q., Xu, H., Huang, Q.Z., Liu, X.B., Liu, D.M., Zhang, J.X., "Effect of Annealing on the Structure and Magnetic Properties of $Mn_{1.1}Fe_{0.9}P_{0.8}Ge_{0.2}$ Compound," J. Appl. Phys. **107**(9), 09A939-1 (2010).

Zeisler, R., Ünlü, K., Heller-Zeisler, S.F., Williamson, R.C., "Current Status, Trends, and Needs in Radiochemical Education: the US and Abroad Panel Summary and Discussion," in "8th International Conference on Methods and Applications of Radioanalytical Chemistry: MARC-VII," edited by Ünlü, K., Heller-Zeisler, S., and Zeisler, R., (AIP Conf. Proc., April 2009 Kona, HI,) **1164**, 3 (2009).

Zeisler, R., Tomlin, B.E., Murphy, K.E., Kŭcera, J., "Neutron Activation Analysis with Pre- and Post- Irradiation Chemical Separation for the Value Assignments of Al, V, and Ni in the New Bovine Liver SRM 1577C," J. Radioanal. Nucl. Chem. **282**(1), 69 (2009).

Zenobia, S.J., Kulcinski, G.L., "Formation and Retention of Surface Pores in Helium-Implanted Nano-Grain Tungsten for Fusion Reactor First-Wall Materials and Divertor Plates," Phys. Scr. **T138**, 014049 (2009).

Zhang, F., Ilavsky, J., Long, G.G., Quintana, J.P.G., Allen, A.J., Jemian, P.R., "Glassy Carbon as an Absolute Intensity Calibration Standard for Small-Angle Scattering," Metall. Mater. Trans. A **41A**, 1151 (2010).

Zhang, X., Yager, K.G., Kang, S., Fredin, N.J., Akgun, B., Satija, S., Douglas, J.F., Karim, A., Jones, R.L., "Solvent Retention in Thin Spin-Coated Polystyrene and Poly(methyl methacrylate) Homopolymer Films Studied by Neutron Reflectometry," Macromol. **43**, 1117 (2010).

Zhao, L., Robinson, L., "A Comparison Between Cold and Thermal Neutron Prompt Gamma Activation Analysis in the Determination of Carbon, Nitrogen, and Phosphorus in Cattail," J. Radioanal. Nucl. Chem. **282**(1), 151 (2009).

Zhou, H.D., Wiebe, C.R., Janik, J.A., Vogt, B., Harter, A., Dalal, N.S., Gardner, J.S., "Spin Glass Transitions in the Absence of Chemical Disorder for the Pyrochlores $A_2Sb_2O_7$ (A=Mn, Co, Ni)," J. Solid State Chem. **183**, 890 (2010).

Zhou, S., Zhang, J., Liu, D., Lin, Z., Huang, Q., Bao, L., Ma, R., Wei, Y., "Synthesis and Properties of Nanostructured Dense LaB_6 Cathodes by Arc Plasma and Reactive Spark Plasma Sintering," Acta Mater., in press.

Zhou, W., "Role of Open Metal Sites on H_2 and CH_4 Adsorption in Metal-Organic Frameworks," in "ACS Division Proceedings, Division of Fuel Chemistry," edited by unknown, (ACS, Fall National Meeting & Exposition 2009 Conf. Proc., August 2009, Washington, D.C.) **54**(2), (2009).

Zhou, W., "Methane Storage in Porous Metal-Organic Frameworks: Current Records and Future Perspectives," Chem. Rec. **10**, 200 (2010).

Zsolt, R., Lindstrom, R.M., Mackey, E.A., Belgya, T., "Neutron-Induced Prompt Gamma Activation Analysis (PGAA)", in "Handbook of Nuclear Chemistry (2nd ed)"edited by: Klencsár, Z., Lovas, R.G., Sándor, N., Rösch, S., and Vértes, A., (Springer), in press.

Instruments and Contacts

Instruments and Contacts: (name, tel. 301-975-xxxx, email)

High Resolution Powder Diffractometer (BT-1):
- Judy Stalick, 6223, judith.stalick@nist.gov
- Qingzhen Huang, 6164, qing.huang@nist.gov
- Mark Green, 4297, mark.green@nist.gov
- Sarah Parks, 8489, sarahp@nist.gov

Residual Stress Diffractometer (BT-8):
- Thomas Gnaeupel-Herold, 5380, tg-h@nist.gov

30-m SANS Instrument (NG-7):
- Yun Liu, 6235, yun.liu@nist.gov
- Paul Butler, 2028, paul.butler@nist.gov
- Jeff Krzywon, 6650, jkrzywon@nist.gov

30-m SANS Instrument (NG-3) (CHRNS):
- Boualem Hammouda, 3961, hammouda@nist.gov
- Steve Kline, 6243, steven.kline@nist.gov
- Susan Krueger, 6734, susan.krueger@nist.gov
- Cedric Gagnon, 2020, cedric.gagnon@nist.gov

USANS, Perfect Crystal SANS (BT-5) (CHRNS):
- Andrew Jackson, 3146, andrew.jackson@nist.gov
- David Mildner, 6366, david.mildner@nist.gov
- Paul Butler, 2028, paul.butler@nist.gov

Reflectometer, Vertical Sample, Polarized Beam Option (NG-1):
- Brian Kirby, 8395, brian.kirby@nist.gov
- Julie Borchers, 6597, julie.borchers@nist.gov
- Chuck Majkrzak, 5251, cmajkrzak@nist.gov

AND/R, Advanced Neutron Diffractometer/Reflectometer (NG-1):
- Joe Dura, 6251, joseph.dura@nist.gov
- Brian Maranville, 6034, brian.maranville@nist.gov

Reflectometer, Horizontal Sample (NG-7):
- Sushil Satija, 5250, satija@nist.gov
- Bulent Akgun, 6469, bulent.akgun@nist.gov

Double-focusing Triple Axis Spectrometer (BT-7)
- Sung Chang, 8369, sung.chang@nist.gov
- Yang Zhao, 2164, yang.zhao@nist.gov
- Jeff Lynn, 6246, jeff.lynn@nist.gov

Triple-axis Spectrometer (BT-9):
- William Ratcliff, 4316, william.ratcliff@nist.gov
- Ross Erwin, 6245, rerwin@nist.gov
- Jeff Lynn, 6246, jeff.lynn@nist.gov

SPINS, Spin-polarized Triple-axis Spectrometer (NG-5) (CHRNS):
- Peter Gehring, 3946, peter@nist.gov
- Deepak Singh, 4863, deepak.singh@nist.gov

MACS, Multi-Analyzer Crystal Spectrometer (NG-0)
- Jose Rodriguez, 6019, jose.rodriguez@nist.gov
- Chris Stock, 6422, chris.stock@nist.gov

FANS, Filter-analyzer Neutron Spectrometer (BT-4)
- Terry Udovic, 6241, udovic@nist.gov
- Juscelino Leão, 8867, juscelino.leao@nist.gov

DCS, Disk-chopper Time-of-flight Spectrometer (NG-4) (CHRNS):
- John Copley, 5133, jcopley@nist.gov
- Yiming Qiu., 3274, yiming.qiu@nist.gov
- Craig Brown, 5134, craig.brown@nist.gov

HFBS, High-flux Backscattering Spectrometer (NG-2) (CHRNS):
- Madhusudan Tyagi, 2046, mtyagi@nist.gov
- Tim Jenkins, 8396, timothy.jenkins@nist.gov

NSE, Neutron Spin Echo Spectrometer (NG-5) (CHRNS):
- Antonio Faraone, 5254, antonio.faraone@nist.gov
- Jason Gardner, 8396, jason.gardner@nist.gov
- Michi Nagao, 5505, michihiro.nagao@nist.gov

Cold Prompt-gamma Neutron Activation Analysis (NG-7):
- Rick Paul, 6287, rpaul@nist.gov

Thermal Prompt-gamma Neutron Activation Analysis (VT-5):
- Rick Paul, 6287, rpaul@nist.gov

Other Activation Analysis Facilities:
- Greg Downing, 3782, gregory.downing@nist.gov

Cold Neutron Depth Profiling (NG-1):
- Greg Downing, 3782, gregory.downing@nist.gov

Neutron Imaging Station (BT-2):
- David Jacobson, 6207, david.jacobson@nist.gov
- Dan Hussey, 6465, daniel.hussey@nist.gov
- Muhammad Arif, 6303, muhammad.arif@nist.gov

Neutron Interferometer (NG-7):
- Muhammad Arif, 6303, muhammad.arif@nist.gov
- David Jacobson, 6207, david.jacobson@nist.gov
- Dan Hussey, 6465, daniel.hussey@nist.gov

Fundamental Neutron Physics Station (NG-6):
- NG-6M: Scott Dewey, 4843, mdewey@nist.gov
- NG-6U: Pieter Mumm, 8355, pieter.mumm@nist.gov
- NG-6: Jeff Nico, 4663, nico@nist.gov

Theory and Modeling:
- Joseph Curtis, 3959, joseph.curtis@nist.gov
- Taner Yildirim, 6228, taner@nist.gov

Sample Environment:
- Toby Herman, 5010, tobias.herman@nist.gov
- Julia Scherschligt, 5328, julia.scherschligt@nist.gov
- Juscelino Leão, 8867, juscelino.leao@nist.gov

User Laboratories:
- Kim Tomasi, 4533, kimberly.tomasi@nist.gov
- Yamali Hernandez, 5295, yamali@nist.gov

NIST CENTER FOR NEUTRON RESEARCH CONTACTS

Copies of annual reports, facility information, user information, and research proposal guidelines are available electronically.

Please visit our website: http://www.ncnr.nist.gov

For a paper copy of this report:

Ron Cappelletti
301-975-6221
ron.cappelletti@nist.gov

For general information on the facility:

Rob Dimeo
301-975-6210
robert.dimeo@nist.gov

Dan Neumann
301-975-5252
dan.neumann@nist.gov

For information on visiting the facility and/or user access questions:

Julie Keyser
301-975-8200
julie.keyser@nist.gov

Mary Ann FitzGerald
301-975-8200
maryann.fitzgerald@nist.gov

For information on performing research at the facility:

Bill Kamitakahara
301-975-6878
william.kamitakahara@nist.gov

Facility address:

NIST Center for Neutron Research
National Institute of Standards and Technology
100 Bureau Drive, Mail Stop 6100
Gaithersburg, MD 20899-6100
USA

NIST CENTER FOR NEUTRON RESEARCH
National Institute of Standards and Technology
100 Bureau Drive, MS 6100
Gaithersburg, MD 20899-6100

www.ncnr.nist.gov